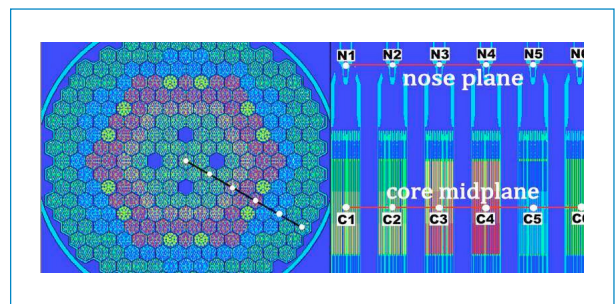
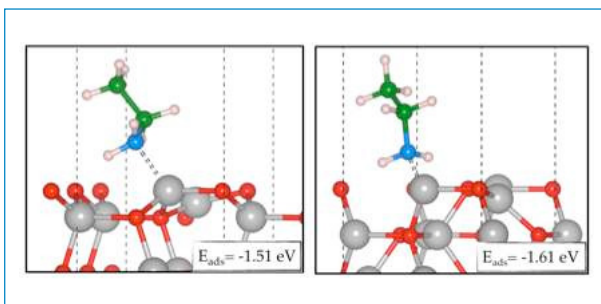
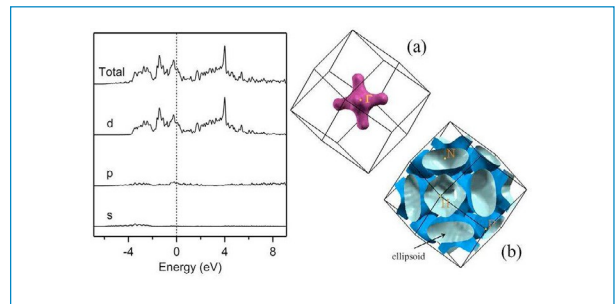
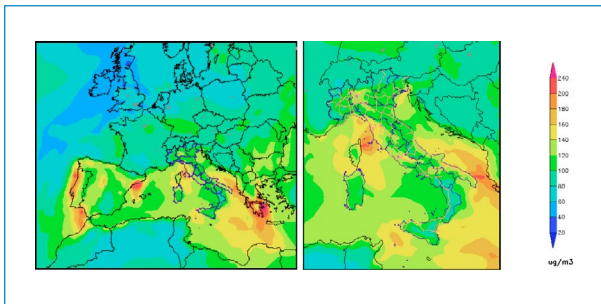
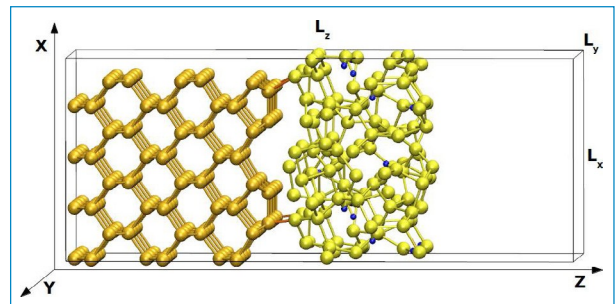
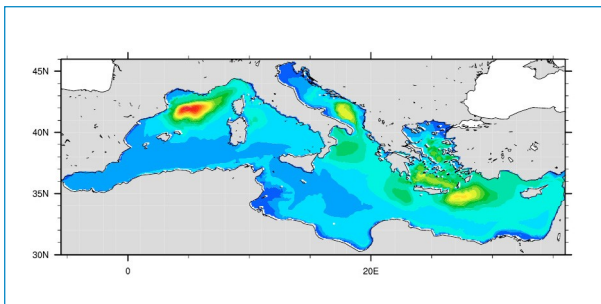


High Performance Computing on CRESCO infrastructure: research activities and results 2015



**High Performance Computing on CRESCO Infrastructure:
research activity and results 2015**

Contributions provided by a selection of users of the CRESCO infrastructure Scientific

Editor: *Giovanni Ponti*, ENEA, DTE-ICT-HPC, Research Centre Portici

Acknowledgements: We wish to thank *Gianclaudio Ferro* for providing the Reporter system (<http://hdl.handle.net/10840/5791>) to collect contributions and to build the Volume

Cover: *Amedeo Trolese*, ENEA, DTE-ICT-PRA, Research Centre Frascati

ISBN: 978-88-8286-342-5

Contents

<i>Foreword</i>	5
<i>Ab Initio Carr-Parrinello Simulations of High Temperature GeO₂: a comparison of the effects of plane waves cut-off and time step choice</i>	
<i>G. Mancini, M. Celino</i>	6
<i>Effects of preferential diffusion on turbulent lean premixed CH₄/H₂ - Air slot flames</i>	
<i>D. Cecere, E. Giacomazzi, N.M. Arcidiacono, F.R. Picchia</i>	10
<i>A homemade Fortran code to analyse results from CPMD Calculations</i>	
<i>E. Burresti, M. Celino</i>	16
<i>Inter-layer synchronization in multiplex networks</i>	
<i>I. Sendiña-Nadal, I. Leyva, R. Sevilla-Escoboza, R. Gutiérrez, J.M. Buldú, J.A. Almendral, S. Boccaletti</i>	21
<i>Atmospheric Pollution Trends simulated at European Scale in the framework of the EURODELTA 3 Project</i>	
<i>G. Briganti, A. Cappelletti, M. Mircea, M. Adani, M. D'Isidoro</i>	26
<i>MCNP simulations supporting PWR GEN-II and III safety studies and feasibility study of minor actinides irradiation in the Tapiro research reactor</i>	
<i>P. Console Camprini, K. W. Burn</i>	31
<i>Monte Carlo study of dose-area-product properties in radiotherapy photon beams with small field sizes</i>	
<i>Claudio Caporali</i>	35
<i>Simulations of linear and nonlinear interactions between alfvén modes and energetic particles</i>	
<i>S. Briguglio, G. Fogaccia, V. Fusco, M. Martone, G. Vlad, X. Wang, T. Wang</i>	39
<i>Analysis of the wave field in front of the U-OWC</i>	
<i>P. Filianoti, L. Gurnari</i>	48
<i>A novel charge-equilibration method for self assembly of organics on metal surface</i>	
<i>A. Palma, M. Satta, S. Tosti</i>	52

<i>Enlightening of water self-assembling phenomena onto the (101) TiO₂ anatase surface by atomistic multi-scale modeling</i>	
<i>F. Gala, L. Agosta, G. Zollo</i>	56
<i>Implementation of an air quality forecast system over Italy</i>	
<i>M. Adani, M. D'Isidoro, G. Briganti, A. Cappelletti</i>	63
<i>First-principles investigation of the amino acids adsorption to hydrated non-polar ZnO surface</i>	
<i>F. Buonocore, C. Arcangeli, M. Celino, F. Gala, G. Zollo</i>	68
<i>Performance analysis of CRESCO clusters by using DGEMM subroutine</i>	
<i>Simone Giusepponi</i>	74
<i>CFD Simulations of hydrocarbons reforming with CO₂ capture in a fluidised bed carbonator</i>	
<i>A. Di Nardo, S. Stendardo, G. Calchetti</i>	80
<i>CP2K performance on CRESCO4 HPC system</i>	
<i>M. Gusso</i>	84
<i>Ab-initio study of silicon based materials for photovoltaic applications</i>	
<i>S. Giusepponi, M. Gusso, M. Celino, U. Aeberhard, P. Czaja</i>	88
<i>Quantum Espresso performance on ENEA and JSC HPC infrastructures</i>	
<i>S. Giusepponi, M. Gusso, M. Celino, U. Aeberhard, P. Czaja</i>	93
<i>Electronic band structure, lattice dynamics, and related superconducting properties of niobium from first-principles calculations</i>	
<i>G. De Marzi</i>	99
<i>Language discrimination via a neural network approach</i>	
<i>A. Mariano</i>	105
<i>Web Crawling tool integration in ENEAGRID</i>	
<i>G. Santomauro, G. Ponti, F. Ambrosino, G. Bracco, A. Colavincenzo, A. Funel, G. Guarnieri, S. Migliori, M. De Rosa, D. Giammattei</i>	110
<i>Fast switching alchemical simulations: a non equilibrium approach for drug discovery projects on parallel platforms</i>	
<i>P. Procacci</i>	115

<i>Simulation of photon beams for radiotherapy application</i>	
<i>L. Silvi, M. Pimpinella</i>	124
<i>Transport study of Neon impurity seeded FTU plasma by Gyrokinetic simulations</i>	
<i>V. Dolci, C. Mazzotta, FTU team</i>	129
<i>Self-Assembly of Triton X100 in Water Solutions: A Multiscale Simulation Study Linking Mesoscale to Atomistic Models</i>	
<i>A. De Nicola, Z. Ying, M. Celino, M. Rocco, T. Kawakatsu, G. Milano</i>	135
<i>Computer Simulation of Triglycerides</i>	
<i>A. Pizzirusso, Y. Zhao, A. De Nicola, G. Milano</i>	141
<i>Biconnectivity of Very Large Social Graphs</i>	
<i>G. Chiapparo, U. Ferraro Petrillo, D. Firmani, L. Laura</i>	144
<i>Do emission policies reduce ozone risk to European forests?</i>	
<i>A. Anav, A. De Marco</i>	148
<i>Multidecadal hindcast of the mediterranean thermohaline circulation</i>	
<i>G. Sannino, A. Carillo, M.V. Struglia</i>	151
<i>The core design of Gen-IV Lead Fast Reactors using the ERANOS code on the CRESCO HPC infrastructure</i>	
<i>M. Sarotto, G. Grasso, F. Lodi</i>	155
<i>Surface functionalization of ZnO for solar energy conversion devices: new insights from a first-principles study</i>	
<i>A.M. Rodríguez, A.B. Muñoz-García, C. De Rosa, M. Pavone</i>	159
<i>Car-Parrinello molecular dynamics of liquid NaNO₃</i>	
<i>R. Grena, M. Celino</i>	164
<i>First-principle determination of equilibrium and out of equilibrium excited state properties of surfaces and 2D materials</i>	
<i>M. Marsili, O. Pulci, M.S. Prete, A. Mosca Conte, P. Gori</i>	168
<i>Study of the Zr Doping in the Cerium Oxide through First-Principles Calculations</i>	
<i>F. Rizzo, G. De Marzi</i>	174
<i>The influence of TiO₂ and Ti dopants on the hydrogen mobility through MgH₂-Mg interface</i>	
<i>R. Vujasin, J. Grbovic Novakovic, N. Novakovic, S. Giusepponi, M. Celino</i>	178

<i>The phase structure of the Naming Game in the stochastic block model</i>	
<i>F. Palombi, S. Toti</i>	182
<i>Transcriptome assembly of C. sativus</i>	
<i>A. Conte, G. Aprea, M. Pietrella</i>	187
<i>Analysis of current fast neutron-flux monitoring instrumentation targeted for the DEMO LFR ALFRED</i>	
<i>L. Lepore, R. Remetti, M. Cappelli</i>	192
<i>Analysis of the chaotic behavior of the Lower Hybrid Wave propagation in magnetised plasma by Hamiltonian theory</i>	
<i>A. Cardinali, A. Casolari</i>	198
<i>Bi(111) nanofilms: quantum confinement and surface states</i>	
<i>G. Cantele, D. Ninno</i>	202
<i>Multiphase rotating turbulent flows in gas turbine internal cooling channel</i>	
<i>D. Borello, F. Rispoli, A. Salvagni, P. Venturini</i>	206
<i>CRESCO numerical combustion analysis of swirling micro-meso combustion chambers</i>	
<i>A. Minotti</i>	210
<i>CFD modeling of a flameless furnace: comparative evaluation of turbulent combustion models with two software on a HPC platforms</i>	
<i>C. Mongiello, G. Guarneri, G. Continillo, D. Iorio, G. Maio, F.S. Marra</i>	214
<i>Role of the sub-surface vacancy in the amino-acids adsorption on the (101) anatase TiO₂ surface: a first principles study</i>	
<i>L. Maggi, F. Gala, G. Zollo</i>	220
<i>Neutronics calculations for the design of DEMO WCLL reactor</i>	
<i>R. Villari, G. Mariano, A. Del Nevo, D. Flammini, F. Moro</i>	227
<i>The network architecture underlying the CRESCO infrastructure of ENEA Portici</i>	
<i>D. Giammattei, M. De Rosa, A. Colavincenzo, R. Guadagni</i>	231

Foreward

During the year 2015, CRESCO high performance computing clusters have provided more than 46 million hours of “core” computing time, at a high availability rate, to more than one hundred users, supporting ENEA research and development activities in many relevant scientific and technological domains. In the framework of joint programs with ENEA researchers and technologists, computational services have been provided also to academic and industrial communities.

This report, the seventh of a series started in 2008, is a collection of 46 papers illustrating the main results obtained during 2015 using CRESCO HPC facilities. We registered an important increase on contributions this year, testifying the importance of the interest for HPC facilities in ENEA research community. The topics cover various fields of research, such as material science, efficient combustion, climate research, nuclear technology, plasma physics, biotechnology, aerospace, complex systems physics. The report shows the wide spectrum of applications of high performance computing, which has become an all-round enabling technology for science and engineering.

Since 2008, the main ENEA computational resources is located near Naples, in Portici Research Centre. This is a result of the CRESCO Project (Computational Centre for Research on Complex Systems), co-funded, in the framework of the 2001-2006 European Regional Development Funds Program, by the Italian Ministry of Education, University and Research (MIUR).

The Project CRESCO provided the resources to set up the first HPC x86_64 Linux cluster in ENEA, achieving a computing power relevant on Italian national scale (it ranked 126 in the HPC Top 500 June 2008 world list, with 17.1 TFlops and 2504 cpu cores). It was later decided to keep CRESCO as the signature name for all the Linux clusters in the ENEAGRID infrastructure, which integrates all ENEA scientific computing systems, and is currently distributed in six Italian sites.

In 2015 the ENEAGRID computational resources attained the level of about 8000 computing cores (in production) and a raw data storage of about 900 TB. Those values have been reached thanks to the availability of the new cluster CRESCO5 (640 cores Intel, 16.4 Tflops, QDR Infiniband network), in addition to the CRESCO3, and CRESCO4 clusters.

The success and the quality of the results produced by CRESCO stress the role that HPC facilities can play in supporting science and technology for all ENEA activities, national and international collaborations, and the ongoing renewal of the infrastructure provides the basis for an upkeep of this role in the forthcoming years.

In this context, 2015 is also marked by the signature of an agreement between ENEA and CINECA, the main HPC institution in Italy, to promote joint activities and projects. In this framework, CINECA and ENEA participated successfully to a selection launched by EUROfusion, the European Consortium for the Development of Fusion Energy, for the procurement of a several PFlops HPC system, beating the competition of 7 other institutions. The new system MARCONI-FUSION started operation in July 2016. The ENEA-CINECA agreement is a promising basis for the future development of ENEA HPC resources in the coming years.

Dipartimento Tecnologie Energetiche,
Divisione per lo Sviluppo Sistemi per l'Informatica e l'ICT
CRESCO Team

Ab Initio Carr-Parrinello Simulations of High Temperature GeO₂: a comparison of the effects of plane waves cut-off and time step choice.

Giorgio Mancini^{1*} and Massimo Celino²

¹Università di Camerino, sezione di Fisica della Scuola di Scienze e Tecnologie, Via Madonna delle Carceri 62032, Camerino (MC), Italy

²ENEA, Ente per le Nuove Tecnologie, l'Energia e lo Sviluppo Economico Sostenibile
C. R. Casaccia, Via Anguillarese 301, 00123 Roma, Italy

ABSTRACT. Ab initio Carr-Parrinello simulations of high temperature GeO₂ have been carried out using a set of different parameters supposedly significantly affecting the results, as well as the computing times. A particular attention has been paid to the effects related with the plane waves cut-off using lower and higher values than commonly suggested. Comparisons of the results for the different values are presented and illustrated indicating that the results are essentially the same.

1 Introduction

We have recently presented the preliminary results of the simulations of a 240 atoms, high temperature GeO₂ system, entirely carried out by *ab initio* (AI) molecular dynamics (MD) simulations using the CPMD (Carr-Parrinello Molecular Dynamics) software [1]: an approach distinct from the ones consisting in using classical molecular dynamics (CMD) results for GeO₂ at much higher temperatures (4000-7000K) as starting configurations for AI simulations to be carried out at lower final temperatures [2]. The main reason to adopt such a hybrid approach is that it allows to bypass both the limitations due to the short time scale accessible from *ab initio* simulations and the usually long, delicate, often unsuccessful process needed to prepare a “stable” system to start with (CPMD simulations on unstable systems abruptly diverge even from the very first runs at temperatures as low as 10~50K).

As for the computation times required by *ab initio* simulations, once the general frame in which they are carried out is set (let's simplistic say, once functionals and pseudo-potentials are chosen), they only depend on the values used for both the time step and the kinetic energy cut-off for electronic plane waves expansion: they must respectively be taken to be short and high enough to allow for meaningful, correct simulations; but shorter time steps and higher cut-offs mean longer computational times and/or larger computational resources.

In the results we have previously presented for GeO₂ [3], strictly abiding by the prescriptions given in the CPMD user's manual for such a choice [4], we have used a time step of 5 a.u (~0.121 fs) and a value of 60 Ry for the plane waves cut-off: respectively a higher and a lower value than the ones commonly suggested and used in literature (3 a.u. and 70-75 Ry) [1, 5].

To evaluate the extent of the possible differences on the results as a consequence of a more demanding choice of such parameters, we have carried out two additional CPMD simulations series to obtain high temperature GeO₂ using higher cut-offs values (80 and 90 Ry) on the same initial system we previously studied.

*Corresponding author. E-mail: giorgio.mancini@unicam.it

2 Computational resources

The calculations have been performed by using the facilities and services available at the ENEA GRID infrastructure (Italy). Molecular Dynamics simulations have been carried out using CPMD v3.15.1 on CRESCO4 cluster, using 512 processors per run, 400 GB of disk storage has been granted on the PFS/porq1_1M file system.

3 Computational details

We have performed three separated series of Carr-Parrinello, first-principles simulations on a GeO₂ system consisting of 240 atoms; the series correspond to kinetic energy cut-off values for plane waves expansion of 60, 80 and 90 Ry, respectively. The initial GeO₂ configuration to start the simulations on has been generated placing 80 germanium and 160 oxygen atoms at random in a cubic simulation box of linear dimensions $L=15.602$ angstroms, corresponding to a density $\rho = 3.66$ gr/cm³; the only condition imposed has been their distances being larger than certain suitable values [3].

To perform CPMD simulations, we have adopted the generalized gradient approximation (GGA) for the exchange and correlation part of the total energy and norm conserving pseudo-potentials with the BLYP exchange–correlation functional using the Troullier–Martins parametrization for the core-valence interactions.

We have run the wave-function optimization processes imposing that the wave-functions be converged very well by setting a very strict convergence criterion ($GEMAX < 10^{-13}$) [4]. The subsequent geometry optimizations too have been performed setting a stricter convergence criterion than usual ($GNMAX < 10^{-6}$) [4]. An integration time step of 3 a.u. (0.072fs) has been used for the initial optimizations. After wave function and geometry optimizations, Carr-Parrinello molecular dynamics simulations have been carried out on the systems heated up and equilibrated at 10K, 50K, 100K, 150K, 200K, respectively, and up to 3000K by steps of 100K.

To allow for shorter equilibration times, “massive” thermostating has been used for the ions (a Nosé-Hoover chain thermostat placed on each ionic degree of freedom). A second Nosé-Hoover chain thermostat has been set on the electronic degrees of freedom to keep electrons on the Born-Oppenheimer surface throughout all MD simulations. Characteristic thermostats frequency of 1000 cm⁻¹ for ions and 10000 cm⁻¹ for electrons have been used. The default value of 400 a.u. has been used for the fictitious electronic mass.

The integration time step of 5 a.u. (0.12fs) used on the entire temperature range for the 60 Ry cut-off have turn out to be too long for the higher cut-offs since the very beginning (the simulations at 5K have diverged after a few steps). We are not able to tell whether this is a generalized behaviour or not, but we systematically have experienced it on several configurations. Consequently a time step of 3 a.u. has been used for the 80 and 90 Ry (this turned out to be the longest possible time step at all temperatures for us to have stable simulations).

On a computer equipped with SD hard disks, 64 GB ram (much larger than effectively used) and a last generation Intel I7 on which CPMD runs on twelve almost perfectly balanced parallel threads, the required time per single step of CPMD has dramatically grown when switched from 60 Ry to 80 or 90 Ry. On the contrary, when run on CRESCO4 cluster batch queues, 512 cpu's have proved sufficient to obtain the same computation times per single CPMD step for all the cut-offs values. As a matter of facts, on the I7, the required times for 80 and 90 Ry were practically the same and approximately three times those for 60 Ry; on the other hand, the simulations for 60 and 90 Ry have run about ten and thirty times faster on CRESCO4 than on I7. In conclusion, the simulation pro-

cesses times have depended only on the time step; the higher cut-offs requiring a time almost twice longer than for 60 Ry: a ratio not to neglect when it comes to *ab initio* simulations.

4 Results and conclusions.

It is important to notice how the geometry optimization processes have determined different initial positions for the three systems, so that they have undergone independent, separate evolutions in time and temperature from the very beginning. Since the simulations have begun at different times, we have compared them in the common time interval they have covered: a total time of 36 ps, 16 ps of which spent at 3000K.

The results of the simulations are depicted in figs. 1-3, showing radial distribution and static structure functions. Similar, almost superposing, results hold for $dn(r)$, angles and bonds distributions.

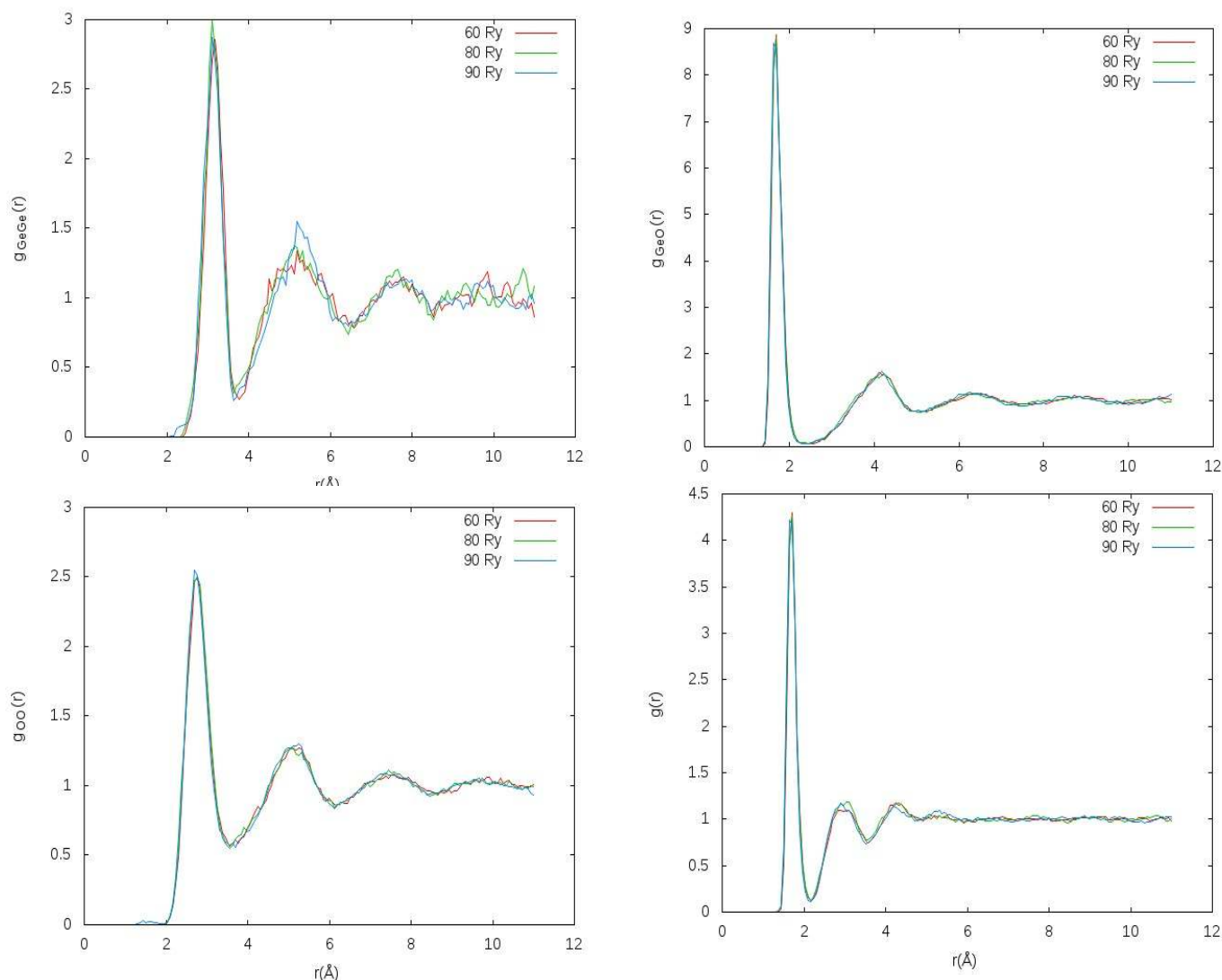


Fig. 1: Partial and total radial distribution functions for cut-offs 60, 80 and 90 Ry.

The simulations have essentially led to the same results for all relevant properties, thus validating the choice of using lower wave-function expansions cut-off for shorter simulations times to get the maximum possible efficiency while maintaining accuracy.

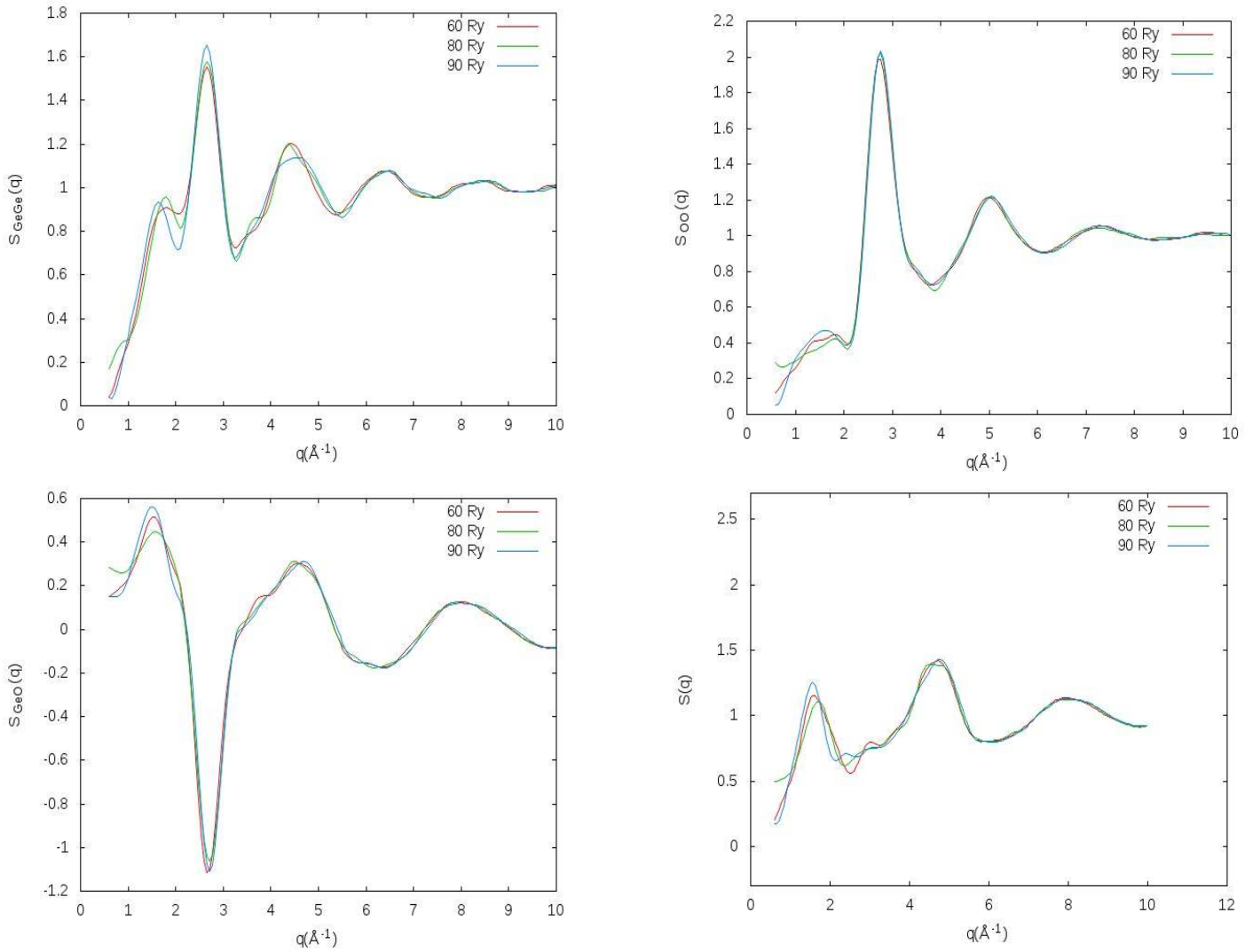


Fig. 2: Partial and total static structure functions for cut-offs 60, 80 and 90 Ry.

References

- [1] CPMD, *Copyright IBM Corp 1990-2008, Copyright MPI für Festkörperforschung Stuttgart 1997-2001.*
- [2] M. Hawlitzky, J. Horbach, S. Ispas, M. Krack, and K. Binder. “*Comparative classical and ab initio molecular dynamics study of molten and glassy germanium dioxide*”. *J. Phys. Condens. Matter* **20** (2008) 285106 (15pp)
- [3] G Mancini, M. Celino, and A. Di Cicco. “*Ab-Initio Molecular Dynamics Simulation of High Temperature GeO₂*”. *High Performance Computing on CRESCO infrastructure: research activities and results 2014*, ISBN: 978-88-8286-325-8 (2015) pp. 46-49.
- [4] The CPMD Consortium. “*Car-Parrinello Molecular Dynamics: An ab initio Electronic Structure and Molecular Dynamics Program. Manual for CPMD, version 3.15.1*”.
- [5] Peter Broqvist, Jan Felix Binder, Alfredo Pasquarello. “*Atomistic model structure of the Ge(100)–GeO₂ interface*”. *Microelectronic Engineering* **86** (2009) pp. 1589–1591,

EFFECTS OF PREFERENTIAL DIFFUSION ON TURBULENT LEAN PREMIXED CH₄/H₂ – Air SLOT FLAMES

D. Cecere^{1*}, E. Giacomazzi¹, N.M. Arcidiacono¹ and F.R. Picchia¹

¹*Process and Energy Systems Engineering Laboratory, ENEA, Rome, Italy.*

ABSTRACT. Nowadays, in the context of CO₂ reduction and gas turbine fuel flexibility, the interest in acquiring know-how on lean Hydrogen Enriched Natural Gas (HENG) is growing. This article provides a detailed analysis of a turbulent ($Re_{jet} = 2476$, $Re_t = 236$) lean ($\Phi = 0.7$) CH₄/H₂ – air premixed slot flames (unconfined and at atmospheric pressure) highlighting the effects of two different hydrogen contents in the inlet mixture (20% and 50% by volume). The data were generated and collected setting up a three-dimensional numerical experiment performed through the Direct Numerical Simulation (DNS) approach and using high-performance computing. Finite difference schemes were adopted to solve the compressible Navier-Stokes equations in space (compact sixth-order in staggered formulation) and time (third-order Runge-Kutta). Accurate molecular transport properties and the Soret effect were also taken into account. A detailed skeletal chemical mechanism for methane-air combustion, consisting of 17 transported species and 73 elementary reactions, was used. The analysis reports average and rms fluctuation of velocity components, temperature and main chemical species mass fractions. New scientific insight is delivered by analysing the probability density functions of several quantities: curvature, shape factor, alignment between vorticity vector and flame surface normal, displacement speed and its components. Correlations between the flame thickness and the progress variable and curvature are also investigated, as well as correlation between strain rates and curvature, and equivalence ratio and curvature. An expression of displacement speed, with diffusion terms taking into account differential diffusion of progress variable species components is derived. The effect of thermal diffusion is also considered. The effects of differential diffusion of several species on the local equivalence ratio are quantified: the maximum variation from the nominal inlet value is $\sim 9\%$ and it is due to H₂ and O₂. The addition of Hydrogen reduces the displacement speed at negative curvatures in a range that depends on the local progress variable value, with a maximum variation of -33% between the two flames. The database will also be helpful to validate subgrid models for Large Eddy Simulation.

1 Test case definition

The test case defined for this study consists in an unconfined premixed slot-burner flame at atmospheric pressure. A slot-burner Bunsen configuration is especially interesting due to the presence of a mean shear in the flow. The configuration is similar to that of the experimental device already analysed in [1] but with smaller dimensions ($h = 1.2\text{mm}$ vs 25.4mm of slot width in the experimental setup) and higher bulk velocities (100m/s) compared to experiment (3 to 12m/s) to artificially decrease the hydrodynamic DNS times. It consists of a central slot-jet of premixed reactants surrounded on both longer sides by two

*Corresponding author. E-mail: donato.cecere@enea.it.

Case	Φ	n_{H_2}	T_u	T_b	S_L^{nS}	δ_L^{nS}	S_L^{S}	δ_L^{S}	δ_D^{S}
A	0.7	0.2	600	2072	1.03	0.368	1.01	0.378	0.1329
B	0.7	0.5	588	2084	1.37	0.314	1.34	0.315	0.1096

Table 1: CH_4/H_2 –Air laminar flames characteristics (A-B) based on the 17-species chemical mechanism adopted in the present DNS [5]. The number of Hydrogen moles n_{H_2} is defined as $n_{\text{H}_2} = x_{\text{H}_2}/(x_{\text{H}_2} + x_{\text{CH}_4})$. The superscripts *nS* and *S* in the laminar flame speed and flame front thickness, respectively stand for “no Soret” and “Soret” effect not included and included in the laminar flame calculation. Units: [K] for temperature, [m/s] for flame speed, [mm] for flame front thickness.

Jets A (B)	$U_{0,in}$	T_{in}	u'_{in}	$\delta_{z,in}^{corr}$	L_{Duct}	h
Central	100 (100)	600 (588.5)	12 (12)	0.4	4	1.2
Surrounding	25 (25)	2072 (2084)	0.01 (0.01)	0.1	-	-

Table 2: Boundary conditions imposed at the inlet of the three channels. In particular, $u'_z = u'_x = u'_y$ and $\delta_{z,in}^{corr}$, $\delta_{x,in}^{corr} = \delta_{y,in}^{corr} = \delta_{z,in}^{corr}/2$ are used as input to the Klein procedure to produce synthetic turbulence at the inlet of the three channels. Units: [m/s] for velocity, [K] for temperature, [mm] for turbulent correlation length scale, duct length, L_{Duct} , and its width, h .

coflowing jets. The central slot-duct is 1.2 mm wide (h) and 4 mm long; its two walls have a thickness $h_w = 0.18$ mm and are assumed adiabatic in the simulation.

The central jet is a lean (equivalence ratio $\Phi = 0.7$) mixture of methane, hydrogen and air with fuel molar fractional distribution of 20% H_2 and 80% CH_4 for the flame A, and of 50% H_2 and 50% CH_4 for the flame B. Mixture temperature is 600 K for flame A, and 588 K for flame B: the latter lower temperature was chosen to achieve the same kinematic viscosity and Reynolds number for the central reactive jet in the two simulations. The surrounding jets have the composition and temperature of the combustion products of the laminar freely propagating flame associated to the central jet mixture. The unstrained laminar flame properties at these conditions computed using Chemkin [2] are summarized in Table 1. In this table, Φ represents the multicomponent equivalence ratio of the reactant jet mixture, $\Phi = [(X_{\text{H}_2} + X_{\text{CH}_4})/X_{\text{O}_2}]/[(X_{\text{H}_2} + X_{\text{CH}_4})/X_{\text{O}_2}]_{\text{stoich}}$, T_u is the unburnt gas temperature, T_b the burnt gas temperature, S_L represents the unstrained laminar flame speed and $\delta_{\text{th}} = (T_b - T_u)/|\partial T/\partial x|_{\text{max}}$ is the flame front thermal thickness based on the maximum temperature gradient.

The central jet has a velocity of 100 m/s (imposed as a mean plug-flow at the inlet of the 4 mm long central duct). Homogeneous isotropic turbulence is artificially generated at the inlet of the central duct by forcing a turbulent spatial correlation scale in the streamwise direction $\delta_{z,in}^{corr} = 0.4$ mm and a streamwise velocity fluctuation $u'_z = 12$ m/s used as inputs to the Klein’s procedure [3] (see Table 2). The surrounding flows have a velocity of 25 m/s (imposed as a mean plug-flow) and no turbulence is forced. The actual jet Reynolds number based on the centerline streamwise velocity peak at the central duct exit and its width h is $Re_{jet} = U_o h/\nu = 2476$. Other parameters characterizing the present lean premixed turbulent flame are reported in Table 3. These parameters locate the present flames in the Thin Reaction Zone of the combustion diagram.

The computational domain is composed of four structured blocks and its characteristics are summarized in Table 4. The domain size in the streamwise (z), crosswise (y) and spanwise (x) directions is $L_x \times L_y \times L_z = 24h \times 15h \times 2.5h$, h being the slot width ($h = 1.2$ mm). The grid is uniform only in the x spanwise direction ($\Delta x = 20 \mu\text{m}$), it is refined in the y and z direction near the inlet duct walls and coarsened (up to $\Delta y \sim 250 \mu\text{m}$) only in the y direction far from the central jet at the surrounding ($y > 0.015$ m) where non reflecting boundary conditions are applied and fluctuations are small. The domain is almost identical and the resolution is the same of the work of Richardson et al. [4] and Sankaran et al. [5]. The DNS was run at atmospheric pressure using a 17 species and 73 elementary

Jet exit velocity peak, U_0 [m s^{-1}]	110
Jet exit velocity fluctuation, u' [m s^{-1}]	12
Jet exit turbulent length scale, L_t [mm]	1.05
Jet Reynolds number, $Re_{jet} = U_0 h / \nu$	2476
Turbulent Reynolds number, $Re_t = u' L_t / \nu$	236
Kolmogorov length scale, η_K [μm]	17.42
Turbulent/chemical speed ratio, u' / S_L	11.88 (8.95)
Turbulent/chemical length scale ratio, L_t / δ_L	2.78 (3.22)
Damkohler number, $S_L L_t / u' \delta_L$	0.238 (0.371)
Karlovitz number, $(\delta_L / \eta_K)^2$	471 (329)

Table 3: Actual turbulent combustion parameters characterizing the simulated $\text{CH}_4/\text{H}_2 - \text{Air}$ lean premixed flames (flame B in parentheses). The turbulent velocity fluctuation and the integral length scale were evaluated at the center of the exit of the central slot-duct. The laminar flame speed and the flame front thickness including the Soret effect were assumed as combustion parameters. The kinematic viscosity used in the calculation of the central jet Reynolds number is that of the inlet $\text{CH}_4 - \text{H}_2/\text{Air A}$ mixture, $\nu = 5.327 \cdot 10^{-5} \text{ m}^2 \text{ s}^{-1}$. It is observed that sometimes the Karlovitz number is estimated using the diffusive thickness: with this definition $Ka = 58$ for flame A, and $Ka = 40$ for flame B.

Domain size ($L_x \times L_y \times L_z$)	$24h \times 15h \times 2.5h$
$N_x \times N_y \times N_z$	$1550 \times 640 \times 140$
Minimum grid space	$9 \mu\text{m}$

Table 4: Characteristics of the computational domain. Note that L_x , L_y and L_z refer to the spanwise, crosswise and streamwise directions, respectively.

reactions kinetic mechanism [5]. Periodic boundary conditions were applied in the crosswise direction, while improved staggered non-reflecting inflow and outflow boundary conditions (NSCBC) were adopted at the edges of the computational domain in the y and z directions [6, 7].

The simulation was performed on the linux cluster CRESCO (Computational Center for Complex Systems) at ENEA requiring 1.5 million CPU-hours running for 20 days on 3500 processors. The solution was advanced at a constant time step of 2.3 ns; after the flame reached statistical stationarity, the data were collected through $4\tau_U$, $\tau_U = 0.218 \text{ ms}$ being the flow through time based on the jet exit duct centerline velocity and the total streamwise domain length.

2 Results and discussion

In order to investigate the effect on local mixture equivalence ratio of differential and thermal diffusion associated with light species as H_2 and H , the local equivalence ratio Φ , is shown for both flames in Fig. 1 as a function of the normalized curvature at different values of the progress variable. The results are obtained from two DNS in which the diffusion term J_n is calculated with only the first term and the complete expression of Eq. (1), respectively.

$$\mathbf{J}_n = -\rho \frac{W_n}{W_{mix}} D_n \nabla X_n - \rho Y_n D_n^T \frac{\nabla T}{T}, \quad (1)$$

The equivalence ratio Φ is positively correlated with curvature at all progress variable iso-surfaces; the strongest variation is seen in the reaction zone ($c \sim 0.7$). This positive correlation can be explained by considering that H_2 and H are preferentially focused into areas with positive curvature and defocused from areas of negative curvature. The further influence of thermal diffusion is that of enhancing the

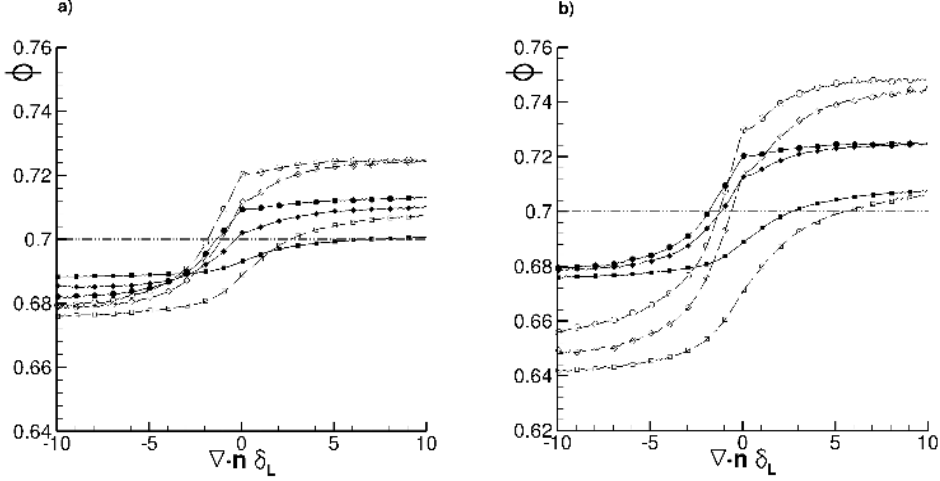


Figure 1: Equivalence ratio at different levels of the progress variable c as a function of the normalized curvature: (\circ) $c = 0.7$, (\diamond) $c = 0.6$, (\square) $c = 0.4$, (Dash dot dot line) nominal flame equivalence ratio Φ . (a) Flame A: (solid line) without Soret effect, (dashed line) with Soret effect. (b) Flame A and B with Soret effect: (solid line) flame A, (dashed line) flame B.

positive correlation with curvature since it promotes diffusion of light molecules towards high temperature regions. In fact, the maximum equivalence ratio variation is $\sim 3.7\%$ for flame A and $\sim 9\%$ for flame B when thermal diffusion effects are considered in the simulation ($\sim 2.6\%$ for flame A when only differential diffusion effect is considered).

The local enrichment of the flame at positive curvatures is also shown in Fig. 2 for the flame A, where the instantaneous flame surface ($c \sim 0.72$) coloured by the normalized mean curvature $\nabla \cdot \mathbf{n} \delta_L$, is shown together with two instantaneous iso-surfaces of the equivalence ratio ($\Phi = 0.657$ and 0.757). While in the laminar flame, the effect of the differential diffusion is only a reduction of the equivalence ratio towards leaner condition, in the 3D DNS, the effect of positive curvature (e.g., see the progress variable isosurface at $c = 0.72$ coloured in yellow in Fig. 2) produces also local enrichment of the flame (e.g., see the orange Φ grid surface in Fig. 2).

In order to quantify differential diffusion effects in the two flames, the general method of Sutherland [9, 8] is adopted, and the contribution of major species (H_2, O_2, H, CH_4) differential diffusion term k_i to the local variation of mixture fraction, is calculated as:

$$k_i = \nabla \cdot \mathbf{j}_i^c, \quad \mathbf{j}_i^c = \gamma_i W_i \nabla \cdot \left[\frac{\rho}{W_{Mix}} (D_i - D) \nabla X_i \right] \quad (2)$$

where $\gamma_i = \sum_{e \in N_e} \delta_e \alpha_{e,i}$, δ_e are the elemental mass fraction weights of Bilgers's mixture fraction, N_e the number of element e defining the mixture fraction, $\alpha_{e,i}$ is the number of atoms of element e in species i , D the diffusivity of the mixture fraction [8], D_i the species mass diffusivity.

Figures 3a-b show the species mixture fraction source terms, as a function of curvature within the flame brush for both flames at two progress variable values. At the leading edge, the largest contribution to the decrease of the mixture fraction at negative curvatures, is due to the k_{O_2} and k_{H_2} , that for flame B (that presents a greater decrease of equivalence ratio with respect to flame A for negative curvatures, see Fig.1b) are both negative. For positive curvatures, and for both flames, the positive value of k_{O_2} for $\nabla \cdot \delta_L > 1$ is counteracted by the negative value of k_{H_2} . This reduces the increase of equivalence ratio since k_H is negative and k_{CH_4} is negligible for positive curvatures. At the trailing edge of the flame (see circles in Fig.1b), the increase of the equivalence ratio is observed for $\nabla \cdot \delta_L > -2$, ($\nabla \cdot \delta_L > -1$) for flame A (flame B). The term k_{O_2} is a source for the mixture fraction for $\nabla \cdot \delta_L > -2$ and it is of

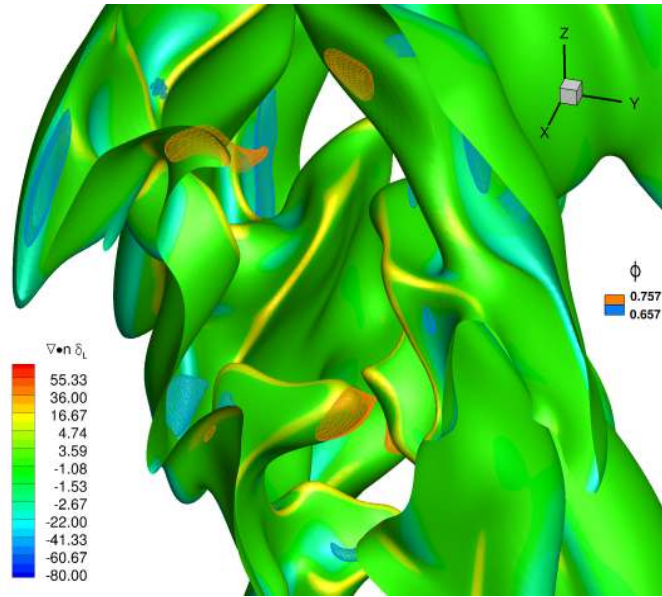


Figure 2: Instantaneous snapshot of the progress variable iso-surface at $c = 0.72$ coloured with normalized curvature $\nabla \cdot \mathbf{n}\delta_L$ and two iso-surfaces of equivalence ratio at $\phi = 0.657$ (blue) and $\phi = 0.757$ (orange), respectively, for the flame A.

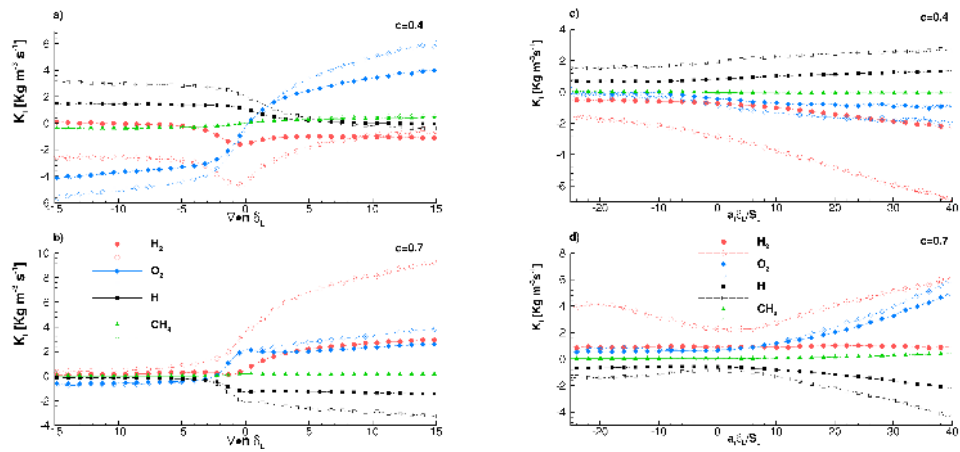


Figure 3: Species differential diffusion source index k_i at two level of the progress variable c as a function of the normalized curvature (a,b) and normalized strain (c,d) for flame A (solid line) and B (dashed line).

the same order for both flames for positive curvatures. In the enriched flame, the k_{H_2} term presents a strongly positive correlation with curvature, and despite the bigger counteracting effect of k_H , it is responsible for the bigger increase of equivalence ratio at positive curvatures of flame B.

Figures 3c-d show the species differential diffusion coefficient as a function of tangential strain rate. The source term related to CH_4 (with $Le \sim 1$) has no correlation with strain. At the leading edge, flame A is weakly affected by tangential strain, the k_{O_2}, k_{H_2} are negative, but counteracted by the positive value of k_H . In flame B the k_{H_2} has a negative correlation with strain; despite the positive correlation of k_H , the net effect is a decrease of the equivalence ratio. At the trailing edge, there is an increase of the equivalence ratio that has a positive correlation with the module of the strain for both flames (with a greater correlation for flame B). The k_{H_2} term is always positive for both flames; while for flame A is approximately constant, it has a stronger positive correlation with the module of strain in flame B. For flame A, the equivalence ratio is approximately constant for compressive strains, since the negative k_H counteracts the positive value of k_{O_2} . For positive strain, the equivalence ratio trend follows that of k_{O_2} . The greater correlation of equivalence ratio of flame B (that for positive strain has a thinner structure than flame A) is completely related to k_{H_2} and k_{O_2} trends.

References

- [1] S.A. Filatyev, J.F. Driscoll, C.D. Carter, J.M. Donbar, Measured properties of turbulent premixed Flames for model assessment, including burning velocities, stretch rates, and surface densities, *Combust. Flame* 141, 1-21, 2005.
- [2] R.J. Kee, G. Dixon-Lewis, J. Warnatz, M.E. Coltrin, Miller JA, Moffat HK, The CHEMKIN Collection III: Transport, San Diego, Reaction Design, (1998).
- [3] M. Klein, A. Sadiki, J. Janicka, A digital filter based generation of inflow data for spatially developing direct numerical or large eddy simulations, *J. Comput. Phys.* 186, (2003), 652-665.
- [4] E.S. Richardson, R. Sankaranb, R.W. Grout, J.H. Chen, Numerical analysis of reaction-diffusion effects on species mixing rates in turbulent premixed methane-air combustion, *Combust. Flame* 157 (2012) 506-515.
- [5] R. Sankaran, E.R. Hawkes, J.H. Chen, T. Lu, C.K. Law, Structure of a spatially developing turbulent lean methane-air Bunsen flame, *Proc. Combust. Inst.*, 31, (2007) 1291-1298.
- [6] T.J. Poinso, S.K. Lele: Boundary Conditions for Direct Simulations of Compressible Viscous Flow. *J. Comput. Phys.*, 101:104-129 (1992).
- [7] J.C. Sutherland, C.A. Kennedy, Improved boundary conditions for viscous, reacting, compressible Flows, *J. Comput. Phys.*, 191:502-524, 2003.
- [8] Fabrizio Bisetti, J.-Y. Chen, Jacqueline H. Chen, Evatt R. Hawkes, Differential diffusion effects during the ignition of a thermally stratified premixed hydrogen-air mixture subject to turbulence, *Proc. Combust. Inst.* 32 (2009) 1465-1472.
- [9] J.C. Sutherland, P.J. Smith, J.H. Chen, Quantification of differential diffusion in non premixed systems, *Combust. Theory Model.* 9, (2005) 365-383.

A HOMEMADE FORTRAN CODE TO ANALYSE RESULTS FROM CPMD CALCULATIONS

E. Burrese^{1*}, M. Celino²

¹ENEA, SSPT Department, PROMAS Division, MATAS Laboratory, C.R. Brindisi

²ENEA, DTE Department, ICT Division, C.R. Casaccia, Rome

ABSTRACT. In order to analyse the ab-initio molecular dynamics trajectories computed by the CPMD (Car-Parrinello Molecular Dynamics) code, we needed to build a customized software package, named QDprop, which is able to manage efficiently its large data outputs. The software package is used to detect the interesting chemical and physical processes happening during the atomic scale dynamics of the system and to calculate the associate structural and electronic properties. The materials which were characterized are quantum dots with spherical and prismatic shape. This software is written in Fortran language and actually does not work in parallel mode. The software has been tested on CdS nanostructures (for quantum dots applications) to analyse their chemical behaviour in the range of temperatures used in the experimental laboratories. Indeed during their production, the temperature can modify their atomic scale structures and thus their chemical and optical properties. Since this modifications are difficult to measure experimentally during the production phase a modeling approach is needed in order to optimize the at the nanoscale the final chemical and physical properties

1 A Fortran code to analyse the dynamic of nanoclusters

A preliminary version of the code was used to analyse structural properties of single wurtzite CdS quantum dots [1], by correlating these properties to the electronic behaviour [2]; the code was named QDprop. Recently, a new version of this code has been realized and employed to analyse a CdS nanocluster with prismatic shape. Actually, the code works only for two classes of atoms, typically chalcogens and metals, considering also the different symmetries.

A brief scheme of the algorithm as it is built is reported in Figure 1.

*Corresponding author: emiliano.burrese@enea.it

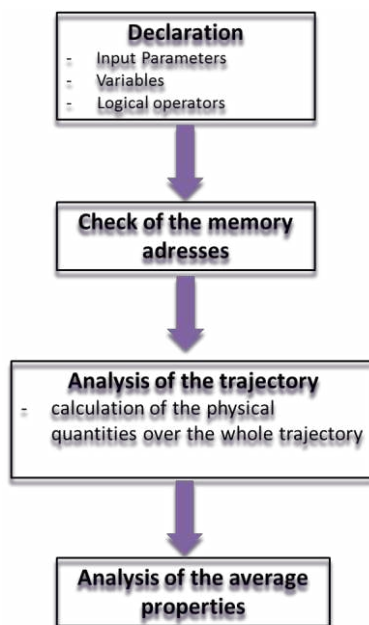


Fig 1: General overview of QDprop

The initial part of the code is dedicated to the static allocation of the memory, declaration of the variables and definition of the input data. The CPMD trajectory is stored in a file named TRAJECTORY (or TRAJ.xyz) where each configuration is written after some number of step (controlled in CPMD input); so that the dimension of this large matrix is an input of the program. The most important input parameters are:

- Size of the matrix of the trajectory (integer)
- Number di atoms specie 1 and number of atoms specie 2 (integer)
- Number of step of the dynamics (integer)
- Atomic number of the atoms (integer)
- Atomic mass of the atoms (real)
- Logical variable to print the results (integer)
- Restart variable which defines the point where the algorithm starts to analyse the trajectory (integer)
- Number of configuration used to calculate the averages (integer)
- Core radius which defines the core and surface layer (real)

In addition, before of the subroutine dedicated to the calculation, a little subroutine is called in order to check the memory addresses. After these primary steps, we show the core of the algorithm in Figure 2.

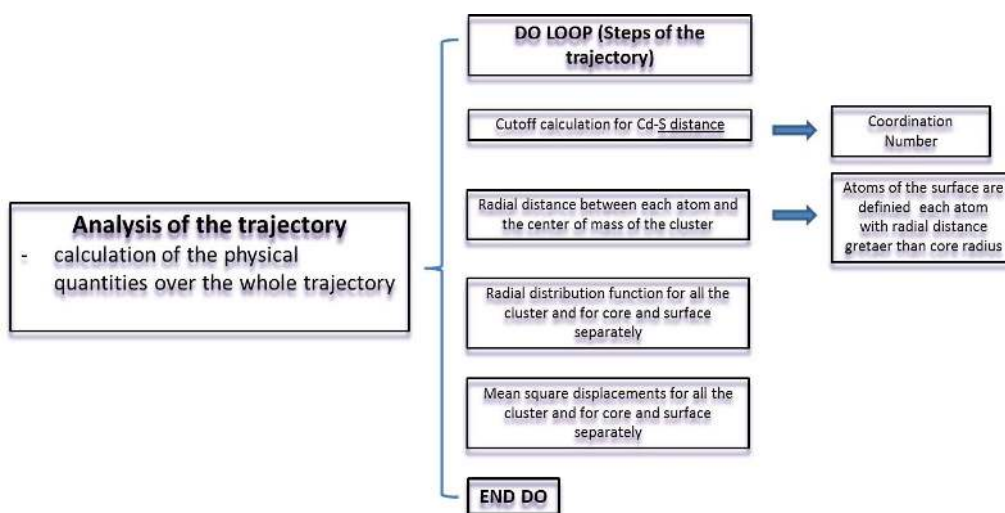


Fig 2: Flowchart of QDprop

For analysing the trajectory a cycle do-loop is executed over the number of steps of the trajectory; for each step of the trajectory, in order to count the number of atoms nearest neighbours, the cutoff of the distance Cd-S is determined. In addition, in order to define the superficial layers the radial distance between each atoms and the center of mass is calculated; if the radial distance is greater than core radius then the atom belongs to the superficial layer. Once we defined the atoms for the surface and for atoms of the core, RDF and MSD were obtained both for core and surface and for the whole cluster. The last section of this algorithm regards the calculation of the average properties. The code allows to set the number of the configurations for calculating the averages; this parameters is an input variable. In Figure 3 we report the average quantities obtained by using this code.

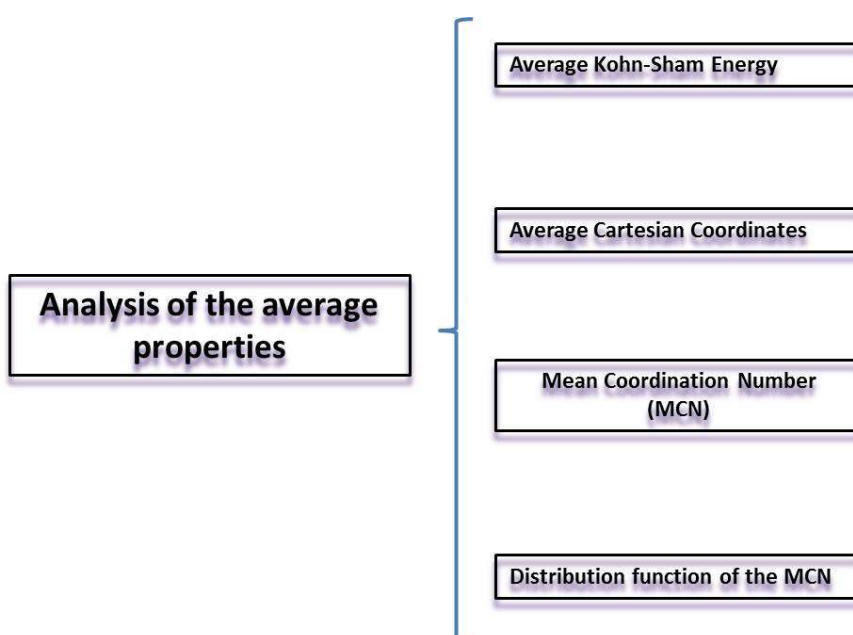


Fig 3: The last section of the code is dedicated to the calculation of the averages properties

The main physical quantities obtained from the code are printed in files ASCII and available for data analysis using software like OriginLAB or Excel.

Regarding the electronic properties, the code performs the calculation of the total and partial density of the electronic states, as well as the inverse participation ratio IPR function. Actually the electronic and the structure properties are calculated separately and the routine for electronic properties will be implemented into QDprop as soon as possible.

2 Application

Previous versions of this code were used to study the dynamics of nanocluster from CPMD data; for example in [1] and [2] as well as in the last CRESCO reports [3,4]. Generally, on the CRESCO platform the average time to perform the analysis of a single step of the trajectory is around 10 seconds. Generally, trajectories are very large because several picoseconds of dynamics are stored during the quantum simulation. The main critical issue is the memory allocation, however new software strategies are under consideration that will be implemented in the next version of the code.

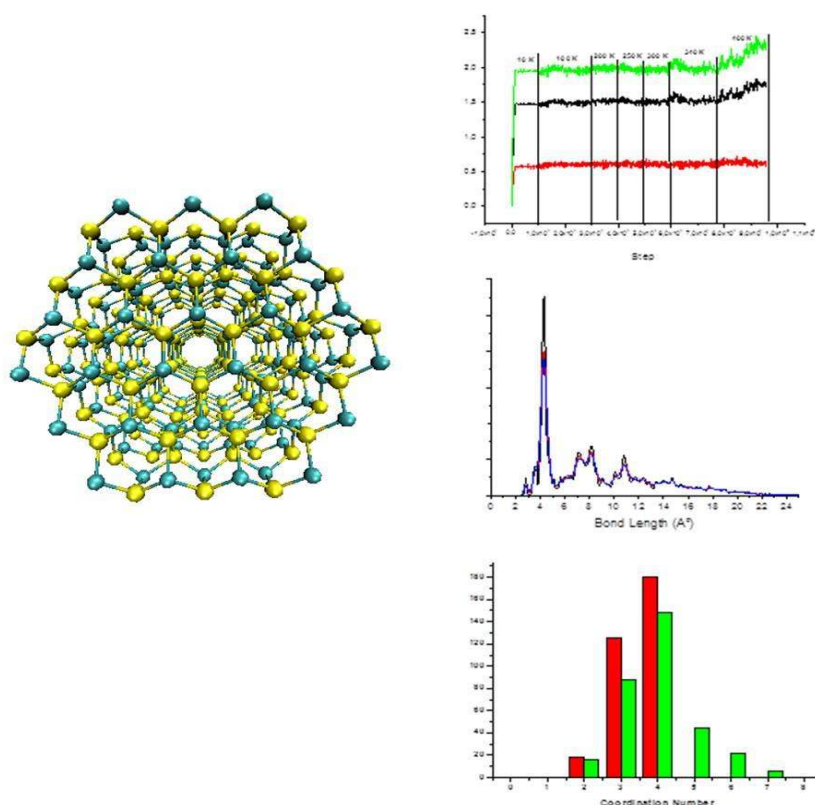


Fig 4: Cluster di CdS has been reported together some results obtained with QDprop

In our last work, not yet published, this code has been used to analyse the trajectory from CPMD calculations of the cluster built with 162 atoms of cadmium and 162 atoms of sulfur. Another cluster that we would simulate is ZnS with spherical shape. The CdS cluster and some graphical output from QDprop are reported in Figure 4.

Reference

- [1] E.BURRESI, M. CELINO “*Methodological approach to study energetic and structural properties of nanostructured cadmium sulfide by using ab-initio molecular dynamics simulations*”. Solid State Science 14 (2012) pp. 567-573
- [2]E. BURRESI, M. CELINO “*Surface states and electronic properties for small cadmium sulfide nanocluster*” (2013), Nanoscience and Nanotechnology Letters 5 pp.1182-1187
- [3] E. BURRESI, M. CELINO (2014) in High Performance Computing on CRESCO infrastructure: research activities and results 2013 ISBN: 978-88-8286-325-8
- [4] E. BURRESI, M. CELINO in High Performance Computing on CRESCO infrastructure: research activities and results 2014 (2015) ISBN: 978-88-8286-325-8

INTER-LAYER SYNCHRONIZATION IN MULTIPLEX NETWORKS

I. Sendiña-Nadal^{1,2}, I. Leyva^{1,2*}, R. Gutiérrez⁴, R. Sevilla-Escoboza³, J.M. Buldú^{1,2}, J. A. Almendral^{1,2} and S. Boccaletti^{5,6}

¹*Complex Systems Group & GISC, Universidad Rey Juan Carlos, 28933 Móstoles, Madrid, Spain*

²*Center for Biomedical Technology, U. Politécnica de Madrid, 28223 Pozuelo de Alarcón, Madrid, Spain*

³*Centro Universitario de los Lagos, Universidad de Guadalajara, Jalisco 47460, Mexico*

⁴*School of Physics and Astronomy, University of Nottingham, Nottingham, NG7 2RD, UK*

⁵*CNR- Institute of Complex Systems, Via Madonna del Piano, 10, 50019 Sesto Fiorentino, Florence, Italy*

⁶*The Italian Embassy in Israel, 25 Hamered st., 68125 Tel Aviv, Israel*

ABSTRACT. Inter-layer synchronization is a distinctive process of multiplex networks whereby each node in a given layer evolves synchronously with all its replicas in other layers, irrespective of whether or not it is synchronized with the other units of the same layer [9]. We analytically derive the necessary conditions for the existence and stability of such a state, and verify numerically the analytical predictions in several cases where such a state emerges. We further inspect its robustness against a progressive de-multiplexing of the network.

1 Introduction

Synchronization in networked systems is one of the hottest topics of current research in nonlinear science [3, 1]. So far, most of the focus has been concentrated on systems where all the constituents are treated on an equivalent footing, while only in the last few years the interest has moved towards incorporating the *multilayer* character of real world networks, by representing them as graphs formed by diverse layers [5, 2], which may either coexist or alternate in time [2]. For dynamical processes, multilayer allows identifying synchronization regions that arise as a consequence of the interplay between the layers' topologies [10], assessing the stability of a global synchronous state in a network of oscillators coupled through different variables [8], as well as defining new types of synchronization based on the coordination between layers [4]. In this work, we consider multiplex networks, i.e. the case where layers are made of a fixed set of nodes and connections exist between each node of a layer and all its replicas in the other layers, and show that a genuinely distinctive form of synchronization emerges, namely *inter-layer synchronization*, occurring when each unit in each layer is synchronized with all its replicas, regardless of whether or not it is synchronized with the other members of its layer.

By means of extensive calculations performed in CRESCO, in the last year we have obtained several

*Corresponding author. E-mail: inmaculada.leyva@urjc.es.

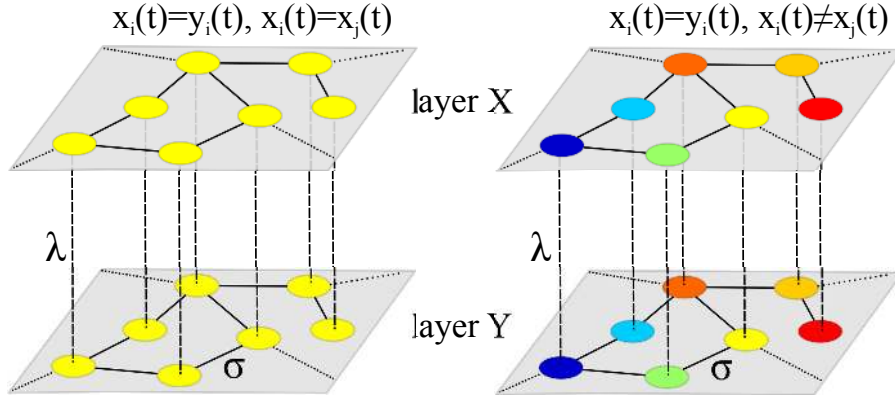


Figure 1: Schematic representation of a multiplex of two layers of identical oscillators, and of the two types of inter-layer synchronization: with (left) and without (right) intra-layer synchronization. Labels σ and λ denote the intra- and inter-layer coupling strengths, respectively. Each node i (j) in the top (bottom) layer is an m dimensional dynamical system whose state is represented by the vector \mathbf{x}_i (\mathbf{y}_j).

important results that provide new insights in the dynamics of synchronization in complex networks. The results were published in Refs. [6, 7, 9] and presented in several international conferences.

2 Model and methods

2.1 Model

We start by considering two layers of identical structure, formed by N identical m dimensional dynamical systems whose states are represented by the vectors $\mathbf{X} = \{\mathbf{x}_1, \mathbf{x}_2, \dots, \mathbf{x}_N\}$ (top layer) and $\mathbf{Y} = \{\mathbf{y}_1, \mathbf{y}_2, \dots, \mathbf{y}_N\}$ (bottom layer) with $\mathbf{x}_i, \mathbf{y}_i$, for $i = 1, 2, \dots, N$, as depicted in Fig. 1. As already mentioned, the inter-layer synchronous state $\mathbf{X} \equiv \mathbf{Y}$ can be realized with or without intra-layer synchronization. The former case (Fig. 1 left) corresponds to all nodes in both layers following the same trajectory, and it therefore reduces to the classical scenario of a globally synchronous solution whose stability can be accounted for by the Master Stability Function (MSF) [3]. The latter case (Fig. 1 right), instead, is far more general, as it only requires that every node i in each layer be synchronous to its replica in the other layer [$\mathbf{x}_i(t) = \mathbf{y}_i(t), \forall i$], with unconstrained intra-layer dynamics.

Let the dynamics of the multilayer system be

$$\dot{\mathbf{X}} = \mathbf{f}(\mathbf{X}) - \sigma \mathcal{L} \otimes \mathbf{h}(\mathbf{X}) + \lambda [\mathbf{H}(\mathbf{Y}) - \mathbf{H}(\mathbf{X})], \quad \dot{\mathbf{Y}} = \mathbf{f}(\mathbf{Y}) - \sigma \mathcal{L} \otimes \mathbf{h}(\mathbf{Y}) + \lambda [\mathbf{H}(\mathbf{X}) - \mathbf{H}(\mathbf{Y})], \quad (1)$$

where $\mathbf{f} : \mathbb{R}^m \rightarrow \mathbb{R}^m$ and $\mathbf{H} : \mathbb{R}^m \rightarrow \mathbb{R}^m$ are respectively the intra- and interlayer coupling vectorial functions, σ, λ are the intra- and inter-layer coupling strengths and \mathcal{L} is the Laplacian matrix encoding the intra-layer topology, considered identical for both layers. In this setting, the layer's dynamical state will be, in general, different at all times, i.e. $\mathbf{X}(t) \neq \mathbf{Y}(t)$. Notice that, if the coupling between layers is diffusive, the inter-layer synchronous state *always* exists, and the manifold $\mathbf{X}(t) = \mathbf{Y}(t)$ is an invariant set.

Let now $\delta \mathbf{X}(t) = \mathbf{Y}(t) - \mathbf{X}(t)$ be the vector describing the difference between the dynamics of the two layers. Considering a small $\delta \mathbf{X}$ and expanding around the inter-layer synchronous solution $\mathbf{Y} = \mathbf{X} + \delta \mathbf{X}$ up to first order, one obtains a set of $N \times m$ linearized equations for the perturbations $\delta \mathbf{x}_i$:

$$\delta \dot{\mathbf{x}}_i = [\mathbf{J}\mathbf{f}(\tilde{\mathbf{x}}_i) - 2\lambda \mathbf{J}\mathbf{H}(\tilde{\mathbf{x}}_i)] \delta \mathbf{x}_i - \sigma \sum_j \mathcal{L}_{ij} \mathbf{J}\mathbf{h}(\tilde{\mathbf{x}}_j) \delta \mathbf{x}_j, \quad (2)$$

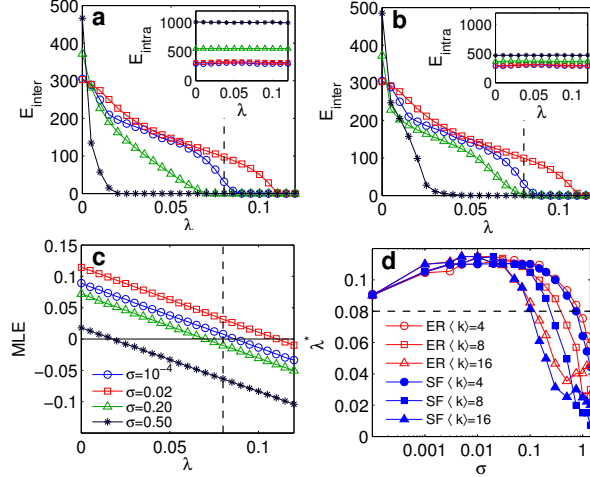


Figure 2: (a) E_{inter} in SF layers of $N = 500$ Rössler oscillators and (c) the corresponding MLE as a function of λ for several σ values. (b) The same as in (a) but for ER layers. Insets in (a) and (b) show E_{intra} in the top layer, and the vertical dashed line is the λ threshold for a pair of nodes ($\sigma = 0$) coupled through the y variable. Each point is an average of 10 realizations, with $\langle k \rangle = 8$. (d) Dependence of the inter-layer synchronization onset, λ^* on σ for ER (red hollow symbols) and SF (blue solid symbols), and several $\langle k \rangle$. The horizontal dashed line is placed at the same value as the vertical line in panels (a)-(c).

where J denotes the Jacobian operator and $\tilde{\mathbf{X}} = \{\tilde{\mathbf{x}}_i\}$ is the state of one isolated layer obeying $\dot{\tilde{\mathbf{x}}}_i = \mathbf{f}(\tilde{\mathbf{x}}_i) - \sigma \sum_j \mathcal{L}_{ij} \mathbf{h}(\tilde{\mathbf{x}}_j)$. The linear equations (2), solved in parallel to the $N \times m$ nonlinear equations for $\dot{\tilde{\mathbf{x}}}_i$, allow calculating all Lyapunov exponents transverse to the manifold $\mathbf{X} = \mathbf{Y}$. The maximum of those exponents (MLE) as a function of the parameter pair (σ, λ) actually gives the necessary conditions for the stability of the inter-layer synchronous solution: whenever $\text{MLE} < 0$, perturbations transverse to the manifold die out, and the multiplex network is said to be *inter-layer synchronizable*.

In the following, the intra- and inter-layer synchronization errors, respectively defined as,

$$E_{intra} = \lim_{T \rightarrow \infty} \frac{1}{T} \int_0^T \sum_{j \neq 1} \|\mathbf{x}_j(t) - \mathbf{x}_1(t)\| dt, \quad E_{inter} = \lim_{T \rightarrow \infty} \frac{1}{T} \int_0^T \|\delta \mathbf{X}(t)\| dt \quad (3)$$

and the MLE, are calculated by performing numerical simulations of Eqs. (1) and (2) respectively ($\|\cdot\|$ stands for the Euclidean norm). Without lack of generality, we consider two possible kinds of topologies where both layers are either Erdős-Rényi (ER) or scale-free with $p(k) \propto k^{-3}$ (SF), in all cases with $N = 500$ Rössler oscillators, whose autonomous evolution is given by $\mathbf{f}(\mathbf{x}) = [-y - z, x + 0.2y, 0.2 + z(x - 9.0)]$.

2.2 Numerical methods and use of computational resources

For the numerical integration of the above model and the analysis of the results we use homemade C codes implementing fix-step fourth-order Runge-Kutta integration algorithms, with an optimized time step $dt=0.01$. The standard GCC compiler was used.

Extensive serial simulations have been performed for large parameters ranges, diverse network topologies and statistical validation of the results. The calculations were performed in Cresco 3 and Cresco 4, using the *h144* queues for full multilayer simulations and *h6* queues for Lyapunov exponent calculations. Homemade MatLab scripts were used for visualizing the results.

3 Numerical results

We start by setting $\mathbf{h} = (0, 0, z)$ so that the corresponding MSF is in class I thus preventing the occurrence of intra-layer synchronization for any possible value of σ at $\lambda = 0$. In addition, the inter-layer coupling function is taken to be $\mathbf{H} = (0, y, 0)$, which generates a class II MSF at $\sigma = 0$ [3].

Results are reported in Fig. 2, where E_{inter} is plotted versus λ for several values of σ , both for SF (a) and ER (b) topologies. In all cases, a smooth transition from an incoherent multiplex dynamics with $E_{inter} > 0$ to an inter-layer synchronous evolution where $E_{inter} = 0$ is observed, always in the absence of intra-layer synchronization [insets in Fig. 2(a,b) show that E_{intra} remains well above zero for the whole explored range of λ]. In Fig. 2 (c) the MLE for the SF case is plotted, showing that E_{inter} vanishes exactly at the same λ at which the MLE gets negative, thus confirming the validity of the analytical approach. To gather a clearer view on the impact of the network heterogeneity, Fig. 2 (d) reports the critical coupling λ^* (the value of λ at the onset of inter-layer synchronization) as a function of σ , for both SF and ER topologies, and several average degrees. As in single layer networks, multiplexes of heterogeneous structures require smaller coupling thresholds to sustain a stable synchronous state. There is a non-monotonic relationship between the synchronization threshold and the *stiffness* within each layer (as measured by σ). The horizontal (vertical) dashed line in Fig. 2(d) [Fig. 2(a,b)] indicates the threshold λ^* for the appearance of a synchronous state at $\sigma = 0$, obtained by analyzing a pair of bidirectionally coupled Rössler units. More rigid layers need larger inter-layer couplings to synchronize (as one would expect), but beyond a certain point in the rigidity, the trend is remarkably reversed.

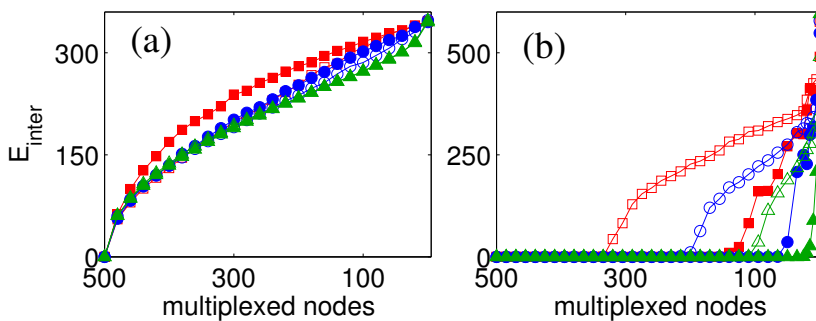


Figure 3: E_{inter} vs. the number of multiplexed nodes for ER (void symbols) and SF (solid symbols) configurations. From a full multiplex, nodes are progressively disconnected following a random (blue circles), and a decreasing (red squares) or increasing degree (teal triangles) sequence. $\lambda = 0.1$ (a) $\sigma = 0.1$, (b) $\sigma = 1.0$. Points are averages over 20 network realizations, with $\langle k \rangle = 8$.

Further insight can be gathered by exploring the robustness of the inter-layer synchronous state under a progressive de-multiplexing of the structure. Starting from the complete multiplex, we then sequentially remove the links between nodes and their replicas, until the layers become uncoupled. In Fig. 3, E_{inter} is reported as a function of the actual number of multiplexed nodes with a disconnecting mechanism following either a random sequence or the increasing/decreasing degree ranking. Robustness is critically dependent on the balance between the inter- and intra-layer couplings. At relatively low and balanced couplings (left panel) E_{inter} grows as soon as the first pair of replica nodes is disconnected, regardless on the node sequence. However, when σ considerably exceeds λ (right panel), inter-layer synchronization persists even if a large fraction of nodes are de-multiplexed. It can be seen that ER layers (void symbols) are less robust than SF layers (solid symbols), since in the last ones synchronization holds up to the point where just a fraction of the hubs are multiplexed (Fig. 3(b)).

4 Conclusion

In conclusion, we provided a full characterization of inter-layer synchronization, a novel and distinctive dynamical phenomenon occurring in multiplex networks of identical layers, in terms of its stability conditions, its relation to intra-layer synchronization and network topology, and its robustness under partial de-multiplexing of the network. Our MSF approach strictly requires that the coupled layers in the multiplex need to be identical. In the more general case of non-identical structures, a rigorous approach should be abandoned in such a case, and one should rely on some kind of (reasonable) approximations and large numerical simulations. Future work in this direction is underway in order to extend the scope of our research to more realistic scenarios.

References

- [1] A. Arenas, A. Díaz-Guilera, J. Kurths, Y. Moreno, and C. Zhou. Synchronization in complex networks. *Phys. Rep.*, 469:93–153, 2008.
- [2] S. Boccaletti, G. Bianconi, R. Criado, C.I. del Genio, J. Gómez-Gardeñes, M. Romance, I. Sendiña Nadal, Z. Wang, and M. Zanin. The structure and dynamics of multilayer networks. *Phys. Rep.*, 544:1–122, 2014.
- [3] S. Boccaletti, V. Latora, Y. Moreno, M. Chavez, and D.-U. Hwang. Complex networks: Structure and dynamics. *Phys. Rep.*, 424:175–308, 2006.
- [4] R. Gutiérrez, I. Sendiña-Nadal, M. Zanin, D. Papo, and S. Boccaletti. Targeting the dynamics of complex networks. *Sci. Rep.*, 2:396, 2012.
- [5] M. Kivelä, A. Arenas, M. Barthélemy, J.P. Gleeson, Y. Moreno, and M. A. Porter. Multilayer networks. *Journal of Complex Networks*, 2:203–271, 2014.
- [6] A. Navas, J. A. Villacorta-Atienza, I. Leyva, J. A. Almendral, I. Sendiña Nadal, and S. Boccaletti. Effective centrality and explosive synchronization in complex networks. *Phys. Rev. E*, 92:062820, 2015.
- [7] I. Sendiña-Nadal, I. Leyva, A. Navas, J.A. Villacorta-Atienza, J.A. Almendral, Z. Wang, and S. Boccaletti. Effects of degree correlations on the explosive synchronization of scale-free networks. *Phys. Rev. E*, 91:032811, 2015.
- [8] R. Sevilla-Escoboza, R. Gutiérrez, G. Huerta-Cuellar, S. Boccaletti, J. Gómez-Gardeñes, A. Arenas, and J M Buldú. Enhancing the stability of the synchronization of multivariable coupled oscillators. *Phys. Rev. E*, 92:032804, 2015.
- [9] R. Sevilla-Escoboza, I. Sendiña-Nadal, I. Leyva, R. Gutiérrez, J.M. Buldú, and S. Boccaletti. Inter-layer synchronization in multiplex networks of identical layers. *Chaos*, 26:065304, 2016.
- [10] F. Sorrentino. Synchronization of hypernetworks of coupled dynamical systems. *New J. Phys.*, 14:33035, 2012.

ATMOSPHERIC POLLUTION TRENDS SIMULATED AT EUROPEAN SCALE IN THE FRAMEWORK OF THE EURODELTA 3 PROJECT

Gino Briganti¹, Andrea Cappelletti¹, Mihaela Mircea², Mario Adani², Massimo D'Isidoro²

¹ ENEA - National Agency for New Technologies, Energy and Sustainable Economic Development, Pisa, Italy

² ENEA - National Agency for New Technologies, Energy and Sustainable Economic Development, Bologna, Italy

ABSTRACT. The present paper shows simulations for the years 1990, 2000 and 2010 performed with the atmospheric modelling system (AMS) of MINNI project at European scale. The modelling system is the reference model of Italian Ministry of Environment developed with the aim to support air quality policy at national and regional level. The work has been carried out in the framework of EURODELTA 3 project, phase 2, designed to investigate the evolution of air pollution since the early 1990s.

1 Introduction

The EU directive 2008/50/EC promotes modelling techniques in order to assess spatial distribution of the ambient air quality, even in place of measurements where lower pollution levels are expected. Air quality models are considered as essential tools, helping to develop emissions control plans, in order to guarantee better air quality levels and to preserve both human health and ecosystems. Since such models incorporate advection/dispersion drivers, coupled with complex chemistry solvers, they require a lot of computation resources; supercomputing architectures, like CRESCO, are then the ideal infrastructure to run them.

The present paper presents the preliminary results achieved by the ENEA's MINNI [1] team in simulating trends on atmospheric pollution at European scale. MINNI is the Italian Integrated Assessment Modelling System for supporting the International Negotiation Process on Air Pollution and assessing Air Quality Policies at national/local level, sponsored by the Italian Ministry of the Environment.

The work has been carried out under the "Trends" phase of the EURODELTA project [2]. Such project is a forum in which European modelling groups share experiences in simulating technically interesting and policy relevant problems, in order to get further understanding in modeling air quality in Europe. EURODELTA is a scientific activity in the framework of EMEP Task Force on Measurement and Modelling [3], under the Convention on Long-range Transboundary Air Pollution.

The focus of EURODELTA-Trends is to assess the efficiency of the Gothenburg protocol in reducing exposure to air pollution in Europe. The exercise also aim to disentangle the role of meteorological variability, long range transport (boundary conditions) and emissions by performing simulations as follows: i) varying emissions (years 1990, 2000, 2010) bringing both meteorology and boundary conditions fixed (year 2010); ii) varying emissions and boundary conditions (years 1990, 2000, 2010), bringing meteorology fixed (year 2010); iii) varying boundary conditions (years 1990, 2000, 2010) with both meteorology and emissions fixed (2010); iv) other additional simulations for completing the decomposition of factors.

2 Modeling set-up

Air quality simulations have been conducted with FARM (Flexible Regional Atmospheric Model) [5] [6], developed by ARIANET s.r.l. (<http://www.aria-net.it/>) in Fortran 77/90 language. FARM is a three-dimensional Eulerian grid model with K-type turbulence closure that accounts for the transport, chemical reactions and ground deposition of atmospheric pollutants. The version used is 4.7, with SAPRC99 [7] gas phase chemical mechanism and AERO3 [8] aerosol model; this version have been recently rewritten in order to support hybrid MPI-OpenMP parallelization [9].

Grids specifications for FARM simulations are shown in Table 1. Horizontal coordinates are in latitude/longitude, whereas vertical levels are in meters above the ground.

SW corner	(-17°E,32°N)
(NX, NY, NZ)	(143,153,16)
Vertical Z levels [m]	Quasi-logarithmic: 20, 75, 150, 250, 380, 560, 800, 1130, 1570, 2160, 2970, 4050, 5500, 7000, 8500, 10000
(ΔX, ΔY)	(0.4°,0.25°)

Table 1: Characteristics of the computational domain.

Meteorological, boundary conditions and emissions data were supplied to all participants at the EURODELTA exercise and they have been processed to be used as input in FARM.

All the input/output data have been stored in the *gporq1_minni* file system. Table 2 summarizes the settings and the resources employed on the Cresco grid adopted in each step described below.

Process	Cores	Queues	Elapsed time	Disk space
Boundary conditions	1	cresco4_h6	~ 20 ⁷ /year	1.6 GB/year
Meteorology	-	local	-	200 GB/year
SURFPRO	1	cresco4_h144 ----- cresco3_h144	~ 45 ⁷ /year ----- ~ 1h20 ⁷ /year	115 GB/year
Emission Manager	12	cresco4_h6 ----- cresco3_h144	~ 2h/year ----- ~ 4h/year	400 GB/year
FARM	16	cresco4minni_h24	~ 1÷1.5 day/year depending on Grid crowding and other I/O simultaneous processes.	220 GB/year
Post-processing	1	cresco4_h144 cresco3_h144 cresco4_h6	~ 2÷3 day/year	38 GB/y

Table 2: Summary of the employed resources on the Cresco grid.

2.1 Boundary conditions

Boundary and initial conditions supplied for the study are a simplified version of those used in the standard EMEP MSC-W model (http://emep.int/mscw/index_mscw.html). The fields are based upon climatological data, except for dust.

Such raw fields have been processed in order to map chemical species into SAPRC99 gas phase chemical scheme, and particulate matter in AERO3 aerosol model.

The yearly archives have been divided in daily files; each of them has been processed separately from the others, by using a scalar job on cresco4_h6 queue; by adopting this way, scalar jobs have been parallelized “by hand”. Initial conditions monthly files contain 14 3D float fields, whereas lateral and top boundary conditions n. 14 2D float variables.

2.2 Meteorology and micrometeorology

Yearly meteorological fields from WRF, (www.wrf-model.org) have been processed by e SURFPRO [10] meteorological post-processor, in order to get boundary layer height and diffusivities and to determine natural emissions (volatile organic compounds, dust and sea salt). Since PBL height has been evaluated by means of a prognostic scheme (relaxation method based on 2D diffusion equations), and the calculation of volatile organic compounds requires the average temperature of the previous day, SURFPRO has been run in a scalar way, by using both cresco3_h144 and cresco4_h144 queues: the entire (identical) runs have been completed in 45’ on cresco4_h144 and 1h20’ on cresco3_h144 (about 70% slower). Output files have dimension of 323 MB/day, for an amount of 115 GB/y storage.

Each meteorological file includes n. 7 3D float fields (geopotential, wind components, temperature, pressure and vapour content) and n. 4 2D float variables (orography, sea surface temperature, cloud coverage and precipitation).

SURFPRO files contain n. 3 3D float fields (geopotential, horizontal and vertical diffusivities) and n. 113 variables (boundary layer turbulence and natural emissions).

2.3 Emissions

The emissions fields were based on TNO_MACC and EMEP databases and were delivered as total yearly and vertically integrated of NO_x, SO_x, VOCs, PM_{2.5}, PM coarse and CO mass in each 2D grid cell and for each anthropogenic categories of SNAP nomenclature (from 1 to 10). A dedicated software (Emission Manager, EMGR), integrated in the MINNI system, performed the needed transformations of these 2D fields in 3D+T fields of chemical species considered in the SAPRC99 and AERO3 schemes. The temporal and spatial disaggregation was performed in several the steps :

- Chemical disaggregation of NO_x, SO_x, VOCs and PM_{2.5} (PM coarse is not speciated in FARM model),
- Vertical distribution according emission category profiles,
- Time modulation according species and category modulation coefficients.

Both vertical and time modulation profiles were provided in EURODELTA project. The natural emissions are computed by MEGAN model in SURFPRO processor.

EMGR is an ensemble of script, makefiles and serial Fortran executables. Due to the non-evolutionary nature of computations, the work can be divided in more than one serial job (12 monthly, or 52 weekly or 365 daily) and submitted to serial queues. Monthly based computations take about 4 hours with cresco3 queues and 2 hours using cresco4 queues.

2.4 FARM chemical dispersion model

For each yearly scenario, concentration fields have been calculated through 12 monthly jobs. For each monthly run, a spin-up period of 15 days has been considered: since domain extension is about 5000 km and mean surface winds about 15 km/h; fifteenth days of spin-up is expected to avoid including transitory effects.

The runs have been mainly performed by using 16 cores and `cresco4minni_h24` queue. The choice of employing 16 cores only is due to optimizing the elapsed times; 16 seems to be a good compromise between resources availability, also considering there is no a prominent advantage in running FARM with more than 56 cores and the performance growth in passing from 16 to 56 is less than 10%. Indeed, the code don't scale exactly as the number of cores, due either to some parts of the software that cannot be parallelized (the chemical module, for example) and to a considerable amount of computational time (with respect to the mere calculation time) spent in saving outputs on the file system in netCDF format.

Calculation requires an elapsed time of about 1÷1.5 day/year, depending mainly on other simultaneous I/O processes and grid crowding. Anyway, the I/O process seems to be the really critical factor on `gporq1_minni` file system, mainly when massive simultaneous I/O operations are in progress (in particular when saving many 3D netCDF output fields). At present, any quantitative test on file system I/O stress has been performed.

Each output file includes 84 float 2D chemical speciated variables (ozone, particulate matter, nitrogen oxides, sulphur dioxide, volatile organic compounds, free radicals, etc.).

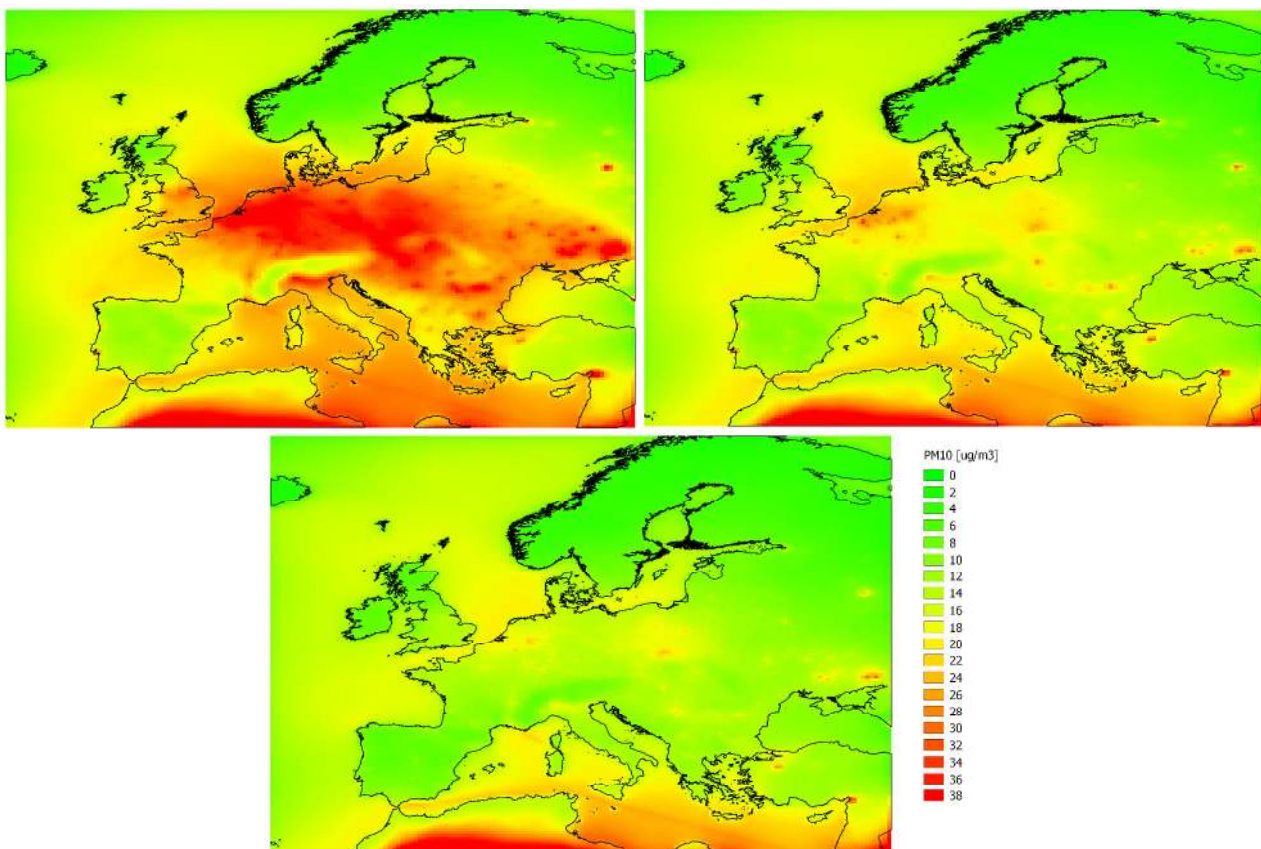


Fig.1: PM10 concentrations [$\mu\text{g}/\text{m}^3$] trend in Europe. Meteorology and boundary conditions for year 2010. Emissions: year 1990 (top left), 2000 (top right), 2010 (bottom center).

3 Discussions

Figure 1 shows an example of output, where it can be appreciated the improvement of air quality, following the abatement of emissions of both primary PM10 and their precursors. High level concentrations of PM10 in the south of domain are due to the Saharan dust emissions; a contribution of natural origin. This is an unambiguous evidence of the effectiveness of EU air quality policies to preserve human health and the potentiality of this kind of models, as essential tools for environment policy management.

In the near future, it is planned to participate at next EURODELTA phase, simulating all 20-years (1990-2010) in order to better understand inter-annual variability of atmospheric pollution.

References

- [1] ZANINI G., MIRCEA M., BRIGANTI G., CAPPELLETTI A., PEDERZOLI A., VITALI L., PACE G., MARRI P., SILIBELLO C., FINARDI S., CALORI G. “*The MINNI project: an integrated assessment modeling system for policy making*”. International Congress on Modelling and Simulation. Zealand, Melbourne, Australia, 12-15 December 2005, pp. 2005-2011. ISBN: 0-9758400-2-9.
- [2] <https://wiki.met.no/emep/emep-experts/tfmmtrendeurodelta>
- [3] <http://www.nilu.no/projects/ccc/tfmm/>
- [4] http://www.unece.org/env/lrtap/lrtap_h1.html
- [5] SILIBELLO C., CALORI G., BRUSASCA G., CATENACCI G., FINZI G. “*Application of a photochemical grid model to Milan metropolitan area*”. Atmospheric Environment **32** (11) (1998) pp. 2025-2038.
- [6] GARIAZZO C., SILIBELLO C., FINARDI S., RADICE P., PIERSANTI A., CALORI G., CECINATO A., PERRINO C., NUSIO F., CAGNOLI M., PELLICIONI A., GOBBI, G.P., DI FILIPPO P. “*A gas/aerosol air pollutants study over the urban area of Rome using a comprehensive chemical transport model*”. Atmospheric Environment **41** (2007) pp. 7286-7303.
- [7] CARTER W.P.L. “*Documentation of the SAPRC-99 chemical mechanism for VOC reactivity assessment*”. Final report to California Air Resources Board, Contract no. 92-329, and (in part) 95-308, (2000).
- [8] BINKOWSKI F.S., ROSELLE S.J. “*Models-3 community multiscale air quality (CMAQ) model aerosol component- 1. Model description*”. Journal of Geophysical Research **108** (2003) p. 4183, <http://dx.doi.org/10.1029/2001JD001409>, D6.
- [9] MARRAS G., SILIBELLO C., CALORI G. “*A Hybrid Parallelization of Air Quality Model with MPI and OpenMP*”. Recent Advances in the MPI: 19th European MPI Users Group Meeting, EuroMPI 2012, Vienna, Austria, September 23-26. Springer Berlin Heidelberg Editor.
- [10] ARIANET S.R.L. “*SURFPRO3 User's guide (SURFace-atmosphere interface PROCessor, Version 3)*”. Software manual. Arianet R2011.31.

MCNP SIMULATIONS SUPPORTING PWR GEN-II AND III SAFETY STUDIES AND A FEASIBILITY STUDY OF MINOR ACTINIDES IRRADIATION IN THE TAPIRO RESEARCH REACTOR

Patrizio Console Camprini^{1*}, Kenneth W. Burn¹

¹ENEA, Fusion and Technology for Nuclear Safety and Security Department, 40129, Bologna, Italy

ABSTRACT. Within the framework of Project B.3.1 funded by the Italian Ministry of Economic Development – Annual Plan 2014 – concerning the Development of Expertise in Nuclear Safety, Monte Carlo simulations have been performed by means of the MCNP6.1 code concerning Nuclear Safety aspects of Gen-II and III PWR's and supporting the design of the Gen-IV Lead Fast Reactor (LFR) systems. Gen-II and III reactor analysis has been carried out working on the MCNP6.1 code source, in order to implement a tool capable of defining a multiple-cell neutron source aiming at an enhanced description of the fission source with respect to the standard pin-by-pin approach. Conversely, the capability of treating nuclear wastes – namely minor actinides – by a Gen-IV system has been evaluated through the preparatory simulations of the irradiation campaign of small samples to be carried out within the TAPIRO reactor in ENEA Casaccia research centre.

1 Fission Source Definition for Gen-II and III PWR Models

Monte Carlo simulations for nuclear reactor cores are normally performed with the MCNP6.1 [1] code defining the fission source by means of a pin-by-pin description, taking advantage of the cell partitioning of the domain.

Ex-core calculations require the definition of a neutron (or gamma) source. According to the standard approach, this source is obtained by a twofold, decoupled, approach.

Either:

- a) a first eigenvalue simulation is performed and a surface source is prepared storing position, velocity and direction of the particles crossing a certain boundary. The responses of the external detectors are then analysed through a second simulation which uses the previously defined surface source.

or:

- b) a volumetric source is defined storing the sites of the fission events in the first eigenvalue simulation. The second simulation then reads this source. No energy or direction are needed since the fission generation spectrum and angular distribution are well known: generally, an analytic spectrum is used and isotropy is assumed.

Note that in the second, fixed source, calculation, the fissions are treated as absorptions.

A precise description of the particle source has an impact on the quality of the ex-core responses and, to this end, a more detailed fission source partitioning has been implemented in this work. In the context of option b) above, we divide the fuel pins into both axial and radial segments.

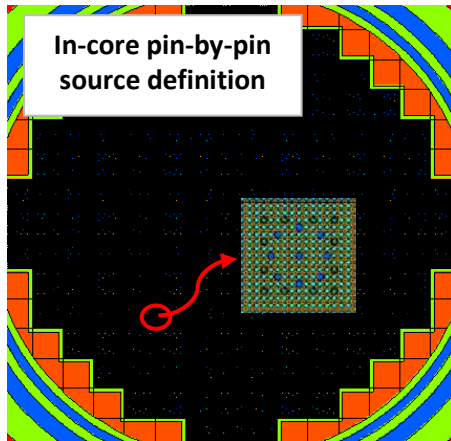


Fig.1: Tihange reactor core cross-section.
(fuel assembly – FA – cross-section is highlighted)

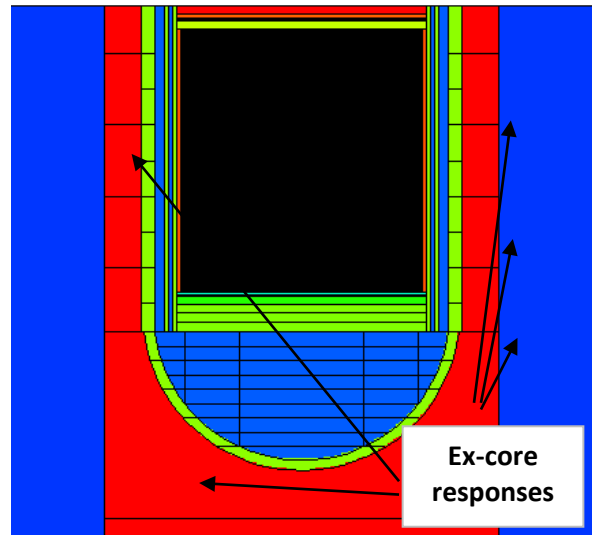


Fig.2: Tihange reactor vessel, vertical section.

Thus, a fortran90 interface code has been prepared with the aim of producing a tool capable of preparing the source and then implementing a fixed source simulation with MCNP. Axial binning has been investigated as well as radial subdivision for fuel pins within the core.

The adopted Gen-II model was the Tihange reactor whilst a generic Gen-III design was employed [2,3]. The context was to evaluate ex-core responses such as radiation damage to the vessel and other equipment employed in the reactor pit as well as establishing calculational routes for ex-core activation for decommissioning.

The first eigenvalue simulation defines the source storing within each cell (or binning of cells) the fission rate for each pin inside the core lattice, as in fig. 1.

The framework of the work is the Project B.3.1 funded by the Italian Ministry of Economic Development – Annual Plan 2014 – about the Development of Expertise in Nuclear Safety. In particular Subproject A2, deliverable ID LP1-063 [4].

2 Simulations of Irradiation Campaign in the TAPIRO Reactor

Within the NEA Expert Group dealing with Integral Experiments for Minor Actinides Management (EGIEMAM), a collaboration between ENEA and the French Atomic Energy Commission (CEA) has been established and a project launched with the aim of irradiating samples of minor actinides inside the TAPIRO research reactor at the Casaccia ENEA Research Center. Samples coming from the OSMOSE irradiation campaign - performed by CEA - are planned to be irradiated in TAPIRO experimental channels in order to obtain integral measurements of the capture cross sections, taking advantage of the well-characterized neutron spectrum available at core and reflector positions. This report concerns the simulations that have been performed with the MCNP6.1 Monte Carlo code, aimed at preliminary estimations of the irradiation performances for all the TAPIRO experimental channels in terms of neutron flux and reaction rates.

The framework of the work is the Project B.3.1 funded by the Italian Ministry of Economic Development – Annual Plan 2014 – concerning the Development of Expertise in Nuclear Safety, and in particular Subproject A1, deliverable ID LP2-083 [5].

The Monte Carlo MCNP6.1 code was the simulation tool in order to represent 3D geometry and the continuous-energy reaction cross-sections.

The nuclear data library utilized was JEFF3-1 provided by the NEA Data Bank and processed at a temperature of 300 K. The normalization of the model is made at the flux peak according to standard reference [6].

The considered operative thermal power was 5 kW and the corresponding peak total neutron flux (at the core centre) was $3.00 \cdot 10^{12}$ n/cm²/s.

The simulated core is composed of a number of fuel cylindrical plates cooled by helium and a calibration pellet. The central part of the diametrical channel is filled by radially oriented pellets as well. Safety Rods and Shim Rods are considered inserted.

The simulation considered the following irradiation channels: diametrical channels (1 and 2), tangential channel and radial channel 1.

The experimental channels are all filled with air and their copper end plugs are removed.

The calculations concerned the evaluation of both the fission and capture reaction rates of the following nuclides:

- | | | | |
|---------------------|---------------------|---------------------|---------------------|
| - ^{235}U | - ^{239}Pu | - ^{241}Am | - ^{243}Cm |
| - ^{238}U | - ^{240}Pu | - ^{243}Am | - ^{244}Cm |
| - ^{237}Np | - ^{242}Pu | | - ^{245}Cm |



Fig.3: The TAPIRO facility hall.

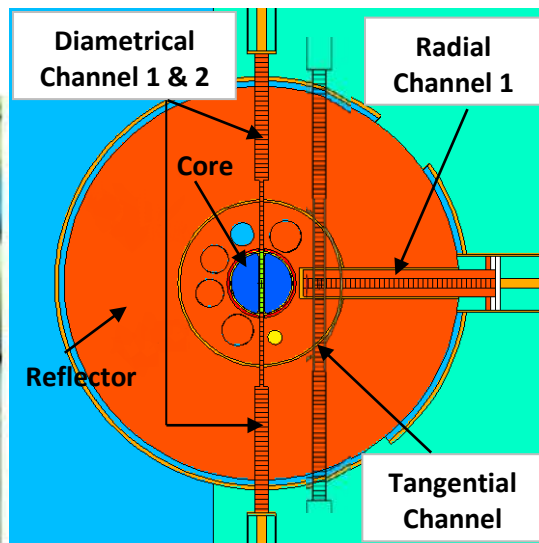


Fig.4: The TAPIRO MCNP model, half-core plane and channels subdivided in cells for responses (in reality tangential channel is positioned at different depth)

The response tallying in the experimental channels has been effectuated through MCNP6.1 tools specific to that purpose (both superimposed mesh tallies and volume domain subdivision).

Firstly highly CPU time-consuming analog calculations (i.e. no variance reduction) were run. Subsequently variance reduction was employed:

- with MCNP6.1 embedded tools such as the weight window generator technique both in volume-based and mesh-based form.
- with ENEA in-house techniques (the DSA, [7], currently based on MCNP5-1.4), producing a single weight window, valid for all the considered responses, that was then employed in MCNP6.1. (Note in this case a single eigenvalue calculation was made that included the optimized variance reduction parameters.)

Acknowledgement

The work on Gen-II and II PWR's was carried out in close collaboration with l'Institut de Radioprotection et de Sûreté Nucléaire. In particular, IRSN supplied the MCNP geometric models and the requested responses: for this the authors would like to thank Mariya Brovchenko and Isabelle Duhamel.

All the information to perform the simulations supporting irradiation in TAPIRO reactor have been provided by Valentina Fabrizio and the ENEA colleagues of research reactor laboratory team (FSN-FISS-RNR), under the guidance of Dr Mario Carta.

References

- [1] GOORLEY J.T. , et al., "Initial MCNP6 Release Overview - MCNP6 version 1.0", LA-UR-13-22934 (2013).
- [2] BROVCHENKO M., et al. "Neutron-gamma flux and dose calculations in a Pressurized Water Reactor (PWR)", International Conference on Radiation Shielding (ICRS13), Paris, 3-6 Oct 2016
- [3] PANEK H., "Qualification du Système NEPTUNE – Ébauche d’une nouvelle chaîne de calcul basée sur les codes APOLLO et Tortise", Note CEA-N-2092, (1979)
- [4] BURN K.W., et al. "Monte Carlo Methods for Core Safety Analysis: Design of Instrumentation for Monitoring PWR Core Degradation in Case of a Severe Accident". ENEA Report RdS 2014/063, September 2014
- [5] CARTA M., et al. "TAPIRO: feasibility study of minor actinides irradiation campaign". ENEA Report RdS 2014/083, September 2014
- [6] CARTA M., et al. "TRIGA RC-1 and TAPIRO, ENEA Research Reactors", ENEA, Italian National Agency for New Technologies, Energy and Sustainable Economic Development C.R Casaccia, Vienna, June 10-12, 2013.
- [7] BURN K.W., "Optimizing variance reduction in Monte Carlo eigenvalue calculations that employ the source iteration approach", *Ann. Nucl. Energy* **73**, 218-240, 2014

MONTE CARLO STUDY OF DOSE-AREA PRODUCT PROPERTIES IN RADIOTHERAPY PHOTON BEAMS WITH SMALL FIELD SIZES

Claudio Caporali^{1*}, Maria Pimpinella¹, Luca Silvi¹

¹ENEA, National Institute of Ionizing Radiation Metrology, Via Anguillarese 301, 00123, Rome, Italy

ABSTRACT. The parameters affecting the integral quantity dose-area product (DAP) in water for radiotherapy photon beams with field diameter below 2 cm have been studied by Monte Carlo simulation. While DAP values result quite independent of height of a flat detector as well as of size of water phantom, the area over which the absorbed dose is integrated, although much larger than the nominal beam size, strongly affects the DAP value and therefore appropriate correction factors are required to ensure traceability of clinical measurements to the primary standards. Detector positioning with regard to the beam central axis has been found not critical for accuracy of DAP measurements.

1 Introduction

Dose-area product (DAP) is a quantity consisting of the integral of the absorbed dose over a specified area in a plane perpendicular to the beam central axis. This quantity, currently used in diagnostic radiology [1], has been recently considered also for dosimetry of radiotherapy small photon beams [2]. A primary standard for absolute measurements of DAP has been developed using an integration area with radius 1.5 cm in photon beams with diameter below 2 cm [3]. Clinical measurements of DAP can be performed by means of a detector having a flat sensitive volume (e.g. a plane-parallel chamber), with a section larger than the beam size [4]. Nevertheless, procedures to ensure traceability of clinical DAP measurements to the primary standard need to be established and, as a first step, parameters affecting the DAP value have to be identified. With this aim, in the present work the properties of the DAP quantity are investigated by Monte Carlo simulations. DAP characteristics have been studied in detail over a wide range of geometrical configurations corresponding to possible measurement set-ups and the main results are reported below.

2 Materials and methods

Monte Carlo simulations were done by means of the EGSnrc/DOSRZnrc code [5][6]. CRESCO4 was used, with a number of cores ranging from 32 to 64. The number of histories for each simulation was not fixed a priori, and the criterion was to go on with the simulation until the achievement of a reasonably low statistical uncertainty for the calculated quantities, usually 0.1%. Referring to a volume irradiated by a radiation field of given characteristics (shape, size, nominal energy), DAP is calculated as the product between the average absorbed dose in the volume, hereafter referred to as 'scoring volume', and the area of the front surface delimiting the volume itself. For the simulations of this work the basic geometry was a cylindrical water tank (water phantom in the following) containing a disc-shaped water volume (i.e. scoring volume) irradiated by high energy photons and the quantity provided by Monte Carlo calculations was the average absorbed dose in the scoring volume (i.e. the ratio of the energy deposited by the radiation to the mass of water in the volume). From the value of absorbed dose, the DAP is easily calculated as reported above. 6 MV radiotherapy photon beams with field sizes of 1.25 cm, 1.5 cm and 2 cm diameter were considered as radiation sources. For each field size the input source was given by the

phase space file, previously obtained simulating with the BEAMnrc usercode [7] the output of a clinical accelerator provided with stereotactic collimators. The influence on the DAP value of quantities like radius (R), height (H) and water depth (z) of the scoring volume and radius (R_{ph}) and height (H_{ph}) of the water phantom was studied.

The choice of the R and H values for the scoring volume is related to the geometry to be used for experimental measurements, and, in particular, to the characteristics of the available measuring devices. In this study, care was taken to match, as closely as possible, the geometrical and physical characteristics of commercial large-area plane-parallel ionization chambers. It was consequently decided to select a range for scoring radii between 1 cm and 10 cm. Three scoring height values were chosen, $H = 0.04$ cm, $H = 0.2$ cm and $H = 1$ cm. Measuring depths, z, ranged from 1 cm to 20 cm. In most cases, fixed values of $z = 10$ cm and $z = 20$ cm were chosen (i.e. the most relevant water depths for dosimetric measurements). The phantom sizes considered for simulations were $R_{ph}=10$ cm, $R_{ph}=20$ cm, $R_{ph}=30$ cm and $R_{ph}=40$ cm, and $H_{ph}=30$ cm and $H_{ph}=50$ cm. These values are consistent with the actual variability of clinical measurement conditions.

The effect of the accuracy in detector positioning on the DAP value has been studied by simulating a misalignment of the scoring volume position with respect to the beam axis. For this purpose, two parameters have been considered, referred to as displacement (δ) and inclination (θ). δ represents the distance between the central axes of radiation beam and scoring volume, respectively, and θ is the angle between the direction of radiation beam and the normal to the entrance surface of the scoring volume. Radiation beam displacement was made to vary between 0 cm and 0.5 cm. Due to symmetry reasons, displacement was assumed to occur only along the positive direction of X axis. Inclination was made to vary between 0 degrees and 0.5 degrees.

3 Results

Figure 1 shows the effect of the scoring radius on DAP value for field diameters (\varnothing) of 1.25 cm (red), 1.50 cm (blue) and 2.00 cm (green) at a measuring depth $z = 10$ cm. The calculated values of DAP are normalized to the value obtained with a scoring radius of 1.5 cm (i.e. the radius of the integration area used for the absolute measurement of DAP [3]). Data in figure 1 refer to a scoring height (H) of 0.2 cm. Effects due to a variation of H from 0.04 cm to 1 cm were found to be insignificant (i.e. below 0.15%).

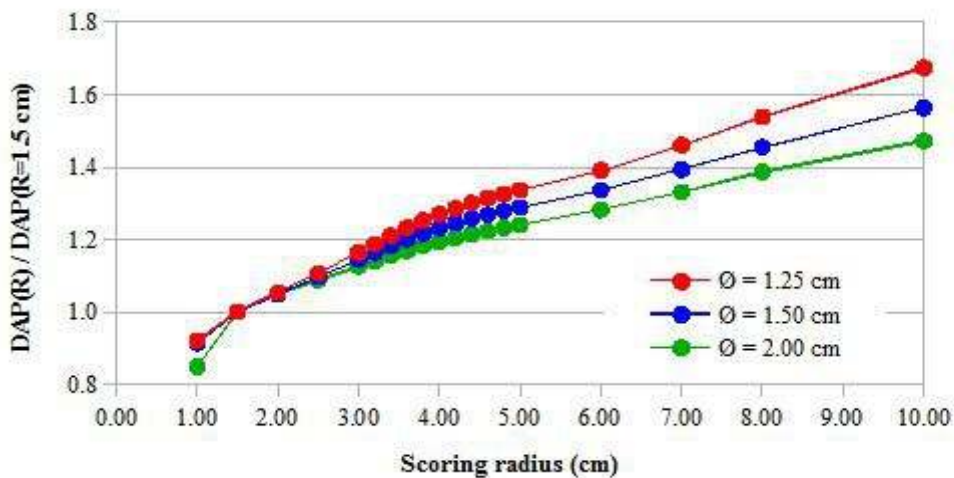


Fig. 1 - Effect of scoring radius (R) on DAP. The DAP values, calculated at 10 cm water depth with a scoring height $H=0.2$ cm are normalized to the values obtained with $R=1.5$ cm. Data are shown for field diameters 1.25 cm (green), 1.5 cm (blue) and 2 cm (red). Statistical uncertainties are about 0.1%.

Due to the scattered radiation, an increase of scoring radius (R) beyond the nominal field radius gives rise to an increase of relative DAP, depending on field size. The variation between $R = 1$ cm and $R = 10$ cm ranges from 50% for $\varnothing = 1.25$ cm to 70% for $\varnothing = 2$ cm. In the subrange from $R = 2$ cm to $R = 10$ cm the functional dependence of relative DAP on scoring radius is roughly linear, specially for $\varnothing = 2$ cm.

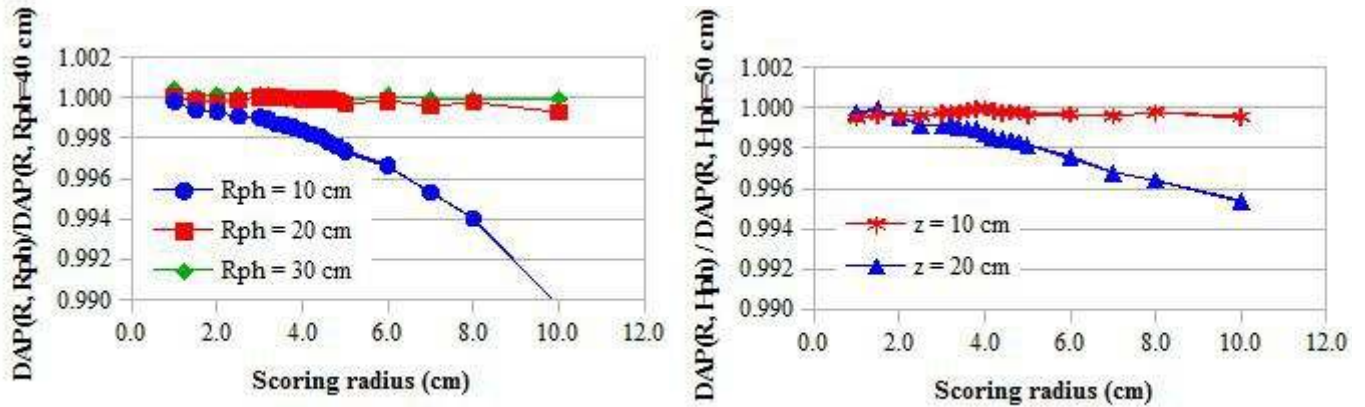


Fig. 2: (Left) Effect of phantom radius (R_{ph}) on DAP.

Data refer to R_{ph} of 10 cm (blue), 20 cm (red) and 30 cm (green) and a water depth of 10 cm. For each scoring radius and R_{ph} data are normalized to the maximum R_{ph} considered for the calculations ($R_{ph}=40$ cm).

(Right) Effect of phantom height (H_{ph}) on DAP at water depths of 10 cm (red) and 20 cm (blue). For each scoring radius and water depth the variation of DAP due to a change of H_{ph} from 50 cm to 30 cm is shown.

Statistical uncertainties are below 0.2%.

The influence of water phantom sizes on the DAP value as a function of the scoring radius is shown in figure 2. In this figure, for each scoring radius, relative DAP has been defined as the ratio between the DAP value calculated for a given phantom radius (left) or height (right) and the corresponding maximum size here considered ($R_{ph}=40$ cm or $H_{ph}=50$ cm). It is, in most cases, unnecessary to operate with exceedingly large phantoms. A phantom radius $R_{ph}=20$ cm appears to be adequate in all cases, considering that a further R_{ph} increase gives rise to DAP variations within the statistical uncertainty. As for phantom height, H_{ph} , the situation is a bit more complex. For measurements done at a depth not exceeding $z = 10$ cm, which is often the case in dosimetric practice, a phantom height $H_{ph}=30$ cm is adequate. For measuring depths from $z=10$ cm to $z=20$ cm this value is still good, but only for scoring radii not exceeding 5 cm. If not, phantom height has to be extended to $H_{ph} = 50$ cm.

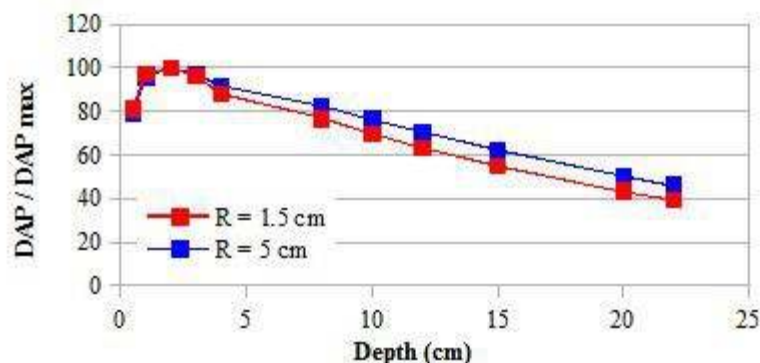


Fig. 3 – DAP calculated with scoring radii $R = 1.5$ cm (red) and $R = 5$ cm (blue) as a function of water depth. Data refer to a field diameter of 1.25 cm and are normalized to the maximum DAP value

Figure 3 shows the percentage depth DAP (PDDAP) curve obtained for a beam diameter of 1.25 cm using a scoring volume with radius 1.5 cm and 5 cm and height 0.2 cm. The functional dependence

of DAP on measuring depth closely resembles the corresponding dependence of the point absorbed dose. The curve exhibits a maximum around $z = 2$ cm and then decreases but the DAP gradient depends on the scoring radius. At the depth of $z = 22$ cm the calculated value for relative DAP was 0.39 ($R = 1.5$ cm) and 0.46 ($R = 5$ cm) respectively. For all given depth values, the dependence of PDDAP on field diameter was negligible.

A displacement of the centre of the scoring volume from the beam axis up to $\delta = 0.15$ cm, and an inclination up to $\theta = 0.5$ degrees for radiation beams can be accepted, as, within these limits, the additional contribution to overall uncertainty due to beam position does not exceed 0.1%. The above ranges for δ and θ cover the positioning errors reasonably occurring in the experimental practice which, therefore, are not expected to give rise to any additional contribution to the overall measurement uncertainty.

4 Conclusions

DAP characteristics have been studied in detail by Monte Carlo simulations over a wide range of geometrical configurations for 6 MV photon beams with field diameters of 1.25 cm, 1.5 cm and 2 cm. From the above reported results, the following conclusions can be drawn: a) water phantoms currently used for clinical dosimetry are also suitable for DAP measurement; b) detector positioning for DAP measurement is less critical than for point dose measurement; c) height of the sensitive volume of a flat detector does not affect DAP measurement; d) DAP signal by a flat detector with section larger than the beam size strongly depends on the detector radius. Such a dependence changes with field size. Therefore to obtain DAP values independent of the detector geometry specific correction factors have to be established as a function of detector radius and beam size. This work is supported by the EMRP joint research project MetrExtRT which has received funding by European Union on the basis of Decision No. 912/2009/EC

References

- [1] INTERNATIONAL ATOMIC ENERGY AGENCY “*Dosimetry in Diagnostic Radiology: an International Code of Practice*” IAEA Technical Report Series Vol 457 (2007) (Vienna:IAEA)
- [2] Pimpinella M., Guerra A.S., Caporali C., De Coste V., Silvi L., Petrucci A., Barile S. “*Perspectives of using an integral quantity for reference dosimetry of small photon beams*” Phys. Med. 32 (2016) e52
- [3] DUFRENEIX S., OSTROWSKY A., LE ROY M., SOMMIER L., GOURIOU J., DELAUNAY F., RAPP B., DAURES J. AND BORDY J. M. “*Using a dose-area product for absolute measurements in small fields: a feasibility study*” Phys. Med. Biol. 61 (2016) pp. 650-62
- [4] Pimpinella M., De Coste V., Guerra A.S., Caporali C., Silvi L., Petrucci A., Barile S. “*Measurements of dose-area-product ratio in small radiotherapy photon beams using two types of large-area plane-parallel ionization chambers*” Phys. Med. 31 (2015) e53
- [5] KAWRAKOW I., MAINEGRA-HING E., ROGERS D.W.O., TESSIER F., WALTERS B.R.B. “*The EGSnrc Code System: Monte Carlo simulation of electron and photon transport*” NRCC Report PIRS-701 (2013)
- [6] ROGERS D.W.O., KAWRAKOW I., SEUNTJENS, J.P. AND WALTER B. R. B. “*NRCC User Codes for EGSnrc*” NRC Report PIRS-702 (2013) (Ottawa: National Research Council of Canada)
- [7] ROGERS D.W.O., FADDEGON B. A., DING G. X., MA C-M., WE J. AND MACKIE T. R. “*BEAM: A Monte Carlo code to simulate radiotherapy treatment units*” Med. Phys. 22 (1995) 503-524

SIMULATIONS OF LINEAR AND NONLINEAR INTERACTIONS BETWEEN ALFVEN MODES AND ENERGETIC PARTICLES

Sergio Briguglio¹, Giuliana Fogaccia^{1*}, Valeria Fusco¹, Michele Martone², Gregorio Vlad¹, Xin Wang³ and Tao Wang⁴

¹*ENEA, CR Frascati, via Enrico Fermi 45, 00044 Frascati, Rome, Italy*

²*HLST, Max-Planck-Institut für Plasmaphysik, Boltzmannstrasse 2, D-85748 Garching, Germany*

³*Max-Planck-Institut für Plasmaphysik, Boltzmannstrasse 2, D-85748 Garching, Germany*

⁴*Institute for Fusion Theory and Simulation and Department of Physics, Zhejiang University, Hangzhou, People's Republic of China*

ABSTRACT. The main activities, regarding numerical simulation of interaction between Alfvén modes and energetic particles in nuclear fusion devices and using CRESCO HPC facilities, are described.

1 Linear benchmarks between HYMAGYC and HMGC codes

The benchmark activity between HYMAGYC [1] and HMGC [2], the two codes developed by the ENEA-Frascati theory group to study the interactions between Alfvén waves and energetic (“hot”) particles in magnetically confined fusion reactors has been continued in 2014. Both codes are hybrid MHD-Gyrokinetic codes, describing the bulk plasma species as a single fluid (MHD) and the energetic particle (EP) species using the gyrokinetic model. HMGC, the first code developed by the ENEA-Frascati theory group, describes the bulk plasma using simple model (“ $O(\epsilon^3)$ reduced MHD”, with ϵ being the ratio between the minor a and major R_0 radius of the toroidal device), thus being limited to circular poloidal cross section of the torus, and, regarding the gyrokinetic model, $k_\perp \rho_H \ll 1$ (k_\perp is the perpendicular component of the wave vector of the perturbation, and ρ_H the Larmor radius of the energetic particle); HYMAGYC, on the other side, uses the full resistive MHD model, in general curvilinear geometry, to describe the bulk plasma, thus being able to consider arbitrary poloidal cross section of the torus, and, regarding the gyrokinetic model, assumes $k_\perp \rho_H \sim O(1)$. During 2014, the linear benchmark using the test case analyzed in the previous report [3] has been completed. In the report 2013 [3], benchmark simulations were been performed varying the normalized energetic particle (EP) density n_{H0}/n_{i0} , while, in the year 2014, numerical results have been obtained varying the normalized EP on-axis thermal velocity v_{H0}/v_{A0} (Fig.1 top) and the normalized EP Larmor radius ρ_{H0}/a (Fig.1 bottom) as free parameters, being $v_{A0} = B_0 / (4\pi m_i n_{i0})^{1/2}$ the on-axis Alfvén velocity, $\rho_{H0} = v_{H0} (m_H c / q_H B_0)$ with B_0 the on-axis magnetic field, m_i and n_{i0} the bulk ion mass and on-axis density, m_H and q_H the mass and charge of energetic particles. The normalized real frequencies (left) and the growth rates (right) of the more unstable modes (lower and upper modes) are shown for HMGC and HYMAGYC codes.

* Corresponding author. E-mail: giuliana.fogaccia@enea.it.

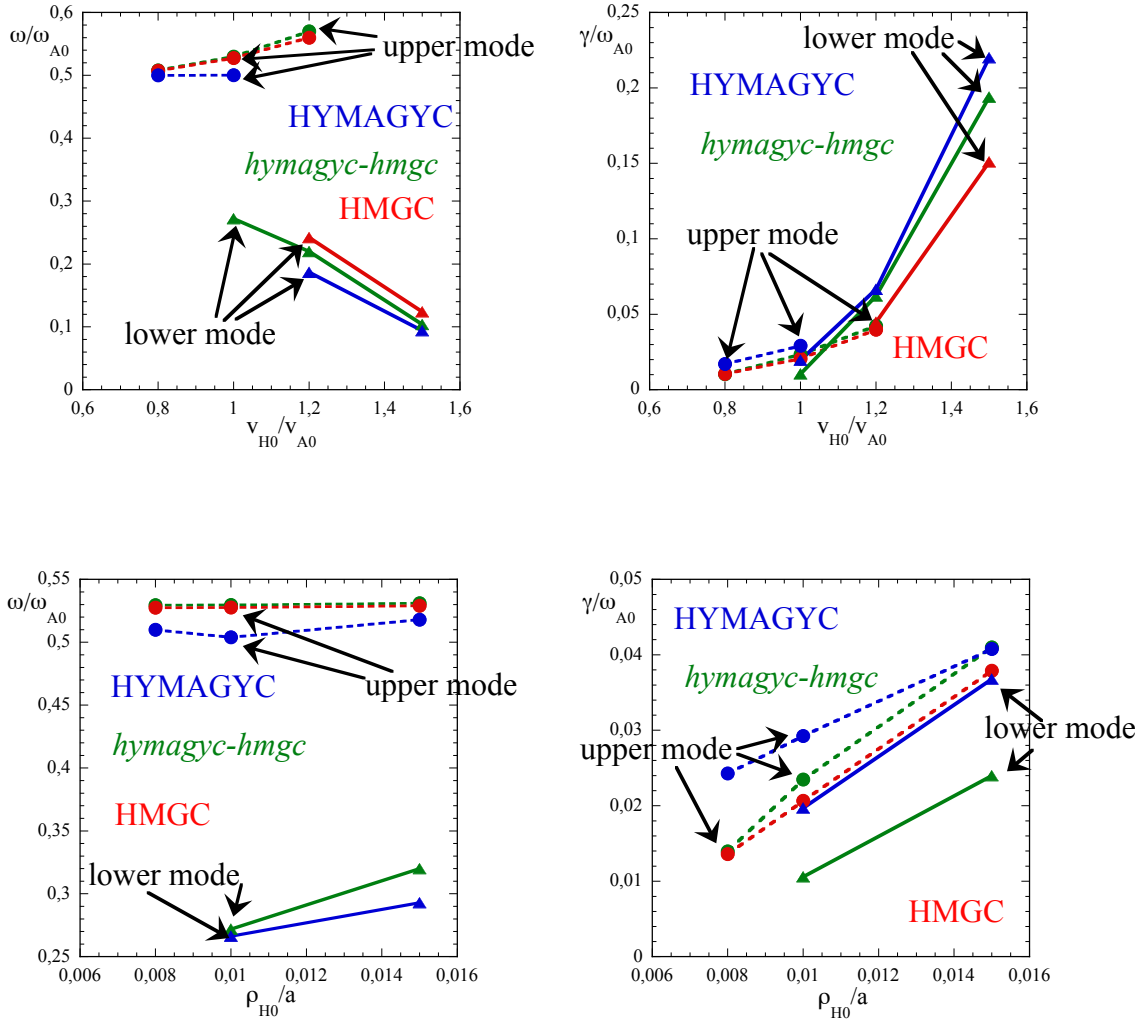


Figure 1. Comparison between HMGC (red symbols), HYMAGYC (blue symbols) and *hymagyc-hmgc* (green symbols) codes: normalized frequency (left) and growth rate (right) vs. EP normalized on-axis thermal velocity (top) and EP normalized Larmor radius (bottom).

Quantitatively, frequencies observed in the HYMAGYC simulations for both modes are lower by 10% with respect to that obtained by HMGC code, whereas the growth rates observed in the HYMAGYC simulations are higher until 50% than that obtained with the HMGC code. Also results of the code “*hymagyc-hmgc*” obtained by the gyrokinetic module of HYMAGYC interfaced to the MHD module of HMGC are shown and are very similar to that obtained from the HMGC code for the “upper mode”, while for the “lower mode” are intermediate between HYMAGYC and HMGC ones.

Figure 2 shows the growth rates of the more unstable mode observed by HYMAGYC (blue symbols) and HMGC (red symbols) vs. v_{H0}/v_{A0} , keeping fixed the ratio between the energetic particle pressure and the magnetic one $\beta_{H0} = (n_{H0}T_{H0}) / (B_0^2/8\pi) = 2(m_H/m_i) (n_{H0}/n_{i0})(v_{H0}/v_{A0})^2$. Varying v_{H0}/v_{A0} , also ρ_{H0}/a and n_{H0}/n_{i0} vary consistently. The behaviour of the curves for HYMAGYC and HMGC are qualitatively in agreement but the absolute values differ considerably. Points (triangle symbol), representing the energetic particle drive of each code, γ_{drive} , are shown. They were obtained by algebraically subtracting to the growth rates the

γ_{damping} , obtained by extrapolating to $n_{\text{H}0}/n_{i0}=0$ (i.e. to zero energetic particle drive) the growth rates shown in Fig.2 (left) of the previous report [3]. The discrepancy between the $\gamma_{\text{drive, HMGC}}$ and $\gamma_{\text{drive, HYMAGYC}}$ is smaller than that between the growth rates. Moreover the smaller drive is observed for the HYMAGYC code though the growth rate, given by $\gamma_{\text{drive}} + \gamma_{\text{damping}}$ is higher than that obtained by HMGC. Then discrepancy between the two codes can be traced back to the consistent difference of the total damping, related to the MHD module and to the time integration numerical scheme.

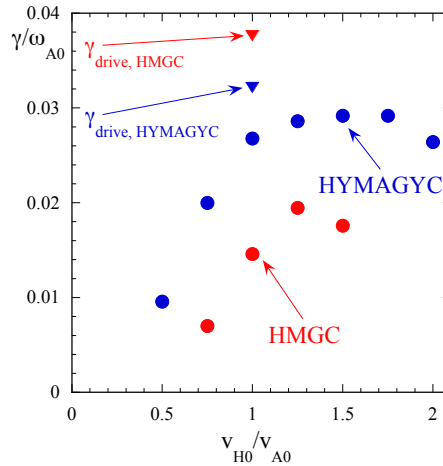


Figure 2. Normalized growth rates versus normalized EP on-axis thermal velocity. Results for HMGC (red symbols) and HYMAGYC (blue symbols) are shown; the triangles are the EP drives for $v_{\text{H}0}/v_{\text{A}0}=1$.

2 Parallelization of the field solver of HYMAGYC

A bottleneck for studying high toroidal mode numbers in the relevant range for Alfvénic modes in ITER scenarios ($n_{\text{tor}} \approx 30$, n_{tor} being the toroidal mode number), is the memory required to solve the linear system associated to the MHD equations. The original initial condition MHD solver of HYMAGYC [1], derived from MARS [4] code solver, uses a serial algorithm, thus having a limitation to the maximum resolution in real space grid that can be solved, being limited by the RAM available on the single computational node. This limit was overcome in 2014, thanks to the development, in collaboration with HLST (High Level Support Team, EUROfusion), of a parallel field solver based on MUMPS (MULTifrontal Massively Parallel Solver), now working on Helios, EUROfusion-Gateway and CRESCO systems, which will allow for running HYMAGYC on, e.g., ITER relevant cases. The MHD module of HYMAGYC uses Finite Elements in the radial-like direction of the torus and Fourier expansion in the generalized poloidal (χ) and toroidal (φ) angles. The number of coupled linear MHD equations are 14, and typical parameters physically significant for studying Alfvénic modes driven by energetic particles are: number of radial grid points $n_s \approx 1000$, number of poloidal Fourier components $m_{\text{pol}}=100$, thus, the number of equations of the linear system to be solved are: (# eqs.)= $n_s \times m_{\text{pol}} \times 14 = 1.4 \times 10^6$. The number of matrix (double complex) elements are (# eqs.)²= 1.96×10^{12} , and the maximum number of non-zero matrix (block tridiagonal) elements: $456 \times n_s \times (m_{\text{pol}})^2 = 4.56 \times 10^9$, which corresponds to 72.96Gb of memory. Tests on CRESCO4 machine has been performed with the results shown in Tab.I.

Memory	cpu time (256 cores), MUMPS	cpu time sequential solver
72.96 Gb	$t_{\text{inversion}} \approx 200$ s (inversion) $t_{\text{bs}} \approx 1$ s (backsolve per step)	$t_{\text{inversion}} \approx 3350$ s (inversion) $t_{\text{bs}} \approx 29$ s (backsolve per step)

Table I: MUMPS version of the MHD solver of HYMAGYC on CRESCO4.

Note that, although the speed-up is far from ideal, the parallelization of the MHD module of HYMAGYC will allow to consider large mesh simulations and, thus, physical cases relevant to ITER; moreover, the already parallelized gyrokinetic module (which was switched off during these tests) is typical much more time-consuming (even by several order of magnitude) than the MHD one, and will represent the actual bottleneck regarding cpu resources.

3 Linear dynamics of electron-fishbone modes

The electron fishbone modes are internal kink instabilities induced by suprathermal electrons. Ion fishbone was first observed experimentally (PDX), opening the path to full theoretical understanding of these phenomena. Stimulated by experimental evidence of electron fishbone (DIII-D, Compass-D, FTU, ToreSupra), theoretical analysis has also been extended to the case of modes excited by fast electrons. Numerical simulations with the XHMGC [5] code (an extended version of HMGC, able to manage several particle species) have been systematically carried out in tokamak equilibria with a slightly inverted safety factor profile. On the one side, theoretical and experimental results are confirmed, while, on the other side, numerical simulations give a deeper insight into the e-fishbone dynamics. Previous work [6] has numerically analyzed the case of energetic electrons with a peaked on axis density profile. It was the first numerical experiment involving electrons that poses the numerical challenge of properly handling the extremely fast parallel electron motion along equilibrium magnetic field lines; the work confirmed the same physical processes supposed for ion fishbone. Finally, the investigation has been carried on with a peaked off axis density profile that was chosen to reproduce the electron density experimental setting. It is worth noting that the two situations (peaked on and peaked off axis density profile) are significantly different in terms of the characteristic resonance frequency as well as the fraction of suprathermal particles involved in the destabilization of the mode, confirming theoretical expectations. In fact the resonance frequency of the energetic electrons corresponds to a mode that propagates poloidally parallel to the bulk electron diamagnetic direction for the peaked on axis profile, and in the opposite direction, which is the bulk ion diamagnetic direction, in the off axis case. Deeply trapped particles drive the mode for the peaked on axis profile whilst, for the peaked off axis case, the particles contributing to drive the mode are the barely trapped/circulating ones which, indeed, give a frequency rotating in the ion diamagnetic direction. In Fig.3, on the left hand side the mode is represented in the poloidal plane and the arrow represents the direction of rotation which is counterclockwise for peaked on axis profile (upper plot) and clockwise for peaked off axis profile (lower plot); on the right hand side, the exchange of energy between the mode and the energetic electrons is shown in the plane (u, μ) , where u is the normalized parallel energetic particle velocity and μ the normalized magnetic moment. The red color represents the maximum amplitude exchange, thus deeply trapped particles are visible for the peaked on axis case (upper plot) whilst barely trapped/circulating particles are evident for the peaked off axis profiles (lower plot), being the parabolas an approximate estimation of the boundary between trapped (inner area) and circulating particles (outer area).

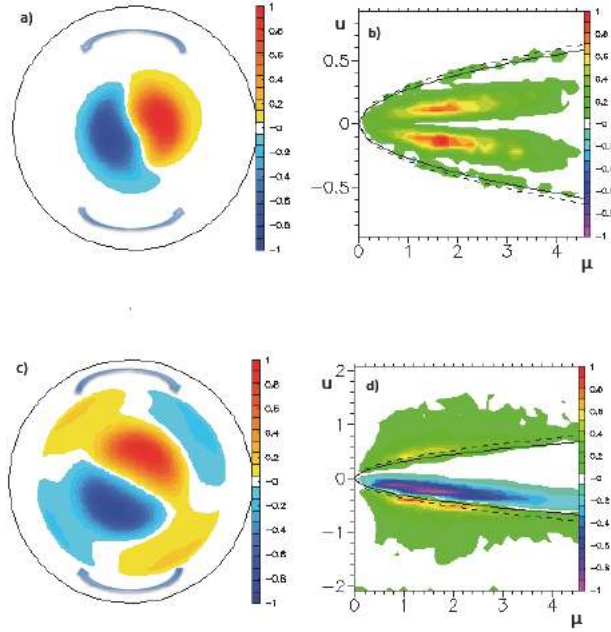


Figure 3. On the left hand side, poloidal structure of the energetic electron driven mode (electrostatic component of the fluctuating electromagnetic field) for peaked on axis density a) and peaked off axis density c). On the right hand side, power exchange between energetic electrons and the mode for peaked on axis density b) and peaked off axis density d) at the radial position of the maximum power exchange in the plane (u, μ) , where u is the normalized parallel energetic particle velocity and μ the normalized magnetic moment.

Such statements are furthermore confirmed in the following numerical experiment. In fact the contribution of deeply trapped particles can be artificially turned off in the peaked on axis simulation; as the system becomes stable, one can claim that deeply trapped energetic electrons actually drive the mode. On the other side, if barely trapped/circulating particles are turned off for the peaked off axis profiles, the mode becomes stable assuring that, in this case, energetic barely trapped/circulating electrons cause the mode to grow. For all these reasons, the choice of the distribution function anisotropy is very important as well. In fact changing the width Δ of the distribution function, the portion of particles, involved in the drive of the mode, changes, including initially deeply trapped particles (small Δ) and then also circulating and well circulating particles (large Δ).

4 Nonlinear frequency chirping of Alfvén modes

A relevant feature of the nonlinear behavior of Alfvén modes in Tokamaks (namely, the mode frequency chirping) has been investigated by means of the XHMGC code [5] and Hamiltonian mapping diagnostics [7]. This phenomenon is shown in Fig.4, representing the time evolution of mode frequency and magnetic energy (proportional to the square mode amplitude). It is possible to see that while the mode is approaching saturation its frequency chirps down. Frequency chirping is accompanied by a modification of the mode radial structure and the phase space resonant region, that is, the region transferring power to the mode (Fig.5). We find that this nonlinear evolution can be interpreted in the following terms: mode radial localization and frequency appear to be locked to the shear Alfvén continuum. Once the resonant particles making the mode unstable in the linear growth phase have exhausted its driving capability (because of density flattening), the mode looks for non-exhausted (non-zero density gradient) particles. It find them in different phase space regions, characterized by slower density flattening (Fig.6).

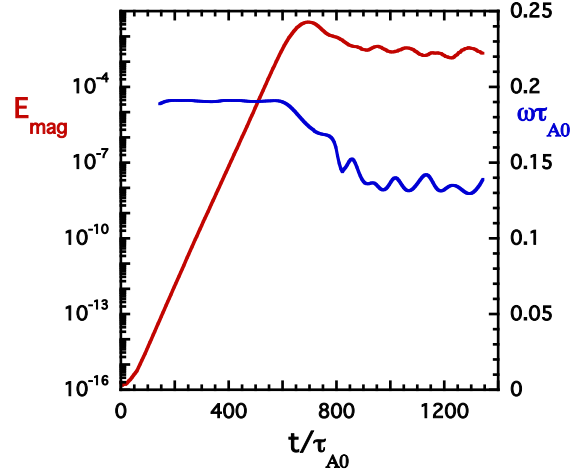


Figure 4. Time evolution of mode frequency (blue line) and magnetic energy (red, in logarithmic scale). During the nonlinear phase, while the mode energy content is approaching saturation, frequency chirps down.

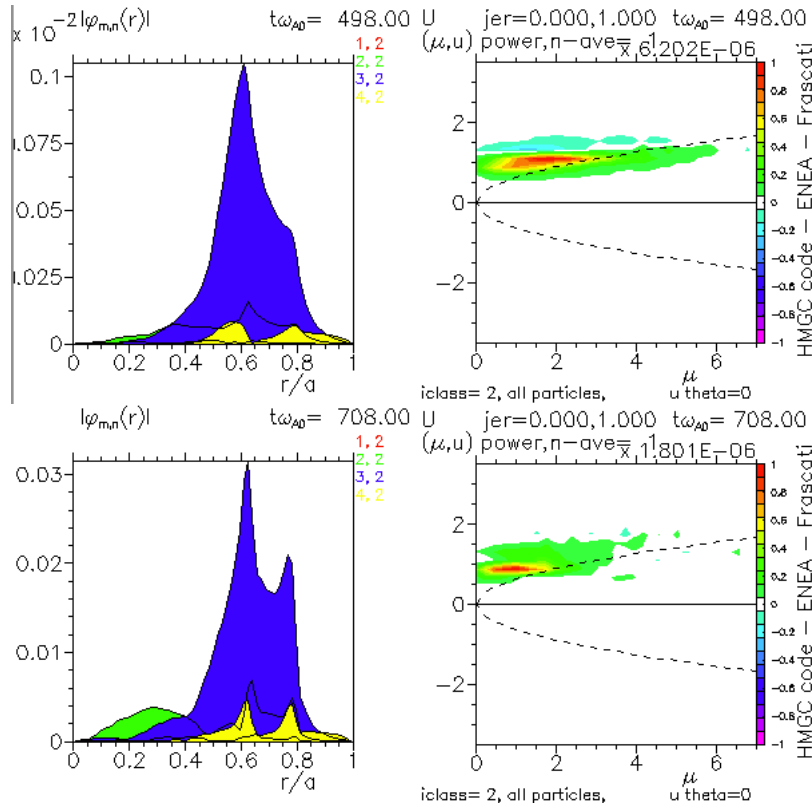


Figure 5. Radial structure of the poloidal harmonics of the electrostatic potential (left frames) and contour plot, in the velocity space, of the power transfer from particles to the mode (right frames). Two times are considered: top frames refer to $t=498\tau_{A0}$, during the linear growth phase; bottom frames, to $t=708\tau_{A0}$, in the nonlinear phase. It is apparent that frequency chirping is accompanied by a modification of mode structure and resonance (in particular, the resonant region moves towards a lower parallel-velocity and magnetic-momentum region).

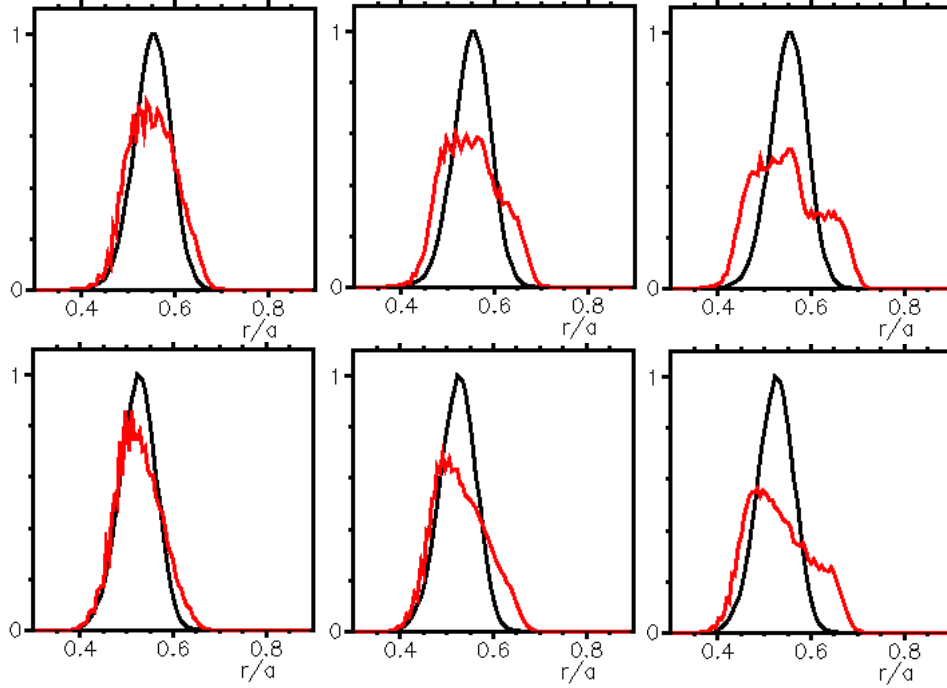


Figure 6. Density profile evolution for different resonant phase space regions. Top frames refer to the resonant region corresponding to the linear growth phase; bottom frames, to the region yielding power to the mode during the nonlinear phase. Black curves represent the unperturbed density profile (after integration over the considered velocity space region); red curves, to perturbed density profiles at different times: $t=498\tau_{A0}$ (left), $t=640\tau_{A0}$, (center), $t=660\tau_{A0}$ (right). It can be seen that the flattening process is slower for the second considered region, allowing it to maintain a driving capability for longer time.

5 Characterization of Alfvén fluctuation spectra on the Divertor Tokamak Test facility (DTT)

A reference scenario of FAST [8] was studied with HMGC code. FAST was designed to work in a dimensionless parameter range similar to ITER, and thus to study integrated ITER physics. Based on the same similar arguments, this reference scenario was also extended to the Divertor Tokamak Test facility (DTT) [9]. Given the reference scenario, “antenna” excitation technique has been adopted in HMGC with the aim of investigating the Alfvén fluctuation spectra, including Alfvén eigenmode frequency, damping rate and mode structures.

The equilibrium used in the simulations is shown in Fig. 7 left, where ϵ is artificially reduced to 0.18 due to the limitation of the “ $O(\epsilon^3)$ reduced MHD” model in HMGC. The radial profile of antenna is a Gaussian function centered at $r/a = 0.55$ (Fig.7 right).

Toroidal Alfvén Eigenmode (TAE) can be readily excited in this way. An example result by $\omega_{\text{ant}}/\omega_A=0.4$ is shown in Fig.8, ω_{ant} and ω_A being antenna and Alfvén frequency, respectively. Moreover, ω_{ant} was varied around TAE frequency, and the maximum response of each antenna frequency was measured accordingly. From the results of the frequency scan, two TAE branches have been isolated. Meanwhile, eigenmode real frequencies and damping rates are also calculated by the antenna response (Fig. 9).

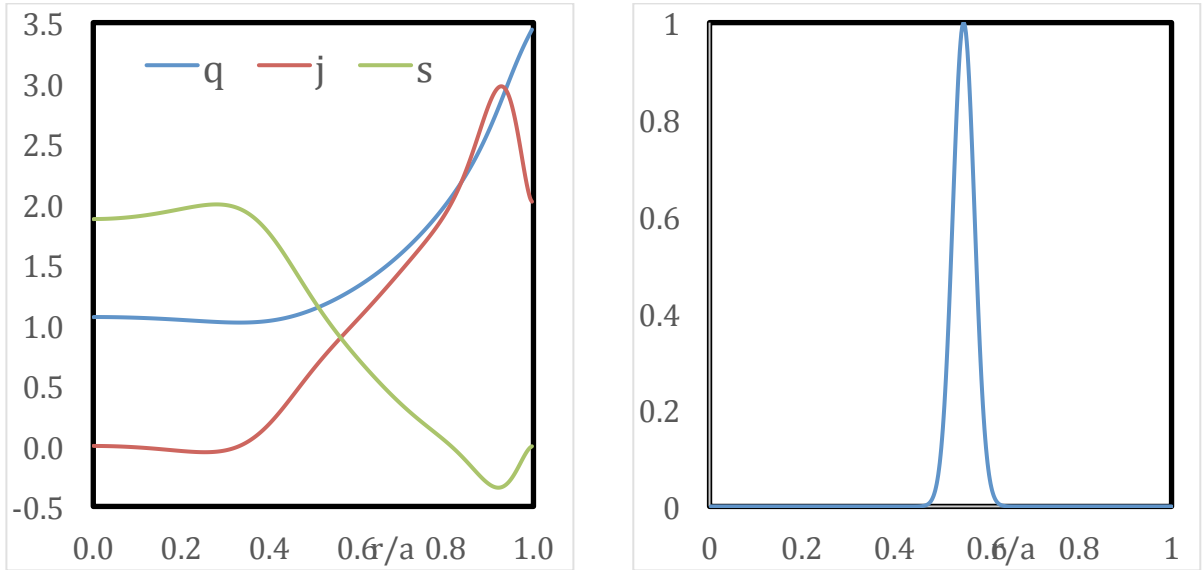


Figure 7. Left: q , current (j), and magnetic shear (s) profiles of the equilibrium. Right: Normalized antenna radial profile.

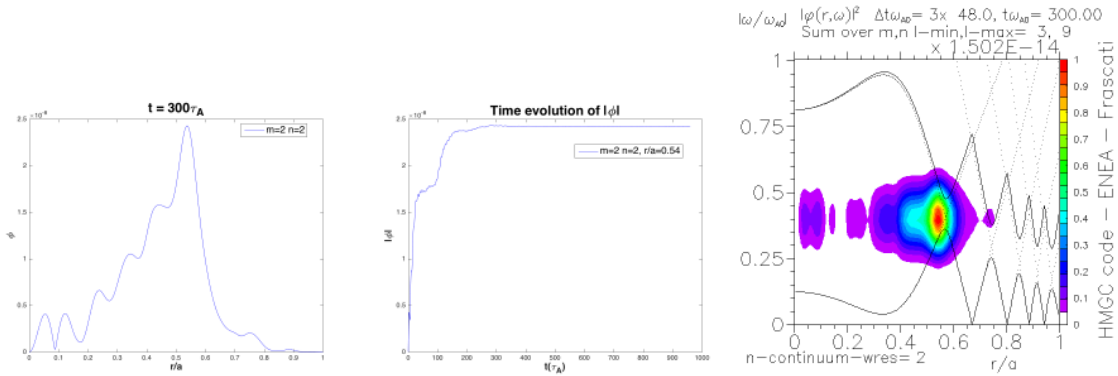


Figure 8. Radial structure of the $m=2, n=2$ poloidal harmonic of the electrostatic potential (left), its time evolution (middle), and contour plot of eigenmode frequency (right).

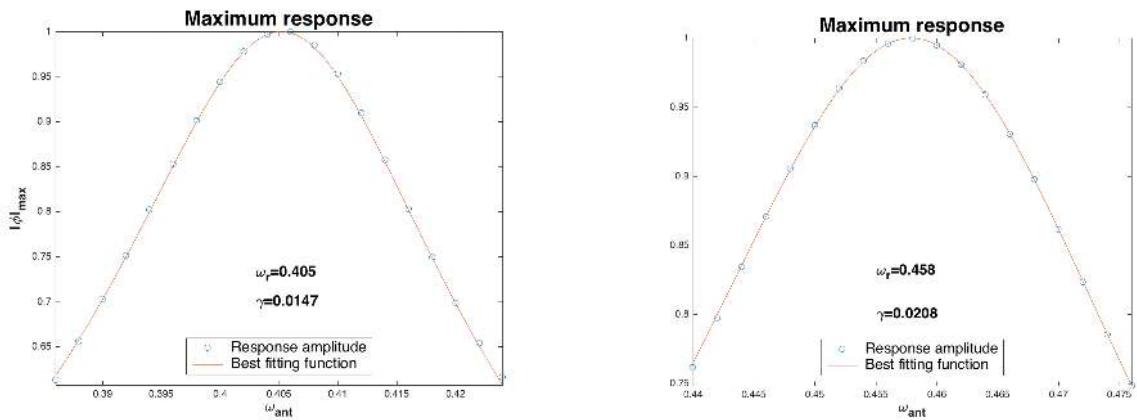


Figure 9. Plots of the maximum response amplitude and the best fitting curve of two frequency scans, the eigenmode real frequencies and damping rates are calculated from the arguments of the fitting curve.

References

- [1] Vlad G., Briguglio S., Fogaccia G., Zonca F. Toward a new hybrid MHD gyrokinetic code: Progresses and perspectives, presented at the 11th IAEA Technical Meeting on Energetic Particles in Magnetic Confinement Systems (Kyiv 2009), paper P-25. Online version of poster at <http://www.afs.enea.it/vlad/Presentations/vlad09iaeatm.pdf>.
- [2] Briguglio S., Vlad G., Zonca F., Kar Hybrid magnetohydrodynamic-gyrokinetic simulation of toroidal Alfvén modes, *Phys. Plasmas* 2, pages 3711-3723, 1995
- [3] Briguglio S., Fogaccia G., Vlad G., Wang X. Particle simulation of Alfvén mode dynamics in nuclear fusion devices, *High Performance Computing on Cresco infrastructure: research activities and results 2013*, pages 112–116, 2014.
- [4] Bondeson A., Vlad G., and Lutjens H. In IAEA Technical Committee Meeting on Advances in Simulations and Modelling of Thermonuclear Plasmas, Montreal, 1992, page 306, Vienna, Austria, 1993. International Atomic Energy Agency.
- [5] Wang X., Briguglio S., Chen L., Fogaccia G., Vlad G., Zonca F. An extended hybrid magnetohydrodynamics gyrokinetic model for numerical simulation of shear Alfvén waves in burning plasmas. *Physics of Plasmas*, 18:052504, 2011.
- [6] Vlad G., Briguglio S., Fogaccia G., Zonca F., Fusco V., Wang X. Electron fishbone simulations in tokamak equilibria using XHMGC. *Nuclear Fusion*, 53:083008, 2013.
- [7] Briguglio S., Wang X., Zonca F., Vlad G., Fogaccia G., Di Troia C., Fusco V. Analysis of the nonlinear behavior of shear-Alfvén modes in tokamaks based on Hamiltonian mapping techniques, *Phys. Plasmas* 21:112301, 2014.
- [8] Pizzuto A. et al., The Fusion Advanced Studies Torus (FAST): a proposal for an ITER satellite facility in support of the development of fusion energy, *Nuclear. Fusion* 50:095005, 2010.
- [9] Divertor Tokamak Test Facility – Project Proposal, A. Pizzuto Ed. (ENEA, Frascati), ISBN: 978-88-8286-318-0, 2015.

ANALYSIS OF THE WAVE FIELD IN FRONT OF THE U-OWC

Pasquale Filianoti¹ and Luana Gurnari¹

¹Università "Mediterranea" degli studi di Reggio Calabria, Dipartimento DICEAM, Loc. Feo di Vito, 89122 Reggio Calabria, Italia. E-mail: filianoti@unirc.it, luana.gurnari@unirc.it

ABSTRACT. The U-OWC is a caisson breakwater for port defence, embodying an OWC with a small opening. Under the wave action, the pressure acting on the outer opening of the vertical duct fluctuates, producing a pulsating water discharge through the plant. The interaction between incoming waves and the pulsating water discharge alters the wave motion in front of the breakwater wall. In this work, we aim to investigate the wave field in front of the absorber breakwater. Therefore, we carried out an experiment in a numerical wave flume. The water-air interaction is taken into account by means of the Volume-Of-Fluid (VOF) model implemented in the commercial CFD code Ansys Fluent. The numerical simulation was carried out through CRESCO platform; we, usually, use the cresco5 or cresco3 clusters and in this work, we used the cresco5_16h24 code with a number of cores set at 48. Several simulation were made with different time periods and in the previous simulations the number of processor were set at 32 (16x2) but in this one, the processors were incremented to 48 (16x3). Both air and water flow fields are assumed to be unsteady and are computed solving the Navier-Stokes equations. The wave flume has been accurately tested on comparing numerical results vs standing wave field. Results revealed found that in front of a U-OWC breakwater, nodes tend to disappear, as a consequence of energy absorption by the plant.

1. The computational Domain

In order to check the wave generation and propagation along the wave flume, a preliminary test has been carried out, by considering a vertical reflecting wall instead of the absorbing wall. The computational domain (see Fig. 1) is a two-dimensional wave-flume having a piston-type wavemaker placed in the left extremity and a vertical breakwater in the right extremity of the contour. The geometry of the wave-flume is indicated in Fig. 1.

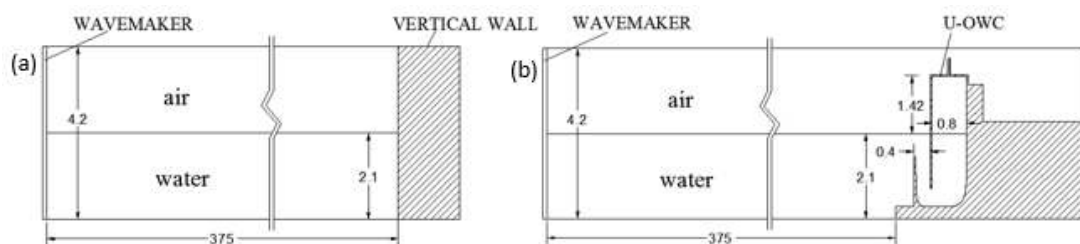


Fig.1: Geometry of the wave flume. The wavemaker is on the left side. (a) with a reflecting vertical wall for carrying out preliminary tests, (b) the U-OWC breakwater (measures are in meters).

The computational domain of Fig.1 is discretised with internal tool of the ANSYS *patch conforming* algorithm and *all triangles* mesh method. The distance between the wavemaker and the wall is 375 m; the flume water depth is 2.1 m. The maximum size of the triangular elements is 7 cm, with a thickening in the proximity of the water-air interface until 7 mm.

The length of the flume has been chosen in order to contain many wave lengths before the wall. This is necessary to establish a stationary condition in front of the wall.

The numerical experiment has been carried out by substituting the vertical wall with the U-OWC (see Fig. 1b). The plant shown has the same size of the plant tested at sea by [1]. Due to the two-dimensional scheme, the circular air tube is substituted by a slit 4.2 cm width.

In order to match the physical behaviour, we have to set the boundary conditions of the numerical wave flume. Smooth *no-slip wall* boundary conditions have been assigned to all solid walls, whilst the upper domain boundary is defined as *pressure outlet*, with zero-gauge pressure.

2. The wave generation by a wavemaker

The free surface displacement η , produced in a wave flume by a piston-type wavemaker starting from rest and moving sinusoidally for a given time interval t , is [2]:

$$\eta(x,t) = \frac{2}{\pi} \int_0^{\infty} \frac{\tanh kd}{k} \cos kx \left[\int_0^t U_0(\tau) \cos \sigma(t-\tau) d\tau \right] dk, \quad (1)$$

where d is the depth, U_0 is the horizontal velocity of the wave board, and $\sigma^2 = gk \tanh(kd)$, where $k=2\pi/\lambda$, λ being the length of the flume. Assuming that the board starts from rest at its extreme backward position, its displacement and velocity are given respectively by

$$x(t) = -\frac{S}{2} \cos(\omega t), \quad (2)$$

$$U_0(t) = \frac{S}{2} \omega \sin(\omega t), \quad (3)$$

where S is the total horizontal stroke excursion and ω is the angular frequency of the wave board. Substituting eq. (3) into eq. (1), and integrating with respect to the time, we obtain

$$\eta(x,t) = \frac{2}{\pi} \int_0^{\infty} \frac{\tanh kd}{k} \cos kx \left\{ \frac{\omega}{\omega^2 - \sigma^2} [\cos(\sigma t) - \cos(\omega t)] \right\} dk, \quad (4)$$

Starting from rest, the wave generation process has been simulated assigning the velocity [eq. (3)] to the left wall of the wave flume, by means of a User Defined Function (UDF). The Fluent dynamic mesh feature has been used for both the wall motion and the deformation of the neighbouring cells. The wave generated for the numerical experiment has height H and period T equals respectively to 0.2m and 3.5 s. The water depth d , is equal to 2.1 m, and the wavelength L , is about 32 m. The time step for the numerical integration was set at 1/1000 of wave period.

At the end of each time step, the water surface inside the wave flume has been recorded, allowing us to analyse in depth the wave motion.

3. Preliminary check of the wave flume

In order to validate the numerical experiment, we carried out some preliminary checks on the numerical wave flume.

Fig. 2 shows four pictures of the free surface elevation $\eta(y,t)$, taken at some wave period from each other. The considered time instants are $5T$, $15T$, $40T$ and $60T$, ranging from panel (a) to (d). The dashed vertical line marks the distance y_0 , that is $9L$, from the wavemaker. As we can see, at $t = 5T$, the wave train has not yet reached the abscissa y_0 . After $15T$, the group head has passed y_0 , and the wave motion is periodic until the waves reflected by the vertical wall (see panel c) reach y_0 (see panel d). To test the wave generation and propagation in the flume, the $\eta(y,t)$ shown in Fig.2, has been compared with the analytical solution. Fig. 3 shows this comparison at $t=5T$; the dashed line is that of Fig. 2a, the continuous line is obtained by means of eq (4).

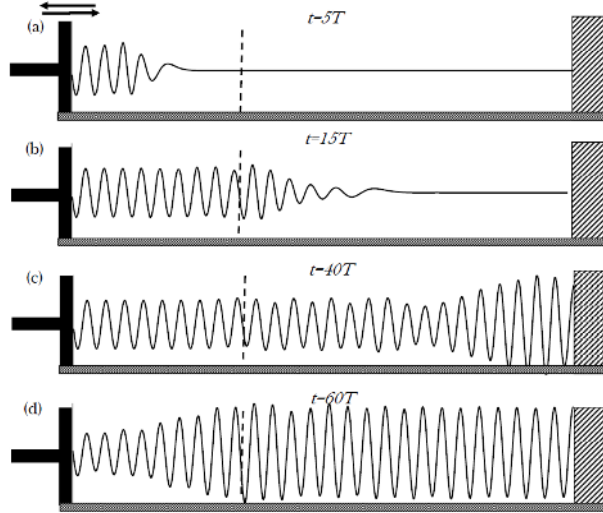


Fig.2: Four pictures of the free surface elevation in a long wave flume with a wavemaker on the left extremity and a vertical wall on right extremity.

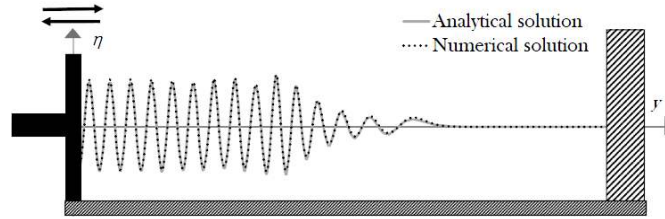


Fig.3: Comparison between the analytical solution for transient waves in a flume [2] and the numerical solution carried out by the preliminary experiment.

4. The wave field in front of the absorber breakwater

The wave field in front of the absorber breakwater is produced by the interaction between the incoming waves and the pulsating discharge in the plant. Therefore, the resultant wave field is quite different from the standing wave field in front of a vertical reflecting wall.

We could assume that the wave field before the U-OWC is periodic in space and time and the surface elevation and the velocity potential in front of the absorber are given by [3]:

$$\eta(y, t) = H \cos(ky) \cos(\omega t) - H' \sin(ky) \cos(\omega t + \varepsilon), \quad (5)$$

$$\varphi(y, z, t) = -g\omega^{-1} \frac{\cosh[k(d+z)]}{\cosh kd} \left[h \cos(ky) \sin(\omega t) + H' \sin(ky) \sin(\omega t + \varepsilon) \right] \quad (6)$$

Fig. 4 shows the overlapping of several instantaneous of the surface wave in the flume. Each frame is taken at $1/20T$ during a time interval of a wave period. As we can see in details in panel (a), the wave envelope represents a standing wave field. In particular, we can see the characteristic “nodes” at $y = (2n+1) L/4$ ($n=0,1,2,\dots$), where the free surface elevation is zero whichever the time instant is. In panel b), we can see as nodes disappear in front of the U-OWC wall, letting the place to “pseudo-nodes”, which are points where the amplitude of η is minimum but different from zero.

Moreover, later than the incident wave train has impacted the absorber breakwater, the wave amplitude at the breakwater wall is smaller than in front of a vertical reflecting wall. Fig. 5 shows some instantaneous of the free surface elevation η , in front of the wall. Panels (1a) – (2a) show the free surface elevation at $t = t_0$ and panels (1b) - (2b), (1c) - (2c), (1d) – (2d), represent η at subsequent instants $t_0 + iT/4$ ($i=0,1,2,3$).

Focusing attention to snapshots of panel 1 in Fig.5, at t_0 and $t_0 + T/2$, the vertical displacement is maximum (except in nodes). At $t_0 + T/4$ and $t_0 + 3T/4$, η is nearly equal to zero in all the flume, according to the theory.

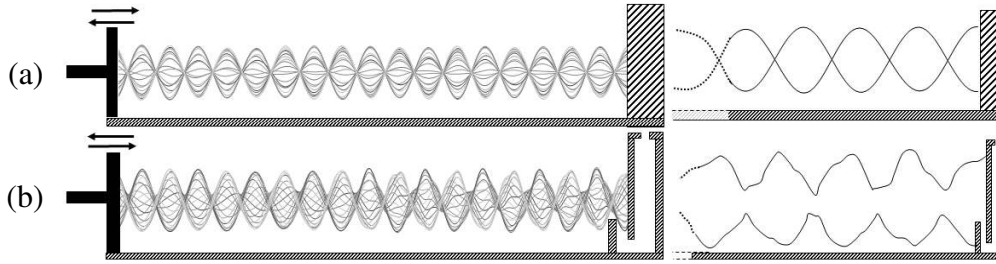


Fig.4: overlapping of several instantaneous of the surface wave in the flume: (a) in front of the perfect reflecting wall and (b) in front of absorber breakwater

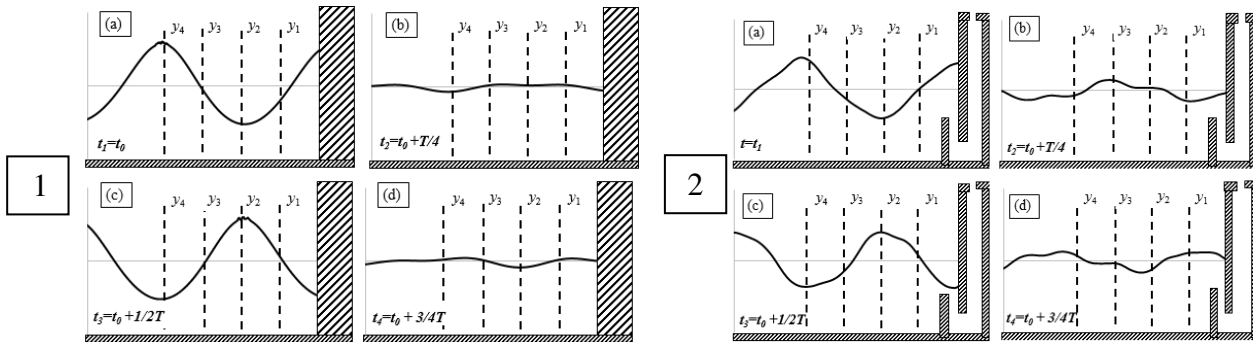


Fig.5: snapshot of the free surface elevation η , in different time instants in front of the vertical wall (panel 1a-d) and in front of the U-OWC breakwater (panel 2a-d).

The stationarity of the wave field is also confirmed by distributions of horizontal velocity v_y , along some fixed vertical section. At time instants t_1 and t_3 , $v_y = 0$, everywhere. For $t = t_2$, and t_4 , $v_y = 0$, at vertical sections y_2, y_4 ; and they are maxima (in absolute value) at y_3 and y_1 . Despite the trend of η is quite similar at the same time instants both in the panel a and b, of Fig.5, the horizontal velocity distributions revelation a quite different trend between standing (panel 1) and quasi-standing (panel 2) wave field.

5. Conclusion

In this work, we carried out a numerical experiment aiming to analyze the interaction between waves and a U-OWC breakwater.

In order to validate the numerical flume, we carried out some preliminary tests, aimed to compare numerical results for a vertical reflecting wall with the analytical solution for linear standing waves. A good agreement between theory and CFD solution was found. The wave field formed in front of the U-OWC differs from a standing wave field, due to the fact that nodes disappear in the latter. In their place, we find a minimum in the wave amplitude different from zero. Also the horizontal velocity is nonzero under wave crests and troughs. These modifications in respect to a standing waves field are due to the necessity to harmonize between them the wave flow and the discharge alternatively entering (or exiting) the plant.

References

- [1] BOCCOTTI P. ET AL., 2007. *Caisson breakwaters embodying an OWC with a small opening - Part II: A small-scale field experiment*, Ocean Engineering 34 (5-6), 820-841.
- [2] HUGHES, S.A., 1993, “*Physical Models and Laboratory Techniques in Coastal Engineering*”, Advanced Series on Ocean Engineering, Vol. 7. World Scientific, London, 568 pp
- [3] BOCCOTTI P., 2007. *Caisson breakwaters embodying an OWC with a small opening - Part I: Theory*, Ocean Engineering 34 (5-6), 806-819.

A NOVEL CHARGE-EQUILIBRATION METHOD FOR SELF ASSEMBLY OF ORGANICS ON METAL SURFACE

Amedeo Palma^{1*}, Mauro Satta², Silvano Tosti³

¹*CNR-ISMN Montelibretti, Monterotondo Scalo, Italy*

²*CNR-ISMN c/o Chem. Dept. of University of Rome "Sapienza", Rome, Italy*

³*ENEA Unita' Tecnica Fusione, C.R. ENEA Frascati, Via E. Fermi 45, Frascati (RM) I-00044, Italy,*

ABSTRACT. We have developed a classical tool able to sample the configuration space overcoming the topological constraints of the standard classical molecular dynamics. Our model is based on the charge equilibration procedure combined with an anisotropic pairwise atomic interactions where an angular dependence, with respect to metal surface, is explicitly taken into account. The D-alaninol molecule has been chosen as a prototype of flexible and multi-functional chemical compound which can form manifold complex configurations upon absorption on metal surface. The experimental STM image of the monolayer is correctly reproduced by our calculations, indicating that this new approach represents a step forward in the efficient simulation of complex molecular self assembly.

1 Introduction

In the last decade supramolecular chemistry at surfaces has become a topic of widespread interest since low-dimensional architectures, having specific functionalities in nano-structured devices, can be designed and realized [1, 2].

The formation of self assembled layers is mainly governed by supramolecular lateral interactions, although the substrate plays an important role in mediating them and imposing its geometrical constraints. Molecules tend to be involved in patterns of several intermolecular interactions of comparable relative strength: the structure of the resulting aggregated system is determined by the balanced interplay of adsorption energy, steric effects and charge transfer [3]. This is a challenging issue and a relevant subject for technological purposes in many fields [4]. Tailoring the properties of self assembled 2D nanostructures is further complicated if chirality transfer from chiral molecule to surfaces is involved. This increasing complexity of the assembly mechanisms makes necessary the development of new approaches and modeling techniques.

Our approach allows us to describe the angular dependence of the surface/molecule interaction and correctly reproduces the lateral forces which are important in self assembly processes. The configuration space has been sampled with this efficient and robust algorithm. We have preferred to run hundreds of annealing simulations instead of very long dynamics runs: we have found a new more stable local energy minimum of D-alaninol on the copper surface and we eventually obtained a tetrameric unit of the full-coverage whose STM image, calculated by DFT, is in agreement with experiments.

*Corresponding author. E-mail: amedeo.palma@ismn.cnr.it.

2 Computational Details

These parameters have been determined by fitting the quantum energetics and geometry of small molecules adsorbed on the Cu(100) surface: the choice of these molecules is because they have the same chemical groups of the D-alaninol. In particular we have performed Plane-Wave Density Functional Theory (PW-DFT) calculations on CH_4 , NH_3 , CH_3OH adsorbed on the Cu(100) surface. We have used the Quantum Espresso Simulation Package [5] to carry out quantum calculations within the Kohn-Sham implementation of DFT. PBE (Perdew-Burke-Ernzerhof) exchange-correlation functional ultrasoft pseudopotentials has been used, Kohn-Sham (KS) valence states were expanded in a plane-wave basis set with a cutoff of 340 eV for the kinetic energy. Further details are given elsewhere [6].

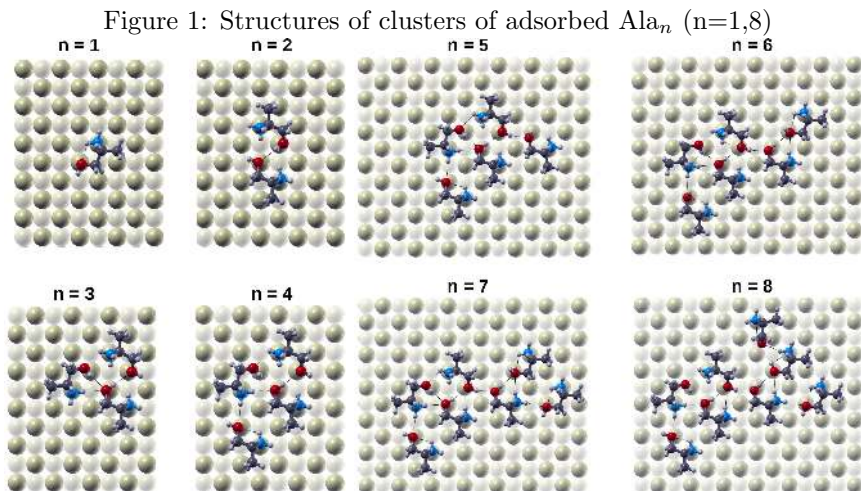
The standard Qeq approach, which well describes systems controlled by isotropic coulomb forces, has not been built for simulation involving chemical bonds with angular dependencies which play a fundamental role in the interaction between organic molecules and metal surfaces. Therefore, we have developed an anisotropic interaction energy term (E_{Ang}) which considers the non-coulomb forces between the atoms of the molecules and of the metal. This term depends on the interatomic distance r_{ij} and on the angle θ_{ij} between the normal to the surface of the metal and the line connecting the i^{th} molecular atom and the j^{th} metal atom:

$$E_{Ang} = \sum_{ij}^N \beta_{ij} \left[\left(1 - e^{-\alpha_{ij}(r_{ij} - R_{ij}^o)} \right)^2 - 1 \right] e^{-b_{ij}\theta_{ij}} \quad (1)$$

where all the parameters $\beta_{ij} = \sqrt{\beta_i^o \beta_j^o}$, $\alpha_{ij} = \sqrt{\alpha_i^o \alpha_j^o}$, $R_{ij}^o = \sqrt{\rho_i^o \rho_j^o}$, $b_{ij} = \sqrt{b_i^o b_j^o}$ depend on the type of the i^{th} and j^{th} atoms.

3 Results and Discussions

Here we report the study of the adsorption mechanism at low-coverage, from 1 to 8 adsorbed molecules. From now on the alaninol molecule in the cluster is named Ala. The approach described in the computational section is valid in the dynamic regime where the time interval between the arrival of two subsequent molecules on the surface is much longer then the lifetime of the thermal relaxation involved



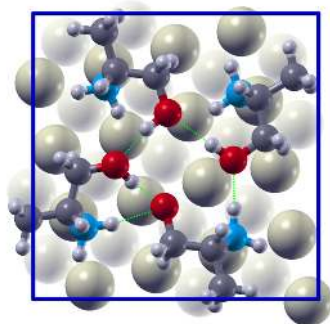
in the adsorption process itself (low flow of impinging gas molecules). At variance with this fast thermal relaxation regime, a slow thermal relaxation can occur when the time interval between the sticking of two molecules, arriving one after the other, is equal or shorter than the thermal cooling of the previously adsorbed molecules. In this last case the relaxation towards the minimum energy structures of the molecules on the surface involves a large amount of molecules at the same time, this is a typical cooperative process usually associated with the formation of an ordered monolayer of deposited molecules. We study here the differences of these two dynamic regimes by comparing the structural and energetic properties of small adsorbed clusters (fast thermal relaxation) and full-coverage monolayer (slow thermal relaxation) of Ala molecules.

In fig. 1 we report the structures of Ala_n clusters adsorbed on the Cu(100) surface as obtained by simulated annealing in the fast thermal relaxation case. In all the energy minima we have found that N and O atoms are on the top of vicinal Cu atoms, the methyl groups are always directly interacting with the metal surface by means of dispersion energy contribution (E_{VdW}) which is, on average, of about 6 Kcal/mol for every Ala molecule, and it is mostly additive.

The hydrogen bonds (HB) involving both the OH and NH_2 groups are present in all the adsorbed clusters, they connect molecules in complex patterns characterized by inter and intra molecular HB interactions. This energy contribution (E_{HB}) is almost linear with the size of the clusters, the ratio between the total HB interaction and the number of molecules in the cluster is in the range between 2.5 and 3.5 Kcal/mol, indicating no magic number effects or other types of discontinuities in both the intra- and inter- molecular hydrogen bonds.

The process of self assembly of the monolayer does occur when the thermal relaxation of the deposited Alas is slow compared with the time interval between the arrival of two successive molecules on the Cu surface (high flux of gas molecules impinging on the metal surface). We have calculated the molecular structure of the monolayer, the unit cell of this monolayer is sketched in fig. 2 together with the four Ala molecules which form the tetramer already seen by STM [7]. Here all the Alas have N atoms on top position, while the O atoms are in between top and bridge positions, all the methyl groups interacts by dispersion forces with the Cu metal surface. The intermolecular HB network among the four Alas involves the OH groups forming a quadrilateral structure whose vertexes are occupied by the oxygen atoms. The amino groups are less involved in the intermolecular HB network, with a preference for the intramolecular HB. The tetramer is characterized by exhibiting almost always the alkyl groups towards the neighboring tetramers, and there is not HB interactions among tetramers. A proper quantitative analysis of the energy components is required to characterize the nature of the interactions and the supramolecular effects on the monolayer formation. The AQueq total adsorption binding energy of the tetramer in the ML is almost 10 Kcal/mol lower than that of the Ala_4 cluster. The coulomb attraction between the Ala and the Cu atoms beneath neighboring Alas is considered (a slanting coulomb attraction). In the ML-tetramer this attraction is higher than in the Ala_4 cluster because of

Figure 2: Tetramer structure of the D-alaninol molecules in the full coverage monolayer.



the compact structure of the ML-tetramer with respect to the Ala_4 , where the Σ_{qCu} of the ML-tetramer is almost half of the cluster Ala_4 . The reliability of these results is supported by both experimental STM imaging and quantum calculations based on PW-DFT. In the ML the adsorption binding energy per molecule of the quantum calculation is 14.30 Kcal/mol, in good agreement with AQeq data of 14.12 Kcal/mol. The characteristic interatomic distances obtained from AQeq and quantum calculations are: $R_{Cu-N}^{AQeq} = 2.12 \text{ \AA}$, $R_{Cu-O}^{AQeq} = 3.17 \text{ \AA}$, $R_{Cu-N}^{DFT} = 2.24 \text{ \AA}$, $R_{Cu-O}^{DFT} = 3.90 \text{ \AA}$.

4 Conclusions

We have studied the process of surface molecular adsorption by a new computational tool that combines the charge equilibration model and the pairwise atomic interactions with a surface angular anisotropic dependence. This approach makes unnecessary the topological constraints of standard MD model. Our model has been parametrized by comparison with quantum calculations, and we have performed an extensive set of simulated annealing to find the minimum energy structures of clusters of Ala_n ($n=1,8$) adsorbed on the Cu(100) surface and ML formation. This procedure yielded new structures not found previously by PW-DFT calculations combined with standard MD. The calculated STM image is in good agreement with the experimental STM data.

5 Acknowledgement

The authors thank the Computing resources and related technical support provided by CRESCO/ENEAGRID High Performance Computing infrastructure and its staff; see <http://www.cresco.enea.it> for information.

References

- [1] J. V. Barth, G. Costantini, and K. Kern. *Nature*, 437:671–679, 2005.
- [2] C. Joachim, J. K. Gimzewski, and A. Aviram. *Nature*, 408:541–548, 2000.
- [3] Andrea Floris, Alessio Comisso, and Alessandro De Vita. *ACS Nano*, 7(9):8059–8065, 2013.
- [4] Giulia Tomba, Lucio Colombi Ciacchi, and Alessandro De Vita. *Adv. Mat.*, 21(10-11):1055–1066, 2009.
- [5] P. Giannozzi, S. Baroni, N. Bonini, M. Calandra, R. Car, C. Cavazzoni, D. Ceresoli, G. L. Chiarotti, M. Cococcioni, I. Dabo, A. Dal Corso, S. Fabris, G. Fratesi, S. de Gironcoli, R. Gebauer, U. Gerstmann, C. Gougoussis, A. Kokalj, M. Lazzeri, L. Martin-Samos, N. Marzari, F. Mauri, R. Mazzarello, S. Paolini, A. Pasquarello, L. Paulatto, C. Sbraccia, S. Scandolo, G. Sclauzero, A. P. Seitsonen, A. Smogunov, P. Umari, and R. M. Wentzcovitch. *Phys. Condens. Matter.*, 21:395502, 2009.
- [6] A Palma and M Satta. A new anisotropic charge-equilibration method for self-assembly of organics on metal surface: d-alaninol on cu(100). *J. Chem. Theory Comput.*, 2016. accepted DOI: 10.1021/acs.jctc.6b00430.
- [7] G. Contini, P. Gori, F. Ronci, N. Zema, S. Colonna, M. Aschi, A. Palma, S. Turchini, D. Catone, A. Cricenti, and T. Prospero. *Langmuir*, 27:7410–7418, 2011.

ENLIGHTENING OF WATER SELF-ASSEMBLING PHENOMENA ONTO THE (101) TiO₂ ANATASE SURFACE BY ATOMISTIC MULTI-SCALE MODELING

Fabrizio Gala^{1*}, Lorenzo Agosta² and Giuseppe Zollo¹

¹*Dipartimento di Scienze di Base e Applicate per l'Ingegneria, Università di Roma "La Sapienza", Via A. Scarpa 14-16, 00161 Rome Italy*

²*Department of Materials and Environmental Chemistry, Stockholm university, 2014 Arrhenius Laboratory, Svante Arrhenius väg 16C, Stockholm Sweden*

ABSTRACT. (101) anatase TiO₂ surface in water ambient is of crucial importance for biocompatibility. Experiments show that water molecules are mobile at as low temperature as 190 K and tend to form clusters along the $[11\bar{1}]/[1\bar{1}\bar{1}]$ surface direction. In this article we report a self-consistent theoretical characterization of the dynamical properties of the first water layer on the (101) anatase TiO₂ surface is presented using a various computational techniques in the context of the transition state theory in the harmonic regime with a multi-scale approach. Indeed *first-principles* total energy calculations, density functional perturbation theory, minimum energy path search and kinetic Monte Carlo simulations are employed to explain the experimental evidences on water kinetics on the (101) anatase TiO₂ surface.

1 Introduction

Titanium dioxide (TiO₂) surfaces are important systems in many technological areas such as medicine and pharmacology[19], photocatalysis and solar-hydrogen production[7], and surface recognition by organic materials[2]. In particular, while the macroscopic TiO₂ ground state phase is rutile, TiO₂ nanoparticles prefer the anatase phase.

As a consequence, because TiO₂ nano-devices employed for most of the above applications involve aqueous environment, the interaction between water and TiO₂ (101) anatase surface has been extensively studied in the last years[20, 13, 11, 3]. However the interest has been mainly focussed on the adsorption properties of water on the titania surface, while little is known on the kinetic properties. Furthermore, it has been shown that water molecules mediate the adsorption of biological molecules on TiO₂ (101) surface [2]; thus selectivity properties of biological matter on TiO₂ (101) surface might be strongly affected by the diffusion properties of water on such surfaces.

From the experimental point of view, it has been shown[13] that water adsorbed on anatase surface is thermodynamically stable in vacuum up to ~ 200 K, even if in presence of subsurface defects water adsorption on anatase has been observed up to 400 K[11]. Moreover a tendency to form small water aggregates along the $[11\bar{1}]/[1\bar{1}\bar{1}]$ direction of the (101) anatase surface has been observed by STM [11]

*Corresponding author. E-mail: fabrizio.gala@uniroma1.it.

that is not fully explained so far. In the following we report on a complete characterization of the kinetic behavior of the first water layer deposited onto the (101) anatase surface giving, for the first time, a complete insight to the above mentioned experimental observation of water clustering along preferential surface directions. The study has been performed in the context of quantum mechanical transition state theory (TST) in the harmonic regime using ground state Density Functional Theory (DFT), Density functional perturbation theory (DFPT), minimum energy path (MEP) search and kinetic Monte Carlo (KMC) simulations.

2 Theoretical Method

The DFT[14, 15] scheme here employed adopts a generalized gradient approximation (GGA) of the electron exchange and correlation energy using Perdew-Burke-Ernzerhof formula (PBE)[18] as implemented in QUANTUM-ESPRESSO (QE) package[9]; ultra-soft pseudopotentials (US-PP) have been employed that, according also to other authors [16], have been demonstrated to be suitable for this system. The (101) anatase TiO₂ surface has been modelled using a slab geometry laying in the xy plane composed by two surface unit cells along the y and the z directions and one along x . The slab contains 48 TiO₂ atoms and the supercell includes two vacuum regions nearly of 16.2 Å thick each. The artificial electric field across the slab induced by the PBCs has been corrected following Ref. [5] and a 4x4x1 Monkhorst-Pack (MP) k -point grid[17] for the Brillouin zone (BZ) sampling has been employed. The ground state configurations have been fully relaxed using the Broyden-Fletcher-Goldfarb-Shanno (BFGS) algorithm[6] with the Hellmann-Feynman forces acting on the ions, together with empirical long-range corrections[10].

TST predicts the hop rate ν between two local minima as:

$$\nu = \frac{k_B T}{h} \frac{Z_{vib}^s}{Z_{vib}} \exp\left(-\frac{\Delta E}{k_B T}\right) \quad (1)$$

where k_B and h are the Boltzmann and the Planck constants, Z_{vib} and Z_{vib}^s are the partition functions of the initial and transition (saddle) states and ΔE is the difference in energy between the saddle-point and the minimum energy configurations. ΔE energy barriers and the corresponding diffusion paths, or minimum energy paths, have been studied through the Nudged Elastic Band (NEB) method[12] as implemented in QE.

On the other hand, quantum statistical mechanics in harmonic approximation allows to rewrite the hop rate defined in Eq.(1) as a function of the Helmholtz free energy F of the system, as:

$$\nu = \frac{k_B T}{h} \exp\left(-\frac{\Delta E + \Delta F_{vib}(T)}{k_B T}\right) = \nu^* \exp\left(-\frac{E_a}{k_B T}\right) \quad (2)$$

being

$$F_{vib}(T) = \frac{k_B T}{\Omega} \int_{\text{BZ}} d\mathbf{q} \sum_{i=1}^{3N} \log \left[2 \sinh \left(\frac{\hbar \omega_i(\mathbf{q})}{2k_B T} \right) \right] = \int_0^\infty d\omega g(\omega) \left[\frac{\hbar \omega}{2} + k_B T \log \left(1 - \exp \left(-\frac{\hbar \omega}{k_B T} \right) \right) \right] \quad (3)$$

where $E_a = \Delta E + \Delta F_{vib}(0)$ is the activation energy, Ω is the area of the Brillouin Zone (BZ), N is the total number of atoms, and $\omega_i(\mathbf{q})$ is the frequency of the i -th mode at wave-vector \mathbf{q} and $g(\omega)$ is the phonon density of states (PHDOS) normalized to the number of phonon branches (i.e. $3N$).¹ In the vibrational partition function of the saddle configuration one of such branches, corresponding to the reaction coordinate, is a pure imaginary number, and must be excluded in the evaluation of the free

¹The temperature dependent prefactor ν^* is then defined as:

$$\nu^* = \frac{k_B T}{h} \exp\left(-\int_0^\infty d\omega \Delta g(\omega) \log \left(1 - \exp \left(-\frac{\hbar \omega}{k_B T} \right) \right)\right)$$

energy; thus in the following it will be treated as a negative frequency, being excluded from the integral defining $F_{vib}(T)$.

Phonon frequencies $\omega_i(\mathbf{q})$, evaluated in the framework of DFPT[4] with QE, are solutions of the secular equation:

$$\det \left| \frac{1}{\sqrt{M_s M_t}} C_{\alpha\beta}^{st}(\mathbf{q}) - \omega^2(\mathbf{q}) \mathbf{I} \right| = 0 \quad (4)$$

where $C_{\alpha\beta}^{st}(\mathbf{q})$ are the *interatomic force constants* (IFCs) between atoms s and t (of mass M_s and M_t respectively) evaluated in reciprocal space[4], and α, β run over cartesian the indexes $\{x, y, z\}$; a $2 \times 2 \times 1$ \mathbf{q} point uniform grid has been employed to calculate the entire phonon spectra: indeed such mesh has been tested to be sufficient for convergence. The semi-empirical term accounting for long-range interactions has been neglected in the calculation of the phonon spectra because its contribution to the IFCs, evaluated analytically, resulted negligible for all the configurations studied. Lastly, Kinetic Monte Carlo (KMC) simulations have been performed to follow the diffusion and clustering events of water molecules on the (101) anatase surface at various temperature and coverage values. The rates used in the using the KMC simulations have been defined on the basis of the migration energy and hopping rates calculated as specified above and corrected for local effects as discussed in the following section.

3 Results and Discussion

As mentioned above, the adsorption of a single water molecule on a (101) TiO_2 surface occurs trough three bonds: one $O_w - \text{Ti}_{5c}$ and two $H_w - O_{2c}$ hydrogen bonds (H-bonds)[2]. The adsorption energy of such ground state configuration ("stable configuration") is equal to $E_{ads} = -0.73$ eV. This fact suggests to look for diffusion paths connecting Ti_{5c} equivalent surface atoms, i.e. the adsorption sites where a water molecule can be adsorbed; following this criterion, two migration paths have been chosen along the $[010]$ and $[11\bar{1}]/[1\bar{1}\bar{1}]$ directions parallel to the surface, that basically connect two adjacent adsorption sites where the water can stay in its ground state configuration.

In Fig. 1 the energy barriers are reported for respectively the $[010]$ and the $[11\bar{1}]/[1\bar{1}\bar{1}]$ diffusion paths with the relevant error bars.

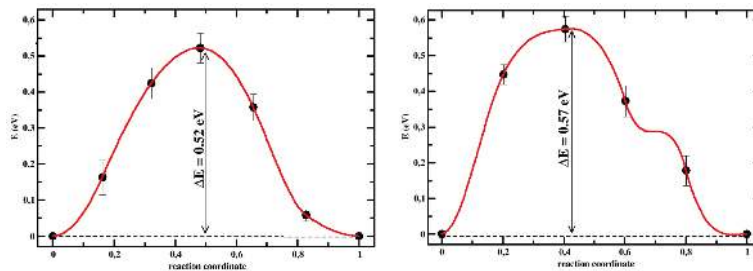


Figure 1: MEP and total energy profile for water diffusion along the $[010]$ (a) and the $[11\bar{1}]/[1\bar{1}\bar{1}]$ (b) directions on the TiO_2 surface

The total energy profiles here calculated, exhibit a symmetric and an asymmetric barrier for $[010]$ and $[11\bar{1}]/[1\bar{1}\bar{1}]$ respectively, similarly to previous ones obtained with a semi-empirical model[20]; the energy barriers here measured for migration along the $[010]$ and the $[11\bar{1}]/[1\bar{1}\bar{1}]$ paths are respectively $\Delta E_{[010]} \simeq 0.52$ eV and $\Delta E_{[11\bar{1}]/[1\bar{1}\bar{1}]} \simeq 0.57$ eV, indicating that those calculated by semi-empirical methods[20] are severely overestimated by 130 and 150 meV respectively.

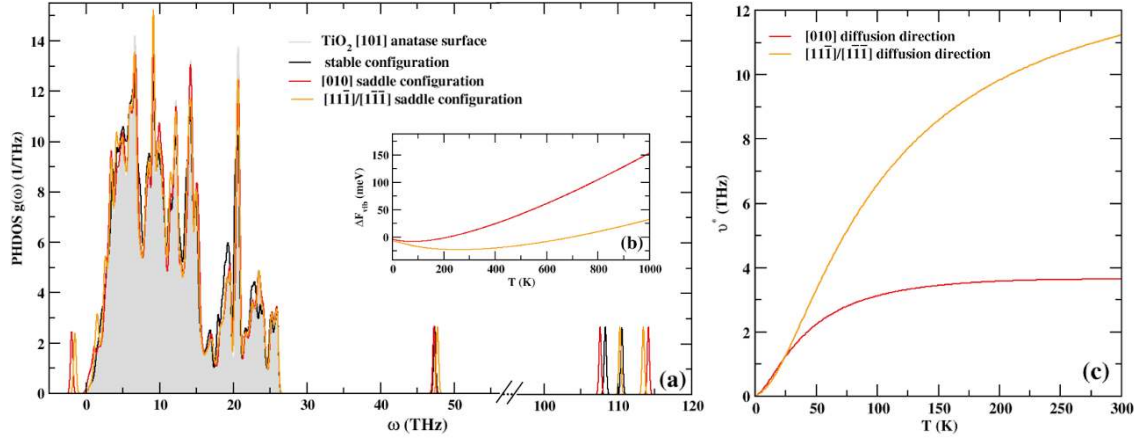


Figure 2: Calculated PHDOS (convoluted with gaussian functions) of the anatase (101) surface (grey area), of the stable configuration (black line), and of the two saddle configurations studied (red and orange lines respectively) (a); variation of the vibrational free energy as a function of the temperature for both the saddle configurations (b); frequency pre-factor for the two directions of migrating water (c).

In both cases TiO_2 surface atoms are little affected by relaxation and the main contribution to the calculated energy barrier is due to bond breaking and forming between the diffusion water and the surface. Along [010], water shifts almost rigidly and the largest contribution to the energy barrier is due to the breaking of the $O_w - \text{Ti}_{5c}$ bond, while at least one hydrogen bond is maintained along the entire migration path. The saddle point configuration of water migration along [010] ("[010] saddle configuration") is such that the water oxygen stays in the middle point between the initial and the final Ti_{5c} adsorption sites of the diffusion step. Along $[11\bar{1}]/[1\bar{1}\bar{1}]$, instead, a sort of "rolling stone" behavior of the water molecule occurs[1]; again the covalent bond breaking contributes most to the energy barrier. The saddle point (the "[11 $\bar{1}]/[1\bar{1}\bar{1}]$ saddle configuration") is such that the H_2O molecule lies in the plane orthogonal to the surface.

Following TST, the hopping rate of the water molecules along the two diffusion paths depends on the pre-factor ν^* that is related to the vibrational properties of both the saddle and the stable configurations. The PHDOS of the stable configuration, reported in Fig.2(a) shows that the adsorption of the water molecule slightly affects the TiO_2 surface $g(\omega)$ (that is in the range from 0 to 27 THz) in the range from 15 to 25 THz; moreover three local water vibrational peaks are visible outside the surface region. Those peaks (corresponding to the modes 151, 152, and 153 with frequency values reported in Table 1) are respectively a bending mode and a symmetrical and an asymmetrical stretching modes of the O-H bonds of the H_2O molecule. In particular the 153 peak is down-shifted by ~ 1.53 THz with respect to the isolated water molecule.

In the [010] saddle configuration, a new imaginary eigenvalue of the secular equation (an imaginary frequency peak) appears at $2.08i$ THz; such imaginary solution corresponds to the reaction coordinate of the diffusion process and shows no dispersion in the BZ. The other localized peaks are still present, even if they are shifted (see Table 1), and the 152 mode is an asymmetrical stretching mode instead of a symmetrical one. Similarly, the PHDOS of the $[11\bar{1}]/[1\bar{1}\bar{1}]$ saddle configuration has an imaginary eigenvalue at $1.60i$ THz (along the reaction coordinate), and three localized modes outside the frequency region of the surface.

On the basis of the above PHDOS, the change of the vibrational free energy of the saddle point with respect to the stable configuration $\Delta F_{vib}(T)$ have been calculated and are reported in Fig.2(b); the zero point energy (ZPE) differences (i.e. $\Delta F_{vib}(0)$) are quite small and negative (see Table 2) being almost

negligible with respect to the energy barriers ΔE (first column of Table 2). The resulting vibrational prefactors ν^* shown in Fig.2(c) are rather different: while in the [010] diffusion direction ν^* is already nearly saturated at T=150K, being withing 5% of the saturation value (and reaches the saturation value at T=200 K), in the $[11\bar{1}]/[1\bar{1}\bar{1}]$ case ν^* increases monotonically in a much wider range containing the room temperature (RT); hence the vibrational prefactor at RT results four times larger for $[11\bar{1}]/[1\bar{1}\bar{1}]$ than for [010] (see Table 2). This circumstance makes the rate along [010] to behave nearly as a simple Arrhenius function of the temperature (with a constant prefactor) in the range $150K \leq T \leq 300K$ where the harmonic approximation is likely to hold, with the saturated pre-factor value being $\nu^* = 3.64THz$ (see Table 2). In any case the two pre-factors are of the same order of magnitude. This is the reason why the rates are mainly dependent on the activation energies along the two directions considered.

Table 1: Frequencies and classification of normal modes for the configurations studied. Modes are classified as: bending(B), asymmetrical stretching (aS), and symmetrical stretching (sS).

conf.	Imaginary Mode [THz]	Mode 151 [THz]	Mode 152 [THz]	Mode 153 [THz]
isolated water	-	47.93 (B)	108.72 (sS)	112.031 (sS)
stable	-	47.34 (B)	108.27 (sS)	110.50 (aS)
[010] saddle	2.08 <i>i</i>	47.24 (B)	107.60 (aS)	114.12 (aS)
$[11\bar{1}]/[1\bar{1}\bar{1}]$ saddle	1.60 <i>i</i>	47.76 (B)	110.27 (sS)	113.43 (aS)

Indeed the final calculated jump frequencies at room temperature, that are of the same order of magnitude, are such that $\nu_{[010]} = 7.82 \cdot 10^3$ Hz is greater than $\nu_{[11\bar{1}]/[1\bar{1}\bar{1}]} = 3.94 \cdot 10^3$ Hz, due to the larger diffusion energy barriers along $[11\bar{1}]/[1\bar{1}\bar{1}]$ (with respect to the [010] one) affecting the exponential factor in Eq. (2).

Table 2: Diffusion barriers, variations in the ZPE, vibrational prefactors and jump frequencies for the [010] and $[11\bar{1}]/[1\bar{1}\bar{1}]$ diffusion directions. Prefactors and jump frequencies have been calculated at room temperature (i.e. T= 300 K).

direction	ΔE (eV)	$\Delta F_{vib}(0)$ (eV)	$\nu^*_{(300)}$ (THz)	$\nu_{(300)}$ (kHz)
[010]	0.52	$-4.04 \cdot 10^{-3}$	3.64	7.82
$[11\bar{1}]/[1\bar{1}\bar{1}]$	0.57	$-7.20 \cdot 10^{-3}$	11.23	3.94

On the basis of the calculated values of the pre-factor ν^* and of the activation energy E_a , we have implemented a kinetic Monte Carlo model in order to explain the preferential water clustering along the $[11\bar{1}]/[1\bar{1}\bar{1}]$ directions observed by STM [11]. We have considered six possible jumping events for each isolated water molecule: two along [010] towards the two nearest neighbours Ti adsorption sites and four along $[11\bar{1}]/[1\bar{1}\bar{1}]$ towards the next nearest neighbours Ti surface adsorption sites. Technical details can be found in the recent literature [8].

Because the activation energy must be modified depending on the local environment of the migrating water molecule, the calculated energy barriers have been corrected using the ground state data reported in the article by He and co-workers [11] as better explained in Agosta and co-workers [8]; therefore all the possible local environments have been taken into account ranging from one by six nearest and next nearest neighbours occupied, to five by six nearest and next nearest neighbours occupied; all corrections to the energy barriers were derived from the total energy data by He and co-workers [11]. The values used for ΔE , $\Delta F(0)$ and the prefactor ν^* , instead, are the ones here calculated for an isolated water molecule along the [010] and $[11\bar{1}]/[1\bar{1}\bar{1}]$ direction paths. Following the experiments by He and co-workers, we have considered 0.11 ML of water on the (101) anatase surface at 190 K by using a surface with 1600 surface Ti adsorption site (i.e. about a $21 \times 14 nm^2$ surface) and 176 water molecules. The initial configuration has been chosen randomly, without nearest or next nearest neighbours water pairs.

In Fig.3(a) we report the snapshots of the KMC simulations performed at the above conditions. The

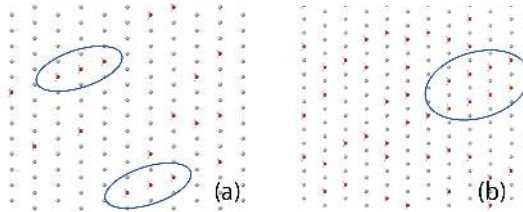


Figure 3: Kinetic Monte Carlo simulations at $T=190$ K with 0.11 ML of coverage and $T=150$ K with 0.25 ML of coverage (b).

number of water pairs, i.e. the pairs of waters staying at nearest (along the $[010]$ direction) or next nearest (along the two $[11\bar{1}]/[1\bar{1}1]$ -type directions) neighbours during time reaches the stationary value of 60 for $[11\bar{1}]/[1\bar{1}1]$ after 100 s, while the number of pairs along $[010]$ is negligible. We have also measured the average length of the $[11\bar{1}]/[1\bar{1}1]$ alignments that is nearly 6.5 Å and the average latency time of the alignments (i.e. the average life time of water pairs alignments calculated in the time interval $[0, t]$) is $t_{lat} = 10$ s which means that the time needed to observe water migrating on the surface should be at least 10 s in these conditions. In the same article, He and co-workers reported on the formation of a water super-structure at lower temperature (150 K) and larger coverage (0.24 ML). We have replicated this experiment in the context of KMC showing the frequent formation of water superstructures basically made of two parallel stable alignments along the $[11\bar{1}]/[1\bar{1}1]$ separated by one empty row.

In Fig. 3(b) we show the typical snapshot occurring in this case where a typical super-structure arise during the simulation. It is seen that such superstructures are long lasting because the latency of the $[11\bar{1}]/[1\bar{1}1]$ alignments is measured in hours and the coverage value ensures the surface density needed to form alternated $[11\bar{1}]/[1\bar{1}1]$ rows with and without water alignments. Then the observed superstructure is due both to the reduced hopping along the $[11\bar{1}]/[1\bar{1}1]$ direction at as low temperature as 150 K (while the one along $[010]$ is still large in comparison due to the lower barrier) and to the large coverage value that favors the formation of longer clusters along $[11\bar{1}]/[1\bar{1}1]$ (the average length is measured as about 7.5 Å); moreover, these clusters are likely to stay at $[11\bar{1}]/[1\bar{1}1]$ next nearest rows because of the large surface density and because the clustering at adjacent rows is inhibited for energetic reasons (the energy penalty for the alignment along $[010]$ is quite large). Then, while the clustering along $[11\bar{1}]/[1\bar{1}1]$ is explained on the basis of the different diffusion properties and energetic penalty values for the alignments along $[11\bar{1}]/[1\bar{1}1]$ with respect to $[010]$, the formation of the super-structured water patterns observed at $T=150$ K and 0.24 ML of coverage is also strictly related to the large coverage ratio used in the experiments and to the large latency that makes such structures stable.

References

- [1] L. Agosta, F. Gala, and G. Zollo. Water diffusion on TiO_2 anatase surface. *AIP Conf. Proc.*, 1667:020006–1–020006–9, 2015.
- [2] L. Agosta, G. Zollo, C. Arcangeli, F. Buonocore, F. Gala, and M. Celino. Water driven adsorption of amino acids on the (101) anatase TiO_2 surface: an *ab initio* study. *PCCP*, 17:1556–1561, 2015.
- [3] U. Aschauer, Y. He, H. Cheng, S.-C. Li, U. Diebold, and A. Selloni. Influence of subsurface defects on the surface reactivity of TiO_2 : Water on Anatase (101). *J. Phys. Chem. C*, 114:1278–1284, 2010.
- [4] S. Baroni, S. de Gironcoli, A. Dal Corso, and P. Giannozzi. Phonons and related crystal properties from density-functional perturbation theory. *Rev. Mod. Phys.*, 73:515–562, 2001.

- [5] L. Bengtsson. Dipole correction for surface supercell calculations. *Phys. Rev. B*, 59:12301–12304, 1999.
- [6] R. Fletcher. A new approach to variable metric algorithms. *The Computer Journal*, 13(6):317–22, 1970.
- [7] A. Fujishimaa, X. Zhangb, and D. A. Trykc. TiO₂ photocatalysis and related surface phenomena. *Surf. Sci. Rep.*, 63(12):515–582, 2008.
- [8] Fabrizio Gala, L. Agosta, and Giuseppe Zollo. Water kinetics and clustering on the (101) tio2 anatase surface. *The Journal of Physical Chemistry C*, 120(1):450–456, 2016.
- [9] P. Giannozzi, S. Baroni, N. Bonini, M. Calandra, R. Car, C. Cavazzoni, D. Ceresoli, G. L. Chiarotti, M. Cococcioni, I. Dabo, A. Dal Corso, S. de Gironcoli, S. Fabris, G. Fratesi, R. Gebauer, U. Gerstmann, C. Gougoussis, A. Kokalj, M. Lazzeri, L. Martin-Samos, N. Marzari, F. Mauri, R. Mazzarello, S. Paolini, A. Pasquarello, L. Paulatto, C. Sbraccia, S. Scandolo, G. Sclauzero, A. P. Seitsonen, A. Smogunov, P. Umari, and R. M. Wentzcovitch. Quantum espresso: a modular and open-source software project for quantum simulations of materials. *J. Phys.: Condens. Matter*, 21:395502–1–19, 2009.
- [10] S. Grimme. Semiempirical GGA-type density functional constructed with a long-range dispersion correction. *J. Comput. Chem.*, 27(15):1787–99, 2006.
- [11] Y. He, A. Tilocca, O. Dulub, A. Selloni, and U. Diebold. Local ordering and electronic signatures of submonolayer water on anatase TiO₂ (101). *Nature Materials*, 8:585–589, 2009.
- [12] G. Henkelman, B. P. Uberuaga, and H. Jónsson. A climbing image nudged elastic band method for finding saddle point and minimum energy paths. *J. Chem. Phys.*, 113(22):9901–9904, 2000.
- [13] G. S. Herman, Z. Dohnhalek, N. Ruzycki, and U. Diebold. Experimental investigation of the interaction of water and methanol with anatasetio₂(101). *J. Phys. Chem. B*, 107:2788–2795, 2003.
- [14] P. Hohenberg and W. Kohn. Inhomogeneous electron gas. *Phys. Rev.*, 136:B864–B871, Nov 1964.
- [15] W. Kohn and L. J. Sham. Self-consistent equations including exchange and correlation effects. *Phys. Rev.*, 140:A1133–A1138, Nov 1965.
- [16] M. Lazzeri, A. Vittadini, and A. Selloni. Structure and Energetics of Stoichiometric TiO₂ Anatase Surfaces. *Phys. Rev. B*, 63:155409, 2001.
- [17] H.J. Monkhorst and J.D. Pack. Special points for brillouin-zone integrations. *Phys. Rev. B*, 13(5):5188–92, 1973.
- [18] J.P. Perdew, K. Burke, and M.Ernzerhof. Generalized Gradient Approximation Made Simple. *Phys. Rev. Lett.*, 77(4):3865–68, 1996.
- [19] K. Shiba. Exploitation of peptide motif sequences and their use in nanobiotechnology. *Current opinion in biotechnology*, 21(4):412–25, 2010.
- [20] Z. Zhao, Z. Li, and Z. Zou. Understanding the interaction of water with anatase TiO₂ (101) surface from density dunctional theory calculations. *Phys. Lett. A*, 375:2939–2945, 2011.

IMPLEMENTATION OF AN AIR QUALITY FORECAST SYSTEM OVER ITALY

Mario Adani¹, Massimo D'Isidoro^{1*}, Gino Briganti² and Andrea Cappelletti²

¹ENEA SSPT-MET-INAT, Via Martiri di Monte Sole, 4 40133, Bologna, Italy

²ENEA SSPT-MET-INAT, Pisa, Italy

* e-mail: massimo.disidoro@enea.it

ABSTRACT. We present the description of a modelling chain implemented in CRESCO-HPC and operating on a daily basis producing 5-days air quality forecasts. The system is based on the Atmospheric Modelling System (AMS) of MINNI [1,2], and runs two nested domains: the first one at 48km resolution over most of Europe; the second centred over Italy at 12km resolution.

1 Introduction

Since the year 2012 ENEA developed, supported by the Italian Ministry of Environment, the Italian Integrated Assessment Modelling System for supporting the International Negotiation Process on Air Pollution and assessing Air Quality Policies at national/local level (MINNI [1,2]). Since then, the MINNI has been continuously upgraded at the state of the art, in particular the atmospheric modelling system (AMS-MINNI) part, used also for research purposes [3,4].

The AMS-MINNI is a modelling chain based on the Chemistry Transport Model (CTM) FARM [5,6], which simulates transport, diffusion and chemical reactions of pollutants (gas and aerosols) in the atmosphere. Meteorological fields such as temperature, humidity, wind, precipitation and cloud cover in input to FARM are provided by the mesoscale non-hydrostatic meteorological model RAMS [7]. Turbulence parameters in the boundary layer are provided by the preprocessor SURFPRO [8], which also computes deposition velocities and natural emissions that are dependent on turbulence parameters. Anthropogenic emissions are processed by Emission Manager (EMMA) [9], while the initial and boundary conditions for concentrations are provided by the EMEP model EMEP/MSC-E: http://www.emep.int/mscw/index_mscw.html, EMEP/MSC-W: <http://www.msceast.org/>).

With the aim of obtaining a constant monitoring of pollutant levels in the atmosphere, ENEA developed a forecast modelling system based on SMA-MINNI which provides hourly 5-days forecasts of main pollutants concentrations on a daily basis.

2 Description of the forecast system

The forecast chain is based on the AMS-MINNI numerical modules described above, with some differences regarding the input fields. Details of the configuration follow.

Input data used for the air quality forecast are provided by different sources. Initial and boundary conditions for meteorology (RAMS inputs) are from GFS (Global Forecasting System), which has free access to global forecasts. Every day 3D fields are downloaded from the 18UTF GFS run. Boundary conditions (3-hourly) for concentrations are downloaded every day from the servers of the Copernicus Atmosphere Monitoring Service (CAMS, atmosphere.copernicus.eu). Emissions for Italy are computed starting from the national inventory (<http://www.sinanet.isprambiente.it/it/sia-ispra/inventaria/disaggregazione-dellinventario-nazionale-2010/aggiornamento-con-dati-della-submission-2013/view>), while for the other countries included in the domain the source is TNO 2005 (<https://www.tno.nl/>).

RAMS model is devoted to the meteorological step, running 5 days plus a 6h spin-up period. Output fields are then interpolated over FARM grid and passed to SURFPRO which computes turbulence parameters, deposition velocities for gases and natural sources (resuspension and sea salt). Emissions are elaborated by EMMA which makes the spatial/temporal disaggregation and the speciation. Finally FARM runs with the following configuration, represented schematically in Figure 1:

- GAS: chemical mechanism SAPRC99 [10], with inclusion of mercury [11,12] and Polycyclic Aromatic Hydrocarbons (PAH)[13];
- AEROSOLS: module AERO3 [14] for aerosols with SORGAM [15] and ISORROPIA (<http://nenes.eas.gatech.edu/ISORROPIA>), for secondary aerosol formation organic and inorganic, respectively. AERO3 uses a three modal representation for particles dimension and simulates nucleation, condensation and coagulation processes.
- DEPOSITION: dry and wet deposition for gases and aerosols are computed; the former uses a resistance analogy approach [16], while the latter in-cloud and sub-cloud scavenging in similar way as in EMEP [17].

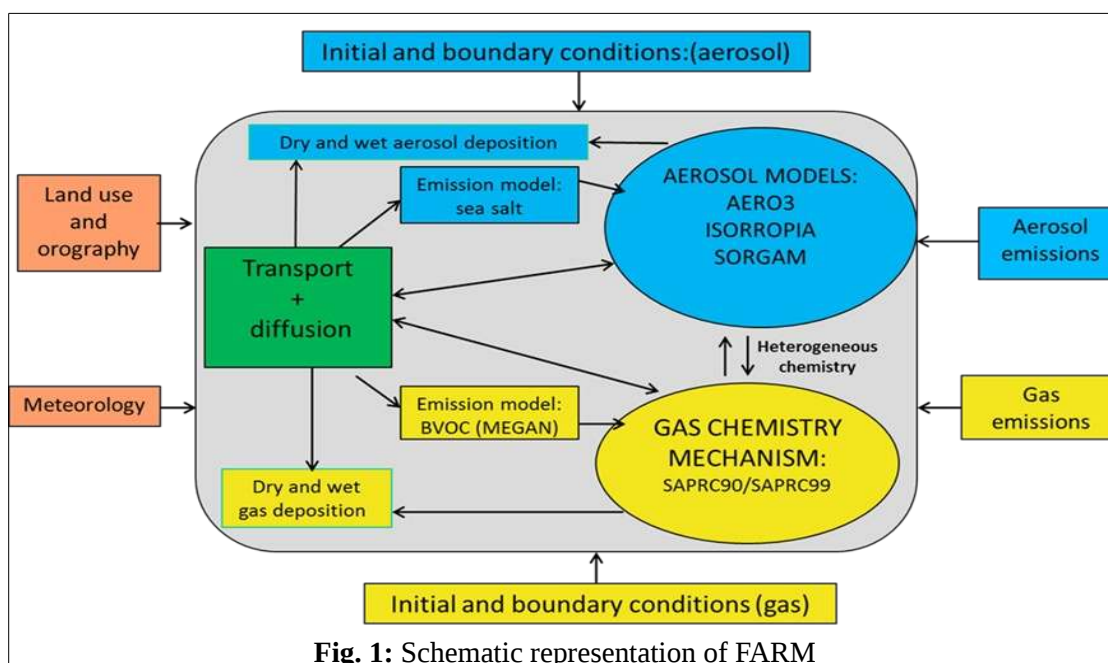


Fig. 1: Schematic representation of FARM

The forecast system operates over grids nested in a two-way mode, covering large part of Europe and Italy (Figure 2) at 48 and 12km horizontal resolution, respectively. Both grids have 16 vertical levels from 20m to 10000m above the surface.

Every day the system provides 5 days forecasts of hourly 3D concentration fields for the following pollutants: PM10, PM2.5, O₃, NO₂, NO, CO and SO₂.

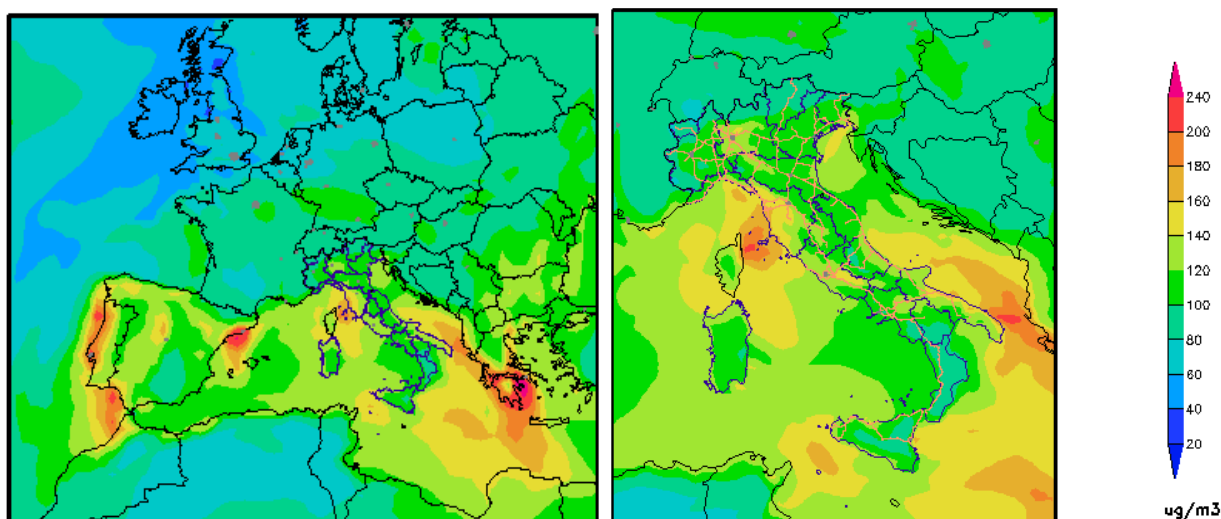


Fig. 2: Example of max 8h ozone field at lowest model level computed over the 48km resolution grid covering large part of Europe (left) and over 12km grid covering Italy (right).

3 Technical specifications

At present, the system is implemented and runs daily on CRESCO4 HPC. The chain is divided into two main blocks dealing with meteorology and chemistry. The first is devoted to the pre-processing, forecast and post-processing of meteorological quantities. The second block, starting once the first one has finished, is devoted to pre-processing, forecast and post-processing of pollutants fields. All input/output processes are done over the *gporq1_minni* file system. Details of the two blocks are presented in Tables 1 and 2.

Start Time	Process description	Cores	Time	Disk space
~18:30	Download input grib data from NCEP-GFS	1	~35m	900MB
	Preprocessing 3D grib data	1	~9m	4GB
	Preprocessing 2D grib data	1	<1m	1MB
	Make 2D input for RAMS	1	<1m	2MB
	Make 3D input for RAMS	1	~5m	485MB
	Run RAMS meteorological model (5days)	128	~35m	6GB
	Post-processing RAMS outputs	1	~5m	3.5GB
	Interpolate results over FARM grid	1	~6m	1.5GB
~20:30(END)	Prepare turbulence parameters (SURFPRO) and graphical elaborations (maps)	1	~5m	1.5GB

Table 1: Processes involved in the meteorological block of the forecast chain

Start Time	Process description	Cores	Time	Disk space
~22:30	Download input netcdf data from CAMS	1	~20m	1.4GB
(*)	Preprocessing of 3d netcdf data	1	~6m	2GB
(*)	Creation of IC/BC for FARM	1	~10m	65MB
(*)	Processing emissions (EMMA)	1	~1m	1.7GB
(*)	Run FARM for concentrations forecasts	96	~10m	4.5GB
~20:30(END)	Elaborate some statistics and maps	1	<1m	20MB

Table 2: Processes involved in the chemical block of the forecast chain. (*) Loop over 5 days.

4 Discussion and future work

A forecast chain for atmospheric pollutants concentrations is presented. The system is based on AMS-MINNI numerical codes and operates on a daily basis on CRESCO4-HPC, providing 2D maps of concentrations for the main pollutants (particulate matter and gases) for 5 days ahead. The system is composed into two blocks containing serial and parallel processes. With the configuration adopted, the system uses 96 to 128 cores in the parallel tasks and a total of about 50GB of disk space daily. The plan for the next future, thanks to the cpu power provided by CRESCO, is to refine horizontal resolution up to ~20km over Europe and ~4km over Italy. Preliminary tests are in progress to tune the optimal number of cores to be used.

References

- [1] D'ELIA, I., BENCARDINO, M., CIANCARELLA, L., CONTALDI, M., VIALETTO, G. *Technical and Non-Technical Measures for air pollution emission reduction: The integrated assessment of the regional Air Quality Management Plans through the Italian national model.* Atmospheric Environment, 43, (2009), 6182-6189, ISSN 1352-2310, <http://dx.doi.org/10.1016/j.atmosenv.2009.09.003>.
- [2] D'ELIA, I., PESCHI, E. *Lo scenario emissivo nazionale nella negoziazione internazionale.* Rapporto Tecnico RT/2013/10/ENEA, ENEA, (2013) ISSN 0393-3016, <http://openarchive.enea.it/handle/10840/4505>.
- [3] MIRCEA M., GRIGORAS G., D'ISIDORO M., RIGHINI G., ADANI M., BRIGANTI G., CIANCARELLA L., CAPPELLETTI A., CALORI G., CIONI I, CREMONA G., FINARDI S., LARSEN B.R., PACE G., PERRINO C., PIERSANTI A., SILIBELLO C., VITALI L., ZANINI G. *Impact of Grid Resolution on Aerosol Predictions: A Case Study over Italy*, Aerosol and Air quality Research, 2016, 16(5) 1253 - 1267.
- [4] ADANI M., MIRCEA M., D'ISIDORO M. *Heavy Metal Modelling Study over Italy: Effects of Grid Resolution, Lateral Boundary Conditions and Foreign Emissions on Air Concentration.* Water Air Soil Pollution (2015) 226: 46.

- [5] SILIBELLO C., CALORI G., BRUSASCA G., CATENACCI G., FINZI G. *Application of a photochemical grid model to Milan metropolitan area*. Atmospheric Environment 32 (11), (1998) PP. 2025-2038.
- [6] GARIAZZO C., SILIBELLO C., FINARDI S., RADICE P., PIERSANTI A., CALORI G., CECINATO A., PERRINO C., NUSIO F., CAGNOLI M., PELLICIONI A., GOBBI, G.P., DI FILIPPO P. *A gas/aerosol air pollutants study over the urban area of Rome using a comprehensive chemical transport model*. Atmospheric Environment 41, (2007) PP. 7286-7303.
- [7] COTTON W.R., PIELKE R. A., WALKO R. L. , LISTON G. E., TREMBACK C. J., JIANG H., MC ANELLY R. L., HARRINGTON J. Y., NICHOLLS M. E., CARRIO G. G. AND MCFADDEN, J. P. *RAMS 2001: CURRENT STATUS AND FUTURE DIRECTIONS*. METEOROLOGY AND ATMOSPHERIC PHYSICS, 82, (2003) 5-29.
- [8] ARIANET. *SURFPRO3 User's guide (SURFace-atmosphere interface PROcessor, Version 3)*. Ariamet report R2011.31 (2011).
- [9] ARIANET. *Emission Manager – Processing system for model-ready emission input. User's guide*. Ariamet report R2013.19 (2013)
- [10] CARTER W.P.L., *Documentation of the SAPRC-99 chemical mechanism for VOC reactivity assessment*. Final Report to California Air Resources Board, Contract No. 92-329, and (in part) 95-308. May 8, 2000.
- [11] YARWOOD G., LAU S., JIA Y., KARAMCHANDANI P., VIJAYARAGHAVAN K. *Modeling Atmospheric Mercury Chemistry and Deposition with CAMx for a 2002 Annual Simulation*. Final Report., ENVIRON, 2003
- [12] SEIGNEUR C., ABECK H., CHIA G., REINHARD M., BLOOM N.S., PRESTBO, E., SAXENA P. *Mercury adsorption to elemental carbon (soot) particles and atmospheric particulate matter*. Atmospheric Environment, 32, 1998, 2649-2657, ISSN 1352-2310, [http://dx.doi.org/10.1016/S1352-2310\(97\)00415-9](http://dx.doi.org/10.1016/S1352-2310(97)00415-9).
- [13] SILIBELLO C., CALORI G., COSTA M.P., DIRODI M.G., MIRCEA M., RADICE P., VITALI L., ZANINI G. *Benzo[a]pyrene modelling over Italy: comparison with experimental data and source apportionment*. Atmospheric Pollution Research, 3, 2012, 399-407, ISSN 1309-1042, <http://dx.doi.org/10.5094/APR.2012.046>.
- [14] BINKOWSKI F.S., ROSELLE S.J. *Models-3 community multiscale air quality (CMAQ) model aerosol component 1. Model description*. Journal of Geophysical Research, 2003, 108, 4183, <http://dx.doi.org/10.1029/2001JD001409>, D6.
- [15] SCHELL B., ACKERMANN I.J., HASS H., BINKOWSKI F.S., ABEL A. *Modeling the formation of secondary organic aerosol within a comprehensive air quality modeling system*. J Geophys. Res., 2001, 106, D22, 28275-28293
- [16] WESEL, M.L. *Parameterization of Surface Resistance to Gaseous Dry Deposition in Regional-Scale Numerical Models*. Atmos. Environ., 1989, 23, 1293-1304.
- [17] EMEP. *Transboundary acidification, eutrophication and ground level ozone in Europe. Part I: Unified EMEP model description*. EMEP status Report 1/2003.

First-principles investigation of the amino acids adsorption to hydrated non-polar ZnO surface

Francesco Buonocore^{1*}, Caterina Arcangeli¹, Massimo Celino¹, Fabrizio Gala² and Giuseppe Zollo²

¹ *ENEA Italian National Agency for New Technologies, Energy and Sustainable Economic Development, C.R. Casaccia, Via Anguillarese, 301, I-00123 Rome, Italy*

² *Department of Fundamental and Applied Sciences for Engineering, University of Rome "La Sapienza", Via A. Scarpa 14-16, I-00161 Rome, Italy*

ABSTRACT. In last years, a great attention has been focused on the interface of biological molecules with inorganic surfaces. Experimentally some amino acids are evidenced to play a critical role in the adhesion and selectivity on oxide surfaces; however detailed information on how the water molecules on the hydrated surface are able to mediate the adsorption is still missing. In the present report we investigate, with the support of density functional theory (DFT) calculations, the adsorption of selected amino acids on the hydrated ZnO(10 $\bar{1}$ 0) surface. Accurate total energy ab-initio calculations based on dispersion-corrected density functional theory have been performed. We have also investigated the role played by water in the determination of the most energetically favourable adsorption configurations of the selected amino acids. Our calculations requested the use of the high performance computer facility CRESCO.

1 Introduction

Recently, a great attention has been focused on bio-inorganic interfaces and their possible applications in biomedical and nanotechnological areas [1-3]. Nowadays several experimental techniques are able to design engineered peptides that have demonstrated the ability to adhere selectively on specific inorganic surfaces. Moreover metal based materials are the most considered for this kind of interfaces due to their extensive utilization in several technological applications including biomedical ones. Nevertheless a fundamental understanding of the adhesion mechanism of the engineered peptides on the inorganic surfaces is still elusive because many physico-chemical phenomena are concurrently involved in the adhesion process: both structure and charge of the amino acids, amino acids sequence, amino acids cooperation /interactions, overall peptide conformation. The story is even more challenging due to the presence of water molecules that mediate the interaction between peptide and surface. Titanium and zinc are considered inorganic materials of great interest to play the role of support to biological functionalizations due to their biocompatibility and extensive use in many optical and optoelectronic applications.

In the present report we present our study [4] by first principles calculations based on the dispersion-corrected density functional theory (DFT) the adsorption to the ZnO(10 $\bar{1}$ 0) surface of the following amino acids: arginine (R, Arg), glutamine (Q, Gln), lysine (K, Lys) and aspartate (D, Asp). Indeed Arg, Gln and Lys are in the preferential binding sequence for ZnO [5], while Asp is not. We have additionally considered Asp to make a comparison with the similar study conducted for titania [6]. The ZnO(10 $\bar{1}$ 0) surface has been found to be the energetically most favorable surface [7]. The binding mechanisms will be analyzed in terms of structural information, charge density and binding energies. Arg, Lys and Asp were modeled in their corresponding charge states due to the protonation (Lys and Arg) and de-protonation (Asp) of the side chains occurring in water solutions at physiological pH. The goal is to describe the binding mechanisms of the single amino acids with the surface in the ground state configurations, where we have focused on the specific amino acids that are supposed to favor the adhesion of the peptide to the metal oxide. Currently it is not clear what role water plays in the interaction between peptide and surface. For this reason our model goes further the investigation of the interaction with a dry surface by including explicitly in the model also the intermediation of the water molecules that deeply affect the selectivity and the strength of adhesion.

2 Computational details

Our study is based on a pseudopotential planewave method. All calculations have been performed using the generalized gradient approximation (GGA) with the Perdew, Burke and Ernzerhof (PBE) correlation functional [8]. The pseudopotential plane-wave calculations were performed using Vanderbilt ultrasoft pseudopotentials [9]. The convergence of the total energy has been checked by varying cut-offs to reach a good compromise between accuracy and computational times. Vanderbilt-type ultrasoft pseudopotentials have been used with a plane-wave energy cutoff of 60 and 420 Ry for the electronic wave functions and the total charge density, respectively, allowing a convergence of the total energy below 0.0002 Ry/atom. The optimized geometries are obtained using the Hellman-Feynman forces with the Broyden-Fletcher-Goldfarb-Shanno algorithm to minimize the total energy with respect to the atomic positions. The dispersion forces have been included through a semi-empirical correction term [10] We use a Quantum-ESPRESSO code [11] compiled with Intel Fortran compiler, Math Kernel Library (MKL) and Message Passing Interface (MPI) parallelization on the Cresco3 cluster of the high performance computer facility CRESCO [12], with a good scalability up to hundreds of cores.

3 Results and discussion

3.1 Adsorption on the dry surface

The ground state adsorption configurations of protonated Lys and Arg, de-protonated Asp and neutral Gln on the dry ZnO(10 $\bar{1}$ 0) surface are reported in Figures 1 and 2. The adsorption energy values for the dry surface are reported in the first row of the Table 1. The amino acid with the strongest adhesion is the arginine with a binding energy of 4.385 eV, due to the strong interaction with the surface of the two NH₂ groups, followed by the lysine with 3.531 eV. The aspartate is bound with 2.769 eV and the neutral glutamide with 1.431 eV is the less adhered amino acid among those investigated, so that the binding energy of Asp is twice the binding energy of Gln. Therefore the considered amino acids can be easily adsorbed from the dry ZnO(10 $\bar{1}$ 0) surface, due to the ZnO dimers prone to chemically interact with the side-chains and the electrostatic interaction of charged groups. The binding energies are larger than the thermal energy at room temperature, so that adhesions are stable in standard conditions.

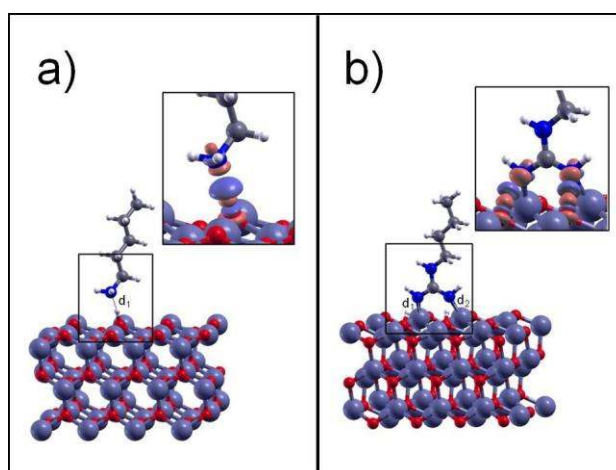


Fig. 1: Relaxed geometry of (a) lysine and (b) arginine on the dry ZnO(10 $\bar{1}$ 0) surface (Zn in violet, O in red, C in gray, H in white, N in blue). In the insets the red (blue) isosurface corresponds to the electron-charge accumulation (depletion) region.

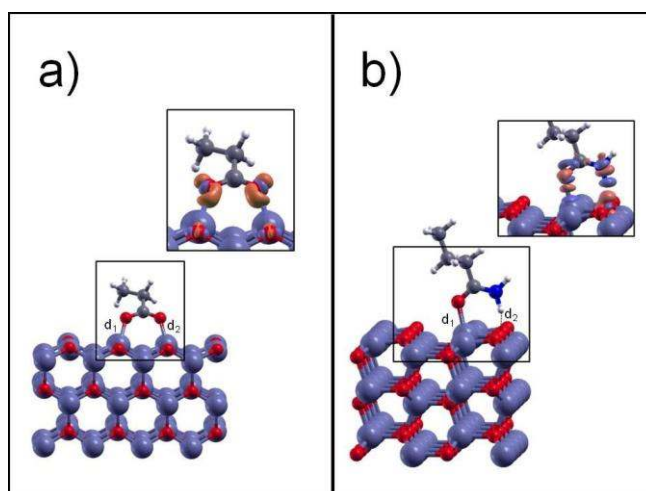


Fig. 2: Relaxed geometry of (a) aspartate and (b) glutamine on the dry $\text{ZnO}(10\bar{1}0)$ surface (Zn in violet, O in red, C in gray, H in white, N in blue). In the insets the red (blue) isosurface corresponds to electron-charge accumulation (depletion) region.

	Lys	Arg	Asp	Gln
Dry	-3.531	-4.385	-2.769	-1.431
one layer hydrated	-3.027	-2.856	-1.327	-0.942
two layers hydrated	-2.837	-2.640	-	-

Table 1: Adsorption energies in eV of amino acids on the dry, one-layer hydrated and two-layers hydrated $\text{ZnO}(10\bar{1}0)$ surfaces.

3.2 Adsorption on the hydrated surface

In the experiments, amino acids and peptides usually interact with metal oxides surfaces in aqueous environment. One or more layers of water are separating the biological molecules from the inorganic substrate, forming a hydrated surface. We studied how the water molecules influence the adsorption by considering one monolayer and two monolayers of water for all of the considered amino acids and the two strongest interacting configurations, respectively.

The ground state adsorption configurations on one-monolayer hydrated surface obtained after full relaxation are shown in Figures 3 and 4. We observe the de-protonation of Lys and the protonation of the substrate. We see that the interaction of the Arg with the surface is not completely mediated by water. This happens also for the aspartate, while the interaction of Gln with the surface is mediated by water.

The adsorption energy values are lower than the corresponding values calculated on the dry surface and reported in Table 1. The bonds formed by Lys are stronger than the two H- bonds formed by Arg, so that the binding energy hierarchy on the hydrated surface is reversed with respect to the dry one, with the Lys forming the strongest bond to the hydrated surface with 3.03 eV. The adsorption energy difference between Lys and Arg is 0.17 eV, while it was 0.85 eV for the dry surface. The adsorption energies of Asp and Gln on the hydrated surface are very much reduced compared to the dry case, indeed the Asp binding energy is 0.38 eV larger than that of Gln. By

resuming, we can distinguish two well distinct kind of interactions for amino acids with hydrated ZnO: the strong positive charged side-chain adhesion of Lys and Arg and the less strong negative charged and neutral side-chain adhesion of Asp and Gln, respectively.

We have investigated the role played by a second water layer on the amino acid adhesion. We have limited this study just to Arg and Lys that resulted to have the most stable adhesion to the surface. The structures obtained by DFT total energy optimization are shown in Figure 5 and resulted in an adsorption energy of 2.84 eV and 2.64 eV for Lys and Arg, respectively, each one with the formation of two hydrogen bonds. Notably, the de-protonation of the amino acid and the protonation of the substrate does not occur for neither of them. It is evident that a considerable surface adhesion is still present also when the amino acid are separated by two water layers. We can infer that the screening of the closest hydration shell reduces the adsorption energy of Arg and Lys, but the interaction remains basically electrostatic. The charge density exhibits just small changes compared to the case with only one layer of water so that the effect of the second layer of water on the charge transfer is negligible.

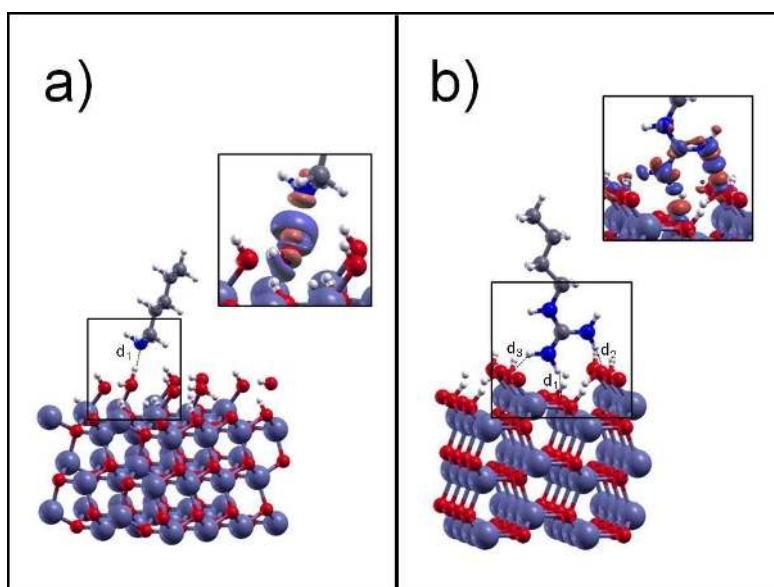


Fig. 3: Relaxed geometry of (a) lysine and (b) arginine on the hydrated ZnO($10\bar{1}0$) surface. In the insets the red (blue) isosurface corresponds to electron-charge accumulation (depletion) region.

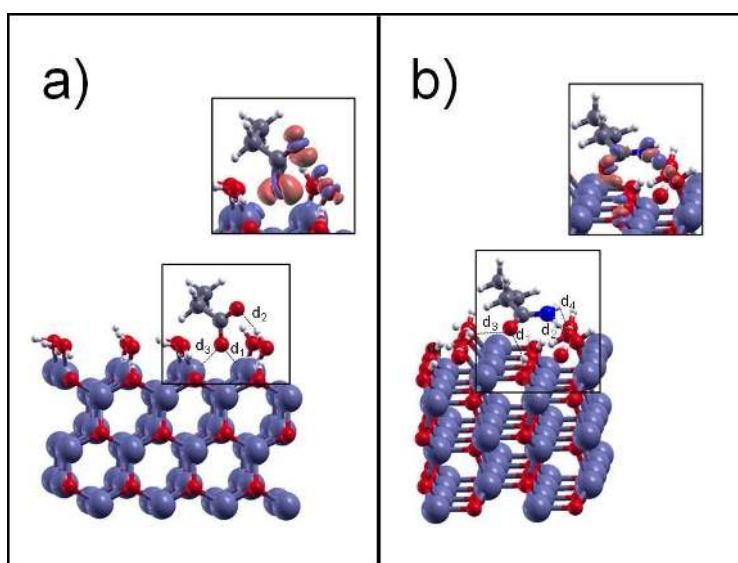


Fig. 4: Relaxed geometry of (a) aspartate and (b) glutamine on the hydrated ZnO($10\bar{1}0$) surface. In the insets the red (blue) isosurface corresponds to electron-charge accumulation (depletion) region.

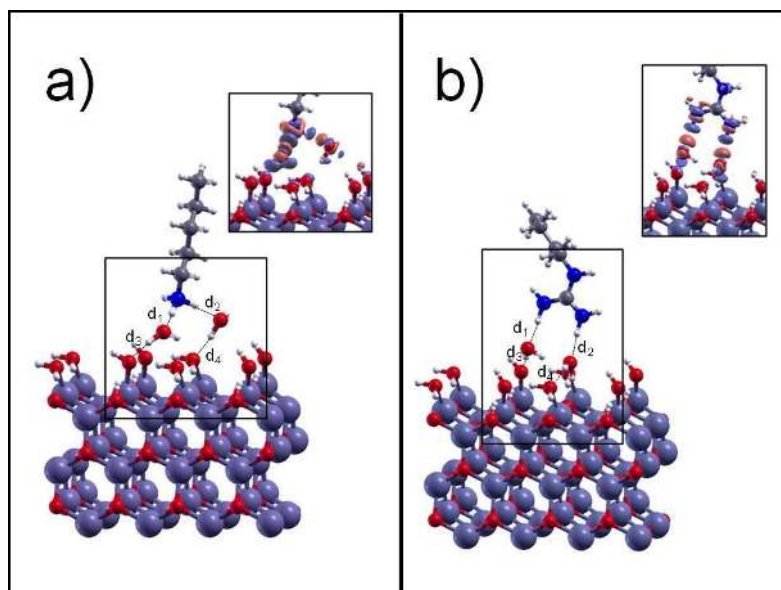


Fig. 5: Relaxed geometry of (a) lysine and (b) arginine on the two-layers hydrated ZnO($10\bar{1}0$) surface. In the insets the red (blue) isosurface corresponds to electron-charge accumulation (depletion) region.

3 Conclusions

In conclusion, DFT can clarify the nature of the interaction of peptides with inorganic surfaces, including the effects of the water environment. We have found from the structural properties and binding energetics that the mediation of water can influence the interaction of amino acids with ZnO($10\bar{1}0$) surface. Indeed we have seen that the binding energy hierarchy is inverted for Lys and Arg: Arg is the amino acid with the strongest adhesion on the dry surface, while Lys is the most stable on the hydrated surface. However we have found that both Lys and Arg as hydrated have comparable binding energy: 3.0 eV for Lys and Arg is just 0.2 eV less stable. The adhesion to the hydrated surface is probably more relevant in the practical applications, where the adhesion of the peptide to the metal oxide is experimented in aqueous solution. However the adhesion of peptides is not simply related to the adhesion of every single amino acid in its sequence, but rather it is ruled by the presence of particular groups. We can infer that the structural and electronic correlations among the amino acids in the sequence as well as the distribution of the electrostatic potential on the surface play a key role in the determination of the peptide adsorption. On the other hand, we have calculated the structure in the ground state of single amino acids as static systems and we have just included a few layers of water. Instead, probably, the study and understanding of the adsorption mechanisms require to model the full sequence in the water environment by using the appropriate computational approaches.

This work was partly supported by META- Materials Enhancement for Technological Application-Project (FP7-PEOPLE-2010- IRSES-Marie Curie Actions, PIRSES-GA-2010-269182).

The computing resources and the related technical support used for this work have been provided by CRESCO/ENEAGRID High Performance Computing infrastructure and its staff [12]. CRESCO/ENEAGRID High Performance Computing infrastructure is funded by ENEA, the Italian National Agency for New Technologies, Energy and Sustainable Economic Development and by Italian and European research programmes, see <http://www.cresco.enea.it/english> for information.

References

- [1] SHIBA, K. “*Exploitation of Peptide Motif Sequences and their Use in Nanobiotechnology*” *Curr. Opin. Biotechnol.* **21** (2010) pp. 412-425.
- [2] BUSSERON, E.; RUFF, Y.; MOULIN, E.; GIUSEPPONE, N. “*Supramolecular Self-Assemblies as*

Functional Nanomaterials” *Nanoscale* **5** (2013) pp. 7098-7140.

[3] COSTA, D.; GARRAIN, P-A.; BAADEN, M. J. “Understanding Small Biomolecule-Biomaterial Interactions: A Review of Fundamental Theoretical and Experimental Approaches for Biomolecule Interactions with Inorganic Surfaces” *Biomed. Mater. Res. Part A* **101A** (2013) pp. 1210-1222.

[4] BUONOCORE, F.; ARCANGELI A.; GALA, F.; ZOLLO G.; CELINO M. “*Adsorption of Modified Arg, Lys, Asp, and Gln to Dry and Hydrated ZnO Surface: A Density Functional Theory Study*” *J. Phys. Chem. B* **119** (2015), pp 11791–11797

[5] THAI, C.; DAI, H.; SASTRY, M.S.R.; SARIKAYA, M.; SCHWARTZ, D.T.; BANEYX, F. “*Identification and Characterization of Cu(2)O- and ZnO-Binding Polypeptides by Escherichia coli Cell Surface Display: Toward an Understanding of Metal Oxide Binding*” *Biotechnol. Bioeng.* **87** (2004) pp 129-137.

[6] AGOSTA, L.; ZOLLO, G.; ARCANGELI, C.; BUONOCORE, F.; GALA, F.; CELINO, M. “*Water driven adsorption of amino acids on the (101) anatase TiO2 surface: an ab initio study*” *Phys. Chem. Chem. Phys.*, **17** (2015) p 1556.

[7] MEYER, B.; MARX, D. “Density-Functional Study of the Structure and Stability of ZnO Surfaces” *Phys. Rev. B* **67** (2003) p 035403.

[8] PERDEW, J. P.; BURKE, K.; ERNZERHOF, M. “*Generalized Gradient Approximation Made Simple*” *Phys. Rev. Lett.* **77** (1996) pp 3865–3868.

[9] VANDERBILT, D. “*Soft Self-Consistent Pseudopotentials in a Generalized Eigenvalue Formalism*” *Phys. Rev. B* **41** (1990) p 7892.

[10] GRIMME, S. “*Semiempirical GGA-Type Density Functional Constructed with a Long-Range Dispersion Correction*” *J. Comput. Chem.* **27** (2006) pp 1787-1799.

[11] GIANNOZZI, P.; BARONI, S.; BONINI, N.; CALANDRA, M.; CAR, R.; CAVAZZONI, C.; CERESOLI, D.; CHIAROTTI, G.L.; COCCIONI, M.; DABO, I.; et al “*QUANTUM ESPRESSO: A Modular and Open-Source Software Project for Quantum Simulations of Materials*” *J. Phys.: Condens. Matter* **21** (2009) p 395502.

[12] G. PONTI et al., “*The role of medium size facilities in the HPC ecosystem: the case of the new CRESCO4 cluster integrated in the ENEAGRID infrastructure*”, Proceedings of the 2014 International Conference on High Performance Computing and Simulation, HPCS 2014, art. no. 6903807, pp. 1030-1033.

PERFORMANCE ANALYSIS OF CRESCO CLUSTERS BY USING DGEMM SUBROUTINE

Simone Giusepponi*

ENEA, C. R. Casaccia, via Anguillarese 301, 00123 Rome, Italy

ABSTRACT. A performance analysis of the ENEA CRESCO computing facilities, is made considering a floating-point matrix multiplication, using the DGEMM subroutine of the Basic Linear Algebra Subprograms, and its implementation in the Intel Math Kernel Library and AMD Core Math Library.

1 Introduction

In this paper we report results concerning the performances of the ENEA CRESCO computing facilities available in the ENEA-GRID [1, 2]. The CRESCO HPC supercomputers are based on the multi-core x86_64 architecture and is made up of various clusters: we tested the CRESCO systems located in Portici ENEA centre that consist of three clusters: CRESCO2, CRESCO3 and CRESCO4.

CRESCO2 is equipped with Intel Xeon E5530 processor which operates at a clock frequency of 2.4 GHz and has sse4.2 instructions set; CRESCO3 is equipped with AMD Opteron 6234TM processor which operates at a clock frequency of 2.4 GHz with avx and fma4 instructions set; CRESCO4 is equipped with Intel Xeon E5-2680 processor which operates at a clock frequency of 2.6 GHz and has avx instructions set. Further hardware/software details of the clusters are reported in Tab. 1.

To evaluate the computer performances, we consider the time required to execute a floating-point matrix multiplication using the DGEMM subroutine of the Basic Linear Algebra Subprograms (BLAS) [3] library, and its implementation in the Intel Math Kernel Library (MKL) [4] and AMD Core Math Library (ACML) [5]. Then we derive the floating-point operations per second (Gflops). The DGEMM subroutine performs the following operation:

$$C = \alpha A \times B + \beta C$$

where α and β are scalars and A , B and C are matrices. For our calculations $N \times N$ square matrices were chosen, with $\alpha = 1$ and $\beta = 0$.

2 Serial execution

We started considering a serial execution of the matrix multiplication on the CRESCO clusters using different compilers: gfortran and ifort, and different mathematical libraries: BLAS, MKL and ACML. The matrices were filled with $N \times N$ double precision floating-point numbers with $N = 2500$. On CRESCO2 cluster are available gfortran 4.1.2 and ifort 11.0, moreover are available the following libraries: BLAS 3.3.0/3.5.0, MKL 10.1/10.3/11.0/11.1 and ACML 5.0.3. In Fig. 1 are showed the results produced by

*Corresponding author. E-mail: simone.giusepponi@enea.it.

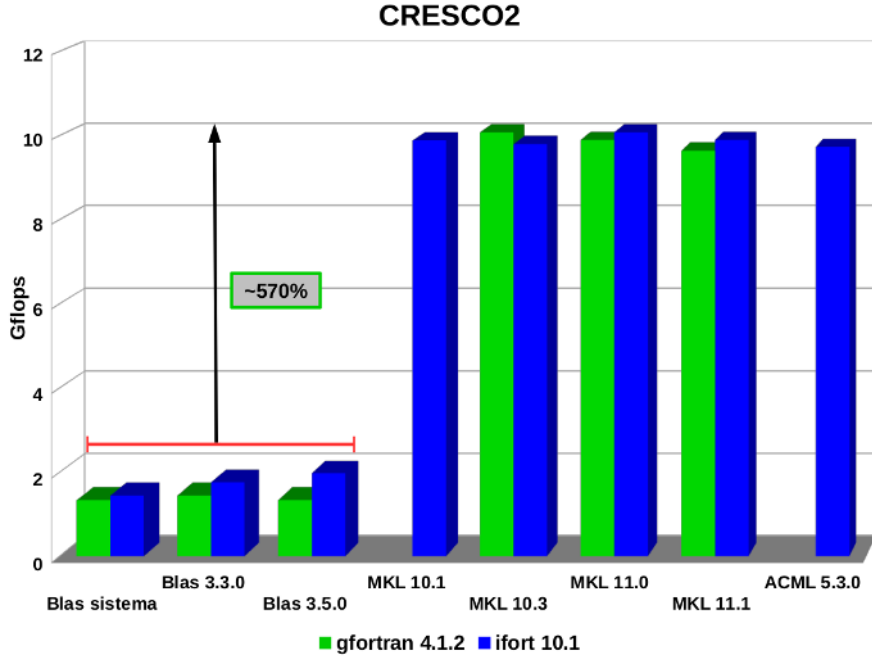


Figure 1: Results for CRESCO2 cluster.

CRESCO2, from which it is clear that MKL and ACML have better performances compared to BLAS. Results for BLAS libraries are in the range of $1 \div 2$ Gflops, whereas, they reach ~ 10 Gflops for MKL and ACML libraries with an enhancement of about six times. Finally, we observe that compiler and library versions do not have great impact on the execution time in the matrix multiplication.

On CRESCO3 cluster are available gfortran 4.4.6/4.8.2 and ifort 12.0/14.0, moreover, are available the following libraries: BLAS 3.3.0/3.5.0, MKL 10.1/10.3/11.0/11.1 and ACML4.4.0/5.1.0/5.0.3. Now the results (see Fig. 2) are less evident than the previous case. As before, BLAS libraries have the worst performances, on the contrary, MKL 11.0/11.1 have the best results reaching ~ 17 Gflops. Older versions of MKL (10.1/10.3), despite having better performances than BLAS, can execute only 5 Gflops, less than a third compared to MKL newer versions. The same considerations can be done for ACML libraries. In fact, newer versions have almost the highest values (~ 16 Gflops), whereas, older versions have halved performances (~ 8 Gflops), even if, better than the older versions of the MKL. An observation must be

Table 1: Some of the hardware and software characteristics for the CRESCO clusters

	CRESCO2	CRESCO3	CRESCO4
Processor	Intel E5530 (Q1'09)	AMD 6234TM (Q3'11)	Intel E5-2670 (Q1'12)
Clock (GHz)	2.40	2.40	2.60
Cores per node	2×4	2×12	2×8
RAM per node (GB)	16	64	64
Instruction set	sse4.2	avx, fma4	avx
Compiler	gfortran 4.1.2 ifort 11.0	gfortran 4.4.6/4.8.2 ifort 12.1/14.0	gfortran 4.4.6/4.8.2 ifort 12.1/14.0

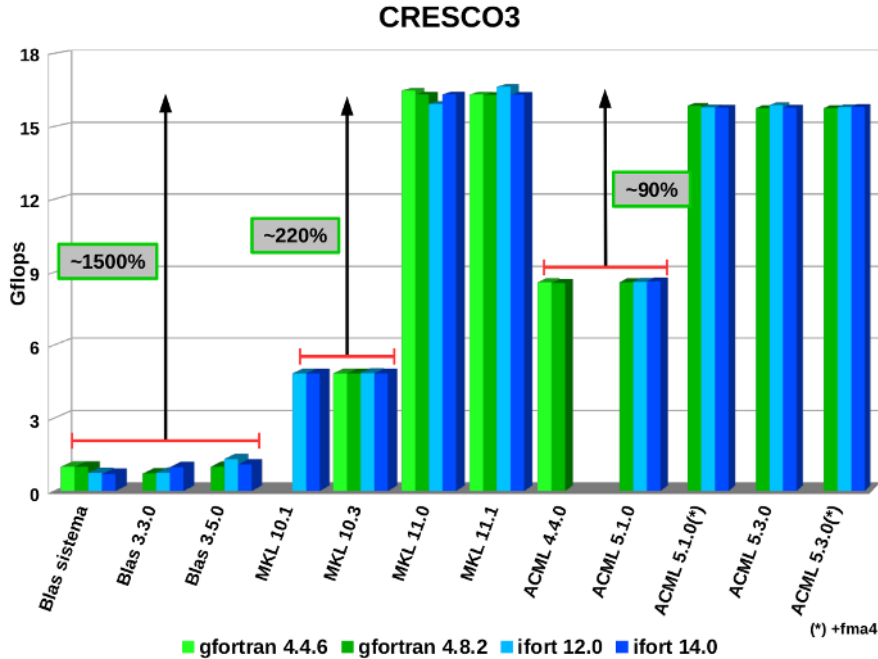


Figure 2: Results for CRESCO3 cluster.

done with regard to ACML 5.1.0. This version of ACML can reach the highest results, only if the fma4 instructions set is specified at the compilation.

On CRESCO4 cluster are available the same compilers and libraries of CRESCO3, however, there is a clear difference between MKL and ACML libraries results (see Fig. 3). ACML libraries can execute less than 10 Gflops, whereas MKL libraries reaching ~ 25 Gflops are more than 150% faster. The exception are the MKL 10.1 that have halved performance compared to the other versions of MKL. BLAS libraries have still the worst performances. At the end, we observe that compilers do not have great impact on the performances.

3 Parallel OpenMP execution

To have a deeper insight on the CRESCO clusters performances, we consider the OpenMP [6] implementation of DGEMM, provided by MKL and ACML libraries. We limit this analysis to CRESCO3 and CRESCO4 clusters considering only gfortran 4.8.2 and ifort 14.0. Moreover, in the $N \times N$ matrices multiplication we set $N = 10000$. The cores used in the calculations range from 1 to 24 for CRESCO3 cluster, and range from 1 to 16 for CRESCO4 cluster, to have a full node utilisation.

Results for CRESCO3 cluster are depicted in Fig. 4: on left using gfortran 4.8.2 and on right using intel 14.0. As in the serial execution, newer libraries give better performances. With regard of the number of cores, we observe that, with 1, 2 and 4 cores, almost the same number of floating-point operations per second are executed (~ 16 Gflops). With a 8 cores executions, performances are still good, even if, they are decreased of about 10%. The increase of number of the used cores to 12, to have a half node utilisation, produces a reduction of the performances that are further deteriorated with full node utilisation (24 cores).

In Fig. 5 the results for CRESCO4 are shown: on left for gfortran 4.8.2 and on right for intel 14.0.

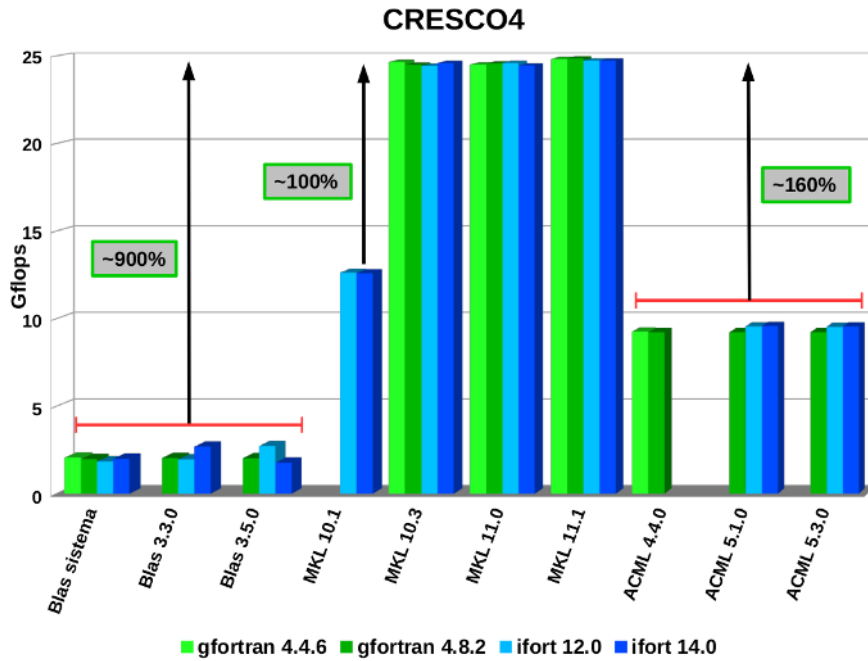


Figure 3: Results for CRESCO4 cluster.

ACML libraries give bad outcomes as for serial cases (less than 10 Gflops). MKL libraries exhibit very good results (~ 25 Gflops) for executions with 1, 2 and 4 cores, like in the CRESCO3 case. Doubling the number of cores to 8, a reduction of the performances of about 10% is produced as before, but now, about 22 Gflops are reached. The full node utilisation (16 cores) is not completely favourable, in fact, the performances are decreased to have only ~ 18 Gflops. In this case, these outcomes are absolutely better than those achieved for CRESCO3 full node utilisation.

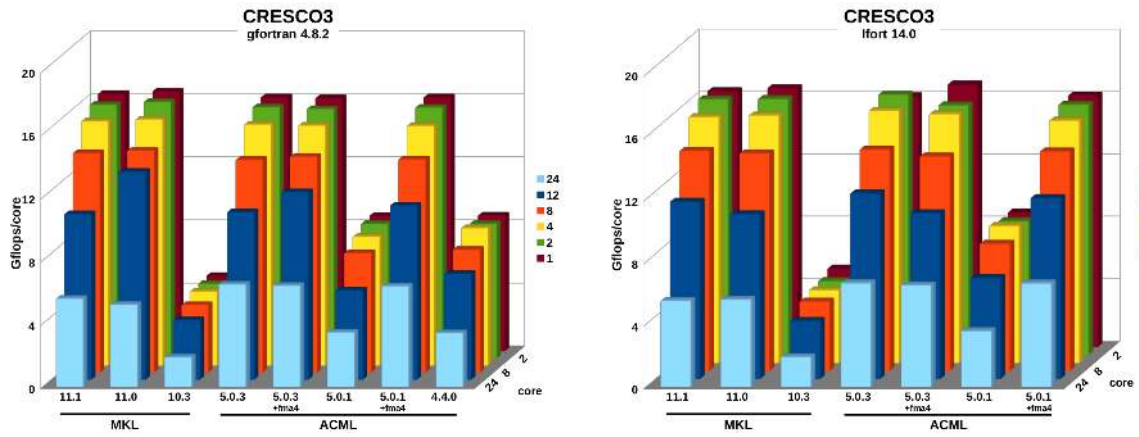


Figure 4: Results for CRESCO3 cluster with OpenMP parallelization.

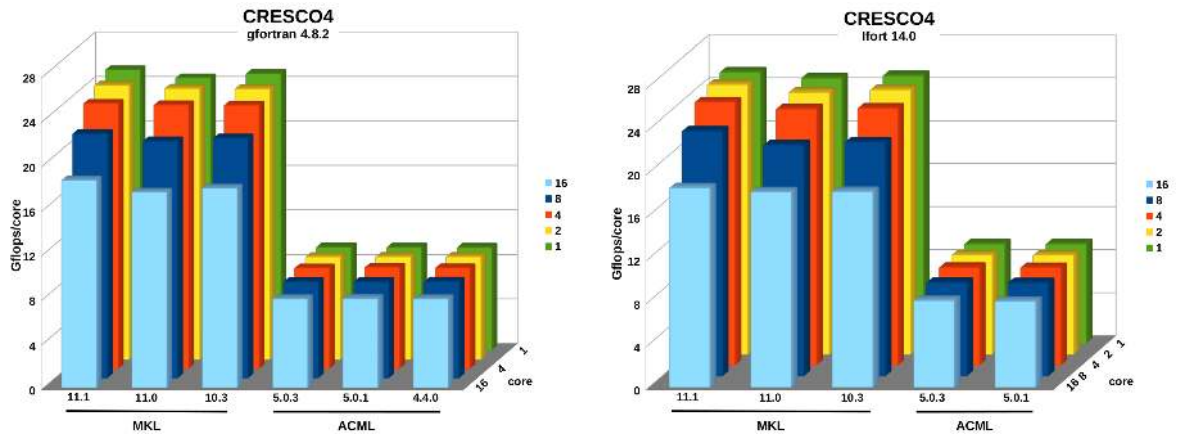


Figure 5: Results for CRESCO4 cluster with OpenMP parallelization.

References

- [1] www.cresco.enea.it.
- [2] www.eneagrid.enea.it.
- [3] www.netlib.org/blas/index.html.
- [4] <https://software.intel.com/en-us/intel-mkl>.
- [5] <http://developer.amd.com>.
- [6] <http://openmp.org/wp>.

CFD SIMULATIONS OF HYDROCARBONS REFORMING WITH CO₂ CAPTURE IN A FLUIDISED BED CARBONATOR

Antonio Di Nardo, Stefano Stendardo, Giorgio Calchetti

*ENEA Italian National Agency for New Technologies, Energy and Sustainable Economic Development
Energy Technologies Department*

ABSTRACT. 3D simulations of hydrocarbons reforming with CO₂ capture for hydrogen production are presented in this paper. The simulations have been performed by means of an Eulerian-Lagrangian approach, using the commercial software Barracuda® and the multiphase particle in cell (MP-PIC) method. The Numaguchi and Kikuchi model modified according to De Smet model has been used for the simulation of steam methane reforming (SMR) and water gas shift (WGS) reaction, whereas the separation of the CO₂ has been simulated via the Stendardo and Foscolo grain model.

1 The MP-PIC method

Mathematical CFD models for multiphase flows are based on two different approaches. In the Eulerian-Eulerian approach the phases are treated as pseudo continuum. In the Eulerian-Lagrangian approach the gas phase is treated as a continuum while the dispersed solid phase is calculated solving particles equation of motion. In the first approach models are needed for the several terms in the equations, as for example viscous stresses and particle-particle stresses and the equations set has to be solved for each dimensions and particle type. For the second approach many different variations are available. The solution of the flow field around each particle is possible only in the case of few particles, as in the Lattice-Boltzman method. These kind of methods make sense only for the study of fluid-particle interaction and then in the development of models useful for closure terms in the equations relative to other approaches. On the other hand the Discrete Particle or the Discrete Elements methods are based on the calculations of a limited number of particles, supposed rigid and spherical, interacting each other by means of contact forces and with the fluid phase by means of a drag model. When the solid volume fraction exceeds 5 % because of high collision frequency these methods are applicable only for two-dimensional cases, with a maximum number of particles of the order of 10⁵. Also the MP-PIC method [1,2] of Barracuda® uses the Lagrangian-Eulerian approach, but instead of calculating the trajectories of each single particle, they are grouped by size, species, etc., in computational particles. The gaseous phase is considered as a continuous fluid with its own density, temperature and velocity whereas the solid phases are modelled by means of a discrete Lagrangian phase. As a consequence, it is possible to model fluidised bed systems with a high number of particles and relative low computational burden, since collisions are not directly evaluated but modelled as spatial gradient calculated on the Eulerian calculation grid via interpolated functions. For an accurate interpolation of the Lagrangian phase on the Eulerian grid the size of the physical particles have to be small enough compared to the Eulerian grid. The gaseous and solid phases are fully coupled by species, momentum and energy transfer. Barracuda® is developed with the ability to take the advantage of the graphic processors GPU for parallel calculation. GPU (Graphics Processing Unit) is defined as a hardware device originally built specifically for graphics rendering. The GPU has been designed to do one thing, always performing the same type of instructions as fast as possible. However, in recent years GPUs have been used more and more for general-purpose computations. The GPU has many cores (typically thousands today) for the treatment of large blocks of data in parallel. This contrasts with a typical central processing unit (CPU), which has a significantly lower number of cores, each of which is

more sophisticated and suitable to work on independent instructions. The GPU is not practical for all kinds of calculation, but for cases in which the same instructions are to be performed on large data sets, as millions of particles, becomes a personal supercomputer. While a GPU cannot rival the fastest parallel processing systems in the world, does not require specialized cooling systems, it is not expensive and does not require a specialized team for its handling and use. In practice, a supercomputer in a box, small and powerful, offering a significant acceleration in the calculation, at a fraction of the cost of a parallel network. The GPUs then represent the possibility of mass supercomputing. For the present work a CRESCO computer equipped with a TESLA S2050 GPU has been used, which mounts 448 CUDA Cores and delivers up to 515 Gigaflops of double-precision peak performance in each GPU, enabling 2 Teraflops of double precision performance in a 1U of space. Single precision peak performance is over a Teraflop per GPU.

2 Simulations results

Special attention is being paid to hydrogen production and carbon free electricity from biomass or fossil fuels for mitigation of climate changes. In the technical literature a number of process options have been investigated to accomplish this purpose. In this work an innovative reformer-based technology will be analysed, which recovers both hydrogen and carbon dioxide from coal (or biomass) syngas or natural gas. The idea behind this process option is to take advantage from coupling multiple catalytic reactions (water gas shift and methane steam reforming, more generally hydrocarbons steam reforming) with the non-catalytic gas-solid reaction that allows for CO₂ uptake by a solid sorbent. In this section simulations results focused on CH₄ reforming with CO₂ capture are reported. To this end CFD simulations of a fluidised bed carbonator via an Eulerian-Lagrangian approach have been performed, using Barracuda®. The Numaguchi and Kikuchi [3] model modified according to De Smet [4] model has been used for the simulation of steam methane reforming and water gas shift reaction reaction, whereas the separation of the CO₂ has been simulated via the Stendardo and Foscolo [5] grain model. The geometry used for the simulation referred to an existing ENEA test rig. The reactor is a cylinder of 0.15 m of diameter and is 2 m high. A uniform flow of methane and water vapour enters the reactor from the bottom end fluidising the solid sorbent (calcined dolomite) particles bed, having size distribution reported in fig. 1.

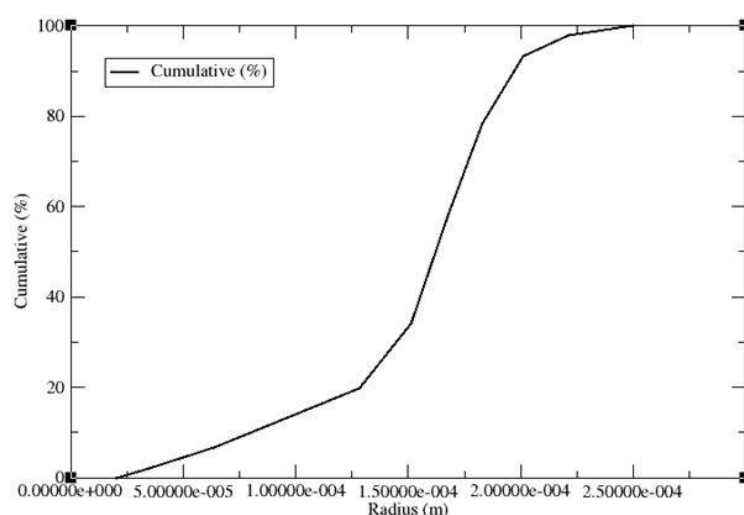


Fig. 1: Cumulative dolomite particles size distribution.

A cyclone separates the lighter transported particles from the exiting gas. The main parameters of the three simulated cases are reported below:

1. Dolomite bed: initial bed 3 kg, initial bed composition CaO/MgO (1/1 mass ratio); Gas mixture: inlet mixture 6.37 kg/h H₂O/CH₄ (3/1 mole ratio), inlet temperature 600 °C. Initial reactor temperature 600 °C.
2. Dolomite bed: initial bed 3 kg, initial bed composition CaO/MgO (1/1 mass ratio); Gas mixture: inlet mixture 6.37 kg/h H₂O/CH₄ (3/1 mole ratio), inlet temperature 750 °C. Initial reactor temperature 750 °C.
3. Dolomite bed: initial bed 9 kg, initial bed composition CaO/MgO (1/1 mass ratio); Gas mixture: inlet mixture 6.37 kg/h H₂O/CH₄ (3/1 mole ratio), inlet temperature 600 °C. Initial reactor temperature 600 °C.

Number of computational cells: 80.000; Drag model: Wen-Yu; Heat exchange: adiabatic; Turbulence model: Large-Eddy-Simulation.

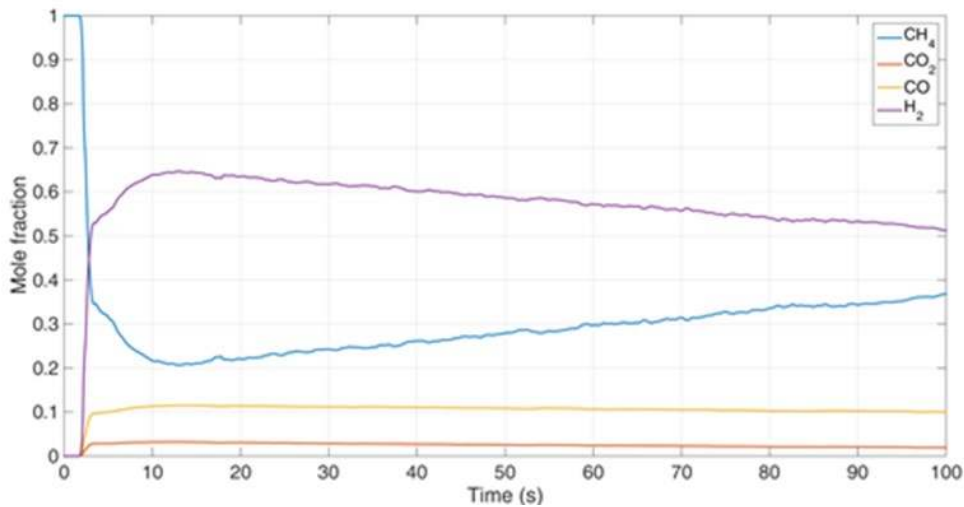


Fig. 2: Species mole fraction (dry) at outlet. Initial bed 3 kg, inlet temperature 600 °C.

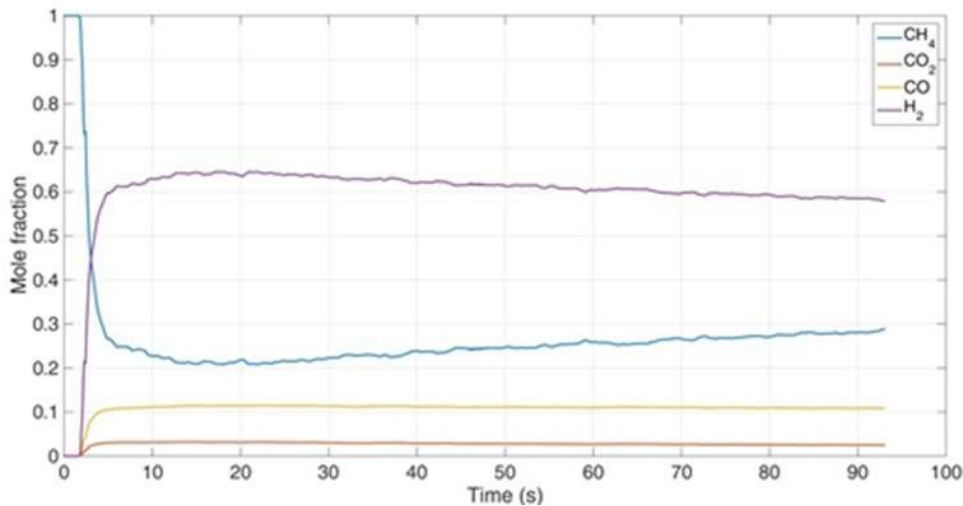


Fig. 3: Species mole fraction (dry) at outlet. Initial bed 3 kg, inlet temperature 750 °C.

Figures 2, 3, 4 show the behaviour of the fluidized bed carbonator in term of mole fraction of the exiting decarbonised gas. With the increase of the inlet gas temperature, the pre-breakthrough time of the reactor increases. Tripling the amount of dolomite in the reactor allows the methane to almost fully convert, even at lower temperature. The gas inlet velocity is sufficient to achieve a deep fluidisation, but just a small amount of particles are dragged outside. A snapshot representing the particles distribution inside the reactor is reported in figure 5.

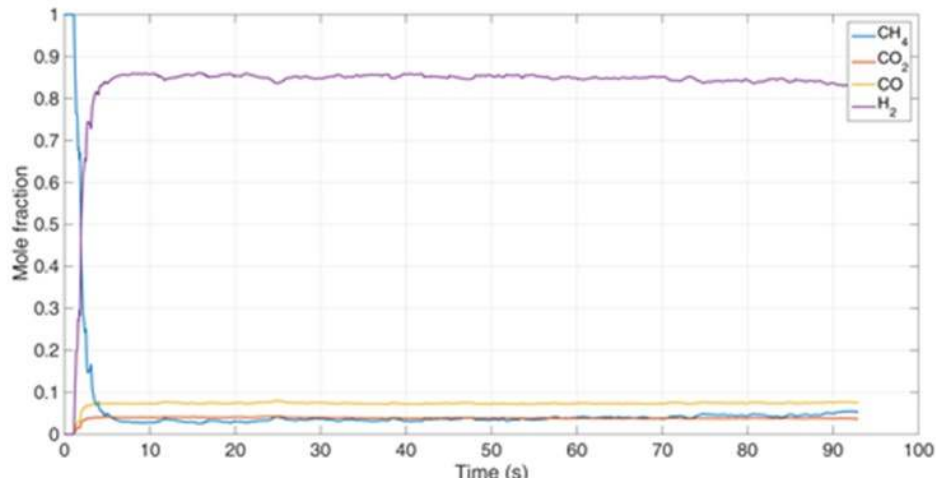


Fig. 4: Species mole fraction (dry) at outlet. Initial bed 9 kg, inlet temperature 600 °C.

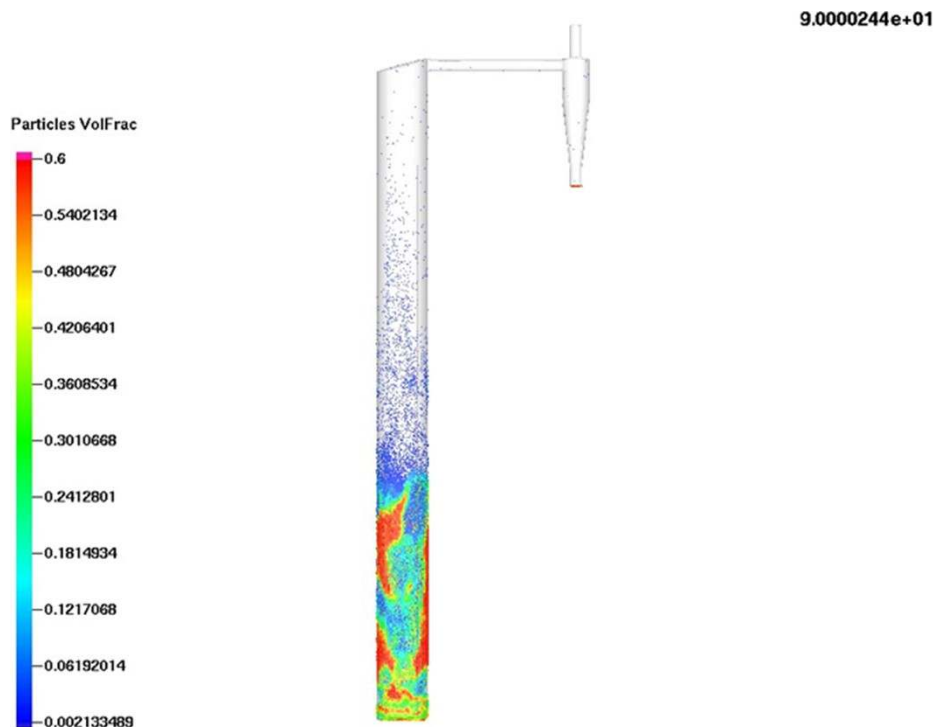


Fig. 5: Particles volume fraction. Initial bed 9 kg, inlet temperature 600 °C.

References

- [1] SNIDER D.M., "An Incompressible Three-Dimensional Multiphase Particle-in-Cell Model for Dense Particle Flows *Journal of Computational Physics*". **170** (2001) pp. 523–549.
- [2] ANDREWS J., O'ROURKE P.J., "The Multiphase Particle-In-Cell (Mp-Pic) Method For Dense Particulate Flows". *Int. J. Multiphase Flow* **22** (1996) pp. 379-402.
- [3] NUMAGUCHI T., KIKUCHI K., "Intrinsic Kinetics and Design Simulation in a Complex Reaction Network; Steam-Methane Reforming". *Chem. Eng. Sci.* **43** (1998) pp. 2295-2301.
- [4] "DE SMET C.R.H., DE CROON M.H.J.M., BERGER R.J., MARIN G.B., SCHOUTEN J.C., "Design of adiabatic fixed-bed reactors for the partial oxidation of methane to synthesis gas. Application to production of methanol and hydrogen-for-fuel-cells". *Chemical Engineering Science* **56** (2001) pp. 4849–4861.
- [5] STENDARDO S., FOSCOLO P.U., "Carbon Dioxide Capture with Dolomite: a Model for Gas-Solid Reaction within the Grains of a Particulate Sorbent". *Chem. Eng. Sci.* **64** (2009) pp. 2343–2352.

CP2K PERFORMANCE ON CRESCO4 HPC SYSTEM

Michele Gusso *

ENEA, C. R. Brindisi, S.S. 7 Appia km 706, 72100 Brindisi, Italy

ABSTRACT. Several benchmarks of CP2K code are performed on ENEA CRESCO4 platform to show its scaling behaviour. A comparison with the Piz Daint super-computer is also reported.

1 Introduction

CP2K [1, 2] is a freely available powerful and scalable program for atomistic simulations of a wide range of systems, including condensed phase, molecular systems and complex interfaces. Especially aimed at ab-initio molecular dynamics simulations with different level of DFT approximations. It is optimized for the mixed Gaussian and Plane-Waves method based on pseudopotentials. In this brief report we show results of an optimized compilation on ENEA CRESCO4 system and make a comparison with a machine with same processors but a different architecture: the CRAY system Piz Daint. Table 1 reports the characteristics of the two systems. CP2K ver. 2.6.2 was compiled on CRESCO4 with intel compiler ver. 14.0 using the mathematical library MKL ver. 11.1 and OpenMPI ver. 1.4.3. To know how to use CP2K on CRESCO4 see [3]. The results of the performance of CP2K on Piz Daint were taken from the benchmarks reported in [4].

2 Results and Discussion

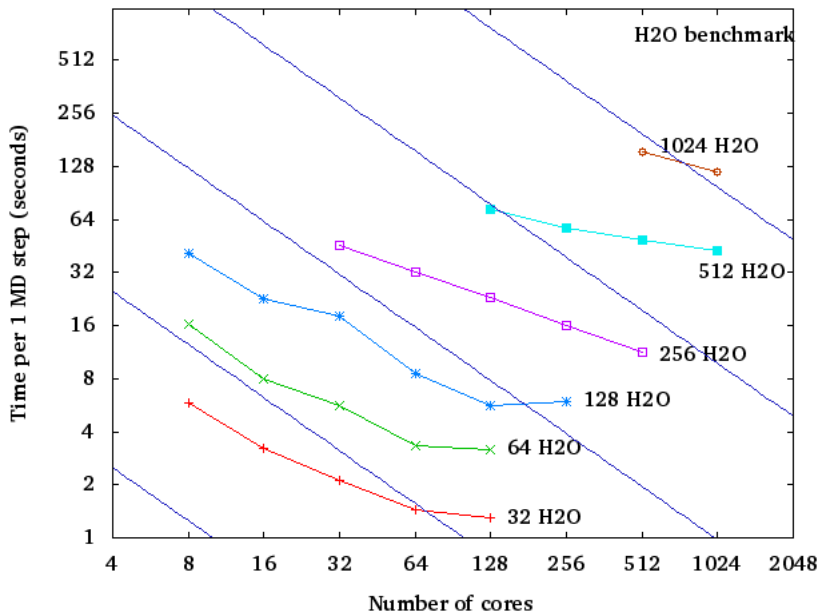
Fig. 1 reports a benchmark of CP2K on CRESCO4 using a system made of 2^n H₂O molecules ($n = 5, 6, \dots, 10$). Ab-initio Born-Oppenheimer MD was performed with the Quickstep DFT module. The basis set was TZV2P and a PW cutoff of 280 Ry with LDA for Exchange-Correlation energy. The figure reports the time per MD step against the number of CPU cores used. The straight diagonal blue lines indicate perfect linear scaling.

Fig. 2 compares the results of CRESCO4 and Piz Daint for the system made of 64 H₂O molecules. The cpu times for 10 MD steps are reported. For CRESCO4 the results of a compilation with mpi-mvapich2 are also shown. It can be seen that mvapich2 are better than openmpi up to 256 cores. Indeed we have checked that MPI times for mvapich2 are lower than openmpi times up to 256 cores. On the other hand there is no point in going beyond 256 cores with this small system: the time spent in MPI routines becomes comparable to pure computational time. A comparison of openmpi and mvapich2 for a bigger system (1024 H₂O molecules) using 512 and 1024 cores have also shown a better performance of mvapich2.

*Corresponding author. E-mail: michele.gusso@enea.it.

Table 1: SYSTEM SPECIFICATIONS

Name	Processor	Clock (GHz)	Network	Nodes	Cores/Node	Peak (TFlop/s)
Cresco4	Intel Xeon E5-2670 Sandy-Bridge 8-Core (2 sockets)	2.6	IB 4xQDR 40 Gb/s Switch Qlogic 12800	304	16	101
Piz Daint Cray-XC30	Intel Xeon E5-2670 Sandy-Bridge 8-Core + NVIDIA Tesla K20X	2.6	Aries routing and comm. ASIC. Dragonfly topology	5272	8 (+14)	877 (+6911)

Figure 1: Performance of CP2K on CRESCO4 using a system made of 2^n H₂O molecules with $n = 5, \dots, 10$

Although Born-Oppenheimer MD with traditional Exchange-Correlation potentials is one of the most used methods of CP2K, this package includes many other approaches so that a single benchmark system is not enough to give useful information about what performance to expect from the code. Fig. 3 reports a short classical molecular dynamics run of 1000 time steps in a NPT ensemble at 300K. It consists of 28000 atoms - a 10^3 supercell with 28 atoms of iron silicate (Fe₂SiO₄, also known as Fayalite) per unit cell. The simulation employs a classical potential (Morse with a hard-core repulsive term and 5.5 Å cutoff) with long-range electrostatics using Smoothed Particle Mesh Ewald (SPME) summation. The low execution times, which are lower than Piz Daint times, were obtained by compiling CP2K with the intel option `-assume buffered_io` (an analogous result can be obtained by exporting the environmental variable `FORT_BUFFERED` or, when using `gfortran` by exporting the variable `GFORTRAN_UNBUFFERED_ALL=0`). In this way the time spent by the `cp2k` routine `write_traj` (which write the MD trajectory file) drops from about 255s to 70s (for 16 cores). (This option does not seem to be used in the Piz Daint compilation). Note that I/O operations are not MPI implemented in `cp2k`.

We now reports on three more demanding benchmarks. In order to analyse the scaling behaviour of CP2K they require a huge amount of computational resources, as possessed by Piz Daint. Nonetheless the results of CRESCO4 are quite interesting and compare well, in the limited range of cores where

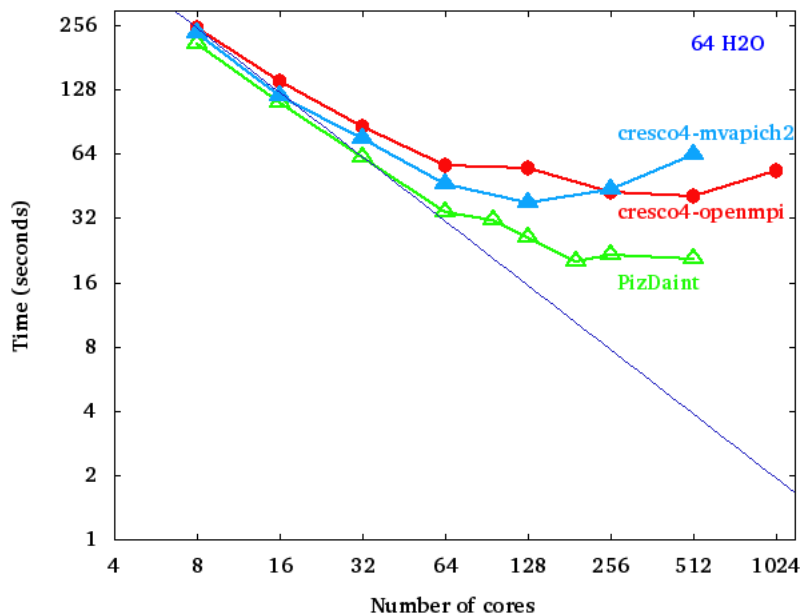


Figure 2: Comparison of CP2K performance between CRESCO4 and Piz Daint machines using a system made of 64 H₂O molecules

comparison can be made, with Piz Daint. Fig. 4 reports the results of a single-point energy calculation using Quickstep GAPW (Gaussian and Augmented Plane-Waves) with hybrid Hartree-Fock exchange. It consists of a 216 atom Lithium Hydride crystal with 432 electrons in a 12.3 Å³ cell. These types of calculations are generally around one hundred times the computational cost of a standard local DFT calculation. Note that these calculations benefit particularly from using OpenMP. While Piz Daint data were obtained by using from 1 to 4 OpenMP threads, for CRESCO4 we used pure MPI.

Fig. 5 shows the results of a singlepoint energy calculation using linear-scaling DFT. It consists of 6144 atoms in a 39 Å³ box (2048 water molecules in total). An LDA functional is used with a DZVP MOLOPT basis set and a 300 Ry cutoff. The linear scaling approach for solving Self-Consistent-Field equations was used.

Finally fig. 6 shows the results a single-point energy calculation using 2nd order Mller-Plesset perturbation theory (MP2) with the Resolution-of-the-Identity approximation to calculate the exchange-correlation energy. The system consists of 64 water molecules in a 12.4 Å³ cell.

In conclusion CP2K compares quite well with the Piz Daint system. The generally higher computational times of CRESCO4 with respect to Piz Daint are likely due to the better performance of the Piz Daint communication network.

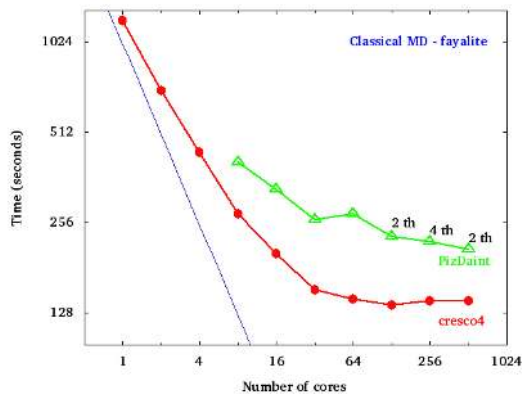


Figure 3: Comparison of CP2K classical MD module between CRESCO4 and Piz Daint systems (*th* stands for the number of threads used).

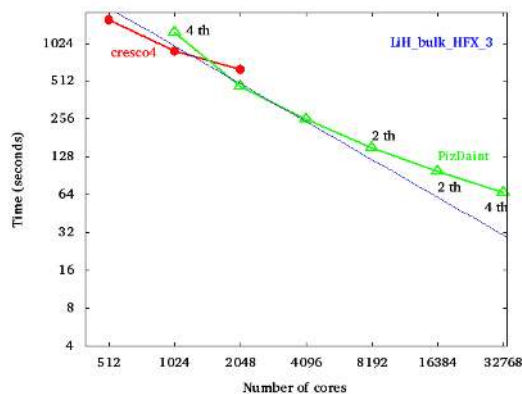


Figure 4: Comparison of CP2K implemented hybrid Hartree-Fock exchange functionals between CRESCO4 and Piz Daint systems.

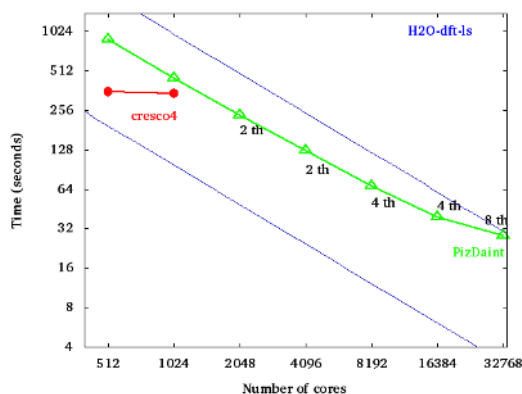


Figure 5: Comparison of the self-consistent-field linear scaling algorithm implemented in CP2K between CRESCO4 and Piz Daint systems.

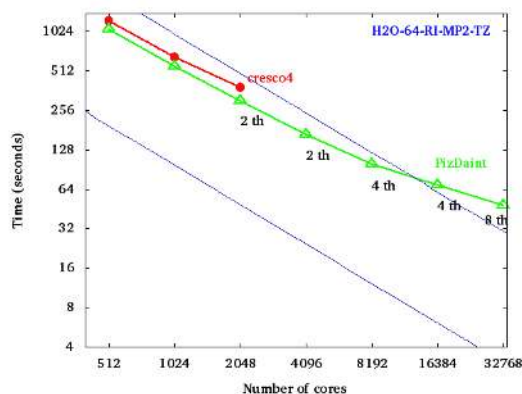


Figure 6: Comparison of the Møller-Plesset perturbation theory as implemented in CP2K between CRESCO4 and Piz Daint systems.

References

- [1] J. Hutter, M. Iannuzzi, F. Schiffmann, and J. VandeVondele, CP2K: Atomistic Simulations of Condensed Matter Systems, Wiley Interdisciplinary Reviews: Computational Molecular Science, vol. 4, no. 1, pp. 1525, 2014. [Online]. Available: <http://dx.doi.org/10.1002/wcms.1159>
- [2] The CP2K Developers Group. CP2K: Open Source Molecular Dynamics. [Online]. Available: <http://www.cp2k.org>
- [3] http://www.afs.enea.it/software/cp2k/index_cp2k.html
- [4] <https://www.cp2k.org/performance>

AB-INITIO STUDY OF SILICON BASED MATERIALS FOR PHOTOVOLTAIC APPLICATIONS

Simone Giusepponi^{1*}, Michele Gusso², Massimo Celino¹,
Urs Aeberhard³ and Philippe Czaja³

¹ ENEA, C. R. Casaccia, via Anguillarese 301, 00123 Rome, Italy

² ENEA, C. R. Brindisi, S.S. 7 Appia km 706, 72100 Brindisi, Italy

³ IEK-5 Photovoltaik, Forschungszentrum Jülich, D-52425 Jülich, Germany

ABSTRACT. In order to optimize the optoelectronic properties of novel solar cell architectures, such as the crystalline-amorphous interface in Silicon heterojunction (c-Si/a-Si:H) devices, an analysis of the local microscopic structure at the interface is essential. To this aim, reliable physical models for c-Si and a-Si:H were developed.

1 Introduction

In view of a study of an amorphous-crystalline interface in Silicon heterojunction, reliable physical models for crystalline Silicon (c-Si) and hydrogenated amorphous Silicon (a-Si:H) were developed. The *ab-initio* PWscf (Plane-Wave Self-Consistent Field) code of the Quantum ESPRESSO suite was used [1, 2] to perform total energy calculations and Born-Oppenheimer Molecular Dynamics (BOMD) simulations of c-Si and a-Si:H models in order to check their ability in reproducing experimental and structural properties. PWscf performs many different kinds of self-consistent calculations of electronic structure properties within Density-Functional Theory (DFT) [3, 4], using a Plane-Wave (PW) basis set and Pseudo-Potentials (PP). All the calculations were performed in the supercell approximation with periodic boundary conditions (PBC) meant to mimic infinitely extended systems. We used the Si and H ultrasoft pseudopotentials with Perdew-Burke-Ernzerhof (PBE) [5] approximant GGA exchange-correlation potential, available in the Quantum ESPRESSO library [2].

2 Crystalline Silicon: c-Si

A cubic supercell composed of a $2 \times 2 \times 2$ array of fcc conventional cells and 64 Si atoms was considered to simulate the silicon crystalline structure. The electronic wave functions were expanded in a plane-wave basis set with a kinetic energy cut-off equal to 40 Ry, the charge density cut-off is set to 240 Ry and a $4 \times 4 \times 4$ Monkhorst-Pack mesh of k points is employed [6]. The kinetic energy cut-offs and the mesh of k points were optimized by preliminary calculations on Silicon and Hydrogen pseudopotentials. By using *ab-initio* zero-temperature total energy calculations we computed lattice constant a and bulk modulus B . The third-order Birch-Murnaghan equation of state was used to calculate the equilibrium

*Corresponding author. E-mail: simone.giusepponi@enea.it.

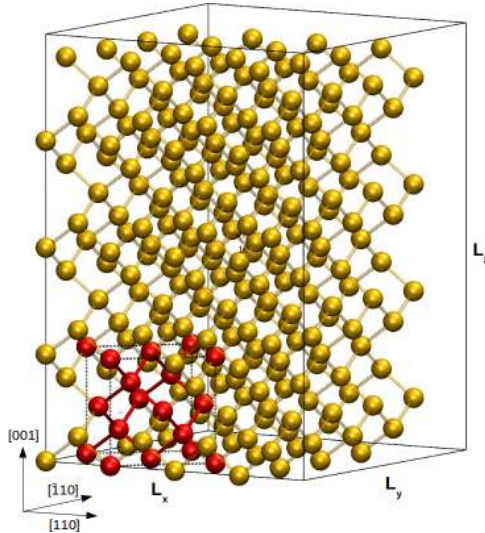


Figure 1: Tetragonal supercell used to build the Si(001) surface and its reconstruction. The silicon fcc conventional cell is highlighted in red.

lattice constant $a_0 = 5.47 \text{ \AA}$ and bulk modulus $B = 89 \text{ GPa}$. These results are in good agreement with the corresponding experimental values and with others *ab-initio* computations (see Table 1). Moreover, to check the mechanical stability of the system, the elastic constants C_{11} ; C_{12} and C_{44} were calculated. It is known that if the elastic constants obey the conditions $C_{11} - C_{12} > 0$; $C_{11} + 2C_{12} > 0$; $C_{11} > 0$ and $C_{44} > 0$ then the material is mechanically stable. The elastic isotropy is also examined by the evaluation of the ratio $A = 2C_{44}/(C_{11} - C_{12})$. In an isotropic solid $A = 1$. The following values were obtained: $C_{11} = 153 \text{ GPa}$, $C_{12} = 57 \text{ GPa}$ and $C_{44} = 75 \text{ GPa}$, from which we infer that the four conditions of mechanical stability are fulfilled. The full set of our results for crystalline Silicon are reported in Table 1 with experimental and other theoretical values. The comparison with experimental results faces the difficulty of the temperature dependence of the experiments.

3 Silicon (001) surface

To analyse the Si(001) surface and its reconstruction, we considered a tetragonal cell composed of 32 fcc cells and 256 Si atoms. The x , y and z axes correspond to the $[110]$, $[\bar{1}10]$ and $[001]$ directions of Silicon fcc conventional cell, respectively (see Fig 1). The cell has $L_x = L_y = 4 \times \frac{a_0}{\sqrt{2}}$, and $L_z = 4 \times a_0$. Using

Table 1: Calculated values of equilibrium lattice constant a_0 , bulk modulus B , elastic constants C_{11} , C_{12} , C_{44} and elastic isotropy A . Values computed in this work are compared with both numerical and experimental results from literature.

	a_0 (Å)	B (GPa)	C_{11} (GPa)	C_{12} (GPa)	C_{44} (GPa)	A
Cal.	5.47	89	153	57	75	1.56
Refs.	5.43	99[7]	168[7]	65[7]	80[7]	1.55[7]
	5.44[8]	98[8]				

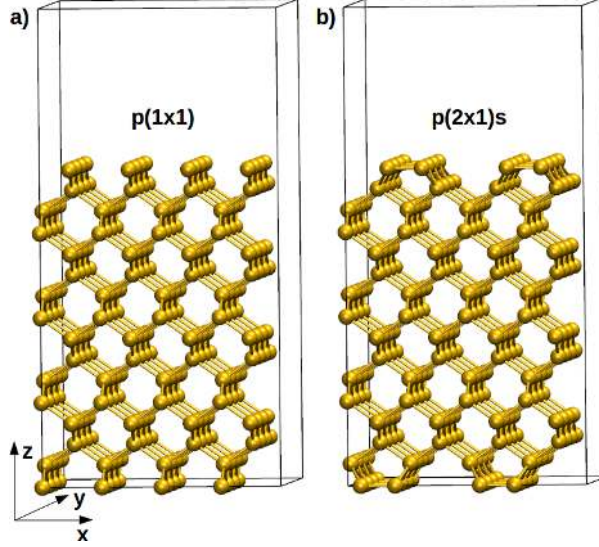


Figure 2: a) The unreconstructed (ideal) Si(001) surface. b) The symmetric $p(2 \times 1)$ reconstructed Si(001) surface.

the previous values for the kinetic energy cut-offs and a $2 \times 2 \times 2$ Monkhorst-Pack mesh of k points we found the same value for the equilibrium lattice constant $a_0 = 5.47 \text{ \AA}$. Surfaces were constructed using the previous tetragonal cell with 256 Si atoms adding a void region ($\sim 10 \text{ \AA}$) in z -direction to suppress the interaction due to the periodic boundary conditions. This was checked to be sufficient to eliminate interactions between mirror images in the z -direction. In Fig. 2a) is shown the unreconstructed (ideal) Si(001) surface. Moreover, the symmetric $p(2 \times 1)$ reconstructed Si(001) surface was analysed (see Fig. 2b). The reconstruction is formed by surface atoms moving together in pairs to form dimers and therefore the dangling bonds from the unreconstructed Si(001) surface are halved. Distance of the dimers is 2.30 \AA , and the energy gain for each dimer is 1.5 eV/dim . In Ref. [9] the following values were found : 2.23 \AA and 1.8 eV/dim .

We examined surfaces with increasing number N of layers, each of them composed of 16 Si atoms, then we calculated the total energy of the surface systems with respect to the number of slabs (up to $N = 16$) and using $2 \times 2 \times 1$ k point mesh. Two class of configurations were considered: surfaces in which all atoms were kept fixed, and relaxed surfaces in which only the bottom four layers of atoms were kept fixed. The latter choice were done to attain the semi infinite bulk crystal beneath the surface.

There is a linear growth of the total energy E_{slab}^N with respect of the number of the slabs N , this permit to calculate the surface energy σ for both Si(001) surfaces using the following equation [10]:

$$E_{slab}^N \approx 2\sigma + NE_{bulk}$$

where E_{bulk} is the bulk total energy. Calculations of the surface energy per unit area $\gamma = \sigma/A$ (where $A = L_x \times L_y$), gave $\gamma = 2.12 \text{ J/m}^2$ for unreconstructed Si(001) surface and gave $\gamma = 1.42 \text{ J/m}^2$ for symmetric $p(2 \times 1)$ reconstructed Si(001) surface. Other numerical calculations gave similar results. In Refs. [11, 12] it was calculated $\gamma = 2.36 \text{ J/m}^2$ and $\gamma = 2.39 \text{ J/m}^2$ for the former surface and $\gamma = 2.51 \text{ J/m}^2$ and $\gamma = 1.45 \text{ J/m}^2$ for the latter one.

The surface relaxations of the Si(001) surfaces were also analysed. Surface relaxation can be characterized as the percent change $\Delta_{ij} = (d_{ij} - d_0)/d_0$ of the spacing d_{ij} between layers i and j versus the equilibrium layer spacing d_0 . For the Silicon (001) surfaces d_0 is $a_0/4$. A positive value indicates expansion, whereas a negative one indicates a contraction of the spacing. The surface relaxation of the unreconstructed Si(001) surface system with 16 Silicon slabs with the four bottom atom layers kept

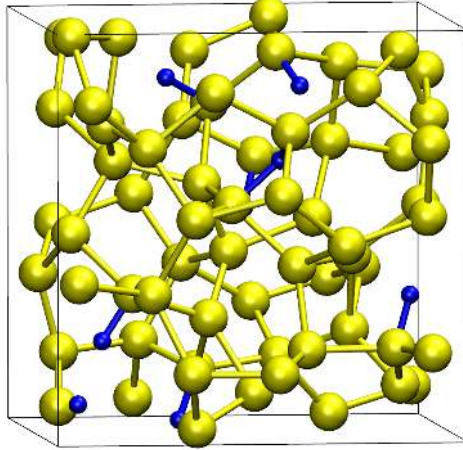


Figure 3: Schematic of the a-Si:H in the simulation box. Hydrogen atoms and bonds with Silicon atoms are in blue, Silicon atoms and their bonds are in yellow.

fixed, was found to be $\Delta_{12} = -1.7\%$, $\Delta_{23} = -0.38\%$, and $\Delta_{34} = -0.66\%$. While for the symmetric $p(2 \times 1)$ reconstructed Si(001) surface we measured $\Delta_{12} = -21.4\%$, $\Delta_{23} = 0.21\%$, and $\Delta_{34} = 0.13\%$.

4 Hydrogenated amorphous Silicon: a-Si:H

The model of the hydrogenated amorphous Silicon was generated using a simulate annealing quench from a melt simulation protocol, currently used to generate high-quality amorphous samples [13]. A system of 64 Si + 8 H atoms in a cubic supercell with size $L=11.06 \text{ \AA}$, with a density of 2.214 gr./cm^3 was considered. A BOMD simulation on the electronic ground state at constant volume and constant temperature ($T=300 \text{ K}$) was performed for 6.5 ps (timesteps $ts = 20 \text{ Ry}$), controlling the ionic temperature by using Andersen thermostat. In Fig. 3 it is shown the a-Si:H system at the end of the simulation. The initial 1.5 ps of simulation was sufficient to thermalize the system, then the remaining 5 ps of simulation was used to characterize the system. Fig. 4 shows the radial pair correlation functions $g(r)$ yielded in this 5 ps of simulation. The yellow line was computed taking in consideration only the Silicon atoms, whereas, the blue line was computed considering Si and Si + H atoms. There is a peak at 2.37 \AA for the Si/Si $g(r)$, and there is a peak at 1.52 \AA for the Si/Si+H $g(r)$. Moreover, the coordination analysis was performed in the last 5 ps of simulation (see Tab. 2). A geometrical criteria was adopted for identify the number of bonds in the coordination analysis. The following distance cutoffs were chosen: 2.9 \AA for Si-Si pairs and 1.8 \AA for Si-H pairs. It is observed that 4 Silicon atoms have three-fold coordination (6.3%), 58 Silicon atoms have four-fold coordination (90.6%) and the remaining 2 Si atoms

Table 2: Coordination analysis of the hydrogenated amorphous Silicon: a-Si:H.

Coordination	n	Si	Si+H
3	4	4 (3Si)	
4	58	51 (4Si)	7 (3Si+1H)
5	2	1 (5Si)	1 (4Si+1H)

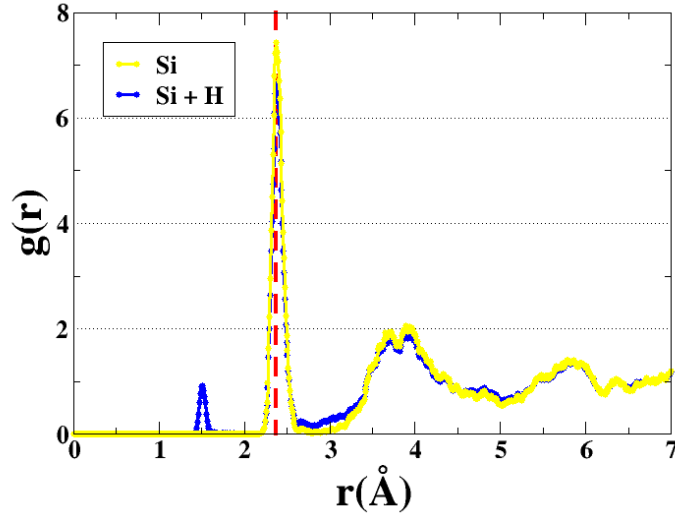


Figure 4: Radial pair correlation functions $g(r)$ computed considering Si and Si+H atoms (blue line) and Si and Si atoms (yellow line).

have five-fold coordination (3.1%). The first group of Si atoms (coordination 3) are surrounded only by Silicon atoms; 51 Si atoms of the second group are four-fold coordinated with others Si, whereas the residual 7 Si atoms are coordinated with 3 Si and 1 H. Finally, of the last two atoms, 1 Si is five-fold coordinated with others Si, and 1 is surrounded by 4 Si and 1 H.

References

- [1] P. Giannozzi *et al.* *J. Phys.: Condens. Matter.*, 21:395502, 2009.
- [2] www.quantum-espresso.org.
- [3] P. Hohenberg and W. Kohn. *Phys. Rev.*, 136:B864, 1964.
- [4] W. Kohn and L.J. Sham. *Phys. Rev.*, 140:A1133, 1965.
- [5] K. Burke J.P. Perdew and M. Ernzerhof. *Phys. Rev. Lett.*, 77:3865, 1996.
- [6] H.J. Monkhorst and J.D. Pack. *Phys. Rev. B*, 13:5188, 1976.
- [7] H.J. McSkimin and P. Andreatch Jr. *J. Appl. Phys.*, 35:3312, 1964.
- [8] J. Leszczynski M. Yengui, H. P. Pinto and D. Riedel. *J. Phys. Condens. Matter*, 27:045001, 2015.
- [9] G Brocks A. Ramstad and P. J. Kelly. *Phys. Rev. B*, 51:14504, 1995.
- [10] V. Fiorentini and M. Methfessel. *J. Phys. Condens. Matter*, 8:6525, 1996.
- [11] M. Cuma G-H. Lu, M. Huang and F. Liu. *Surface Science*, 588:61, 2005.
- [12] J. Furthmuller A.A. Stekolnikov and F. Bechstedt. *Phys. Rev. B*, 65:115318, 2002.
- [13] M. Legesse M. Nolan and G. Fagas. *Phys. Chem. Chem. Phys.*, 14:15173, 2012.

QUANTUM ESPRESSO PERFORMANCE ON ENEA AND JSC HPC INFRASTRUCTURES.

Simone Giusepponi^{1*}, Michele Gusso², Massimo Celino¹,
Urs Aeberhard³ and Philippe Czaja³

¹ *ENEA, C. R. Casaccia, via Anguillarese 301, 00123 Rome, Italy*

² *ENEA, C. R. Brindisi, S.S. 7 Appia km 706, 72100 Brindisi, Italy*

³ *IEK-5 Photovoltaik, Forschungszentrum Jülich, D-52425 Jülich, Germany*

ABSTRACT. In this paper we report results from a benchmark in which we compare the performances of three HPC clusters: CRESCO4 and CRESCO5 located in the Portici ENEA centre, and JURECA located in Jülich Supercomputing Centre.

1 Introduction

In view of an intensive use of computational resources for an ab-initio study of a crystalline Silicon (c-Si) and hydrogenated amorphous Silicon (a-Si:H) interface (see Fig. 1), a measure of the performances of three HPC infrastructures (CRESCO4, CRESCO5, JURECA) was carried out. This enabled us to set the optimal computational resources and give an estimation of the computational time. The benchmark is based on the time required to execute a self-consistent calculation, for a single energy minimization in the computation of the ground-state energy of the c-Si/a-Si:H interface depicted in Fig. 1. The calculation is performed using the ab-initio PWscf (Plane-Wave Self-Consistent Field) code of the Quantum ESPRESSO suite [1, 2].

The ENEA CRESCO computing facilities are based on the multi-core x86_64 architecture and is made up of various clusters: we tested the CRESCO4 and CRESCO5 clusters located in Portici ENEA centre [3, 4].

CRESCO4 is composed by 304 compute nodes. Each node hosts a dual-socket 8 cores CPU Intel E5-2670 processor (Sandy Bridge architecture) which operates at a clock frequency of 2.6 GHz and has 20 MB of cache and avx instructions set. The total number of cores is 4864.

CRESCO5 is composed by 40 compute nodes. Each node hosts a dual-socket 8 cores CPU Intel E5-2630 v3 processor (Haswell architecture) which operates at a clock frequency of 2.4 GHz and has 20 MB of cache and avx 2.0 instructions set. The total number of cores is 640.

Both clusters have 64 GB of RAM memory per node (4 GB per core) and are interconnected via an IB 4xQDR Qlogic/Intel 12800-180 switch. The Operating System for the clusters is the Red Hat Enterprise Linux ver. 2.6.32-220.7.1.el6.x86_64. Quantum Espresso ver. 5.1.2 is compiled with intel compiler ver. 14.0 using the mathematical library MKL ver. 11.1 and OpenMPI ver. 1.4.3.

The third cluster is JURECA HPC hosted at Jülich Supercomputing Centre (JSC) [5].

*Corresponding author. E-mail: simone.giusepponi@enea.it.

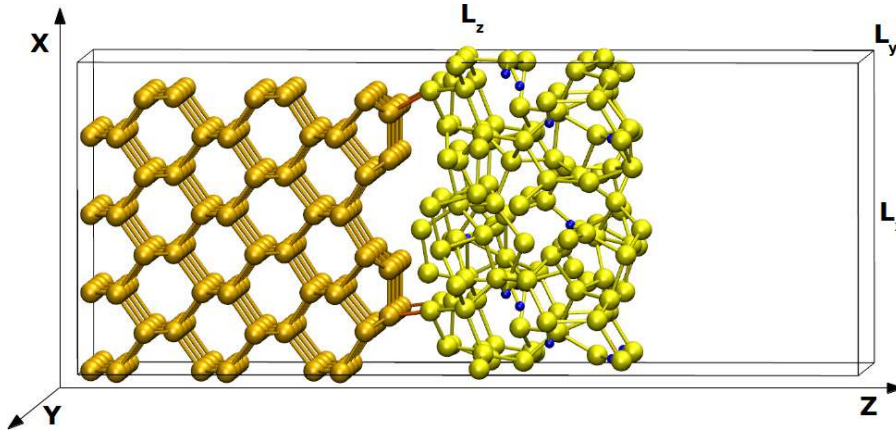


Figure 1: Snapshot of the initial a-Si:H/c-Si interface in the simulation box. The structure is infinitely extended in both x and y directions. A void region is considered to suppress the interaction, due to periodic boundary conditions, between the external surfaces. Free surfaces and a-Si:H/c-Si interface are perpendicular to the y axis. Hydrogen atoms are in blue, Silicon atoms are in orange in the c-Si side and are in yellow in the a-Si:H side.

JURECA is composed by 1872 compute nodes. Each node hosts a dual-socket 12 cores CPU Intel E5-2680 v3 processor (Haswell architecture) which operates at a clock frequency of 2.5 GHz and has 30 MB of cache and avx 2.0 instructions set. The total number of cores is 44928, the cluster has 128 GB of RAM memory per node that are interconnected via a Mellanox EDR InfiniBand. The Operating System for the cluster is the CentOS 7 Linux ver. 3.10.0-327.10.1.el7.x86_64. Quantum Espresso ver. 5.1.1 is compiled with intel compiler ver. 15.0 using the mathematical library MKL ver. 11.2 and ParaStationMPI ver. 5.0.

2 Results and discussion

To compare the performance and scalability of the three clusters, we collected the time necessary to perform a self consistent calculation, for a single energy minimization in the computation of the ground-state energy of the c-Si/a-Si:H interface depicted in Fig. 1. Total cpu and wall times for the three clusters using 48, 96, 192 and 384 cores are reported in Tab. 1 and illustrated in panel a) of Fig. 2. The calculation is performed considering only the Γ point and using MPI parallelization.

Moreover, in Fig. 2, there are shown the speed up (panel b) and the resulting efficiency (panel c) calculated for each cluster with respect to the time measured in the 48 cores execution. This type of computation has a good parallel scalability until 192 cores with an efficiency of about 75%.

In addition, in Tab. 1 for each row, it is reported the percent gain in time (numbers in parenthesis) for CRESCO5 and JURECA with respect to the CRESCO4 execution time. The results confirm that the more recent processors, E5-2630 v3 and E5-2680 v3 mounted on CRESCO5 and JURECA clusters, respectively, have the best performance with reductions of execution times, in the range 30÷40% for JURECA and in the range 10÷20% for CRESCO5. Then, even if, they have the same architecture (Haswell) and the same instruction set (avx 2.0), E5-2680 v3, being two and half times more expensive, legitimises its cost having better performance. This is also emphasised in panels b) and c) of Fig. 3, in which the speed up and efficiency were calculated with respect to the execution time for 48 cores on CRESCO4 cluster.

Finally, in the last two columns of Tab. 1, the difference between wall and cpu times, and the corresponding percent variations are shown. Data indicate that CRESCO4 and CRESCO5 have differences in time less

Table 1: Total cpu and wall time to perform a single energy minimization in the computation of the ground-state energy for the c-Si/a-Si:H interface, at different number of cores used in the calculation. Differences between wall and cpu times and the corresponding percent variations are shown in the last two columns. Moreover, for each row, the percent gain of times on CRESCO5 and JURECA clusters with respect to the time on CRESCO4 cluster are reported.

cores	cluster	Total cpu time t_1 (s)	Total wall time t_2 (s)	$t_1 - t_2$ (s)	$\frac{t_2 - t_1}{t_1}$ (%)
48	CRESCO4	966.3	1037.8	71.5	7.4
	CRESCO5	889.2 (-8.0%)	957.5 (-7.7%)	68.3	7.7
	JURECA	695.7 (-28%)	743.1 (-28%)	47.4	6.8
96	CRESCO4	571.7	610.4	38.7	6.8
	CRESCO5	483.1 (-15%)	520.1 (-15%)	37.0	7.7
	JURECA	346.8 (-39%)	411.7 (-33%)	64.9	19
192	CRESCO4	371.7	389.9	18.2	4.9
	CRESCO5	306.5 (-18%)	317.9 (-18%)	11.4	3.7
	JURECA	211.5 (-43%)	277.6 (-29%)	66.1	31
384	CRESCO4	291.3	306.7	15.4	5.3
	CRESCO5	224.9 (-23%)	238.2 (-22%)	13.3	5.9
	JURECA	180.9 (-38%)	253.2 (-17%)	72.3	40

than 8%, in fact, they use the same interconnection network. On the contrary, JURECA has differences in time that enlarge with the number of cores used in the calculation: from about 7% with 48 cores up to 40% at 384 cores. This is maybe due to the size of the cluster (1872 compute nodes and 44928 cores), in which there are hundreds/thousands concurrent jobs.

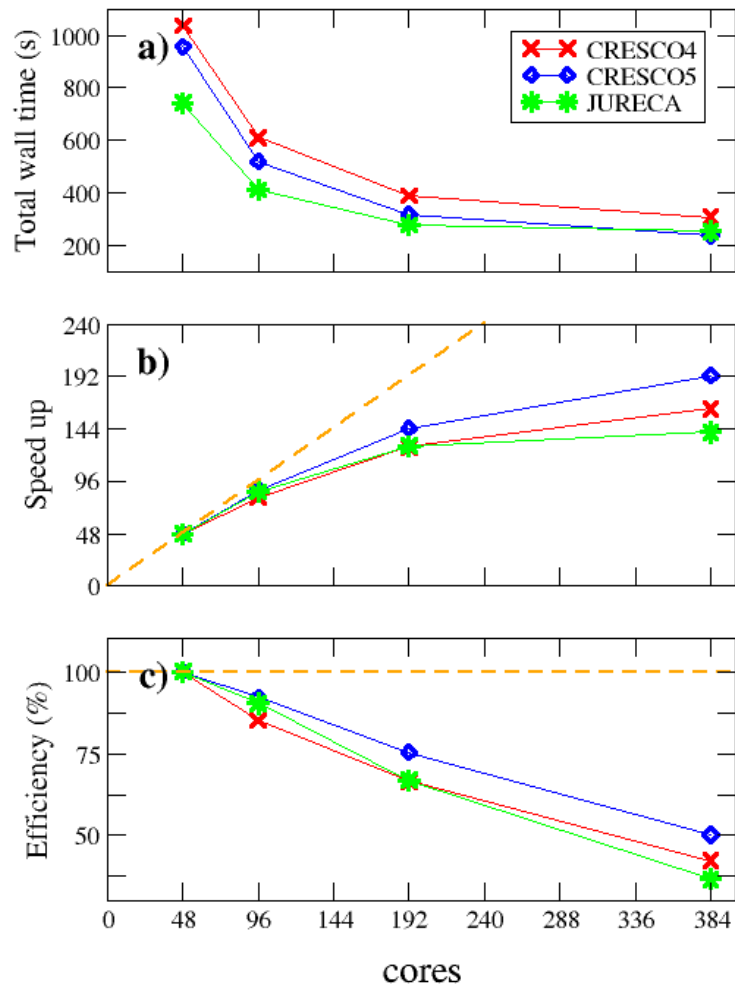


Figure 2: a) Total wall time (s) for a self consistent calculations for a single energy minimization. b) Speed up calculated with respect to the time in the 48 cores calculation, and c) the corresponding efficiency (%). Red lines(symbols) are for CRESO4, blue lines(symbols) are for CRESO5 and green lines(symbols) are for JURECA. Dashed orange lines represent ideal parallel scalability.

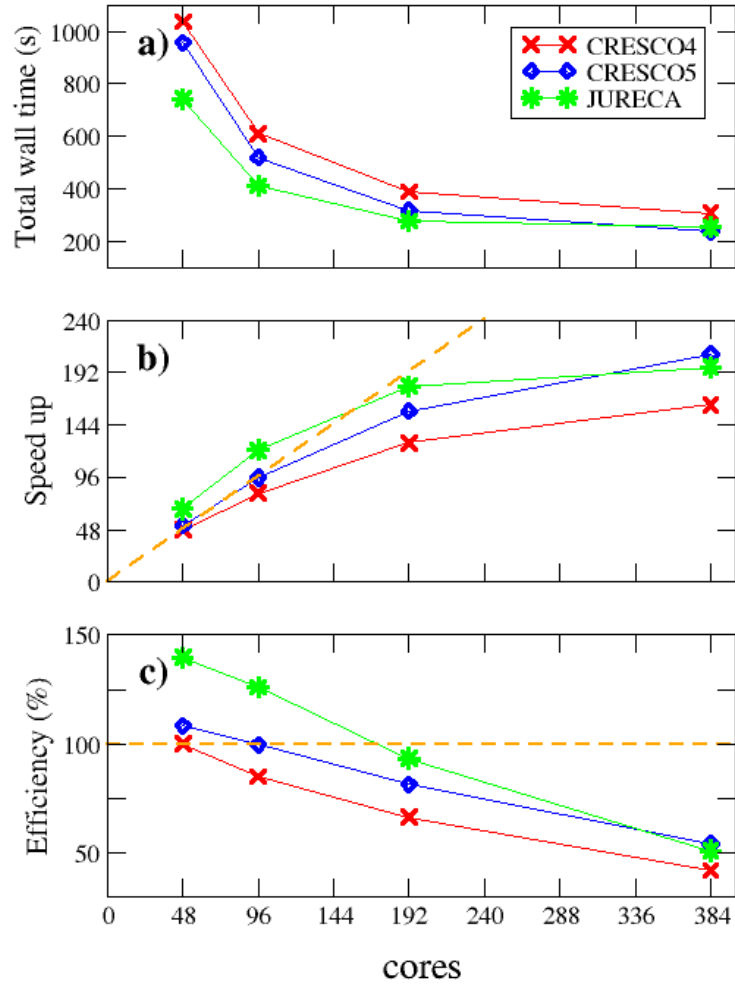


Figure 3: a) Total wall time (s) for a self consistent calculations for a single energy minimization. b) Speed up calculated with respect to the time in the CRESOCO4 48 cores calculation, and c) the corresponding efficiency (%). Red lines(symbols) are for CRESOCO4, blue lines(symbols) are for CRESOCO5 and green lines(symbols) are for JURECA. Dashed orange lines represent ideal parallel scalability.

References

- [1] P. Giannozzi *et al.* *J. Phys.: Condens. Matter.*, 21:395502, 2009.
- [2] www.quantum-espresso.org.
- [3] www.cresco.enea.it.
- [4] www.eneagrid.enea.it.
- [5] www.fz-juelich.de/ias/jsc/en/expertise/supercomputers/jureca/jureca_node.html.

ELECTRONIC BAND STRUCTURE, LATTICE DYNAMICS, AND RELATED SUPERCONDUCTING PROPERTIES OF NIOBIUM FROM FIRST-PRINCIPLES CALCULATIONS

Gianluca De Marzi

ENEA, FSN C.R. Frascati, Via Enrico Fermi 45, 00044 Frascati, Italy¹

ABSTRACT. Niobium attracts much interest because of its highest superconducting transition temperature among all the elements in the periodic table. Moreover, the use of niobium in a variety of superconducting alloys and compounds makes it effectively the material of excellence in every field of applied superconductivity. In this work, the main physical properties related to superconductivity in elemental niobium have been addressed by means of first principles methods based on density functional theory. The electronic band structure, electronic density of states and Fermi surfaces are found to be in excellent agreement with previously published studies. The phonon dispersion curve have been calculated along different high-symmetry directions in the Brillouin zone and compared with available experimental data. The elastic constants have been inferred from the slopes of the acoustic phonons along the [100] direction, and compared with experimental results. Starting from the calculated averaged phonon frequencies and electron-phonon coupling, the superconducting characteristic critical temperature of the material, T_c , has been estimated by means of the Allen-Dynes modification of the McMillan formula. The results of this work can provide a sound basis for further theoretical insights onto other Nb-based superconductors.

1 Introduction

Niobium-based alloys have been widely used in most technological applications of superconductors since the early 1960s [1]. In facts, multifilamentary NbTi wires have been successfully employed in the superconducting electromagnets and detectors of the Large Hadron Collider (LHC) accelerator at CERN [2], whereas its High-Luminosity upgrade (HiLumi) will require a new generation of Nb₃Sn high field superconducting quadrupoles and dipoles [3]. Within the framework of nuclear fusion projects, the coils of the International Thermonuclear Experimental Reactor (ITER) comprise both NbTi and Nb₃Sn wires [1, 4]. It is also worth mentioning that the high-performances Nb₃Al is being considered as a promising candidate for high-field magnets, although km-grade wires are still not available for large-scale applications [5]. In electronics applications, niobium and niobium-titanium nitrides are used in Josephson junctions, RF devices and IR detectors [6]. Moreover, Nb-based superconductors are currently employed in commercial Magnetic Resonance Imaging (MRI) systems [7], and in several other applications, including magnets for Nuclear Magnetic Resonance (NMR) spectroscopy, superconducting magnetic energy storage (SMES) and levitated trains.

Niobium, a ductile refractory transition metal element with atomic number $Z = 41$, has the highest superconducting transition temperature ($T_c = 9.25$ K) among any other elemental superconductor; it is also one of the few elemental superconductors exhibiting type-II magnetic properties and some non-negligible transport critical current capability. By virtue of the key role played by niobium in the aforementioned technological superconductors, we here present a detailed theoretical study of the superconducting properties of Nb, with the aim to provide a sound basis for further Density Functional Theory (DFT) insights onto other Nb-based superconductors.

¹ Corresponding author. E-mail: gianluca.demarzi@enea.it.

2 Computational details

The DFT [8, 9] scheme here employed adopts a Generalized Gradient Approximation (GGA) of the electron exchange and correlation energy using Perdew-Wang formula (PW91) [10] as implemented in the QUANTUM-ESPRESSO (QE) package [11]; electron-ion interactions have been modelled with ultra-soft pseudopotentials (US-PP) in the context of a plane wave expansion basis set. US-PPs have allowed the usage of an energy cut-off of 40 Ry for the wave functions and 400 Ry for the electron density.

An artificial thermal broadening (*smearing*) and a 16x16x16 Monkhorst-Pack (MP) \mathbf{k} -point grid [12] for the Brillouin zone (BZ) sampling have been employed for the body-centered cubic cell, whereas \mathbf{k} -points convergence tests were performed in order to determine the amount of \mathbf{k} -points necessary to perform accurate calculations. The ground state configurations have been obtained via the Broyden-Fletcher-Goldfarb-Shanno (BFGS) algorithm [13].

Phonon frequencies $\omega_{\nu}(\mathbf{q})$, have been computed in the framework of Density-Functional Perturbation Theory (DFPT) [14] with QE, whereas a 16x16x16 \mathbf{q} -point uniform grid, previously tested to be sufficient for convergence, has been employed to calculate the entire phonon spectra.

3 Results

3.1 Electronic band structure, Density Of States (DOS) and Fermi surface

Niobium is characterized by 5 valence electrons, with electronic structure $[\text{Kr}]4d^45s^1$: four electrons occupy highly localized d -orbitals, whereas the fifth electron occupies a less localized s -orbital. Consequently, the band structure is characterized by the overlap and hybridization of a rather large d band with a larger, hybridized sp -band [15].

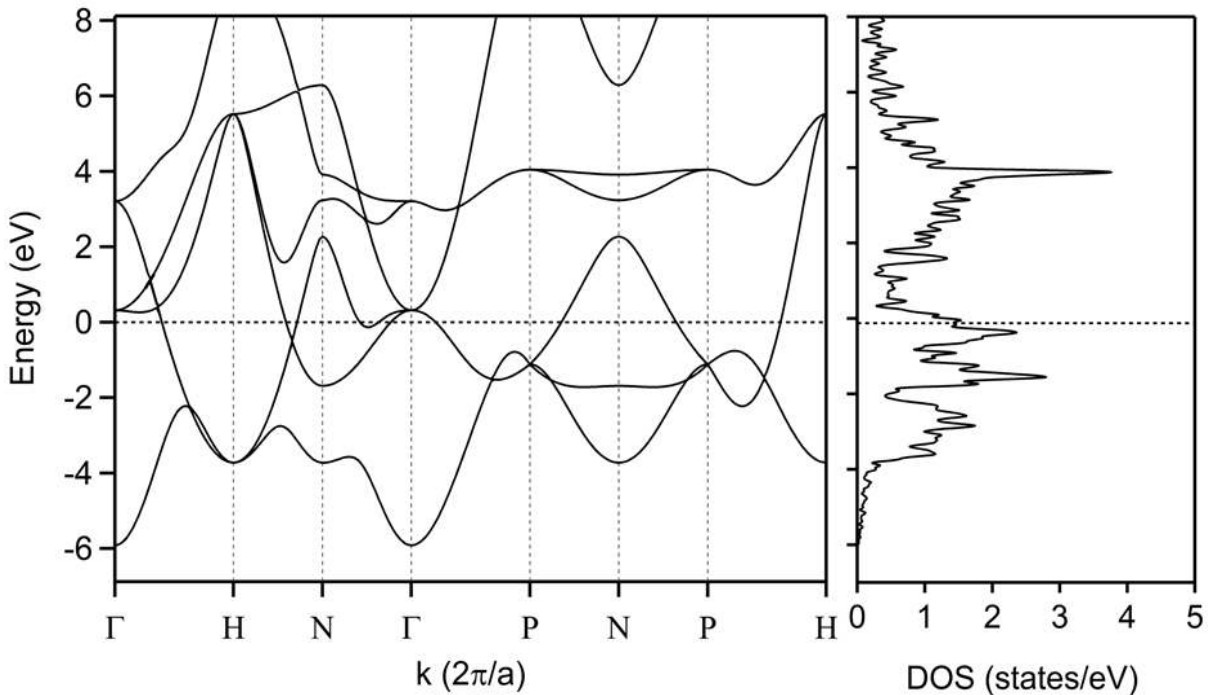


Fig.1: Band structure (left) and Density of States (DOS) of Nb. The dotted line represents the Fermi level, which is set to zero.

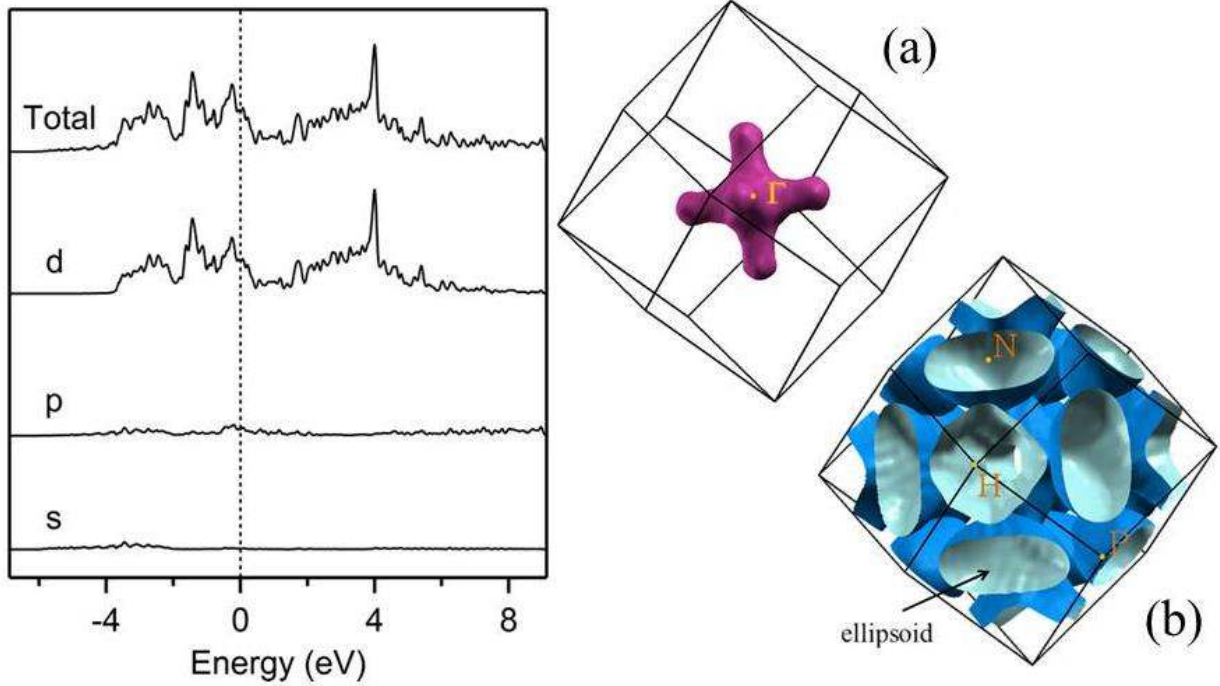


Fig.2: Density of States projected on atomic orbitals (PDOS). The main contribution comes from $4d$ -orbitals (82%). The dotted line represents the Fermi level (conventionally set to zero). The Fermi surface of niobium is represented in the right side: (a) closed structure with octahedron symmetry, centred at the Γ point (second BZ); (b) ellipsoids centred at the N points, together with the “jungle-jim” geometry (third BZ).

In Fig. 1, plots of the E - k relations calculated along several main symmetry directions (Δ , G , Σ , Λ , D , F) of the Brillouin Zone are shown. On the right side of Fig. 1, the corresponding electronic DOS is plotted: as it can be clearly seen, there are several peaks, which can be correlated to measured data from photoemission experiments (a band with a width of ~ 3 eV comprised of three peaks at ~ 0.4 , ~ 1.1 and ~ 2.3 eV below ε_F) [16]. The DOS at ε_F is $N(\varepsilon_F) = 1.46$ states/eV $^{-1}$.

The DOS projected onto the atomic orbitals of Nb is plotted as a function of the energy in Fig. 2. In the whole considered energy range, the main contribution to the total DOS comes from $4d$ -orbitals, for about 82%, with small contributions from the remaining s - (5%) and p -orbitals (13%).

With five electrons per atom, the Fermi surface extends outside the first Brillouin Zone (BZ), the k -states being occupied up to the third BZ. Niobium is characterized by a rather topologically complex Fermi surface, which has been firstly calculated in 1970 by Mattheiss by means of the Augmented Plane-Wave method [17]. Fig. 2 also depicts, in the reduced zone scheme, the Fermi surface sheets that enclose the unoccupied regions in the second and third BZ (the first BZ is completely filled by electrons). In the second zone, the Fermi surface is characterized by a hole surface with the shape of a distorted octahedron centred at Γ , with rather large effective masses (1.4 - $2.0 m_0$) [16, 18]. In the third zone, the hole Fermi surface is comprised of six distorted ellipsoidal structures centred at the points N , plus a multiply connected sheet which extends along $\langle 100 \rangle$ directions, from Γ to H . This is often referred to as “jungle-jim” structure.

3.2 Phonon dispersion curves and elasticity

The phonon dispersion curves have been calculated for three different *smearing* values (0.005, 0.01, e 0.02 Ry). The phonon dispersion curves calculated with *smearing* = 0.01 Ry [19] (Fig. 3) are in excellent agreement with the experimental data [20], with the exception of the double degenerate Transverse Acoustic (TA) phonons in the long wavelength limit in the Γ - H direction [21], and the high-frequency branches along the H - P direction. All major experimental findings are reproduced

by calculations: along the Γ - H direction a cross-over of the longitudinal and transverse branches near $\mathbf{q}=(0.0, 0.0, 0.7)$ is found, with the concomitant presence of a maximum and minimum. Moreover, the transverse branches cross near $\mathbf{q}=(0.3, 0.3, 0.0)$ along the Γ - N direction. From the phonon dispersion curves, one can infer information about the elastic constants. In fact, in a perfect crystal the elastic constants can be directly obtained from the slopes of the acoustic branches in the long wavelength limit ($|\mathbf{q}| \rightarrow 0$). For a cubic lattice, the expressions for C_{11} and C_{44} can be written as:

$$\left. \frac{\partial \omega_{[\xi 00]L}(\mathbf{q})}{\partial |\mathbf{q}|} \right|_{\mathbf{q} \rightarrow 0} = \sqrt{\frac{C_{11}}{\rho}}, \quad \left. \frac{\partial \omega_{[\xi 00]T}(\mathbf{q})}{\partial |\mathbf{q}|} \right|_{\mathbf{q} \rightarrow 0} = \sqrt{\frac{C_{44}}{\rho}} \quad (1)$$

where ω and \mathbf{q} represent the frequency and the wave vector of a given phonon mode ($\langle 100 \rangle$ direction), respectively.

By considering a density of 8.57 g/cm^3 , from the slope of the TA branch in the Γ - H direction a value $C_{11} = 2.27 \text{ Mbar}$ is calculated, in good agreement with experiments ($C_{11,exp} = 2.46 \text{ Mbar}$ [22]). On the other hand, the elastic constant C_{44} is largely underestimated: $C_{44} = 0.179 \text{ Mbar}$ for a *smearing* value of 0.02 Ry , whereas the experimental value is $C_{44,exp} = 0.287 \text{ Mbar}$ [22]. Finally, C_{12} can be obtained from the bulk modulus $B_0 = (C_{11} + 2 \cdot C_{12})/3$. Table 1 reports the experimental values for the elastic constant of niobium, together with DFT calculations obtained with different exchange functionals.

As mentioned earlier, the TA frequencies in the long wavelength limit along the Γ - H direction are largely underestimated by DFT calculations, and this reflects to the value estimated for the elastic constant C_{44} . On the other hand, the Longitudinal Acoustic (LA) branch is in excellent agreement with the experimental results for any wavelength. The elastic constant associated to those LA phonons, C_{11} , is therefore more accurate. The reason for such inaccuracy in calculating C_{44} is not known. Some authors [23] suggest that the softening of C_{44} could be due to the concomitant presence of a van Hove singularity near the Fermi surface.

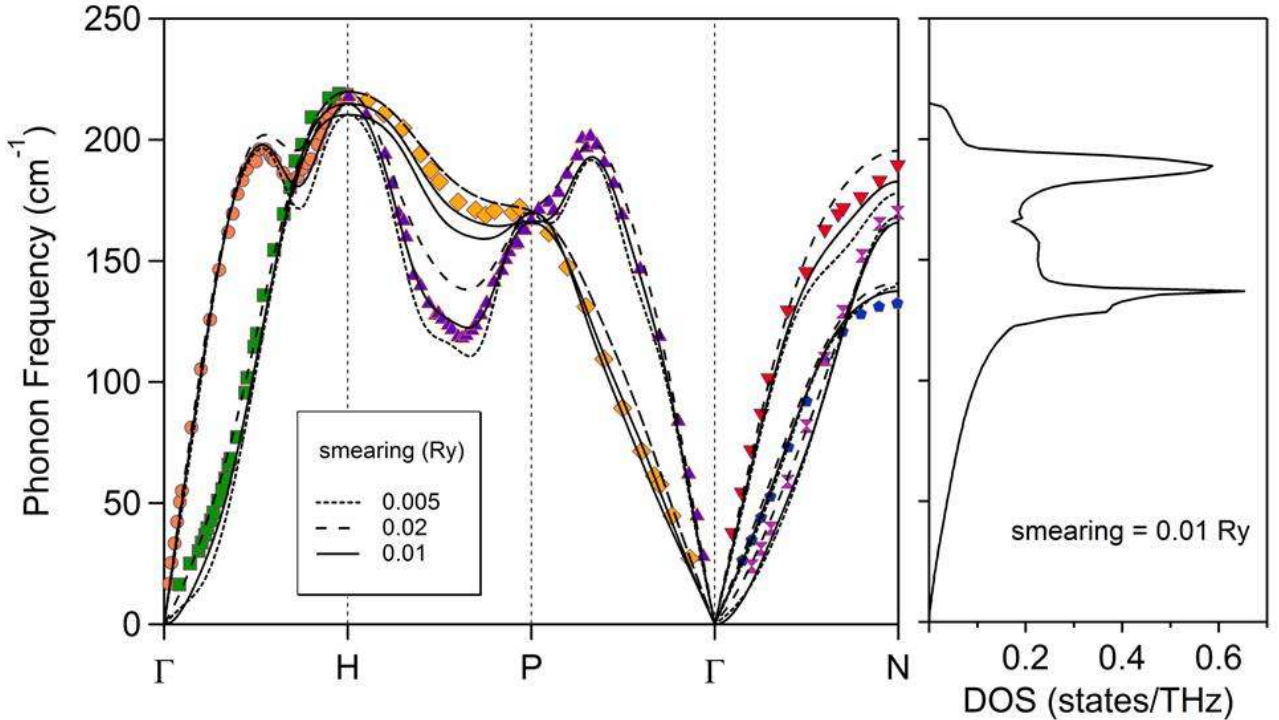


Fig. 3: Phonon dispersion curve of niobium and corresponding phonon DOS. Dotted and continuous lines represent the DFT calculation, whereas symbols are experimental data from [20].

	B_0	C_{11}	C_{12}	C_{44}
This work	1.720	2.27	1.45	0.179
GGA (PBE)	1.712	2.5242	1.3006	0.2112
GGA (PW91)	1.7226	2.4499	1.3589	0.1519
LDA	1.9182	2.7619	1.4963	0.1445
Exp. [22]	1.718	2.46	1.347	0.287
Exp. [24]	1.7303	2.5270	1.3319	0.3097

Table 1: Elastic constants of niobium, calculated with different exchange functionals (LDA; GGA) and measured [22, 24]. In the GGA calculations, the correlation energy is introduced by means of the gradient-corrected PW91 (as proposed by Perdew and Wang [25]) or PBE (Burke-Ernzerhof [26]) functionals.

3.3 Superconducting properties

Finally, in this subsection we provide a brief account on the prediction of the superconducting critical temperature of niobium. Once the electronic and vibrational properties are known, it is possible to estimate the critical temperature with the formula proposed by McMillan [27]:

$$T_c = \frac{\theta_D}{1.45} e^{\frac{1.04(1+\lambda)}{\lambda - \mu^*(1+0.62\lambda)}} \quad (2)$$

where θ_D is the Debye temperature, μ^* the effective Coulomb repulsion parameter, and λ the electron-phonon coupling constant. Later, Allen and Dynes [28] refined the McMillan formula by substituting the phenomenological quantity $\theta_D/1.45$ with the quantity $\omega_m/1.2$, where the logarithmically averaged characteristic frequency ω_m can be calculated by means of *ab-initio* methods. In the vast majority of cases, μ^* varies in a range comprised between 0.1 and 0.25. By using the empirical relation proposed by Bennemann and Garland [29] and considering that $N(\varepsilon_F) = 1.46$ states/eV⁻¹, the effective Coulomb repulsion is found to be $\mu^* \approx 0.15$. Unfortunately, the estimation of T_c by means of Eq. (2) lacks of accuracy, because of the uncertainty in the Coulomb pseudopotential μ^* , the electron-phonon coupling parameter λ and the Debye temperature θ_D (or, equivalently, ω_m). The experimental and theoretical values μ^* , λ and θ_D are spread in a range comprised between ≈ 0.1 -0.15 (μ^*), ≈ 0.7 -1.2 (λ), and 250-276 K (θ_D). If we consider $\lambda \sim 0.9$ and $\mu^* \approx 0.15$, then T_c varies in the range 8.9 K to 9.8 K for θ_D comprised between 250 K and 276 K ($T_{c,exp} = 9.25$ K).

For more precise self-consistent calculations, a denser sampling of the Fermi surfaces is required, although this is currently limited by the available CPU time and memory.

References

- [1] DE MARZI G., MUZZI L., LEE P. J. “*Superconducting Wires and Cables: Materials and Processing*”. In “Reference Module in Materials Science and Materials Engineering” Elsevier (2016).
- [2] HELLER R., BOTTURA L. “*Preface to the Special Issue on Low- T_c Superconducting Materials*”. *Cryogenics* **48** (2008) pp. 281-281.
- [3] AMBROSIO G. “*Nb3Sn High Field Magnets for the High Luminosity LHC Upgrade Project*”. *IEEE Transaction on Applied Superconductivity* **25** (2015) 4002107 (7pp).
- [4] MUZZI L., DE MARZI G., DI ZENOBIO A., DELLA CORTE A. “*Cable-in-conduit Conductors: Lessons from the Recent Past for Future Developments with Low and High Temperature Superconductors*”. *Superconductor Science and Technology* **28** (2015) 053001 (25pp).
- [5] PAN X. F., YAN G., QI M., CUI L. J., CHEN Y. L., ZHAO Y., LI C. S., LIU X. H., FENG Y., ZHANG P. X., LIU H. J., LI L. F. “*Fabrication of Nb3Al Superconducting Wires by Utilizing the Mechanically*

-
- Alloyed Nb(Al)ss Supersaturated Solid-Solution with Low-Temperature Annealing*". *Physica C* **502** (2014) pp.14-19.
- [6] FLÜKIGER R. "Overview of Low T_c Materials for Conductor Applications". In "Handbook of Superconducting Materials". Edited by David A Cardwell and David S Ginley (Institute of Physics Publishing, Ltd, Bristol 2003), Volume I: Superconductivity, Materials, and Processes, chapter B3.3.1, pp 585-602.
- [7] MORROW G. "Progress in MRI Magnets". *IEEE Transaction on Applied Superconductivity* **10** (2000) pp. 744–751.
- [8] HOHENBERG P., KOHN W. "Inhomogeneous Electron Gas". *Physical Review* **136** (1964) pp. B864-871.
- [9] KOHN W., SHAM L. J. "Self-Consistent Equations Including Exchange and Correlation Effects". *Physical Review* **140** (1965) pp. A1133-1138.
- [10] PERDEW J., WANG Y. "Accurate and Simple Analytic Representation of the Electron-Gas Correlation Energy". *Physical Review B* **45** (1992) pp. 13244-13249.
- [11] GIANNOZZI P., *et al.* "QUANTUM ESPRESSO: a Modular and Open-Source Software Project for Quantum Simulations of Materials". *Journal of Physics: Condensed Matter* **21** (2009) 395502 (19pp).
- [12] MONKHORST H. J., PACK J. D. "Special Points for Brillouin-Zone Integrations". *Physical Review B* **13** (1976) pp. 5188-5192.
- [13] FLETCHER R. "A New Approach to Variable Metric Algorithms". *The Computer Journal* **13** (1970) pp. 317-322.
- [14] BARONI S., DE GIRONCOLI S., CORSO A. D., GIANNOZZI P. "Phonons and Related Crystal Properties from Density-Functional Perturbation Theory". *Reviews of Modern Physics* **73** (2001) pp. 515-562.
- [15] JANI A. R., BRENER N. E., CALLAWAY J. "Band Structure and Related Properties of bcc Niobium". *Physical Review B* **38** (1998) pp. 9425-9433.
- [16] EASTMAN D. E. "Photoemission Studies of d-band Structure in Sc, Y, Gd, Ti, Zr, Hf, V, Nb, Cr and Mo". *Solid State Communications* **7** (1969) pp. 1697-1700.
- [17] MATTHEISS L. F. "Electronic Structure of Niobium and Tantalum". *Physical Review B* **1** (1970) pp. 373-380.
- [18] KARIM D. P., KETTERSON J. B., CRABTREE G. W. "A de Haas-van Alphen Study of Niobium: Fermi Surface, Cyclotron Effective Masses, and Magnetic Breakdown Effects". *Journal of Low Temperature Physics* **30** (1978) pp. 389-423.
- [19] DE GIRONCOLI S. "Lattice Dynamics of Metals from Density Functional Perturbation Theory". *Physical Review B* **51** (1995) pp. 6773-6776.
- [20] POWELL B. M., MARTEL P., WOODS A. D. B. "Phonon Properties of Niobium, Molybdenum, and their Alloys", *Canadian Journal of Physics* **55** (1977) pp. 1601-1612.
- [21] SALVETTI M. "Hyperelastic Continuum Modeling of Cubic Crystals based on First-Principles Calculations". PhD Thesis (2010) Massachusetts Institute of Technology.
- [22] BOLEF D. I. "Elastic Constants of Single Crystals of the bcc Transition Elements V, Nb, and Ta" *Journal of Applied Physics* **32** (1961) 100-105.
- [23] NAGASAKO N., JAHNATEK M., HAFNER J. "Anomalies in the Response of V, Nb and Ta to Tensile and Shear Loading: Ab Initio Density Functional Theory Calculations". *Physical Review B* **81** (2010) 094108 (13pp).
- [24] SIMMONS G., WANG H. In "Single Crystal Elastic Constants and Calculated Aggregated Properties. A Handbook" (1971) MIT Press (2nd Edition), Cambridge, Massachusetts and London, England.
- [25] PERDEW J.P. in "Electronic Structure of Solids". Edited by P. Ziesche and H. Eschrig (1991) Berlin: Academic.
- [26] PERDEW J.P., BURKE K., ERNZERHOF M. "Generalized Gradient Approximation Made Simple". *Physical Review Letters* **77** (1996) pp. 3865-3868.
- [27] MCMILLAN W. L. "Transition Temperature of Strong-Coupled Superconductors". *Physical Review* **167** (1968) pp. 331-344.
- [28] ALLEN P. B., DYNES R. C. "Transition Temperature of Strong-Coupled Superconductors Reanalyzed", *Physical Review B* **12** (1975) pp. 905-922.
- [29] BENNEMANN K. H., GARLAND J. W. In "Superconductivity in d- and f-Bands Metals". Edited by D. H. Douglass (1971) American Institute of Physics, New York.

LANGUAGE DISCRIMINATION VIA A NEURAL NETWORK APPROACH

Angelo Mariano^{1*}

¹*ENEA, viale Japigia 188, I-70126 Bari, Italy*

ABSTRACT. We show here some of our computational activities based on complex systems. The model presented is involving the discrimination and ultrametric structure obtained from a large set of sentences in 21 Indo-European languages by using a neural network approach.

1 Model

Our main objective is to define a distance among a given set of languages and identify sub-groups of languages that are more similar. In our case study, the set is made up of 21 Indo-European languages. More details are available in Ref. [9]. The strategy consists in asking a feed-forward neural network with back-propagation [11] to distinguish them two by two. The error will be taken as a measure of the similarity between the two languages: a large error signifies closeness between the two languages, while a small error indicates a large separation. The neural network is fed with 20,000 sentences (10,000 per language), taken from the Leipzig Corpora Collection [10] and different in length. The first 40 characters are extracted from each sentence; spaces, accents, numbers and punctuation are removed and special (non ASCII) characters are replaced by their ASCII counterpart (e.g. French and Spanish “ç” is replaced by “c” and German “ß” by “ss”). These replacements make languages more similar and language discrimination more difficult, so that the task of the neural network is harder. Each character is encoded in a 26-dimensional vector [6, 2]. Other types of input encoding offer no guarantee on the correct association of the weights of the synapsis to different characters and the sensibleness of the ensuing language discrimination. The neural network is made up of three layers. The first layer contains 1040(= 26 × 40) input nodes, the central layer 500 nodes, the output layer 2 nodes. Each time, one language is discriminated against another language: the two output nodes give the probability of correctly interpreting the input. The scheme is depicted in Fig. 1.

The results are averaged according to a 5-fold cross-validation technique. Specifically, our validation set is made up of 4,000 sentences. The neural network makes an error when, if fed with language *A*, it mistakenly answers *B* (or *vice versa*). A training period, that minimizes an appropriate cost function, is repeated against the remaining 16,000 sentences, until the error against the validation set is steady. In this way, a set of 5 errors is obtained. The labels *A* and *B* are then interchanged and after a new training period, 5 additional errors are obtained. The error ϵ used in the following is the average over the afore-mentioned 10-fold run.

*Corresponding author. E-mail: angelo.mariano@enea.it.

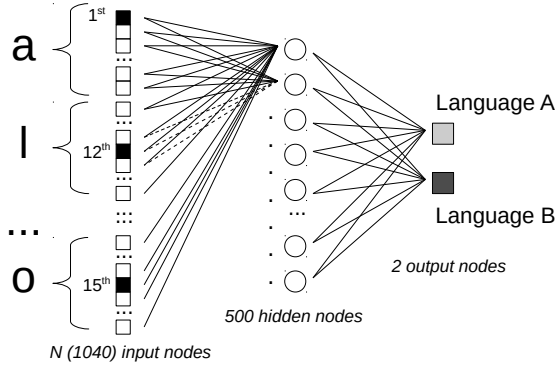


Figure 1: The discrimination scheme. A 40-character-long sentence is fed to the neural network, whose input, central and output layers consist of 1040(= 26 × 40), 500 and 2 nodes respectively. After a training period, during which 16,000 sentences in two languages are fed to the network, the two output nodes yield the probability that a given sentence is classified as belonging to one of the two languages. Spaces, accents and punctuation are removed, and the sentence is always cut at 40 characters, so that “Alice thought she might as well wait, as she had nothing else to do, and perhaps after all it might tell her something worth hearing.”, becomes “alicethoughtshemightaswellwaitasshehadno”.

2 Ultrametric structure

The afore-mentioned neural network works very efficiently, making language discrimination very effective. After the training period, the error is always small (typically a few percent, becoming at most 20% when the two languages are very similar).

We shall make use of the error ϵ to define a distance d between the two languages, according to the formula

$$d = \frac{1}{\epsilon} - 1 \in \mathbb{R}_+. \quad (1)$$

The above definition entails a certain degree of arbitrariness, as any monotonic function of $1/\epsilon$ would be equally suited. One advantage is that d takes values on the positive real half-line $\mathbb{R}_+ = [0, \infty)$. In order to classify languages and identify subgroups in the set, we need a linkage algorithm. Linkage algorithms yield a cluster structure that is displayed in the form of a tree or dendrogram [5]. We will adopt an agglomerative algorithm, by linking the clusters through an iterative process. The original data set \mathcal{S} is made up of $m = 21$ elements (points). At the first level (leaves of the dendrogram) the number of classes in the data set is $m = 21$. At the first iteration the two closest elements are clustered together, reducing the number of classes to $m - 1 = 20$ (if more than two elements are at the closest distance, we pick a random couple among them). At the second iteration one defines a new distance d' between the remaining elements of \mathcal{S} and the first cluster formed. The distances are then recalculated and the two closest objects are joined. At the following iterations one must define a new distance among points and clusters. After m steps, all the points are grouped together in one single cluster, corresponding to the whole data set. Different types of algorithms yield in this case similar results; anyway, the average linkage algorithm seems to perform slightly better. It is based on the following definition of “distance” between two clusters U and V

$$d(U, V) = \sum_{\substack{i \in U \\ j \in V}} \frac{d(i, j)}{|U| * |V|}, \quad (2)$$

where the summations run over the elements of the clusters and $|U|$ and $|V|$ represent the cardinality of cluster U and V . Consider that (2) is not a distance in the mathematical sense, but should rather

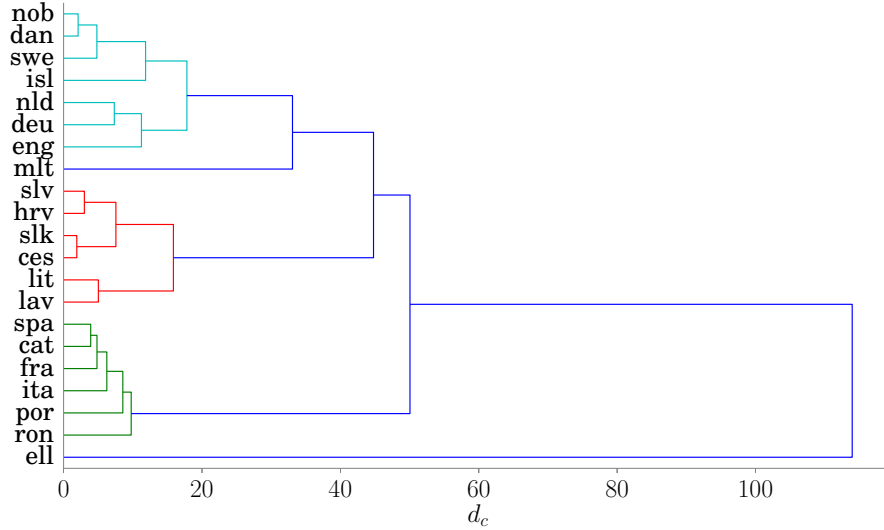


Figure 2: The language tree

be viewed as a “dissimilarity” index [1]. The cophenetic coefficient [12] is a measure of how faithfully a dendrogram preserves the pairwise distances between the points of the original data set. It enables one to judge how close the original metric is to an ultrametric. It is defined as a correlation coefficient between original distance d and cophenetic distance d_c on the dendrogram, defined as the distance at which two leaf nodes i, j are clustered together.

The cophenetic coefficient c is defined as

$$c = \frac{\sum_{i < j} (d(i, j) - \langle d \rangle)(d_c(i, j) - \langle d_c \rangle)}{\sqrt{\sum_{i < j} (d(i, j) - \langle d \rangle)^2 \sum_{i < j} (d_c(i, j) - \langle d_c \rangle)^2}}, \quad (3)$$

where $\langle d \rangle$ and $\langle d_c \rangle$ are the mean original distance and the mean cophenetic distance, respectively, and the sum is over all the nodes of the dendrogram. A value of c close to 1 signifies the presence of a good ultrametric structure. Figure 2 displays the dendrogram obtained and then deriving a cophenetic distance d_c via the average linkage procedure (2). Calculation of cophenetic coefficient (3) yields the value

$$c \simeq 0.82, \quad (4)$$

close to one, so that the “distances” obtained are close to an ultrametric.

In order to unearth a taxonomic classification of the languages in the set one has to cut the dendrogram at a given level (ultrametric or cophenetic distance) d_c . Such a level can be reasonably chosen by relying on a stability criterion of the clustered solution. We therefore search for a stable partition among the hierarchy yielded by the clustering algorithm, in correspondence to an approximately constant value of the cluster entropy S in a certain range of d_c [8]

$$S(d_c) = - \sum_{k=1}^{N_{d_c}} P_{d_c}(k) \ln P_{d_c}(k), \quad (5)$$

where $P_{d_c}(k)$ is the fraction of elements belonging to cluster k , N_{d_c} the number of clusters at level d_c in the dendrogram and $0 \leq S(d_c) \leq \ln 21 \simeq 3.04$. The entropy (5) is plotted in Fig. 3 as a function of

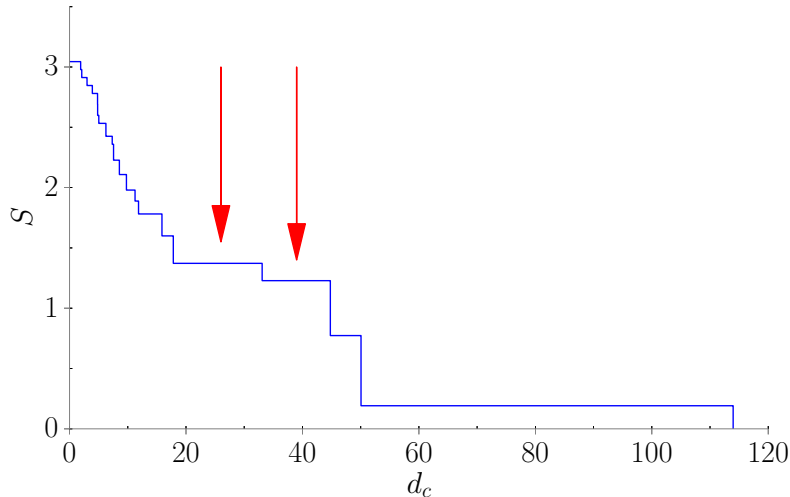


Figure 3: Cluster entropy across the language tree. The plateaus discussed in the text are indicated by red arrows.

d_c . The presence of two large adjacent plateaus is manifest. The first one is between $d_c = 17.82$ and $d_c = 33.08$. If one cuts the dendrogram here, one obtains three large clusters, made up of the Romance (or Latin), Germanic and Slavic languages, and two isolated languages, Greek and Maltese, the latter being a Semitic language (written in Latin script), descended from an Arabic dialect spoken in Sicily and Malta about one thousand years ago. English words make up 15-20% of the Maltese vocabulary. The second plateau is between $d_c = 33.08$ and $d_c = 44.79$. If one cuts the dendrogram here, one obtains three large clusters, made up of the Romance, Germanic (including Maltese) and Slavic languages, and one isolated language, Greek.

3 Implementation

The code is written in Python and SciPy [7] with the MPI4Py package for parallel execution [3] (*ab initio* computation) and it ran on CRESCO4 cluster. It makes use of Theano library [13], originally developed in the field of deep machine learning [4] and optimized for complex tasks.

The model implemented is a single-hidden-layer multi-layer perceptron (or artificial neural network ANN), mathematically represented as a function $f : \mathbb{R}^N \rightarrow \mathbb{R}^2$

$$f(x) = G(b^{(2)} + W^{(2)}(s(b^{(1)} + W^{(1)}x))), \quad (6)$$

where $b^{(1)}$ and $b^{(2)}$ are bias vectors, $W^{(1)}$ and $W^{(2)}$ weight matrices, and G and s activation functions. In our case the activation function s is tanh and G is a softmax function. The training process is a supervised learning with back-propagation [11] (learning rate $l_r = 0.01$) based on stochastic gradient descent on mini-batches of 20 instances, repeated for almost $E = 200$ epochs. The cost function is a negative log likelihood function with two regularization hyper-parameters $l_1 = 0.001$ and $l_2 = 0.0001$, related to the L_1 norm and squared L_2 norm of the weight matrices $W^{(1)}$ and $W^{(2)}$, that avoid an uncontrolled increase of the weights. At every epoch, for every mini-batch, the cost function is evaluated and the ANN parameters are corrected according to the gradient of the cost function, with the learning rate l_r as a multiplying factor. At the end of an epoch, the error between prediction and effective result is computed against the validation set: if it is smaller, it is recorded. Before the 100th epoch, the error

ϵ typically becomes steady and the results on the validation set are considered reliable. The entire process is repeated through a 5-fold cross-validation technique, also by interchanging languages A and B as depicted in Fig. 1.

Acknowledgments

This work is based on some results obtained in Ref. [9]. I thank Prof. G. Parisi and Prof. S. Pascazio for interesting suggestions and conversations.

References

- [1] Nicolas Basalto, Roberto Bellotti, Francesco De Carlo, Paolo Facchi, Ester Pantaleo, and Saverio Pascazio. Hausdorff clustering. *Phys. Rev. E*, 78:046112, Oct 2008.
- [2] Eniko B. Bilcu and Jaakko Astola. A hybrid neural network for language identification from text. In *2006 16th IEEE Signal Processing Society Workshop on Machine Learning for Signal Processing*, pages 253–258, 2006.
- [3] Lisandro D. Dalcin, Rodrigo R. Paz, Pablo A. Kler, and Alejandro Cosimo. Parallel distributed computing using python. *Advances in Water Resources*, 34(9):1124 – 1139, 2011. New Computational Methods and Software Tools.
- [4] Ian Goodfellow, Yoshua Bengio, and Aaron Courville. Deep learning. Book in preparation for MIT Press, 2016.
- [5] Anil K. Jain and Richard C. Dubes. *Algorithms for Clustering Data*. Prentice-Hall, Inc., Upper Saddle River, NJ, USA, 1988.
- [6] Kre Jean Jensen and Sren Riis. Self-organizing letter code-book for text-to-phoneme neural network model. In *in Proceedings of International Conference on Spoken Language Processing*, pages 318–321, 2000.
- [7] Eric Jones, Travis Oliphant, Pearu Peterson, et al. SciPy: Open source scientific tools for Python, 2001–. <http://www.scipy.org/> [Online; accessed 2016-08-26].
- [8] Kunihiko Kaneko. Chaotic but regular posi-nega switch among coded attractors by cluster-size variation. *Physical Review Letters*, 63(3):219, 1989.
- [9] Angelo Mariano, Giorgio Parisi, and Saverio Pascazio. Language discrimination and clustering via a neural network approach. *arXiv:1507.04116 [cond-mat.dis-nn]*, July 2015.
- [10] Uwe Quasthoff, Matthias Richter, and Christian Biemann. Corpus portal for search in monolingual corpora. In *Proceedings of the fifth international conference on language resources and evaluation*, volume 21, pages 1799–1802, 2006.
- [11] David E. Rumelhart, Geoffrey E. Hinton, and Ronald J. Williams. Learning representations by back-propagating errors. *Nature*, 323(6088):533–536, 1986.
- [12] Robert R. Sokal and F. James Rohlf. The comparison of dendrograms by objective methods. *Taxon*, 11(2):33–40, 1962.
- [13] Theano Development Team. Theano: A Python framework for fast computation of mathematical expressions. *arXiv:1605.02688 [cs.SC]*, May 2016.

WEB CRAWLING TOOL INTEGRATION IN ENEAGRID

Giuseppe Santomauro^{1*}, Giovanni Ponti^{1†},

Fiorenzo Ambrosino¹, Giovanni Bracco², Antonio Colavincenzo¹, Agostino Funel¹,
Guido Guarnieri¹, Silvio Migliori³,
Matteo De Rosa¹, Dante Giammattei¹

¹ENE A - C.R. Portici, DTE-ICT-HPC, P.le E. Fermi, 1 - 80055 Portici (NA), Italy

²ENE A - C.R. Frascati, DTE-ICT-HPC, Via E. Fermi, 45 - 00040 Frascati (Roma) - Italy

³ENE A - Sede Legale, DTE-ICT, Lungotevere Thaon di Revel, 76 - 00196 Roma - Italy

ABSTRACT. In this document we provide a brief overview on the development and the integration in ENEAGRID of some tools in order to download data from Web (Web Crawling), manage and display a large amount of data (Big Data), and extract from data significative information (Data Mining).

1 Introduction

All the most popular search engines, such as *Google*, *Bing* and *Yahoo*, need to periodically download the content of a wide web space in order to update their index and then provide the most recent results for the querying tasks. The activity of downloading a large amount of data from the Internet is commonly known as *Web Crawling*. With the aim to equip the Portici CRESCO/ENEAGRID infrastructure of some tools able to download data from the Web, manage/display a large amount of data and extract significative information from them we created the *Web Crawling Project*. This activity falls within the scope of the “Orio Carlini” Research Fellowship, funded by Consortium GARR, whose title is “*Analisi e sviluppo di nuove tecniche per l'estrazione di informazioni da grandi moli di dati provenienti dal Web*”. The paper is organized as follows: in Section 2 we provide a general survey of the Web Crawling tools; in Section 3 we describe the integration in ENEAGRID of *Web Crawling* Virtual Laboratory; and finally in Section 4 we report the results of some Web Crawling sessions performed on ENEAGRID.

2 Web Crawling Tools

Generally, a crawling technique analyzes systematically and automatically the content of a network in order to search for documents to download. The Web crawlers, namely the programs designed to crawl, are based on a list of URLs. They make a textual copy of the all visited pages and save them in an index. When a crawler parses an URL, all hyperlinks in the document are identified and then added to the list of URLs to visit. This process can be manually stopped or when a specified number of connections is reached. Many products to integrate in ENEAGRID are investigated. Among them, the tool *BUBiNG* [1], currently at 0.9.11 version, is chosen as main Web crawler to use. This software allows the simultaneous execution of multiple agents (e.g., *Java* instances that play the role of a crawler). Each agent can communicate with each other one by ensuring not repeated visits of the same pages and balancing the computational load. *BUBiNG* also allows to setup all configuration options inside a single file and many of its parameters can be modified at runtime. Finally, it saves the content downloaded from the Web in compressed *.warc.gz* files. Currently, *BUBiNG* is properly installed, configured and

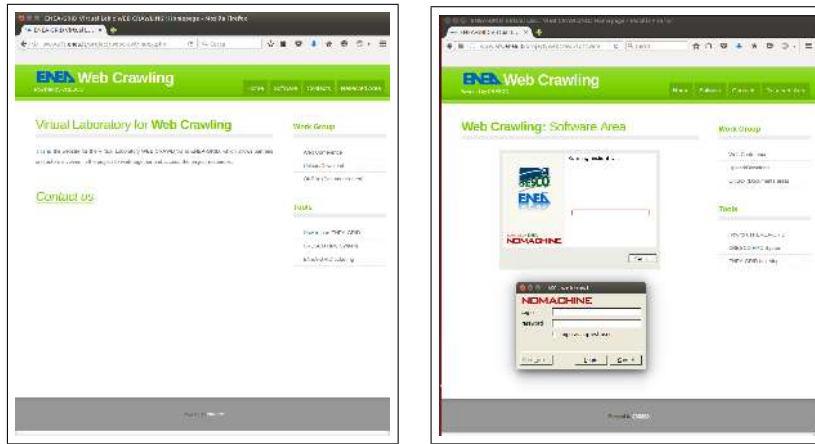
*Corresponding author. E-mail: giuseppe.santomauro@enea.it.

†Corresponding author. E-mail: giovanni.ponti@enea.it.

tested, with the aim of obtaining a good product from the point of view of efficiency, performance and reliability.

3 Integration in ENEAGRID

As hardware resources, a set of 9 machines (8 of them are used for computations, 1 as a front end) is dedicated to the Web Crawling activity. The servers are nodes of the cluster CRESCO2 belonging to the Portici Research Center and integrated in ENEAGRID. Suitable configurations, also from networking side, are carried out to appropriately confine the network traffic. According to the ENEAGRID guidelines, we integrate the web crawling softwares on the infrastructure. More specifically, the binary source of *BUBiNG* tool and all the relative dependencies are then properly installed, configured in the project area of the geographically distributed filesystem *AFS*. For data storing, as the web crawler quickly downloads a large amount of data, we decided to allocate a wide space on the high performance distributed parallel clustered filesystem *GPFS*. Finally, a set of bash scripts are coded to simplify the commands submitting from the software to the resources scheduler *LSF*.



(a) Homepage.

(b) Software area page.

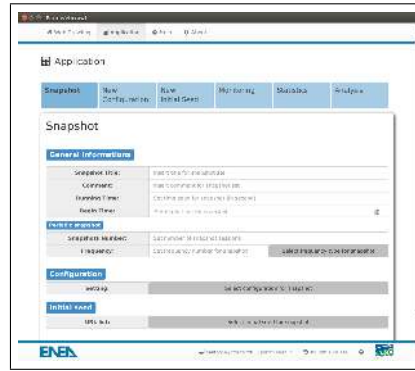
Figure 1: Web Crawling Virtual Lab site.

3.1 Virtual Laboratory

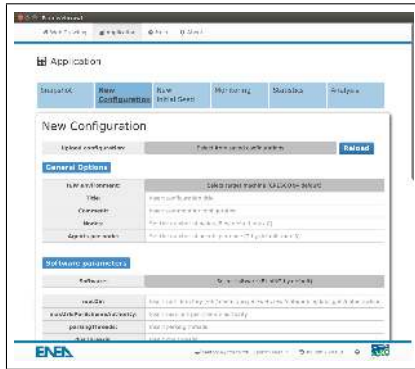
All the Web Crawling instruments are collected in a ENEAGRID Virtual Laboratory, named *Web Crawling*. The goal of the laboratory is to make available to a wide scientific community the crawling tools. In particular, like all the virtual labs developed on the infrastructure, we created a public Web site where users can authenticate and then access to an ad hoc graphical interface to intuitively use the installed softwares. The scientific community of ENEAGRID users, interested to use the Web Crawling tools, can browse at the address <http://www.afs.enea.it/project/webcrawl/index.php>. The site is composed of four main pages: a welcome page (Fig. 1a), a software area access page (Fig. 1b), a contacts page and a reserved documents area page. Once an user enters its ENEAGRID credentials at the software page of site (Fig. 1b), a graphical mask (i.e, a web application) starts on the frontend machine, and he can begin to use the Web Crawling tools. The authentication procedure is managed by an *NX* client installed locally on the user machine, while the interface is based on the *FARO 2.0* technology [2]. The web application is a customized version of *FARO 2.0*, developed over the *JavaFX* framework, that exploits *WebViews* for its interface implementation and its operational logics. Figure 2a shows the interface welcome page. By clicking on the *Application* button on the top bar, different tabs for different operations are displayed. On the first tab (*Snapshot*) Web Crawling sessions with



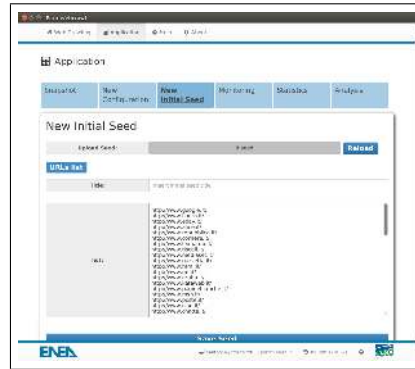
(a) Homepage.



(b) Snapshot tab.



(c) New configuration tab.



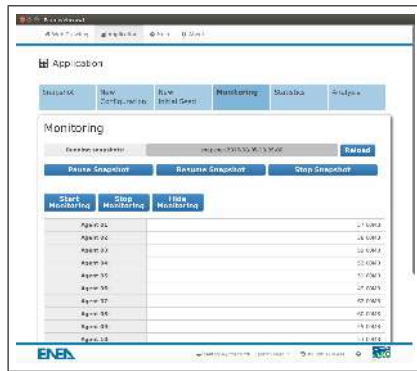
(d) New initial seed tab.

Figure 2: Graphical User Interface (submitting and setting).

the opportunity to perform single or periodic snapshots can be submitted (Fig. 2b). The user can specify a session name, the number of snapshots, the running time for each of them, the starting date, the execution frequency for periodic snapshots, select the setting of the parameters to be used and the URLs initial seed. In the second tab (*New Configuration*) the user can create a new setting for BUBiNG software (Fig. 2c). By default, each software parameter is set up with the corresponding value of best configuration (16 agents). The user can also load an old setting, modify it and save it as new configuration or overwrite over the old one. In the third tab (*New Initial Seed*) a new list of URLs to start the crawling can be created (Fig. 2d). On the fourth tab (*Monitoring*), the generated traffic on the network by a running snapshot, selectable from the list of those that are in run, can be monitored (Fig. 3a). This tab is useful to know in real time the amount of downloaded data, for single agent or total, and detect eventual performance anomalies. On the fifth tab (*Statistics*), user can view some statistics on the performed snapshots, such as: the amount of data downloaded, the number of the visited pages and the downloading speed (Fig. 3b). Finally, on the last tab (*Analysis*) the analysis of data for a single snapshot, selectable among the list of those that are terminated, can be started (Fig. 3c). From this tab, user can launch a session of *Solr* software (based on *Lucene*) which has a graphical interface, viewable via browser (Fig. 3d).

4 Tests and experimental results

Once *BUBiNG* is installed, a set of snapshots having the same running time (15min) but with various choices of the software parameters has been submitted. The aim of this parameter tuning was to find



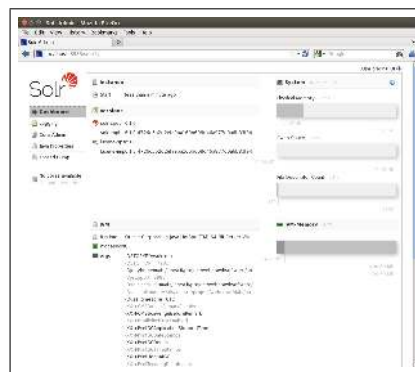
(a) Monitoring tab.



(b) Statistics tab.



(c) Analysis tab.



(d) Firefox window for Solr.

Figure 3: Graphical User Interface (monitoring, statistics and analysis).

out the best configuration for the crawler. At the end of this operation, after more than 40 performed sessions, we observed that the best setup for the software, computed as the amount of data downloaded per time unit ($\sim 1\text{Gbps}$), has been obtained by using 8 nodes and 16 agents (2 agents per node). The best measured speed had the same order of bandwidth of the network system used for the Web crawling activity. Indeed, the bottleneck for the Portici Research Centre network was the firewall that limits the access to 1Gbps. In order to stress BUBiNG crawler we decided to perform some large Web crawling sessions. We have taken into account the following aspects: we selected some periods with low network traffic in Portici ENEA Research Center; we informed the network managers to prevent conflicts with other activities and/or fully saturate the available bandwidth; we used all the available hardware resources (8 nodes) and the optimal setting of the software in order to maximize the download speed; and we monitored the snapshots during their running time. Two kinds of snapshot sessions have

Date [dd/mm/yyyy]	Running time [hour]	Agents [#]	Data amount [TB]	Resources amount [#Pages]	Data speed [Mb/s]	Resources speed [#Pages/s]
10/12/2015	8	16	2,94	66.806.790	850	2305
28/12/2015	10	16	3,23	71.667.304	740	1959
05/01/2016	10	8	3,27	75.587.287	756	2048

Table 1: Long time sessions performance.

been considered: in the first ones the execution time was very long in order to evaluate a very slow

performance decay and the robustness of the software; in the second ones we tested the crawler by submitting some scheduled periodic snapshots for ensuring the uniform behaviour along the time, i.e. the software reliability. The harvested material, downloaded from the Internet by tests, was also useful to create a first database on which apply the data mining tools. For all the tests we noted that no interference with the normal network activity is reported. In Table 1 we report the statistics extracted from the log files about the first type of sessions. By observing the table we can remark that: as absolute value, the first test (by exploiting 16 agents) reached the best performance (850Mbps) but, if the running time was equal (10h), the session using 8 agents (756Mbps) was slightly better than that one with 16 agents (740Mbps). In Figure 4 we report the plot of the downloading data speed versus

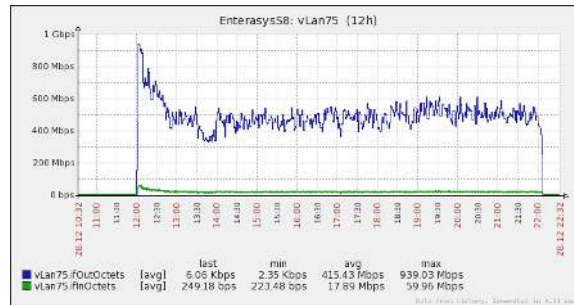


Figure 4: Downloading speed for the test on 28/12/2015.

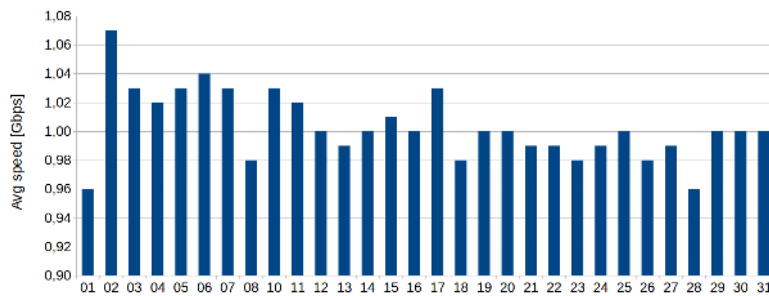


Figure 5: Downloading avg speed for daily periodic snapshots during August 2016.

the time for the second long run test. We should point out that the real speed value was a little greater than the reported one on the graphic because the Web data are compressed before downloading. As we expected, during the crawling, the downloading speed showed an initial peak (up to the limit of 1Gbps) and then a damping around a slight lower constant value (700-800Mbps). This last remark confirmed the software high performance. For the second kind of tests, we considered a long year period when the network conditions were constant and with low activity. It is for this reason that we submitted a set of periodic snapshots during August 2016. We executed 31 daily Web crawling sessions, each of them kept alive for one hour (from 21:00 to 22:00) and by using the best setup of the software. The successfully done tests and the high performance (the downloaded data speeds oscillated between 0,96 and 1,07Gbps as shown in Fig. 5) demonstrated the good reliability of the software.

References

- [1] Paolo Boldi, Andrea Marino, Massimo Santini, and Sebastiano Vigna. BUBiNG: Massive Crawling for the Masses. *CoRR*, abs/1601.06919, 2016.
- [2] Angelo Mariano et al. Fast Access to Remote Objects 2.0 A renewed gateway to ENEAGRID distributed computing resources. *PeerJ Preprints*, 4:e2537v1, 2016.

FAST SWITCHING ALCHEMICAL SIMULATIONS: A NON EQUILIBRIUM APPROACH FOR DRUG DISCOVERY PROJECTS ON PARALLEL PLATFORMS

Piero Procacci*

Dipartimento di Chimica, Università di Firenze, Via della Lastruccia 3, I-50019 Sesto Fiorentino, Italy

ABSTRACT. We present a novel all-atoms molecular dynamics approach for computing ligand-receptor binding free energies in drug discovery projects. The technique is a non equilibrium variant of the alchemical method[1] and effectively combines generalized ensemble (GE) and fast switching double annihilation (FS-DAM) nonequilibrium (NE) technologies. The method is implemented in the ORAC program[2, 3]. The code was equipped with a hybrid Open Multi-Processing (OpenMP), Message Passing Interface (MPI) multilevel parallelism specifically tailored for non uniform memory access (NUMA) multi-core architectures. A demonstrative application of the FS-DAM approach on HPC platforms is presented.

1 Introduction

In the last decade, the exponential growth of the clock rate has finally ended and performance improvements in parallel applications are now coming from the increase in the number of cores on a processor unit (compute node).[4, 5] Cores per chipset doubles every 18 months instead of clock and 64-512 threads per node will become visible soon.[4, 6] The advent of non uniform memory access (NUMA) multi-core architectures substantiates therefore the need for an efficient strategical approach in multi-level parallelization on High Performance Computing (HPC) facilities putting us at a fundamental turning point in the development of software for the Molecular Dynamics (MD) simulation of complex biomolecular systems.

In modern MD codes[7, 8, 9, 10] running on HPC platforms, a huge effort has been invested in the parallelization of the strong scaling non bonded force computations that is handled in a distributed memory environment at the MPI level via the so-called neutral territory domain decomposition (NT-DD) approach.[11] The MPI-only DD parallel algorithm guarantees, at constant processor workload, an equal level of domain-domain communications independently of the size of the system. Like in any strong scaling computation, the scaling behavior of the DD scheme is limited by the mean number of particles assigned to a domain/processor.[12] When the the latter decreases, the mean workload per processor also decreases and the communication overhead fatally increases. In typically sized drug-receptor systems (from 10000 to 30000 atoms), the saturation level of the parallel performances of DD based MD codes are reached within few hundreds or even few tens of cores, depending on network speed, *de facto* limiting the productivity of the simulations to at most few hundreds of ns per day.

On the other hand, many important biophysical phenomena, such as conformational transitions in proteins or binding of a ligand to a receptor, are *rare events*, occurring in the time scale of the microseconds

*Corresponding author. E-mail: procacci@unifi.it.

or even milliseconds, whereby the need for smarter and inherently (weak scaling) parallel methods of configurational sampling such as Hamiltonian Replica Exchange (H-REM), Serial Generalized Ensemble (SGE) or multi-trajectories non equilibrium (NE) techniques. The present release of the hybrid OpenMP/MPI ORAC code[2, 3] for molecular dynamics of biomolecular systems is designed to optimally exploit the recent trend of NUMA HPC systems. The code enforces a weak scaling parallelism for Generalized Ensemble (GE) (H-REM, SGE) and NE technologies on the MPI level and an OpenMP layer to the parallelization of the bonded and non bonded forces within a single shared memory access compute node. As such, ORAC provides an effective and flexible tool for reliably determining the binding free energies in drug-receptor systems using the non equilibrium alchemical method in a hybrid parallel environment. In the so-called fast switching double annihilation method (FS-DAM), the efficiency of the GE approach can be effectively exploited to generate and accurate sampling of the fully coupled states (the bound ligand and the ligand in bulk). From these initial states, a swarm of many independent NE processes are launched, where an externally driven alchemical parameter, regulating the interaction of the ligand with the environment, is varied continuously and rapidly during the multi-step integration of the equations of motion according to a prescribed common time schedule.[13, 14, 15, 16] The drug-receptor absolute binding free energy can be recovered from the annihilation work histogram of the bound and unbound states by applying an unbiased unidirectional free energy estimate. The latter is computed on the assumption that any observed work distribution is the result of a linear combination of normal distributions, whose components are identical in either direction of the non-equilibrium process, with weights regulated by the Crooks theorem.[17, 15, 16] We refer to Refs. [15, 16] for a detailed description of the FS-DAM algorithms in drug design. In this contribution, we present a demonstrative example of an FS-DAM application on the CRESCO HPC platform to a live drug discovery project using the ORAC6.0. The code, along with documentation, testing and ancillary tools, is distributed under the provisions of the General Public License (GPL) and can be freely downloaded at the Internet address www.chim.unifi.it/orac.

2 Code performances for the OpenMP layer on a CRESCO5 compute node

The ORAC code, mostly written in FORTRAN, is highly portable and it compiles successfully with the most common compilers (Intel `ifort`, IBM `xlf90`, PGI `pgfortran` and GNU `gfortran`) on many unix platforms, from laptop computers to HPC facilities including BlueGeneQ IBM architectures. As outlined in the introduction, ORAC implements a weak scaling parallel algorithm via MPI calls in H-REM/SGE generalized ensemble simulations or driven simulations technologies based on NE theorems[18, 19] and a strong scaling parallel approach on the OpenMP layer based on particle decomposition for the computation of the forces. The code does not require any library to run except for the standard mathematical libraries. ORAC can use the efficient FFTW suite[20] for Fourier Transform in the evaluation of the Particle Mesh Ewald (PME) contribution to reciprocal lattice forces, but has its own built-in parallel FFT libraries. The nature of the executable (serial, MPI only and MPI/OpenMP with or without FFTW libraries) is controlled by the specification in the options of the `configure` script provided in the distribution. Parallel execution can therefore be done on either MPI or OpenMP level or on the two combined levels generating the appropriate target executable.

In the Figure 1 (left) we show the OpenMP speedups obtained on a single 16-cores compute node of the ENEA-CRESCO5 cluster, for a system including a penta-alanine mini-protein, solvated in 9300 TIP3P[1] water molecules for a total of 28000 atoms in a cubic MD simulation box with a side-length of $\simeq 64$ Å. The size of such benchmark system, is that typical for alchemically driven TACE-ligands FS-DAM simulations (*vide infra*). The solvated mini-protein was modeled standardly using the AMBER all atom amber force field[22], a direct lattice long range cutoff of 10 Å, constant pressure simulation with isotropic stress tensor,[23] and temperature control via a Nosé Hoover thermostat.[24] The equations of

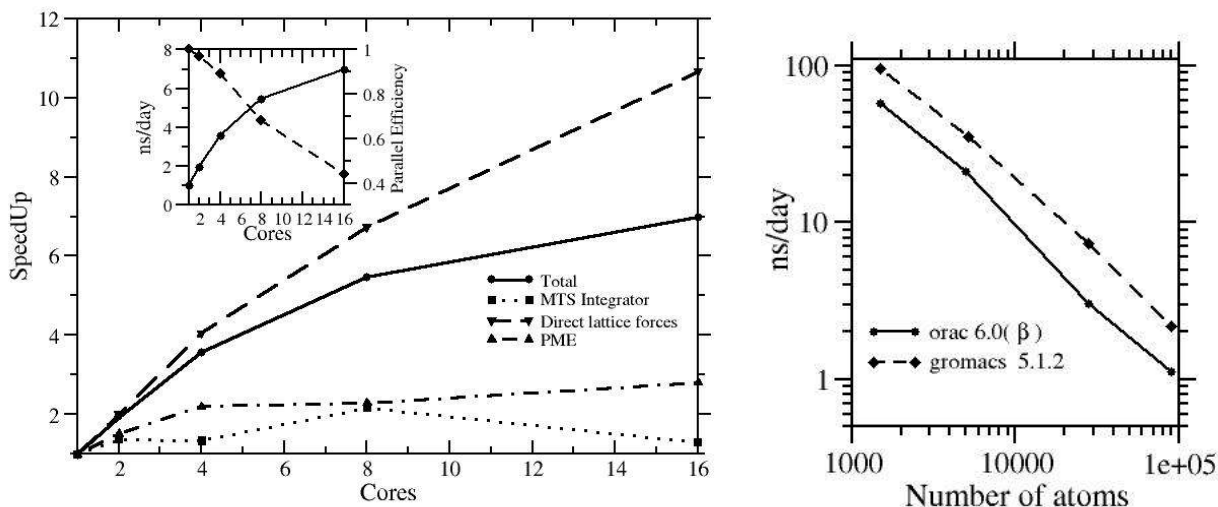


Figure 1: Left:Speedup measurements on the ENEA-CRESCO5[21] compute node (16-cores Intel(R) Xeon(R) CPU E5-2630 v3 2.40GHz) for a 28000 atoms systems (see text for details). Right: ORCA6.0 and gromacs5.1.2 performances for systems of various sizes on 8 cores on the CRESCO5 compute node (CPU E5-2630 v3).

motion were integrated using an efficient multiple time-step scheme specifically tuned for bio-molecular systems in the NPT ensemble.[23]. As the Intel `ifort` compiler generates optimized OpenMP code for the Intel X₆₄ architectures, tests were run on a 16-cores genuine Intel CPU. The latter is the compute node of the CRESCO5 ENEA-grid facility and is made up of 2 sockets each mounting an 8-cores Intel(R) Xeon(R) CPU E5-2630 v3 with clock-rate of 2.40GHz and 64 GB/RAM. With eight processors (one socket), the overall parallel efficiency of the ORAC code is at about 70% with a nearly sixfold speedup factor. Performances are only marginally better when using all 16 cores on the node, with speed up factor at about 7 and with parallel efficiency dropping below 50%. Speedup factors are, however, disparate for the various type of calculations involved in the MD production. So, for example, whereas the scaling of the computation of the direct lattice non bonded forces is indeed satisfactory, with a parallel efficiency hitting 70% with 16 cores, the scaling of the out of place FFT using the parallel FFTW library is rather poor and in line with the recently reported benchmarks.[20] The computation labeled “MTS integrator” in Figure 1 includes constraints enforcing, fast bonded force calculations and asynchronous MTS velocity/coordinates advancement. All these combined tasks yield an overall contribution representing just 3% of the total MD workload for a serial job. However, due to the fine granularity, the MTS integration computation impacts on the overall parallel efficiency when increasing the number of processors. As stated previously, efficiency loss in a ORAC MPI/OpenMP job are exclusively attributable to the OpenMP strong scaling level, as the weak scaling H-REM/SGE or FS-DAM algorithms are implemented on the MPI layer with little of no communication overhead. Therefore, for a given amount of available core-hours, the assignment of too many cores on the OpenMP layer, while producing only moderate increase in the simulation speed, could limit the sampling efficiency in GE or FS-DAM simulations by reducing the number available MPI instances (each representing a GE-replica or a NE trajectory). On the overall, OpenMP speedups are satisfactory and efficiency loss is acceptable when running on a maximum of eight shared memory cores. In Figure 1(right), we compare the performances (measured in ns/day of simulation) of the OpenMP ORAC6.0 β code to those obtained with the latest release of the popular GROMACS program. The latter MD code is admirably efficient due to algorithmic and processor-specific professional optimization, typically running 3-10 times faster

than many simulation programs.[8] Reported tests were done on 8-cores socket of the CRESCO5 CPU using solvated penta-alanine samples of various sizes. ORAC and GROMACS jobs were run using identical set up (constant pressure and temperature, bond constraints on X-H bonds, PME grid spacing of 1 Å, 10 Å cutoff). The log-log plot of Figure 1(c) shows that the performances of the two codes on a single 8-cores socket are comparable. For the largest system (90000 atoms), GROMACS runs at a speed of 2.2 ns/day compared to the 1.3 ns/day of ORAC6.0 β . The efficiency gap between the two codes gets narrower with decreasing system size. For the smallest system (1500 atoms), GROMACS and ORAC produce about 95 and 60 ns of simulation in a day, respectively.

3 Dissociation free energy of TACE ligands via hybrid FS-DAM simulations on HPC platforms

In this section we provide a practical demonstration on how ORAC can be used to efficiently evaluate the binding free energy in drug-receptor systems on a HPC platform. To this end, we present some preliminary results obtained on the ENEA-CRESCO3 and Fermi BlueGeneQ HPC facilities using the recently developed FS-DAM technology for drug design on the Tumor necrosis factor converting enzyme (TACE)[25, 26, 27] in complex with the IK682 the tight binding inhibitor.[28] TACE is the membrane-anchored Zinc-protease that releases, from its membrane-bound precursor, the soluble form of the cytokine Tumor necrosis factor TNFa. The latter is a cell signaling protein involved in systemic inflammation and is one of the cytokines that make up the acute phase reaction. When produced in excess, TNFa is known to play a pivotal role in diseases provoking severe disabilities such a rheumatoid arthritis, septic shock, Chron disease and Multiple Sclerosis. We should stress here that the results on the TACE-IK682 complex are presented here for demonstrative purposes. A thorough study on TACE inhibitors using FS-DAM will be the object of a forthcoming paper.

In Figure 2 we show a cartoon representation of the TACE-IK682 tight binding complex. The Zinc atom is the green sphere at the entrance of the binding site, bi-coordinated by the IK682 hydroxamate Zinc binding group (ZBG). The methylquinolin-methoxy-phenyl moiety of the inhibitor is deeply wedged in the hydrophobic environment of the so-called TACE “primed” pocket,[29] shown as surface representation. The TACE-IK682 presents various methodological challenges for the binding free energy determination via alchemical transformations. The TACE protein contains a doubly charged metal ion, interacting directly with the hydroxamate moiety of the ligand. Thus, the annihilation free energy of the ligand crucially depends on the modeling of the Zinc-hydroxamate electrostatic interactions. As a matter of fact, the Zn-ZBG mean electrostatic energy can be estimated to be[28] of the order of 300 kcal mol⁻¹. Hence, an error of few percent on this value may easily be transferred to the annihilation free energy of the binding ZBG, possibly producing discrepancies of several kcal mol⁻¹ in the computed dissociation free energy.

The starting configuration of the bound state was obtained from the X-ray co-crystal structure of the TACE-IK682 complex (pdb code 2fv5). Hydrogen atoms were automatically added by the code and the resulting all atoms experimental structure underwent a preliminary conjugate gradient minimization to adjust bond lengths and bending angles to the AMBER99SB-ILDN force field[31] corresponding equilibrium distances and angles. The complex was then arranged in an orthorhombic box in such a way that the shortest distance between any protein atom and the box walls was larger than 10 Å. The box was filled with TIP3P water at the density of 1g/cm⁻³, discarding the solvent molecules that were found to overlap with the complex. The final simulation system consisted of a TACE-IK682 complex made of 4089 atoms, solvated in 6335 TIP3P water molecules for a total of 23094 atoms. On a local cluster, a preliminary equilibration in the NPT ensemble was carried on for 100 ps obtaining an equilibrated volume of about 225 \pm 1 nm³. The starting configurations of the bound state for the subsequent FS-DAM annihilation were collected at regular time interval of 9 ps from a 5 ns 24 replicas H-REM simulation in the NPT ensemble with torsional tempering of the ligand and of the binding region. See Refs. [3, 16]

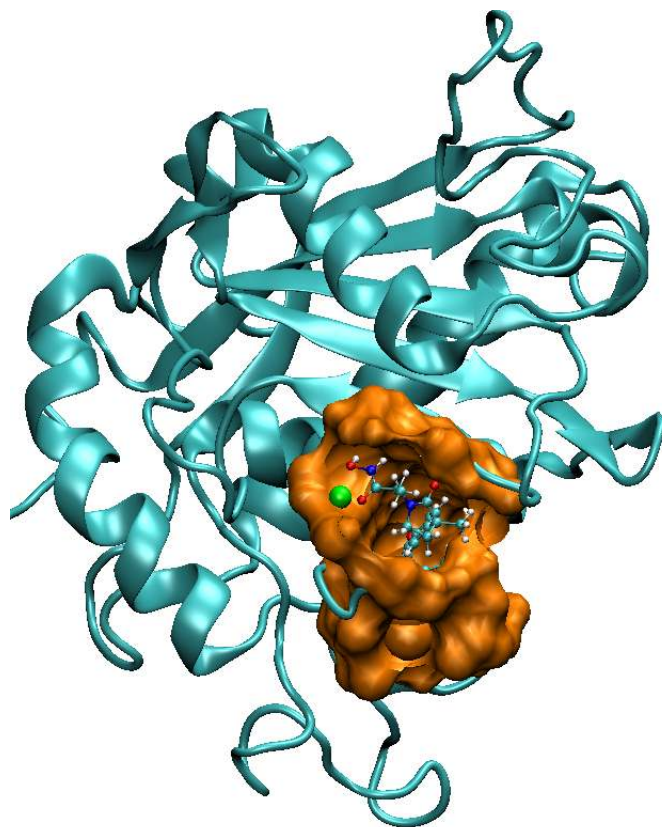


Figure 2: Tumor necrosis factor α converting enzyme in complex with the IK682 tight binding inhibitor. The model structure was built from the experimental structure[28] using the VMD software[30].

for further details on the H-REM torsional scaling scheme. The computation was done on 192 cores of the CRESCO3 cluster using a mixed OpenMP/MPI ORAC6.0 executable with eight OpenMP threads per MPI instance in less than three wall clock days. In order to collect the starting configurations of the unbound ligand, a 5 ns NPT H-REM simulation of torsionally tempered IK682 in bulk water using a cubic MD box of 30 Å side-length was performed in few wall-clock hours on 64 nodes of CRESCO3 using again an hybrid executable with 16 H-REM replicas and 6 OpenMP thread per MPI instance. Once collected, the final 512 starting configurations of the bound and unbound states were transferred to the Fermi/CINECA system. Fermi is made up of about 10,000 compute nodes, each featuring an IBM PowerA2 chip with 16 cores working at a frequency of 1.6 GHz, 16 GB of RAM. Two parallel OpenMP/MPI jobs on 2048 cores were finally submitted, producing the 512 FS-DAM annihilation 0.3 ns trajectories (each engaging 4 OpenMP threads) of the bound (23094 atoms) and unbound (2969 atoms) states, for a total combined 0.3 μ s of simulation. Both jobs ended in a single wall clock day.

In Figure 3, we show the time record of the alchemical work in a subset of the FS-DAM annihilation trajectories of the IK682 ligand in the bound state and in bulk solvent along with the corresponding distribution of the final alchemical work. The nature of the work distribution was checked by computing higher moments of the distributions (skewness and kurtosis) and by using the standard Kolmogorov test as described in Refs. [14]. Both work distributions turn out be the superposition of more than one components. In particular, the work distribution referring to the bound state exhibits a significant left skewness, while that relative to the annihilation of the ligand in bulk showed a large kurtosis. By repre-

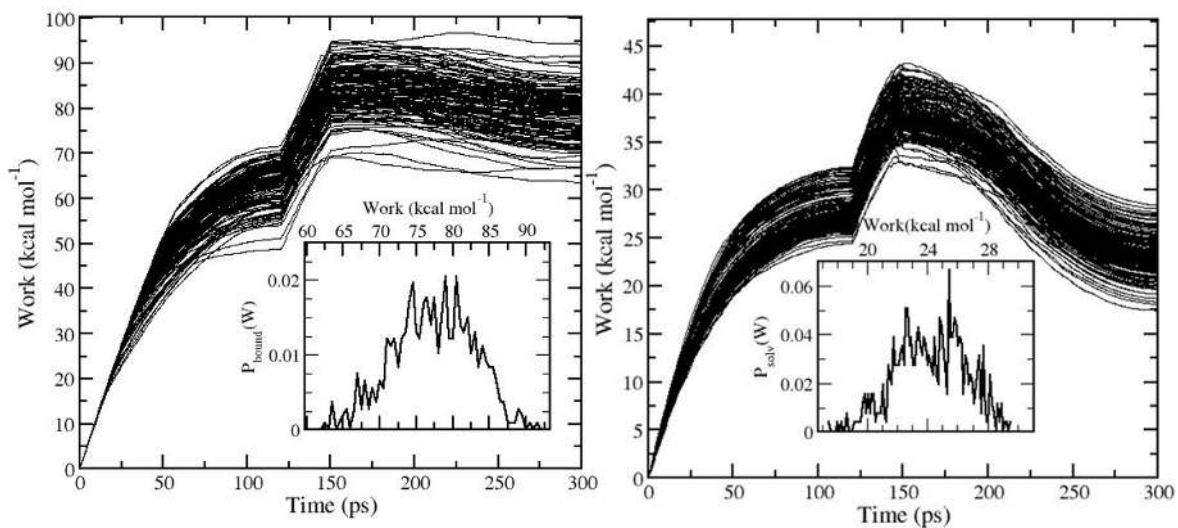


Figure 3: Time record of the annihilation work for a subset of the 512 FS-DAM trajectories of the bound state (left) and for the unbound state (right) for the IK682-TACE ligand-receptor pair. In the inset, the relative work distribution is reported.

senting the overall FS-DAM work distributions with an appropriate combination of normal components, the bound and unbound annihilation free energies (ΔG_b , ΔG_s , respectively) can be straightforwardly computed as described in Ref. [17], finding $\Delta G_b = 43.3 \pm 0.9$ kcal mol⁻¹ and $\Delta G_s = 21.6 \pm 0.3$ kcal mol⁻¹. The errors on these values were computed by block-bootstrapping 20 random subsets containing 128 work samples. The dissociation free energy is given by the difference between these two values plus a standard state correction given by $k_B T \ln \frac{V_{\text{site}}}{V_0}$, where V_{site} and V_0 are the binding site and standard state volumes. If we assume[27] that substrate/ligand binding occurs via the Zinc(II) cation, V_{site} can be taken as the influence volume of the Zinc(II) alone. The latter volume was computed by means of a Voronoi polyhedra analysis[32] on the starting configurations of the complex, finding $V_{\text{site}} = 4.9 \pm 0.7$ Å³ kcal mol⁻¹ and hence yielding a standard state correction of -3.5 ± 0.7 Å³ kcal mol⁻¹. Based on these results the standard dissociation free energy of the TACE-IK682 complex can be estimated as $\Delta G_0 = 18.2 \pm 1.4$ kcal mol⁻¹.

Experimental measurements of the IK682 binding affinity *vs* TACE are very difficult due to the extreme strength of the binding. In any case, IK682 was found to exhibit picomolar activity[28] with an apparent K_i of the order 0.02 nM, yielding a standard dissociation free energy of $\simeq 15$ kcal mol⁻¹ at pH=7.3. As previously stated, the TACE-IK682 is indeed challenging from a computational standpoint with the binding free energy crucially depending on many details (pH modeling, force fields, work distribution resolution). Nonetheless, in spite of the preliminary nature of this demonstrative Open-MP/MPI ORAC application, FS-DAM was able to correctly predict IK682 as a tight binding TACE inhibitor, with a semi-quantitative agreement between computed ($\Delta G_0^{(\text{FS-DAM})} = 18.2 \pm 1.4$ kcal mol⁻¹) and experimental ($\Delta G_0^{(\text{Exp.})} \simeq 15.0$ kcal mol⁻¹) standard dissociation free energies.

4 Conclusions and perspectives

In this paper we have presented an OpenMP/MPI implementation of the ORAC code[2, 3] for multi-core HPC platforms. The hybrid parallelization is designed in such a way that the distributed memory MPI level is reserved for thermodynamic parallelism only (H-REM, GE or FS-DAM low communication computations) while the strong scaling force decomposition algorithm is implemented in the OpenMP layer within the intra-node multi-cores shared memory environment. Such design is specifically tuned so as to maximize the sampling efficiency in complex heterogeneous systems that are characterized by a manifold of competing free energy attractors. Hence the need for an effective exploitation, in MD codes of biological system, of the so-called non Boltzmann methodologies that artificially enhance the probability of rare fluctuations on auxiliary thermodynamic states by rigorously re-weighting the statistics onto the target thermodynamic state. In some sense, H-REM and GE methodologies, as well as FS-DAM techniques are all aimed at expanding the statistics (i.e. the number of statistically *independent* simulated proteins) rather than the time scale of the system. These latter techniques are especially advantageous in a massively parallel environment where one can efficiently exploit the limited communication overhead that is needed for their implementation, easily producing, in a single wall clock day, an overall simulation time in the order of the microseconds. The OpenMP/MPI ORAC MD code is based on this simulation paradigm and is perfectly tailored for the current architectural trends in super-computing, limiting the strong scaling force computation to the intra-node shared memory environment with a moderate subtraction of resources to be assigned to the thermodynamic parallelism for enhanced sampling. In the Table below, based on tests done on the the 8-cores E5-2670 Intel CPU, we report the projected productivity on the full dedicated CRESCO4 cluster (4864 cores) in terms of processed ligand per day for a typical drug discovery project such as the TACE system. For each ligand-receptor pair, a 5 ns 16 H-REM simulation is assumed for the generation of the initial states, followed by the production of 256 0.3 ns FS-DAM trajectories for the computation of the work histograms. The gain in

OpenMP speed (ns/day)	$N_{\text{MPI}}/\text{socket}$	Ligands/day (overall)
1.9	4	16
3.0	2	20
4.9	1	25

Table 1: ORAC6.0 β predicted throughput for a drug discovery project on the dedicated CRESCO4 cluster (4864 cores) using FS-DAM. Productivity is measured in the number of processed ligand-receptor pairs per wall-clock day based on full cluster occupancy

productivity as the number of MPI instance per socket increases, reflects the corresponding OpenMP efficiency loss as the the number of threads per MPI instance increases. A typical 100 ligand-receptor pairs drug discovery project could hence be completed in 4 wall clock days on the CRESCO4 cluster.

References

- [1] W.L. Jorgensen and C. Ravimohan. Monte carlo simulation of differences in free energies of hydration. *J. Chem. Phys.*, 83:3050–3054, 1985.
- [2] P. Procacci, E. Paci, T. Darden, and M. Marchi. Orac: A molecular dynamics program to simulate complex molecular systems with realistic electrostatic interactions. *J. Comput. Chem.*, 18:1848–1862, 1997.
- [3] S. Marsili, G. F. Signorini, R. Chelli, M. Marchi, and P. Procacci. Orac: A molecular dynamics simulation program to explore free energy surfaces in biomolecular systems at the atomistic level. *J. Comput. Chem.*, 31:1106–1116, 2010.

- [4] Herb Sutter. The free lunch is over: A fundamental turn toward concurrency in software. *Dr. Dobbs's Journal (DDJ)*, 3:30, 2005.
- [5] Christian Märtin. Multicore processors: Challenges, opportunities, emerging trends,. In *Proceedings Embedded World Conference 2014, 25-27 February, 2014, Nuremberg, Germany, Design & Elektronik*, pages 25–27, 25-27 February 2014.
- [6] Giovanni Erbacci. Trends in HPC Architectures and Parallel Programming, PRACE Winter school 2012: http://www.training.prace-ri.eu/uploads/tx_pracetmo/ParallelArchitectures-Erbacci.pdf (accessed 22 January 2016).
- [7] Berk Hess, Carsten Kutzner, David van der Spoel, and Erik Lindahl. Gromacs 4: algorithms for highly efficient, load-balanced, and scalable molecular simulation. *J. Chem. Theory Comput.*, 4(3):435–447, 2008.
- [8] Mark James Abraham, Teemu Murtola, Roland Schulz, Szilrd Pll, Jeremy C. Smith, Berk Hess, and Erik Lindahl. Gromacs: High performance molecular simulations through multi-level parallelism from laptops to supercomputers. *SoftwareX*, 1-2:19–25, 2015.
- [9] J. C. Phillips, R. Braun, W. Wang, J. Gumbart, E. Tajkhorshid, E. Villa, C. Chipot, L. Skeel, and K. Schulten. Scalable molecular dynamics with namd. *J. Comput. Chem.*, 26:1781–1802, 2005.
- [10] Steve Plimpton. Fast parallel algorithms for short-range molecular dynamics. *J. Comput. Phys.*, 117(1):1 – 19, 1995.
- [11] David E. Shaw. A fast, scalable method for the parallel evaluation of distance-limited pairwise particle interactions. *J. Comput. Chem.*, 26(13):1318–1328, 2005.
- [12] Kevin J Bowers, Ron O Dror, and David E Shaw. Overview of neutral territory methods for the parallel evaluation of pairwise particle interactions. *Journal of Physics: Conference Series*, 16(1):300, 2005.
- [13] Piero Procacci and Chiara Cardelli. Fast switching alchemical transformations in molecular dynamics simulations. *J. Chem. Theory Comput.*, 10:2813–2823, 2014.
- [14] Robert B. Sandberg, Martina Banchelli, Carlo Guardiani, Stefano Menichetti, Gabriella Caminati, and Piero Procacci. Efficient nonequilibrium method for binding free energy calculations in molecular dynamics simulations. *J. Chem. Theory Comput.*, 11(2):423–435, 2015.
- [15] Piero Procacci. I. dissociation free energies of drug-receptor systems via non-equilibrium alchemical simulations: a theoretical framework. *Phys. Chem. Chem. Phys.*, 18:14991–15004, 2016.
- [16] Francesca Nerattini, Riccardo Chelli, and Piero Procacci. Ii. dissociation free energies in drug-receptor systems via nonequilibrium alchemical simulations: application to the fk506-related immunophilin ligands. *Phys. Chem. Chem. Phys.*, 18:15005–15018, 2016.
- [17] Piero Procacci. Unbiased free energy estimates in fast nonequilibrium transformations using gaussian mixtures. *J. Chem. Phys.*, 142(15):154117, 2015.
- [18] G. E. Crooks. Nonequilibrium measurements of free energy differences for microscopically reversible markovian systems. *J. Stat. Phys.*, 90:1481–1487, 1998.
- [19] C. Jarzynski. Nonequilibrium equality for free energy differences. *Phys. Rev. Lett.*, 78:2690–2693, 1997.
- [20] Matteo Frigo and Steven G. Johnson. The design and implementation of FFTW3. *Proceedings of the IEEE*, 93(2):216–231, 2005. Special issue on “Program Generation, Optimization, and Platform Adaptation”.

- [21] G. Ponti, F. Palombi, D. Abate, F. Ambrosino, G. Aprea, T. Bastianelli, F. Beone, R. Bertini, G. Bracco, M. Caporicci, B. Calosso, M. Chinnici, A. Colavincenzo, A. Cucurullo, P. Dangelo, M. De Rosa, P. De Michele, A. Funel, G. Furini, D. Giammattei, S. Giusepponi, R. Guadagni, G. Guarnieri, A. Italiano, S. Magagnino, A. Mariano, G. Mencuccini, C. Mercuri, S. Migliori, P. Ornelli, S. Pecoraro, A. Perozziello, S. Pierattini, S. Podda, F. Poggi, A. Quintiliani, A. Rocchi, C. Scio, F. Simoni, and A. Vita. The role of medium size facilities in the hpc ecosystem: the case of the new cresco4 cluster integrated in the eneagrid infrastructure. In *Proceeding of the International Conference on High Performance Computing & Simulation*, pages 1030–1033. Institute of Electrical and Electronics Engineers (IEEE), 2014.
- [22] Viktor Hornak, Robert Abel, Asim Okur, Bentley Strockbine, Adrian Roitberg, and Carlos Simmerling. Comparison of multiple Amber force fields and development of improved protein backbone parameters. *Proteins: Structure, Function, and Bioinformatics*, 65(3):712–725, 2006.
- [23] M. Marchi and P. Procacci. Coordinates scaling and multiple time step algorithms for simulation of solvated proteins in the npt ensemble. *J. Chem. Phys.*, 109:5194–5202, 1998.
- [24] William G. Hoover. Canonical dynamics: Equilibrium phase-space distributions. *Phys. Rev. A*, 31:1695–1697, Mar 1985.
- [25] G. Kassiotis and G. Kollias. Uncoupling the proinflammatory from the immunosuppressive properties of tumor necrosis factor (tnf) at the p55 tnf receptor level: Implications for pathogenesis and therapy of autoimmune demyelination. *J. Exp. Med.*, 193:427–434, 2001.
- [26] C. Dai, D. Li, J. Popovici-Muller, L. Zhao, V.M. Girijavallabhan, and et al. 2-(2-aminothiazol-4-yl)pyrrolidine-based tartrate diamides as potent, selective and orally bioavailable tace inhibitors. *Bioorg. Med. Chem. Lett.*, 21:3172–3176, 2011.
- [27] Carlo Guardiani and Piero Procacci. The conformational landscape of tartrate-based inhibitors of the tace enzyme as revealed by hamiltonian replica exchange simulation. *Phys. Chem. Chem. Phys.*, 15:9186–9196, 2013.
- [28] X. Niu, S. Umland, R. Ingram, B.M. Beyer, Y. H. Liu, J. Sun, D. Lundell, and P. Orth. Ik682, a tight binding inhibitor of tace. *Arch. Biochem. Biophys.*, 451:43–50, 2006.
- [29] Martina Banchelli, Carlo Guardiani, Eleonora Tenori, Stefano Menichetti, Gabriella Caminati, and Piero Procacci. Chemicalphysical analysis of a tartrate model compound for tace inhibition. *Phys. Chem. Chem. Phys.*, 15:18881–18893, 2013.
- [30] W. Humphrey, A. Dalke, and K. Schulten. Vmd - visual molecular dynamics. *J. Mol. Graphics*, 14:33–38, 1996.
- [31] Kresten Lindorff-Larsen, Stefano Piana, Kim Palmo, Paul Maragakis, John L. Klepeis, Ron O. Dror, and David E. Shaw. Improved side-chain torsion potentials for the amber ff99sb protein force field. *Proteins*, 78(8):1950–1958, 2010.
- [32] Piero Procacci and Riccardo Scateni. A general algorithm for computing voronoi volumes: Application to the hydrated crystal of myoglobin. *Int. J. Quantum Chem.*, 42(5):1515–1528, 1992.

SIMULATION OF PHOTON BEAMS FOR RADIOTHERAPY APPLICATION

Luca Silvi* and Maria Pimpinella*

*ENEA, FSN-INMRI**

Via Anguillarese, 301 – 00123 S. Maria di Galeria (Rome, Italy)

ABSTRACT. The BEAMnrc Monte Carlo code has been used for simulating radiotherapy photon beams generated by a clinical linear accelerator. Both open beams shaped by standard movable collimators and stereotactic beams shaped by cones attached to the accelerator head have been simulated. Outputs of simulations are phase-space files (PSF) containing all parameters of particles crossing a plane of interest in the beamline. Phase-space files have been generated at various locations of dosimetric interest for 6 MV and 10 MV beam produced by a Varian DHX with square field side ranging from 10 cm to 0.6 cm and circular field diameter from 2 cm to 1.25 m. These files represent a set of validated data providing information about field size effects on the dosimetric characteristics of photon beams.

1 Introduction

Since the mid-90s Monte Carlo (MC) simulation of radiation transport has been widely used for radiotherapy dosimetry. Indeed availability of MC software packages allowing simulation of clinical beams and radiation detector response has made possible accurate calculation of physical parameters and correction factors needed for radiotherapy metrology and clinical dosimetry.

Nowadays MC simulation is considered one of the most powerful tool to face up the dosimetric challenges posed by modern advanced radiotherapy techniques. In this respect dosimetry of small photon beams has become a compelling need and MC calculation is a viable method to solve the pertaining problems. The first step in this area is to provide series of small photon beam simulations for different types of clinical accelerators and collimating systems in order to study the field size effects on the dosimetric parameters.

The main objective of a beam simulation is to get a "phase-space file " (PSF) where the complete information about each particle (type, position, energy, direction etc.) emerging from a beamline component is stored. The PSFs can be used for different purposes, for example for determining the spatial, energy and angular distributions of the beam in certain experimental conditions, for simulating the beam interactions in media of dosimetric interest (i.e. water, air, tissue etc) and for calculating the radiation response of detectors currently used for clinical dosimetry.

This report describes MC simulations of photon beams generated by a clinical accelerator used for radiotherapy and stereotactic treatments.

2 Materials and Methods

2.1 Accelerator and photon beams

The accelerator used in this work is a Varian DHX clinical accelerator available at San Filippo Neri Hospital in Rome. This accelerator produces radiotherapy photon beams with nominal accelerator potential of 6 MV and 10 MV. Using the standard movable collimators (i.e. the jaws) with aperture in Y and X directions that projected at the reference distance (100 cm) ranges from 0.6 cm to 40 cm

open beams can be produced. According to the international dosimetry codes [1] the open beam with 10 cm x 10 cm field size is the reference field for dosimetric measurements.

In addition to the standard collimators, the Varian accelerator is equipped with Radionics cylindrical cones used for stereotactic treatments. The cylindrical cones attached to the accelerator head behave as tertiary collimators shaping circular small beams with field diameter ≤ 2 cm at the reference distance. The cylindrical cones are made with a base alloy lead, with external dimensions of 12.5 cm in height and 7.5 cm in diameter. An inner conical hole defines the beam size.

In this work open square beams with side from 10 cm down to 0.6 cm and stereotactic circular beams with field diameter 1.25 cm, 1.50 cm and 2.00 cm were simulated.

2.2 Monte Carlo simulations

Photon beam simulations were performed using the BEAMnrc code [2, 3] free available for non commercial aims. BEAMnrc is a simulation package built on the EGSnrc MC code system [4] of radiation transport and first released in 1995. It was specifically developed for modelling external radiotherapy sources and predefined modules are provided to easily model the various components of an accelerator head.

The schematic of the Varian DHX simulation geometry is shown in Fig 1. It includes: x-ray target, primary collimator with fixed aperture, vacuum window, flattening filter, transmission monitor ionization chamber, mirror, secondary collimators including Y (upper) jaws and X (lower) jaws and stereotactic cone. A beam simulation begins with electrons striking the x-ray target with subsequent production of bremsstrahlung photons. All the generated particles are transported through the accelerator head and PSFs can be generated at any location of interest in the beamline.

In this work PSFs were generated at 80 cm, 90 cm and 100 cm from the target and analysed using the BEAMDP data processor [5] to investigate the beam characteristics. PSFs were also used as input source in the DOSXYZnrc code [6] for calculating depth dose curves (PDD) and lateral dose profiles in water.

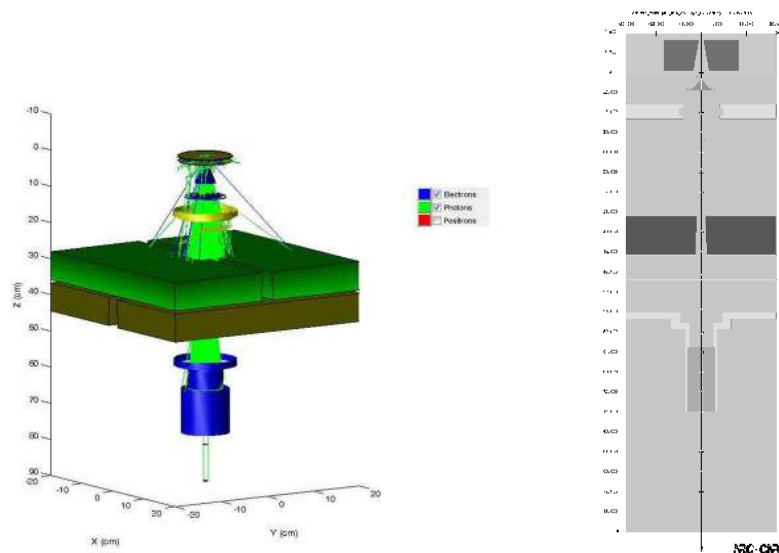


Fig.1 Accelerator model for the BEAMnrc photon beam simulations.

Dimensions of the various accelerator components, their position as well as the material characteristics were taken by the original drawings provided by the accelerator manufacturer. The characteristics of the electron beam impinging on the x-ray target were tuned comparing calculated and experimental dose distributions. A fine tuning of the electron spot size was made comparing calculated and measured dose outputs of circular small beams relative to the reference beam.

The energy cut-offs for radiation transport were set to 0.010 MeV for photons and 0.700 MeV (0.188 MeV kinetic energy) for electrons. To improve the calculation efficiency some variance

reduction techniques were implemented such as “range rejection” and “directional bremsstrahlung splitting” (DBS). The "range rejection" was applied with the parameter $ESAVE = 2$ MeV that means electrons with energy less than 2 MeV are not followed if they can not reach the next beamline component. The calculation speed increases of 2-3 times, having ignored only 0.1% of the secondary bremsstrahlung photons [7]. DBS allows the user to arbitrarily increase the number of photons generated by a single bremsstrahlung event if that event gives rise to photons that can enter a user-defined field. An appropriate weight is associated to DBS photons to obtain correct results. The EGSnrc system was installed on the cluster CRESCO4 in shared mode, in order to allow any authorized user to use the same setup and have in their home user's input and output files. The cluster CRESCO4 is run by ENEA UTICT unit, with the capability to work on 256 dedicated nodes out of 4863 (total), because the calculations were made in job-mode arrays. Each node consists of 2-socket 8-core processor Intel E5-2670 2.6 GHz 64 GB/RAM. In order to obtain output data with good statistics 10^7 histories were simulated with BEAMnrc, and 10^9 with DOSXYZnrc.

3 Results

The comparison of the calculated dose distributions with experimental measurements gave satisfactory results both for the reference and the small stereotactic beams thus confirming the correctness of the accelerator model. The differences obtained are of the order 1.5% and 1 mm with the exception of the build-up region in the PDDs and the edge of the beams in the lateral profiles. Fig. 2 shows such a comparison for the 6 MV stereotactic beam with field diameter 20 mm.

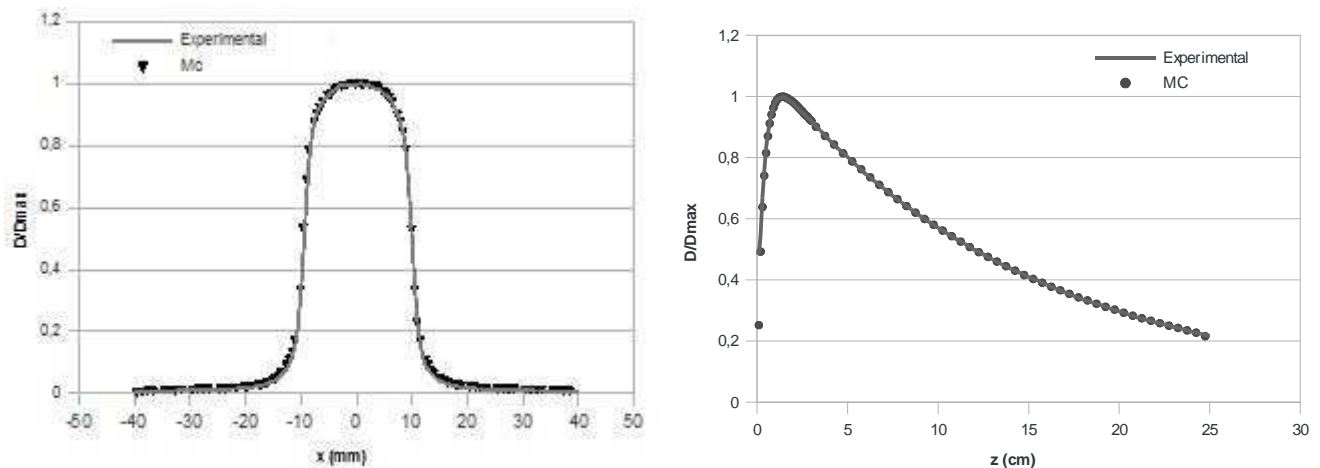


Fig.2

Comparison of experimental and calculated (MC) profiles and PDD curves. Data refer to 6 MV photon beam with field diameter 20 mm.

An example of results obtained by analyzing the PSFs with BEAMDP program is given in Fig. 3 where the photon fluence spatial distribution and the energy spectrum of photons at the exit of a stereotactic collimator are shown.

In Table 1 the photon average energies derived from the calculated spectra at the water phantom surface and in water at 10 cm and 20 cm depths are reported for the 6 MV beam with different field sizes. Weak effects of field size on the beam energy are obtained at the collimator exit while strong variations can be seen between the reference and the stereotactic beams in water. This is mainly due to the contribution of low energy scattered photons generated in water. The number of scattered photons dramatically decreases in absence of lateral equilibrium conditions as it happens in small field sizes.

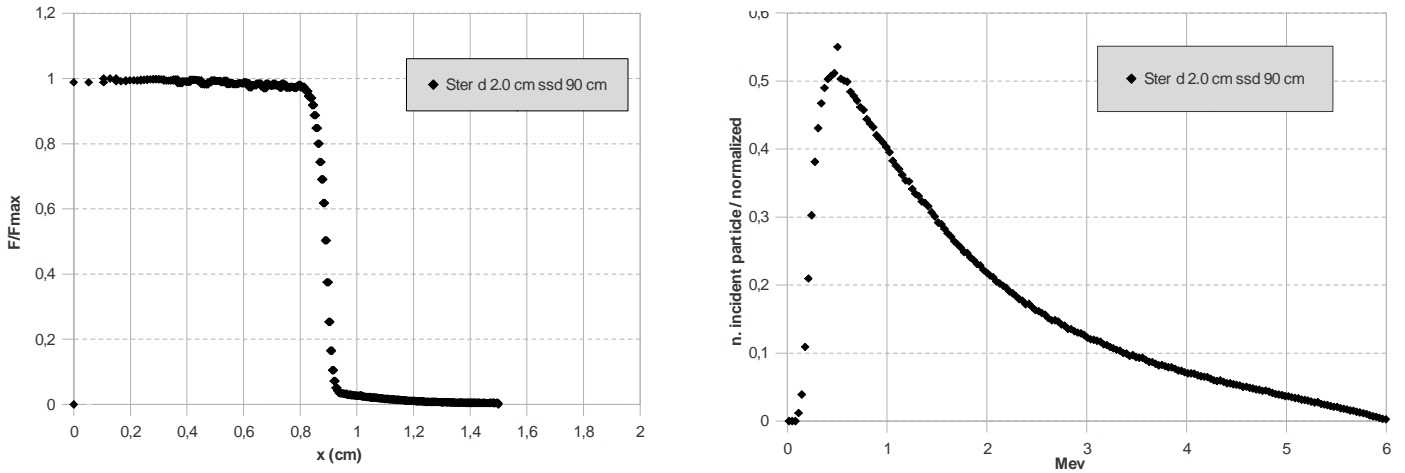


Fig.3

Calculated fluence spatial distribution and energy spectrum of the 6 MV photon beam with 2.0 cm diameter at the collimator exit.

Field size (cm)	Photon mean energy at the collimator exit (MeV)	Photon mean energy at 10 cm water depth (MeV)	Photon mean energy at 20 cm water depth (MeV)
side of square field=10	1.727	1.362	1.442
diameter= 2.00	1.736	1.858	2.092
diameter= 1.50	1.742	1.870	2.097
diameter= 1.25	1.743	1.865	2.095

Table.1

The average energies spectrum calculated of the photon beam in air and deep in water at 10 cm ,20 cm

3 Conclusions

Phase-space files have been generated for 6 MV and 10 MV photon beams produced by a Varian DHX clinical accelerator with square field shaped by the accelerator jaws and circular field shaped by stereotactic cones. These files represent a set of validated data useful for future studies relevant to small field dosimetry.

References

[1] IAEA-TRS 398 “Absorbed Dose Determination in External Beam Radiotherapy: An International Code of Practice for Dosimetry based on Standards of Absorbed Dose to Water” IAEA, Vienna, 2000
 [2] Rogers D.W.O., Faddegon B. A., Ding G. X., Ma C-M., We J. and Mackie T. R. “BEAM: A Monte Carlo code to simulate radiotherapy treatment units” Med. Phys. **22** (1995) 503-524
 [3] Rogers D.W.O., Walters B., Kawaracow I. “BEAMnrc Users Manual” NRCC Report PIRS 509(A), Ottawa, 2013
 [4] Kawrakow I., Mainegra-Hing E., Rogers D.W.O., Tessier F., Walters B.R.B. “The EGSnrc Code System: Monte Carlo simulation of electron and photon transport” NRCC Report PIRS-701, Ottawa, 2013

- [5] Ma C.-M. and Rogers D.W.O., "*BEAMDP User Manual*".NRCC Report PIRS-509(C), 2013
- [6] Walters B., Kawarakow I. and Rogers D.W.O. "*DOSXYZnrc User Manual*". NRCC Report PIRS-794, Ottawa, 2013
- [7] Sheikh-Bagheri "*Monte Carlo Simulations: Efficiency Improvement Techniques and Statistical Considerations*"- Proc. of 2006 AAPM Summer School: Pages 71-91: Published by Medical Physics Publishing,(Madison WI)

Transport study of Neon impurity seeded FTU plasma by Gyrokinetic simulations

Dolci Valerio^{1,2}, Mazzotta Cristina², and the FTU team*

¹*Dip. SBAI, "Sapienza" Università di Roma, Via Antonio Scarpa 14/16, 00161 Roma, Italy*

²*ENEA, Dipartimento FSN, C. R. Frascati, via E. Fermi 45, 00044 Frascati (Roma), Italy*

**See the appendix of G. Pucella et al., proceedings of the 25th IAEA Fusion Energy Conference, Saint Petersburg, Russia, 2014*

ABSTRACT. In FTU ohmic plasmas the seeding of Neon impurity causes a rise of line averaged electron density up to a factor 2, associated with a significant increase of the peaking factor. Although the effect of improved confinement with impurity seeding has been observed and well documented on many devices, the underlying physical mechanisms responsible for this improvement have not been completely understood. As for the particle transport and the microturbulence analysis, the mechanism of density peaking can be linked to the growth rates (GR) of Ion and Electron Temperature Gradients modes (ITG, ETG). This is the motivation of a detailed linear micro-stability analysis presented in this paper. It has been carried out with the gyrokinetic code GKW on a Neon injected discharge in terms of presence of modes, growth rates and fluxes of species.

1 Introduction

As part of research of magnetic confinement fusion, related to the experimental campaigns of FTU (Frascati Tokamak Upgrade at the research center of ENEA Frascati) [1], it is intended to study the effect of impurities in ohmic plasmas. The work is based on experimental observations and in particular on dedicated plasma discharges in which some Neon injections were applied. Aim of this paper is the description of micro-instability analysis conducted on these pulses by using a gyrokinetic code. Indeed has been observed, in the plasma discharges with the presence of light and medium impurities, a spontaneous increase of the density at the centre of the plasma column associated with an edge cooling. In this way is induced a flow of heat and electrons towards the inside of the plasma due to anomalous transport effects. This effect is known in the literature and takes the name of Radiatively Improved (RI) [2,3]. As for the particle transport and the microturbulence analysis, the mechanism of density peaking can be linked to the growth rates of some modes: the Ion Temperatures Gradient (ITG), Electron Temperature Gradient (ETG) and Trapping Electron Mode (TEM) [4,5]. This study helps to understand how the Neon influences the linear growth rates (GR) value and then stabilizing them. The analysis has been carried out with the aid of the gyrokinetic code GKW Gyrokinetic at Warwick [6], which allows to describe the evolution of the microturbulence modes in presence or absence of impurities. The GKW code has been installed on the machines CRESCO ENEA Portici, in particular on CRESCO2 and CRESCO4 clusters. It solves the complex system of equations (Vlasov-Maxwell) that require significant processing time, in this regard it was intended to exploit parallelization of CRESCO to accelerate the delivery of results.

2 Experimental observations

In FTU ohmic plasmas the seeding of Neon impurity (in the absence of Deuterium gas puffing) causes a rise of line averaged electron density up to a factor 2, associated with a significant increase of the peaking factor [7]. The effects of Neon seeding have been studied in a series of dedicated

ohmic discharges, in particular two similar discharges were produced in the same experimental session, described in figure 1: one with a Neon injection at 0.6 s for 50 msec (# 37342, red trace) and a second one at the same current and toroidal field ($I_p = 360$ kA and $B_T = 5.2$ T, #37344, blue trace) with exclusively Deuterium puffing, reaching the same line-average electron density, to be used as reference undoped pulse. It is noted that the two discharge are similar before the injection of Neon, but at 1.2 s the one with impurity presents profiles of temperature and density much more peaked, with a colder edge and less dense. This variation is believed to be entirely due to the effect of Neon as there is placing of Deuterium within the plasma.

It is estimated that the Neon impurity is present in a concentration of 1% with respect to deuterium, and contributes approximately to 10% of the electrons increase during the peaking phase, it is therefore necessary to rely on a change of the transport, in order to justify the density slope observed, since the only electrons of Neon10+ are not enough to explain this increase [7].

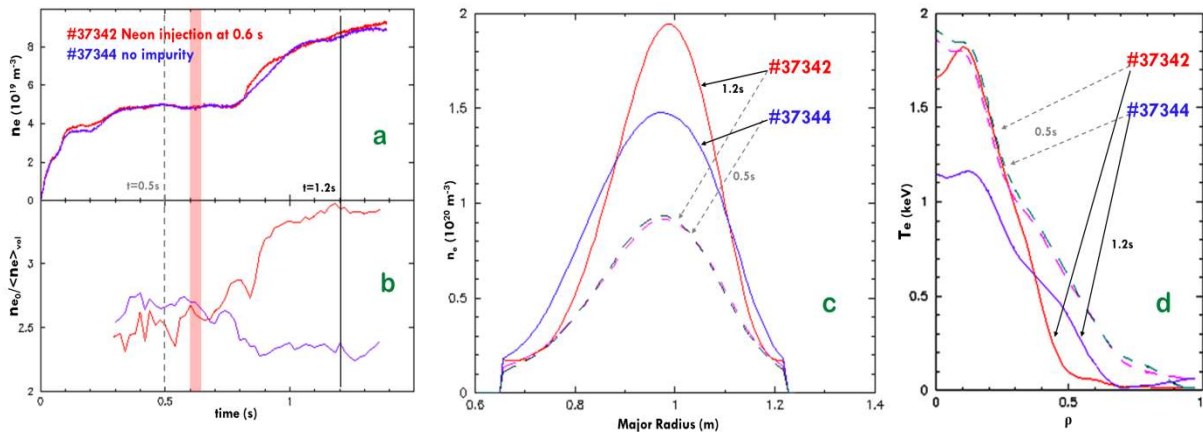


Figure 1) Electron density and temperature. a) Time traces of the line averaged central density, red trace for discharge #37342 with Neon injection at 0.6 s for 50 ms (light red box) while D gas is off, blue trace for the reference discharge #37344 with the central density increase reproduced by D gas-puff. Bottom frame, b) Peaking time trace of the same discharges. Two time intervals are considered to compare density profiles: before the impurity injection at 0.5 s (grey dotted line) and after (1.2 s, black line); the respective inverted profiles are shown in the panel c.

c) Local density profiles. At 0.5 s the profiles of the two discharges are virtually identical (grey dotted arrows, the pink dotted profile is referring to the #37342; the green dotted profile to the #37344); at 1.2 s (black arrows) the line density is doubled and the peaking of the Neon doped #37342 (red profile) reaches 3.4, much more in respect of the #37344 (blue profile).

d) Electron temperature profiles by ECE measurements. Both discharges have the same temperature profiles before the impurity injection (pink and green dotted profiles), at 1.2s the #37344 has lower temperatures for the entire profile (blue trace), the #37342 doped discharge (red trace) keeps the same temperature in the center but lower at the edge (the small hole at center it's due to noise).

3 Transport and microstability analysis

There are various factors which can act as particle transport in the Tokamak plasma configuration, the easiest and most studied is due to collisions and is called neoclassical transport. There is however a significant difference between such carriage and that observed experimentally, which goes under the name of anomalous transport, this category contains a multitude of different phenomena, with the common characteristic of being originated by the highly non-linear nature of the plasma, and so by its instability.

It is now commonly accepted that the anomalous transport source is the formation of turbulences within the plasma. These arise from the generation of fluctuations on small scales of the plasma

quantities: density, temperature and electrical potential. Within the standard Tokamak these structures are of dimensions of a few Larmor radius perpendicularly to the magnetic field, while they are elongate in the parallel direction.

The gyrokinetic approximation used in GKW allow to identify the dominants modes: ITG, TEM, ETG, in particular the study of small lengths with k_{perp} , the perpendicular wavenumber, of the order of the ionic Larmor radius can be carried out, and also frequencies much smaller than the ion cyclotron frequency: a good resolution is obtained and so is possible to extrapolate different sizes modes present in plasma at a given time and radius.

The saturated growth rate of the dominant mode in the system is calculated as:

$$\gamma_N^{max}(t_N) = \ln \left[\frac{\sqrt{\sum_m |\Phi(t_N)|^2}}{\sqrt{\sum_m |\Phi(t_N - \Delta t_N)|^2}} \right] / \Delta t_N$$

where Φ is the normalized Fourier amplitude of the scalar potential and m denotes the summation over all the radial and binormal modes and the grid points on the lines of magnetic field, and where t_N is the single integration time step done N times until convergence.

The code has been used in linear simulations to calculate the levels of saturation of the GR, across the spectrum of the wave vectors (k), and then yo study the variation in the passage between L-mode and RI-mode. In addition, the code computes heat fluxes and particles, and this allows to have a direct indication of their change in function of the GR.

For this study, several local linear analysis have been performed, that are intended for qualitative comparison of the linear growth rates and particle fluxes. The eigenfunctions and fluxes calculated by the code are normalized every time step and they are associated with the dominant mode for a specific wave vector. The magnitude of the flux therefore does not carry information about the saturated flux level, but its sign indicates the direction of the flux in the linear phase of the mode growth. In this analysis the $\vec{E} \times \vec{B}$ contribution has been taken into account and the gyro-centre flux is calculated by GKW neglecting terms of order ρ_*^2 [8].

3.2 Simulation setup

The GKW code has been installed on CRESCO2 and CRESCO4 machines with a minimal "Makefile" and without the use of MPI libraries for parallel computing, not necessary for this linear simulation. The high availability of nodes on CRESCO "farm" enabled the implementation of dozens of parallel run, thus making possible spatial and temporal scanning, as well as varying the parameters of the impurities, never been done before [9].

FTU does not present diagnostic for the ion measurements, so that to perform the gyrokinetic simulations these quantities were obtained with both experimental profiles reconstructions and as output of the JETTO transport code, they were taken from all the input values for the simulations with GKW. In the simulations, the circular geometry is used. Finally all quantities, as input to the code are

Discharge#	37342	37344	37342	37344
Time (s)	1.0	1.0	0.5	0.5
ρ_{tor}	0.4	0.4	0.4	0.4
ξ	1.28	0.91	0.84	0.86
q	1.27	1.55	1.69	1.74
$-a\nabla T_i/T_i$	4.82	3.12	4.95	3.02
$-a\nabla T_e/T_e$	6.89	3.55	6.89	3.55
$-a\nabla T_N/T_N$	0.00	-	0.00	-
$-a\nabla n_i/n_i$	3.33	1.81	3.33	1.81
$-a\nabla n_e/n_e$	3.00	1.81	3.00	1.81
$-a\nabla n_N/n_N$	0.00	-	0.00	-
T_i (eV)	568	397	568	397
T_e (eV)	586	575	586	575
T_{Ne} (eV)	586	-	586	-
$n_e(10^{19} m^{-3})$	9.60	9.79	5.93	5.88
$n_i(10^{19} m^{-3})$	9.50	9.79	5.93	5.88
$n_{Ne}(10^{19} m^{-3})$	0.1	-	-	-

Table 1. Physical parameters for the two simulated FTU cases

standardized according to the GKW system of coordinates: ψ , θ , φ (see table 1 for typical physical input parameters).

GKW has many simulation parameters not directly related to plasma values. A study of these parameters was therefore made to find the optimum values for the simulations. The main ones are:

NX	1	Number of radial wave vectors
N_s_grid	264	Total number of points along the field lines
$NPERIOD$	6	Number of revolutions, and then those toroidal poloidal by the relationship $2*NPERIOD - 1$
N_mu_grid	10	Number of points for the magnetic moment
N_vpar_grid	36	Grid points for the velocity parallel to the lines of field
$NTIME$.	Maximal number of consecutive integration
$DTIME$.	Time step
$NAVERAGE$.	Number of $DTIME$ for cycle
$GAMMATOL$	10^4	Convergence parameter

Table 2: calculation parameters

GKW integrates the equations with a step of $DTIME$ for $NAVERAGE$ times, then prints the result to a file, renormalizes potential and repeats this for $NTIME$ times. The run stops when 3 consecutive values of the Growth Rates is convergence within a $GAMMATOL$ parameter set in input. The condition of stability is defined, by the manual, by $DTIME * NAVERAGE \geq 0.2$.

The different simulations must be made through the use of several input files and then submitted to the queue individually, this is done by the use of the “gkwnlin” bash script that allows both the creation of the folder system, necessary for the proper functioning and organization of the outputs for that set of linear simulations, and the submission of the runs on the required queue, by taking the input file from the appropriate subfolder. These latter are generated by the interaction of a Python script, that interfaces with the FTU data store for the input data and, subsequently, it orders data in a readable input file suitable for GKW by a bash script, which also provides for modification of integration parameters in a scanning for k . Each simulation comprises about 50 runs, one for each k in the range 0-60 ionic Larmor radius in steps of 0.1 between 0 and 2, of 0.5 between 2 and 5 and of 5 from 5 to 50. The individual runs are then launched separately from the script on the queue “cresco4_h144”, each of one using a single processor. The run duration varies from a few tens of minutes to the couple of days, as a function of the convergence speed, in turn directly proportional

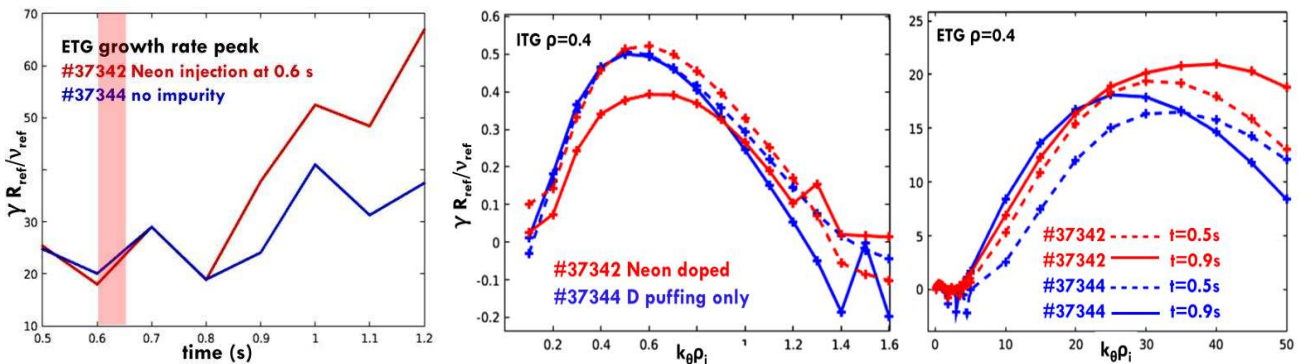


Figure 2. At left: time traces of the GR peaks for the two discharges (red trace for doped, blue for undoped pulse). At center and right: scan in time of the growth rates (normalized at a reference major radius and reference Ion temperature for this radius) as a function of the bi-normal wavenumber, at normalized radius $\rho=0.4$. Center frame: the small wave number region where the ITG modes are dominant. The time of 0.5 s refers to the pre-injection (dotted line), while at 0.9 s the effects of the impurity are well established (continuous traces).

to the GR. Finally the output reading is carried out with some Matlab scripts, they include the ordering of the outputs in the folder system generated by “gkwnlin”. The main outputs as a function of k are: the growth rates, frequencies, flux of heat and particles and, for each k , the radial distribution of the vector and scalar potential, this latter to identify the dominant mode.

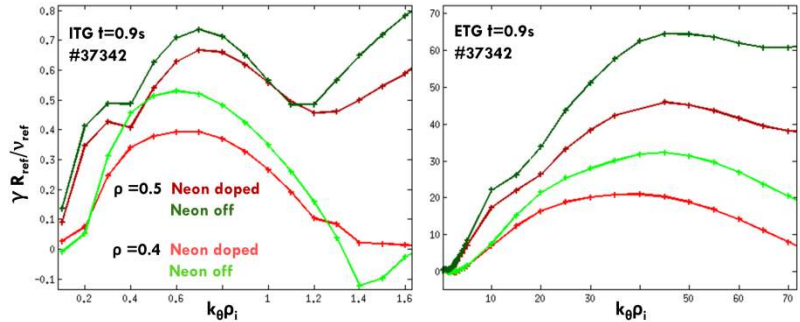


Figure 3. Scan in radius of the growth rates as a function of the bi-normal wavenumber at the time of 0.9 s for the doped discharge (red lines): at left panel ITG, at right the ETG modes. The green traces represent the same pulse with the Neon specie set to zero in the simulation. The intensity of the color indicates the radius: lighter for internal, darker for half radius.

4 Results

In figure 2 the growth rates versus the perpendicular normalized wavenumber $k_{\theta}\rho_i$ of ETG and ITG are shown for both the discharges, at two different times (pre and post injection) [10].

For higher wavenumbers, with the peak around 40, the ETG is the dominant instability (right panel), whereas in the small wavenumber region (<2) the ITG modes dominate (left panel, positive values). The figure reproduces the growth rates at the normalized radius $\rho = 0.4$, but they exhibit a similar behavior even at different values of the radius. Before the density rise, the growth rates of the ITG modes appear almost coincident in both the discharges (dotted traces), whereas, at $t=0.9$ s only the Neon injected pulse presents lower ITG growth rates as a consequence of the enhanced steepness of the density profile (left frame, red continuous line). In order to appreciate the direct effect of the Neon presence at fixed gradients, it’s more appropriate to compare the doped discharge with itself where the impurity is suppressed. This is exposed in figure 3: the green traces represent the GKW growth rates of the #37342 pulse with the Neon specie concentration set to zero. The ITG modes (left frame), as well as the ETG (right frame) in presence of the impurity (outlined by the red traces) are systematically lower than the green ones, to mean the stabilizing effect due to the effect of the Neon on these modes.

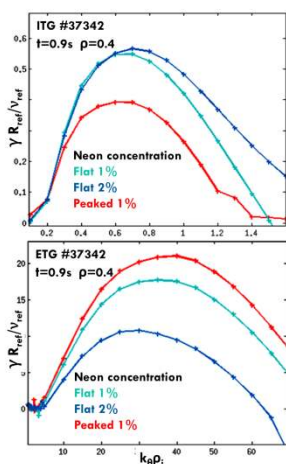


Figure 4. Effect on the Growth rates of the Neon concentration: blue for flat profiles (1%, 2%); red for peaked shape at 1%. Upper/lower panel for ITG/ETG respectively.

In order to figure out how different Neon profiles affects the analysis, three different impurity configurations have been used as input in the GKW code [11]. The first two consist of different flat concentrations, whereas the third is a more realistic radial profile estimated by an Impurity Transport Code. In all the analysis carried out in this work only this last Neon profile has been used. In figure 4 the ETG and ITG are reproduced for these different flat concentrations (light blue trace = 1% and blue trace =2%) and for a peaked shape (red trace) as calculated in ref. [11]. In terms of ETG the stabilizing effect is due to the amount of Neon injected, while for the ITG the beneficial effect derives from the peaking shape of the impurity profile. GKW can produce for each wavenumber $k_{\theta}\rho_i$ the radial structure of the modes, as scalar and vector potential, for the components real and imaginary. The fluxes directions of the species are useful to identify the modes presence, knowing that the drift waves have even parity for the scalar and odd for the parallel vector potential. The scalar potential is three order of magnitude higher than the vector potential, implying that the modes are essentially electrostatic. For the scalar potential the even parity is confirmed as well as the odd one for the potential vectors (figure 5). In these simulated conditions one can neglect the presence of Tearing and Microtearing modes.

Finally, the fluxes analysis shows that for the ETG case, that is relevant in building up the overall density profile, these modes drive the inward flux for electrons and Deuterium, if compared with the pre-injection time. Different is the behavior of the Neon specie, indeed it is yet found to be outward at an internal radius ($\rho=0.4$), but it becomes inward for a more external radius ($\rho=0.6$).

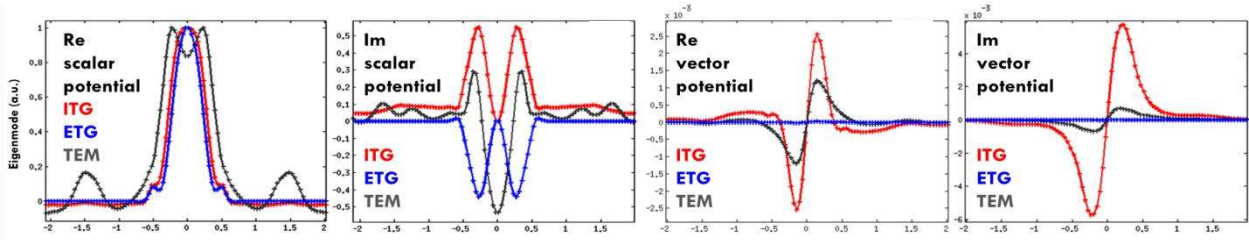


Figure 5: radial structure of the modes for each wavenumber $k_{\theta i}$, as scalar and vector potential (real and imaginary part).

5 Conclusions

GKW code has been used (in linear mode) to establish the role of the impurity in determining the growth rates of the unstable modes and driving the peaking of the electron density profiles. A stabilizing effect has been found as consequence of the Neon injection, which extends its effects up to the center. The shaping of the Neon impurity reconstructed profile, used as input in the simulations, plays an important role in determining the evolution on the modes.

The radial structure of the modes suggests the prevalence of electrostatics drift modes.

The fluxes analysis reveals that the sharp peaking of the density profile is mainly due to the inward pinch brought about by ETG modes.

Acknowledgments. Thanks to: Valeria Fusco, Cesidio Cianfarani, Edmondo Giovannozzi, Carlo Meineri, Gerarda Apruzzese, Maria Ester Puiatti, Massimo Marinucci, Fulvio Zonca, Gianluca Pucella and all the FTU Team for help and support.

"The computing resources and the related technical support used for this work have been provided by CRESCO/ENEAGRID High Performance Computing infrastructure and its staff. CRESCO/ENEAGRID High Performance Computing infrastructure is funded by ENEA, the Italian National Agency for New Technologies, Energy and Sustainable Economic Development and by Italian and European research programs, see <http://www.cresco.enea.it/english> for information".

References

- [1] C. Gormezano et al. (Guest ed), 2004 Special issue on FTU Fusion Sci. Technol. **45**
- [2] A. Messiaen et al., 1996 Phys. Rev. Lett. **77** 2487
- [3] G.L. Jackson et al., 2002 Nucl. Fusion **42** 28
- [4] Romanelli M. et al. 2011 Nucl. Fusion **51** 103008 (9pp)
- [5] Szepesi G. et al. Nucl. Fusion **53** 033007
- [6] Peeters A.G. et al. 2009 Comput. Phys. Commun. **180** 2650
- [7] Mazzotta C. et al. 2015 Nucl. Fusion **55** 073027 (7pp)
- [8] Murakami M. et al. 2001 Nucl. Fusion **41** 317
- [9] Dolci V. *Studio dell'effetto delle impurezze leggere sulla densità elettronica in plasmi fusionistici per reattori avanzati* Tesi di laurea. Università degli studi di Roma "La Sapienza".
- [10] Mazzotta C. et al. *Linear microstability investigation of a Neon impurity ..* 43rd EPS Conf. on Pl. Phys., Leuven, Belgium, July 4-8, 2016. Vol. 40A ISBN: 2-914771-99-1 P5.019 <http://ocs.ciemat.es/EPS2016ABS/pdf/P5.019.pdf>
- [11] Mazzotta C. et al. *Neon transport simulation for highly peaked dens..* 42nd EPS Conf. on Pl. Phys., Lisbon, 22-26 June, 2015. Vol. 39E ISBN 2-914771-98-3. P4.114 <http://ocs.ciemat.es/EPS2015PAP/pdf/P4.114.pdf>

SELF-ASSEMBLY OF TRITON X100 IN WATER SOLUTIONS: A MULTISCALE SIMULATION STUDY LINKING MESOSCALE TO ATOMISTIC MODELS

Antonio De Nicola^{1*}, Zhao Ying², Massimo Celino³, Mattia Rocco⁴, Toshihiro Kawakatsu⁵ and Giuseppe Milano¹

¹*Univeristy of Salerno, Chemistry and Biology "A. Zambelli" Department, Via Giovanni Paolo II, 132, IT-84084, Fisciano, Italy*

²*Institute of Nano-Photonics, School of Physics and Materials Engineering, Dalian Nationalities University, 116600 Dalian, China*

³*ENEA, C.R. Casaccia, Via Anguillarese 301, I-00123 Roma, Italy*

⁴*Department of Physics, Tohoku University, Aoba, Aramaki, Aoba-ku, Sendai 980-8578, Japan*

⁵*Biopolimeri e Proteomica, IRCCS AOU San Martino-IST, Istituto Nazionale per la Ricerca sul Cancro, Largo R. Benzi 10 I-16132 Genova, Italy*

ABSTRACT. We propose and validate a multiscale scheme for Triton X-100 (TX-100), which is a detergent widely employed in biology. The new approach, based on the hybrid particle field formulation allows simulations of large-scale systems. A coarse-grained (CG) model, developed and accurately validated in a wide range of concentrations, shows a critical micelle concentration, shape transition in isotropic micellar phase. Thanks to the fine resolution of CG model, we can obtain, by a reverse mapping procedure, atomistic models of micellar assemblies. In particular, atomistic models of the micelles give structures in good agreement with experimental pair distance distribution functions and hydrodynamic measurements. The picture emerging by detailed analysis of simulated systems is quite complex. Poly-disperse mixtures of spherical-, oblate-, and prolate-shaped aggregates have been found. The shape and the micelle behavior are mainly dictated by the aggregation number (Nagg). Micelles with low Nagg values (~ 40) are mainly spherical, while those with high Nagg values (~ 140 or larger) are prolate. For intermediate Nagg values (~ 70), fluxional micelles alternating between oblate and prolate shapes are found. The proposed model opens the way to investigations of several mechanisms involving TX-100 assembly in protein and membrane biophysics.

1 Introduction

Detergents are a class of molecules widely employed in biology applications[1]. They are used in the crystallization of proteins, as membrane stabilizing, denaturing, permeabilizing agents[3], and also for the isolation of integral membrane proteins[1, 3, 5].

*Corresponding author. E-mail: adenicola@unisa.it.

The name Triton-X is associated to a class of nonionic surfactants whose basic units are composed of a hydrophobic aromatic 4-(1,1,3,3-tetramethylbutyl)-phenyl core and a hydrophilic, variable length poly(ethylene oxide) (PEO) chain, generally expressed as $(C_{14}H_{22}O(C_2H_4O)_n)_{n=10}$. Triton X-100 (TX-100), whose side chain has 910 PEO blocks, is a detergent molecule widely used in the biological sciences[4].

To the best of our knowledge, only a few computational TX-100 models have been reported, such as atomistic study on the conformational behavior of a single TX-100 molecule in vacuum and in water[2]. Very recently, an optimized set of CHARMM parameters for the Triton X-series, suitable for atomistic molecular dynamics (MD) simulations, has been presented[9]. Although atomistic simulations provide very detailed models of surfactants, they are very computationally expensive techniques for studying the assembling processes involving nanostructures occurring on the mesoscopic time and length scales. Indeed, the assembly process of surfactants can be obtained only in some cases from a random mixture of surfactants in aqueous solution within atomic resolution with reasonable simulation time. Typically, this happens only for diluted systems above the CMC, and, more generally, in cases where the self-assembly occurs on a time scale that is attainable with atomistic simulations (100 ns)[6]. For this reason, in most cases, atomistic MD studies are conducted using preassembled aggregates.

MD simulations of CG models allow one to observe the self-assembly process spontaneously[6]. In particular, taking advantage of the large time scales accessible at the CG level, simulations on the order of 110 μ s allow to follow the self-assembly process and to efficiently sample different fluxional size and shapes characterizing assemblies of surfactants.

In the present study we propose and validate a hybrid CG model of TX-100 in a wide range of concentrations ranging from micellar to hexagonal phases. Detailed atomistic models obtained by a suitable reverse mapping procedure are also proposed and validated against several experimentally available structural and hydrodynamic properties[8].

2 Models

The molecular models considered here were developed in a hybrid MD-SCF scheme combining particles and field representations for nonbonded interactions. In the frame of self-consistent field (SCF) theory[7], the interaction of a particle with other nonbonded particles is considered only through a mean field. More details about the MD-SCF approach can be found in the ref. (inserire riferimenti) The adopted mapping scheme for the CG Particle-Field (PF) model of TX-100 molecules, is reported in Figure 1.

Over the chemical structure of molecule has been draw segmented circles, representing the effective beads of the CG model. Bead type label is reported next to each bead type. The parameters of model can be found at references(1-3). In the PF model the bond are described by a harmonic potential having functional form:

$$V_{bond}(l) = \frac{1}{2}K_{bond}(l - l_0)^2 \quad (1)$$

where l_0 is the equilibrium distance and K_{bond} is the force constant fo the bond. In Table 1, equilibrium distance and bond constants are reported.

The stiffness of the chains is taken into account by a harmonic potential $V_{angle}(\theta)$ depending of the cosine of angle between atoms, where is the angle between two successive bonds. In the following are reported the functional form of harmonic potential together with a list of the Kangle force constant and equilibrium bond angle θ_0 .

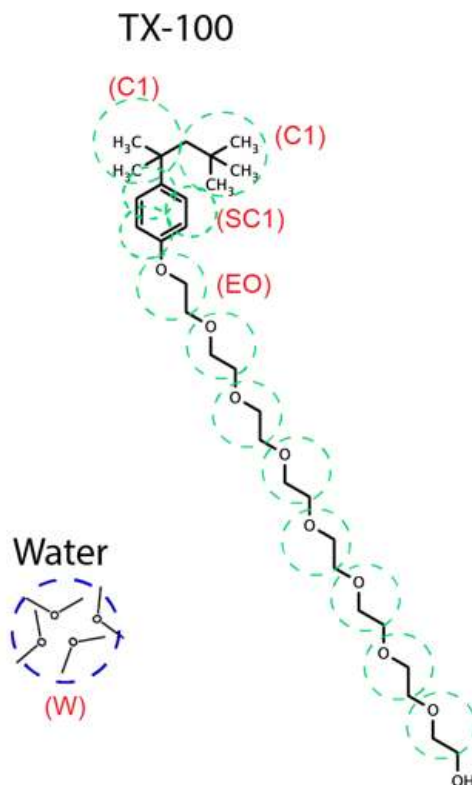


Figure 1: Mapping scheme adopted for the CG model. Next to each atom group is reported the corresponding label of CG effective particle type.

$$V_{angle}(\theta) = \frac{1}{2} K_{angle} (\cos \theta - \cos \theta_0)^2 \quad (2)$$

Particle-Field interactions parameters $\chi_{KK'}$ need to be fixed for every type of interaction between a particle K and the density field obtained from the particles of type K' . In Table 3 are reported the $\chi_{KK'}$ used for the PF simulations.

2.1 Simulation Details

Hybrid MD-SCF simulations of CG models were run with the code OCCAM[7] in the NVT ensemble, in which the temperature was controlled using an Andersen thermostat (collision frequency = 7 ps⁻¹). All of simulations were conducted at 298 K with a time step of 0.03 ps. The density field was updated using a value of Δt_{update} =9 ps. For the density mesh, a grid size of 0.6 nm has been employed for all systems. The MD simulations of atomistic models were carried out with GROMACS 4.5.1 in the NVT ensemble at the same temperatures employed for the MD-SCF simulations. The temperature was held constant with a Berendsen thermostat.

Table 1: Bond Interaction Parameters for TX-100 molecule

Bond	$l_0(nm)$	$K_{bond}(Kj/molnm^2)$
C1-C1	0.37	1250
C1-SC1	0.27	7500
SC1-SC1	0.27	8000
SC1-EO	0.28	5000
EO-EO	0.28	8000

Table 2: Angle Interaction Parameters for TX-100 molecule

Angle	$\theta_0(deg.)$	$K_{angle}(Kj/mol)$
C1-C1-SC1	140	30
C1-SC1-SC1	140	30
SC1-SC1-SC1	120	40
SC1-SC1-EO	140	30
SC1-EO-EO	155	40

Table 3: $\chi_{KK'} \times RT(Kj/mol)$ Interaction Parameters for TX-100 molecule

Bead Type	C1	SC1	EO	W
C1	0.0	2.4	7.8	33.75
SC1	-	0.0	7.8	20.25
EO	-	-	0.0	1.5
W	-	-	-	0.0

3 Discussion and Results

A first validation of the proposed CG model has been done for low TX-100 concentrations. In particular, the CMC of the Triton model has been investigated. The fraction of assembled TX-100 chains, as a function of concentration, compared with the experimental value of the CMC, is reported in Figure 2.

From the behavior of the assembled chains fraction, we can observe that, for concentrations of lower than 0.49, a sharp decrease of the assembled chains is found, in agreement with the experimental range (0.140.35 mM).

Generally, from an experimental point of view, direct information about the micelle shape is not easy to be obtained. Indeed, the same experimental pair distance distribution function can be compatible with different hypothetical shapes. For this reason, the issue about the TX-100 micelle shape is still an open one. Additional indication about the micelle shape can be obtained from the hydrodynamic behavior, especially from $[\eta]$ which is very sensitive to the shape of the aggregates. Considering two

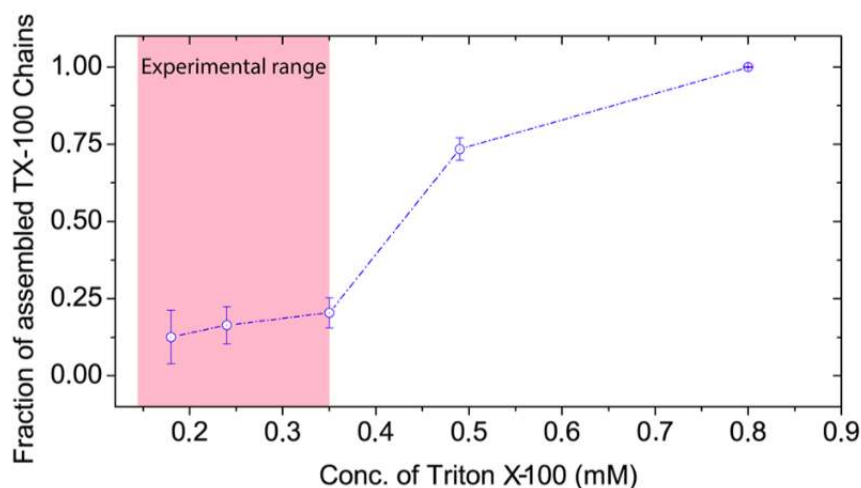


Figure 2: Fraction of assembled Triton X-100 chains at different concentrations. Chains are considered assembled if the number of neighbors is greater than zero. The neighbors are calculated on the base of cutoff criterion (1 nm) on the shorter distance between two beads of two different chains. Each point in the plot corresponds to the average on the last microsecond of each simulation.

shapes (prolate and oblate) the preferred shape for $N_{agg} = 140$ is an oblate shape with an a/b ratio of 1.9, while for small N_{agg} we obtained spherical aggregates. When the N_{agg} is larger than 150, a cylindrical prolate aggregates become more probable. In Figure 3, the shapes of TX-100 aggregates are reported, as function of N_{agg} .

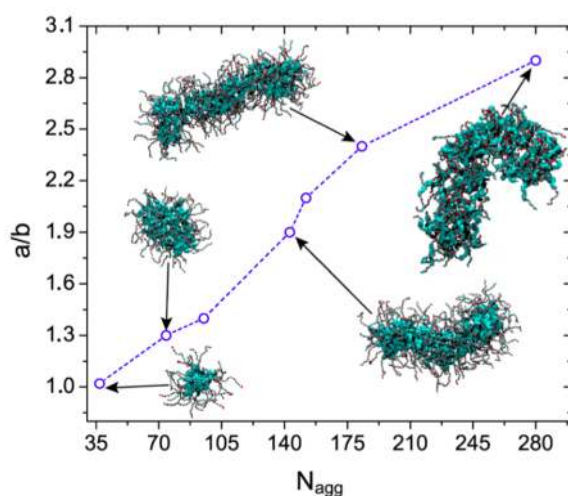


Figure 3: Ratio a/b between the two semi axes a and b of an ellipsoid is reported for micelle having different N_{agg} . The semi axes are calculated from the radius of gyration evaluated along the direction of the main inertia axes of each micelle.

3.1 Conclusions

A coarse-grained (CG) model is proposed and validated for TX-100. Although the adopted CG description is close to atomistic models (3:1 mapping), the hybrid particle field formulation of the models allows simulations of large-scale systems (having beads number ranging from 100.000 to 600.000 for simulation times from 5 μ s to 15 μ s). The CG model has been accurately validated in a wide range of concentrations in aqueous solution; in particular, the critical micelle concentration, shape transition in isotropic micellar phase. The proposed model, because of its computational efficiency for parallel applications, opens the way to investigations of several mechanisms involving TX-100 assembly in protein and membrane biophysics.

4 Cresco Resources

We used, for all activities reported in the present contribution, Cresco infrastructures. In particular, the Section 4 of CRESCO Cluster have been extensively used for parallel process. The average number of cores used for each calculation was 128, even if calculations employing 256 cores have been performed. The main code we used for our project is the parallel version of OCCAM Code (www.smms.unisa.it/occam), developed at University of Salerno. The Disk Quota we have used for our project was close to the limit of 200 GB/user.

References

- [1] D. A. Brown, , and E. London. Functions of lipid rafts in biological membranes. *Annual Review of Cell and Developmental Biology*, 14(1):111–136, 1998. PMID: 9891780.
- [2] Agnes Derecskei-Kovacs, Bela Derecskei, and Zoltan A. Schelly. Atomic-level molecular modeling of the nonionic surfactant triton x-100: the {OPE9} component in vacuum and water1. *Journal of Molecular Graphics and Modelling*, 16(46):206 – 212, 1998.
- [3] Dipankar Koley and Allen J. Bard. Triton x-100 concentration effects on membrane permeability of a single hela cell by scanning electrochemical microscopy (secm). *Proceedings of the National Academy of Sciences*, 107(39):16783–16787, 2010.
- [4] Marc le Maire, Philippe Champeil, and Jesper V Mller. Interaction of membrane proteins and lipids with solubilizing detergents. *Biochimica et Biophysica Acta (BBA) - Biomembranes*, 1508(12):86 – 111, 2000. Detergents in Biomembrane Studies.
- [5] Dov Lichtenberg, Hasna Ahyayauch, and Flix M. Goi. The mechanism of detergent solubilization of lipid bilayers. *Biophysical Journal*, 105(2):289 – 299, 2013.
- [6] S. J. Marrink*, D. P. Tieleman, and A. E. Mark. Molecular dynamics simulation of the kinetics of spontaneous micelle formation. *The Journal of Physical Chemistry B*, 104(51):12165–12173, 2000.
- [7] Giuseppe Milano and Toshihiro Kawakatsu. Hybrid particle-field molecular dynamics simulations for dense polymer systems. *The Journal of Chemical Physics*, 130(21), 2009.
- [8] H. Hasko Paradies. Shape and size of a nonionic surfactant micelle. triton x-100 in aqueous solution. *The Journal of Physical Chemistry*, 84(6):599–607, 1980.
- [9] D. Yordanova, I. Smirnova, and S. Jakobtorweihen. Molecular modeling of triton x micelles: Force field parameters, self-assembly, and partition equilibria. *Journal of Chemical Theory and Computation*, 11(5):2329–2340, 2015. PMID: 26574428.

COMPUTER SIMULATION OF TRIGLYCERIDES

A. Pizzirusso^{1*}, Y. Zhao², A. De Nicola¹ and G. Milano¹

¹ *Salerno University, Department of Chemistry and Biology “Adolfo Zambelli”, 84084, Via Giovanni Paolo II, 132, Fisciano (SA), Italy*

² *Dalian Nationalities University, Institute of Nano-Photonics, School of Physics and Materials Engineering, 116600, Dalian, China*

ABSTRACT. We examine at molecular level the crystal-liquid transition phase behaviour of a most popular triglyceride that compose the cocoa butter, tristearin. Our aim is to investigate, by means of molecular dynamics computer simulation, the melting process at molecular level of detail with a previously tested and validated united atom model used successfully for describing macroscopic triglycerides properties in liquid phase.

1 Introduction

The project is focused on Molecular Dynamics (MD) simulations of triglycerides using an united atom level of detail. These compounds are important constituents of oils and fats and are widely used in foods, in cosmetics, and medicine as nutrients or matrix materials [2]. With this point of view to understand the structural properties of the material and transport properties of drugs in liquid assumes great relevance and depends on molecules conformations [1]. Triglycerides crystallize according to three different polymorphs and in this context crystal-liquid phase transition assumes particular relevance for melting process able to support the formation of end-product quality. With this purpose we want to examine at molecular level the transition phase behaviour of the tristearin (SSS), and, in particular, its melting mechanism. Small differences of melting point in triglycerides drastically affect test and other features (as texture, gloss or color) in foods as chocolate. The relationship between triglycerides and chocolate is due to that one of the most important constituents of chocolate is cocoa butter, composed in great part of tristearin. On the basis of the previous considerations we propose for melting the β crystal samples composed of $N=2184$ molecules of SSS to perform MD simulation using GROMACS as engine, where model parameters are optimized in evaluating the interactions for triglycerides systems [3]. Due to the nature of the process we need to reach at about one microsecond time scale to obtain representative molten structures. For obtaining accessible simulation times to understand how the molecular mechanism of melting influences the macroscopic properties and the nature eutectic point, we opt thus for CRESCO supercomputing resources.

*Corresponding author. E-mail: antonio.pizzirusso80@gmail.com.

Table 1: Experimental and simulated cell parameters of SSS at 293 K.

Cell Parameter	Exp.	Sum UA-FF
a (Å)	12.00	13.12
b (Å)	51.90	53.29
c (Å)	5.44	4.97
α (deg)	73.6	71.40
β (deg)	100.5	102.29
γ (deg)	118.7	119.65
ρ (Kg/m ³)	1028.2	1035.88

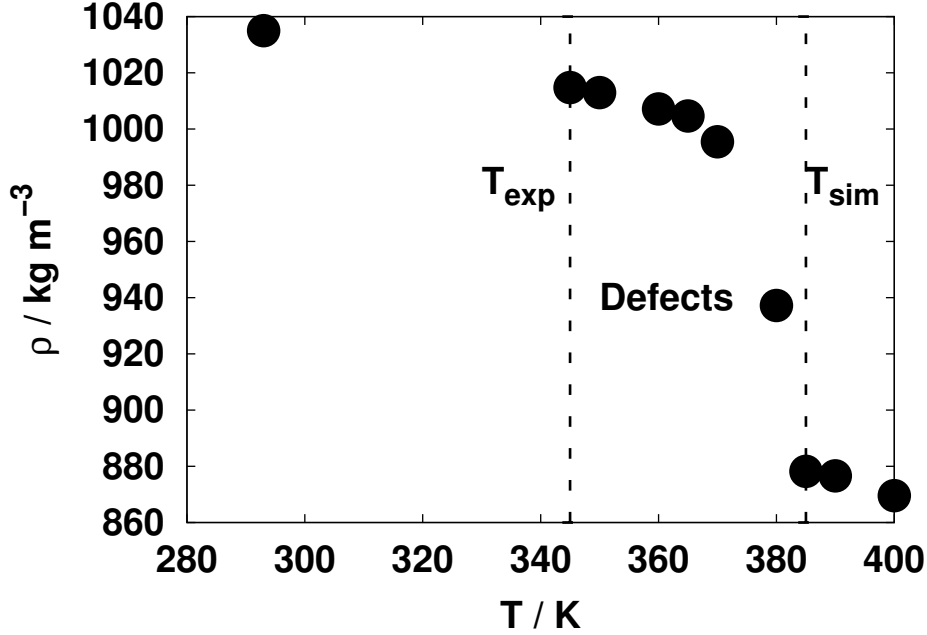


Figure 1: Density as function of temperature for SSS heating process.

2 Simulation Results

Force Field (FF) has been previously validated in terms of the cell parameters and density of SSS β crystal polymorph (the most stable one, see Table 1) available in literature at 293 K [4], finding a good agreement.

The simulated crystal-liquid transition temperature (T_{KL}) is also evaluated by means of MD for pure SSS at 385 K, and over-estimated the experimental one of about 40 degrees, in agreement with the united atom approximation (see Fig. 1). The transition goes through the defects formation in a meta-stable crystal phase. In particular, after the defects formation the crystal rearranges itself in a meta-stable packing at 380 K, and these defects extend until complete transition in an isotropic liquid phase at 385 K.

The heating process needs about 1 μ s to complete the melting for every temperature, and for this purpose we used 72 cPUs on the CRESCO queue cresco3.72h24.

References

- [1] Yuan H., Wang L.L., Du Y.Z., Hu F.Q. You J., and Zeng S. *Colloids and Surfaces B: Biointerfaces*, 60:174–179, 2007.
- [2] Pardeike J., Hommoss A., and Muller R. H. *International Journal of Pharmaceutics*, 366:170–184, 2009.
- [3] Sum A. K., Bidy M. J., de Pablo J. J., and M. J. Tupy. *J. Phys. Chem. B*, 107:1443–14451, 2003.
- [4] van Langevelde A., Peschar R., and Schenk H. *Acta Cryst.*, B57:372–377, 2001.

BICONNECTIVITY OF VERY LARGE SOCIAL GRAPHS

Giuseppe Chiapparo², Umberto Ferraro Petrillo^{1*}, Donatella Firmani³ and Luigi Laura¹

¹*Sapienza University of Rome*

²*University of Rome "Tor Vergata"*

³*Roma Tre University*

ABSTRACT.

The goal of this work was to extend the results presented in [3], by analyzing the biconnectivity properties of very large social graphs. To this end, we considered as dataset in our experiments a recent sample of the Twitter network [4] having approximately 23.1 billion edges. The relevant size of the graph required the usage of compression techniques to reduce its memory occupation so to make it fit in the main memory of the calculator used for our experiments.

1 Introduction

Strong connectivity in directed graphs is a basic notion having both theoretical and practical importance. From the practical viewpoint, for instance, several experimental studies have shown that strongly connected components (in short, SCCs) play a crucial role in the structure of real-world networks.

In this paper, we address this issue by analyzing the inner structure of the largest SCC in real-world very large social graphs. More specifically, we go beyond strong connectivity and characterize the properties of the biconnected (both 2-vertex- and 2-edge-connected) components that lie inside the largest SCC. In particular, we try to compute exactly for the first time the size of the largest biconnected components of a very large social graph having approximately 23.1 billion edges.

2 Basic Terminology

Let $G = (V, E)$ be a digraph with n vertices and m edges. A vertex $v \in V$ is a *strong articulation point* if its removal increases the number of strongly connected components of G . Similarly, an edge $e \in E$ is a *strong bridge* if its removal increases the number of strongly connected components of G . Strong articulation points and strong bridges are related to the notion of *2-vertex* and *2-edge connectivity* of digraphs, as shown by the following definitions. Let G be strongly connected. Then G is said to be *2-vertex connected* if it has no strong articulation points, i.e., the removal of any vertex leaves G strongly connected. Similarly, G is said to be *2-edge connected* if it has no strong bridges, i.e., the removal of any edge leaves G strongly connected. In other words, strong articulation points are exactly the vertex cuts for 2-vertex connectivity, while strong bridges are exactly the edge cuts for 2-edge connectivity. The *2-vertex- (resp., 2-edge-) connected components* of G are its maximal 2-vertex- (resp., 2-edge-) connected

*Corresponding author. E-mail: umberto.ferraro@uniroma1.it.

subgraphs.

3 Experimental Setup and Implementations

In this section we briefly describe the test environment and the implementation details of the algorithms used in our experimental study.

3.1 Test Environment

Due to the huge memory requirements needed for processing very large graphs, we conducted our experiments on the `twitter-2012` graph using the nodes of the CRESCO4SM cluster. Each of these nodes is equipped with 756 of main memory together with two CPU Intel Xeon E5-2643 running at 3.5 GHz. All our implementations have been written in Java and take advantage of the features available with the WebGraph library [1]. Wherever possible, our code has been optimized by resorting to a multithreaded architecture. For this same reason, our tests on CRESCO4SM have been run using up to 12 computing cores at the same time. Despite the significant amount of available main memory, some of the operations we performed (i.e., the initial compression of the `twitter-2012` graph) were partially accomplished using external memory. For this reason, we had to use up to 800GB of local disk space to support these operations.

3.2 Implementations

A simple algorithm that can be used for calculating the 2-edge and the 2-vertex connected components of a graph G consists of repeatedly removing all the strong bridges in G , until no strong bridges are left. Since there can be at most $O(n)$ rounds, the total time is $O(mn)$. However, the authors in [3] observed that this strategy exhibits very long execution times when applied to graphs counting millions of vertices using modern hardware. As an alternative, they propose a memory-efficient *heuristic* that allows to compute the l2ECC and l2VCC of very large graphs in a reasonable time. This heuristic is based on the notion of *dominator trees* [2]. We refer the interested reader to [3] for more info about this heuristic.

4 Experimental Results

The aim of our experiments was to analyze some of the properties of the `twitter-2012` graph. Along with basic properties, like the number of nodes and of edges, we were interested in analyzing some of the connectivity and biconnectivity properties of this graph. From the experimental viewpoint, this goal was somewhat difficult to achieve because of the large size of the considered graph. Thus, in order to make this graph more manageable, we performed a preliminary compression phase aimed at shrinking its memory size as described in the following algorithm:

- **Step 1: WebGraph Compression.** The original graph \mathcal{G} has been compressed with the help of the WebGraph library. The outcoming compressed graph \mathcal{G}' has a size of 64GB against a size of 230GB for the original graph.
- **Step 2: Symmetric Graph Creation.** We derived from \mathcal{G}' its symmetric counterpart \mathcal{G}'_{sym} .

Graph	Repository	n	m	ISCC	#sap	#sb	#scc
twitter-2012	[4]	398.8 M	23.1 G	64%	27.1 M	79.3 M	141.6 M

Table 1: Basic properties of the `twitter-2012` graph.

- **Step 3: LLP Compression.** We further compressed \mathcal{G} by applying the Layered Label Propagation algorithm to \mathcal{G}' and \mathcal{G}'_{sym} . The outcoming compressed graph \mathcal{G}'' reached a size of 32GB.

All the aforementioned steps have been accomplished by implementing and running an ad-hoc Java application developed with the help of the WebGraph library ([1]). Once obtained the compressed graph, it has been analyzed in several ways. First of all, we derived some basic properties about this graph. The outcoming results, presented in Table 1, confirm the sparse nature of this social network. This has been further confirmed by a second experiment where we evaluated the in-degree distribution for the nodes of this graph, whose results are presented in Figure 1.

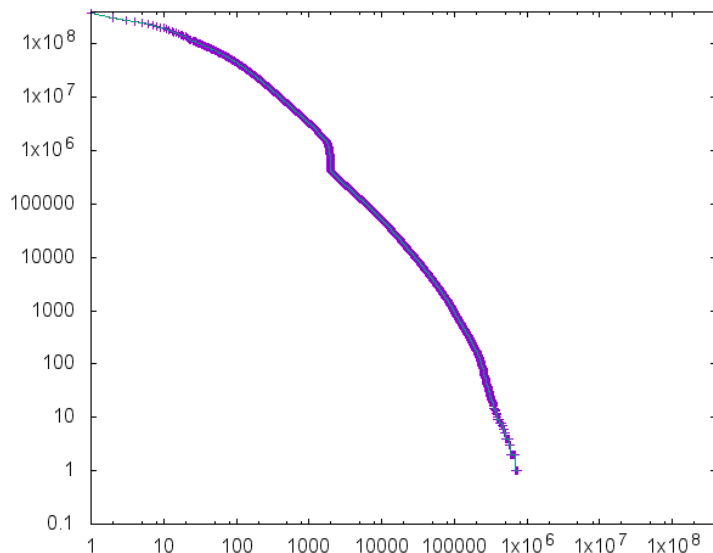


Figure 1: Frequency plot of the in-degree distribution for the nodes of the `twitter-2012` graph.

In a third experiment we analyzed the distribution of the strongly connected components existing in the `twitter-2012` graph. The results, presented in Figure 2, are in line with those obtained in [3] and confirm the existence of a giant connected component in this type of graph, spanning over the 80% of its vertices.

Finally, we performed a fourth experiment aimed at determining the size of the largest 2-edge connected components existing in `twitter-2012`. A simple algorithm that can be used for this purpose consists of repeatedly removing all the strong bridges in G , until no strong bridges are left. Since there can be at most $O(n)$ rounds, the total time is $O(mn)$. During our preliminary experiments, however, we observed that the number of rounds is much smaller than $O(n)$. The above algorithm yields a bound close to [5] whenever the input network is sparse, like in our case (see [6] for more information). Despite this, our attempts to run this algorithm on the `twitter-2012` graph were unsuccessful, because of the very long execution times (i.e., over 2 months of uninterrupted execution were not enough for computing the solution)

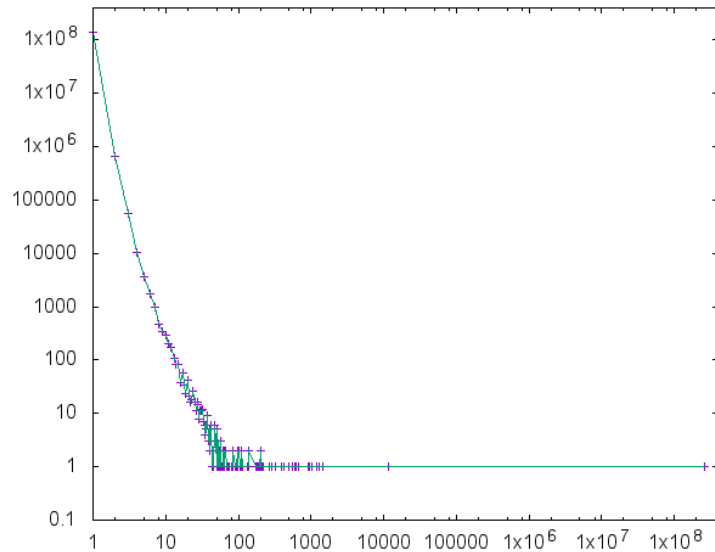


Figure 2: Frequency plot of the strongly-connected component size distribution of the `twitter-2012` graph.

References

- [1] Paolo Boldi and Sebastiano Vigna. The WebGraph framework I: Compression techniques. In *Proc. of the Thirteenth International World Wide Web Conference (WWW 2004)*, pages 595–601, Manhattan, USA, 2004. ACM Press.
- [2] Adam L. Buchsbaum, Haim Kaplan, Anne Rogers, and Jeffery R. Westbrook. A new, simpler linear-time dominators algorithm. *ACM Trans. Program. Lang. Syst.*, 20(6):1265–1296, November 1998.
- [3] Giuseppe Chiapparo, Umberto Ferraro-Petrillo, Donatella Firmani, and Luigi Laura. Biconnectivity of social and web graphs. In *Proceedings of the Symposium on Advanced Database Systems*, 2016.
- [4] Maksym Gabielkov, Ashwin Rao, and Arnaud Legout. Studying social networks at scale: Macroscopic anatomy of the twitter social graph. In *The 2014 ACM International Conference on Measurement and Modeling of Computer Systems, SIGMETRICS '14*, pages 277–288, New York, NY, USA, 2014. ACM.
- [5] Monika Henzinger, Sebastian Krinninger, and Veronika Loitzenbauer. Finding 2-edge and 2-vertex strongly connected components in quadratic time. In *Automata, Languages, and Programming - 42nd International Colloquium, ICALP 2015, Kyoto, Japan, July 6-10, 2015, Proceedings, Part I*, pages 713–724, 2015.
- [6] William Di Luigi, Loukas Georgiadis, Giuseppe F. Italiano, Luigi Laura, and Nikos Parotsidis. 2-connectivity in directed graphs: An experimental study. In *Proceedings of the Seventeenth Workshop on Algorithm Engineering and Experiments, ALENEX 2015, San Diego, CA, USA, January 5, 2015*, pages 173–187, 2015.

DO EMISSION POLICIES REDUCE OZONE RISK TO EUROPEAN FORESTS?

Alessandro Anav^{1*}, Alessandra De Marco¹

¹ *Italian National Agency for New Technologies, Energy and the Environment (ENEA), C.R. Casaccia, S. Maria di Galeria, Italy.*

ABSTRACT. Air pollution interacts with climate change in affecting forest health. How ozone risk to forests responds to this interaction is mostly unknown. Control of ozone injury has been identified as an important measure to safeguard forest ecosystem services. Here we assessed the risk to European forests in the period 2001-2014. Using an atmospheric chemistry model (CHIMERE), we found that ozone concentrations declined following successful control strategies over the emission of ozone precursors. As a consequence, also AOT40, i.e. the accumulation of ozone concentrations >40 ppb, declined, especially in Southern Europe. However, Europe is moving towards a new metric for ozone risk assessment, namely the phytotoxic ozone dose (POD_y) that incorporates the effects of climate on the stomatal uptake of ozone into the plant. Ozone, in fact, is injurious to plants only after uptake through the stomata and stomata respond to climate. We found that the effects of the on-going climate change, in particular higher temperature, compensated for the effects of reduced ozone concentrations on POD₀. Forest protection against the negative impacts of ozone thus requires new strategies that integrate climate policies and air quality policies.

1 Introduction

Ozone (O₃) is an air pollutant that induces respiratory health effects in humans and impairs growth and productivity in plants. It is a secondary pollutant that is formed by reactions among precursors, in particular nitrogen oxides (NO_x), volatile organic compounds (VOC), carbon monoxide (CO) and methane (CH₄). In the Northern hemisphere, O₃ concentrations have almost doubled in the past century. Control measures over the emission of precursors have successfully reduced the peaks in the past 20 years in Europe, thus we wonder how European forests respond to this reduced concentration.

The present legislative standard for plant protection in Europe is the AOT40, i.e. the accumulation of the atmospheric concentrations of O₃ exceeding 40 ppb, over the daylight hours of the plant growing season (Directive 2008/50/EC). The negative effects on vegetation, however, do not depend only on its air concentration, as O₃ is injurious to plants only when it enters the leaves through the stomata. For such reason has been proposed a new metric for plant protection from O₃, i.e. the phototoxic ozone dose (POD_y), where y stands for the threshold of stomatal uptake above which injury to plants is assumed.

To assess how ozone stress on vegetation has changed in the last decade, we built up a multi-model framework at high spatial resolution over Europe [1]. It relies on a mesoscale model to generate climate forcing to be used offline for running a chemistry transport model (CTM). The O₃ concentrations are computed through the CTM and the climatic variables obtained by a regional weather forecast model.

^{1*} Corresponding author. E-mail: alessandro.anav@enea.it

2 Models description

Meteorological data are simulated through the Weather Research and Forecasting (WRF3.6); it is a limited-area, non-hydrostatic, terrain-following eta-coordinate mesoscale model. The model domain covers almost all Europe (except northern Scandinavia and Iceland) and part of North Africa (400x300 grid points) with a spatial resolution of 12 km [1].

To simulate gas-phase chemistry, aerosol formation, transport and deposition at regional scale we used the chemistry-transport model CHIMERE (version 2013b). The model was forced by WRF output and anthropogenic emissions, at the same spatial resolution of the atmospheric model.

Both models are parallel and have been compiled with the intel compiler and ran over CRESCO3 with 144 CPUs; the domain decomposition has been achieved with MPI.

The hourly models output, needed to assess the potential ozone impacts on forests, required a large disk space (~80T for time period 2001-2014).

Surface air temperature, surface air humidity, solar radiation and soil moisture simulated by WRF, and O₃ concentrations modelled through CHIMERE are used to assess the impacts of ozone. Two different indices are used for ozone risk assessment: 1) the AOT40, defined as the sum of the exceedances above 40 ppb computed over the whole year and when the stomatal conductance is greater than 0 and 2) an index based on stomatal O₃ uptake, where the functional amount of O₃ to which plants are exposed is defined as Phytotoxic Ozone Dose with a hourly threshold of 0 nmol O₃ m⁻² s⁻¹ (POD0) [1].

3 Results

The reduction of anthropogenic emissions translates into a reduction of simulated mean daily NO_x concentration and NMVOCs over central Europe and a relevant reduction of ozone on Southern Europe (not shown).

According to the overall O₃ reduction, AOT40 shows a decline all over Europe with the highest reductions (up to -1000 ppb h y⁻¹) in Southern Europe, while the spatial distribution of POD0 has a rather patchy structure with some area showing increasing/decreasing trend (**Fig. 1, upper panels**).

The overall annual European-averaged AOT40 trend is negative, indicating a weaker ozone injury on forests, while POD0 exhibits a positive trend, suggesting that ozone is still a problem for forest protection in Europe (**Fig. 1, lower panels**). This response is due to the effects of the on-going climate change on the stomatal uptake of O₃, in particular to the increased air temperature which increases stomatal opening and thus O₃ uptake.

We believe that the positive feedback between climate change and POD0 will be stronger in the near future and the efforts in controlling emissions could be offset by climate changes, increasing thus the O₃ risk for vegetation. We identify three main reasons explaining the increased risk for vegetation in the near future: 1) warmer temperatures promote the chemical reactions that lead to ozone formation, 2) plants emit more volatile organic compounds at higher temperatures, which, in turn, can increase ozone formation, 3) warmer temperatures lead to increased stomatal conductance, hence higher O₃ uptake.

Our results suggest that new strategies integrating both climate policies and air quality policies are needed to protect forests against the negative impacts of O₃.

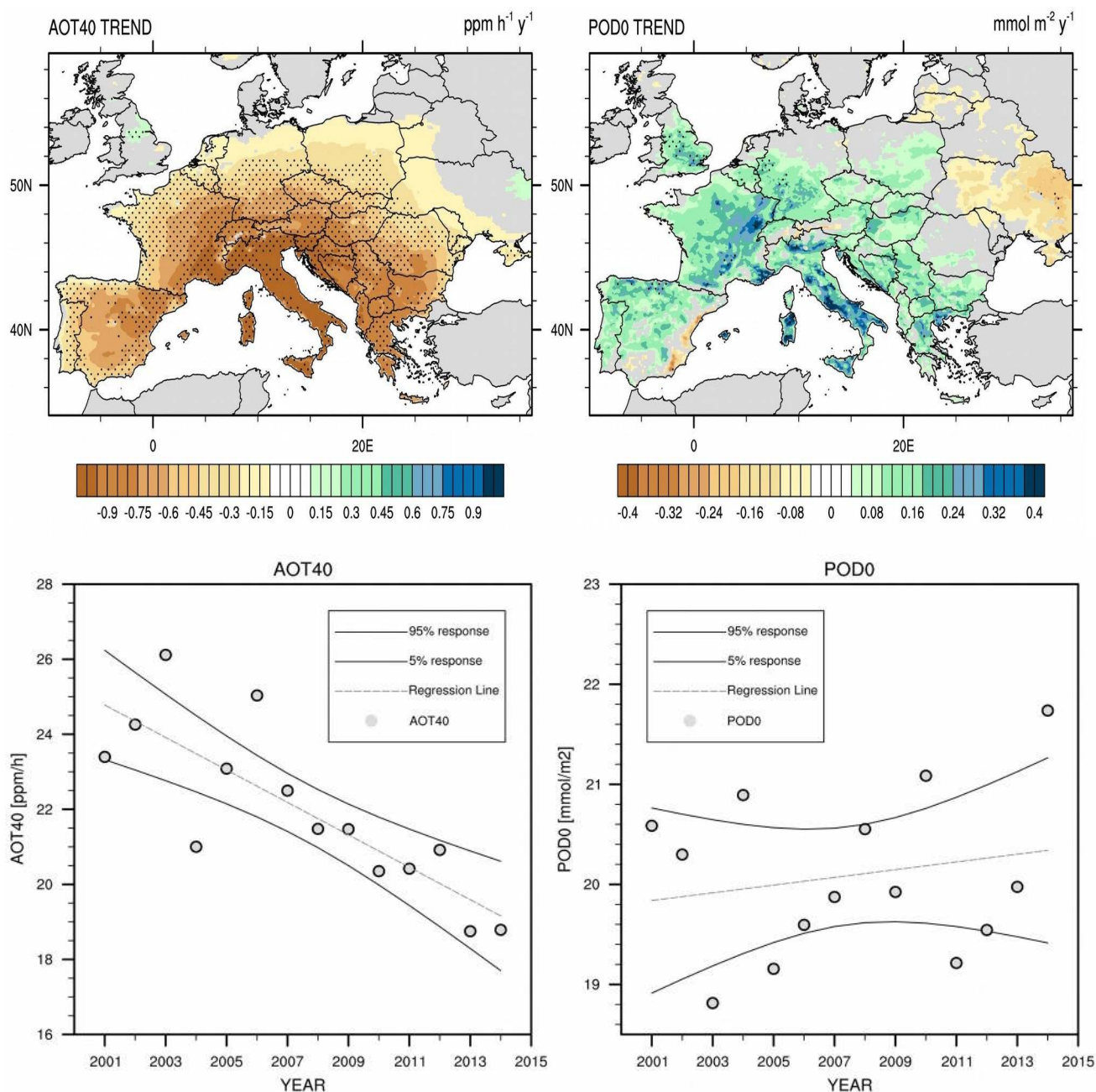


Fig 1. Spatial pattern of AOT40 and POD0 trends (upper panes); stipples indicate trends that are statistically significant at 95% confidence level (two tailed t-test). Lower panels show the yearly variability of AOT40 and POD0 averaged over the domain along with regression lines and 95% confidence interval.

References

- [1] ANAV A., DE MARCO A., PROIETTI C., ALESSANDRI A., DELL'AQUILA A., CIONNI I., FRIEDLINGSTEIN P., KHVOROSTYANOV D., MENUT L., PAOLETTI E., SICARD P., SITCH S., VITALE M. "Comparing concentration-based (AOT40) and stomatal uptake (PODY) metrics for ozone risk assessment to European forests". *Global Change Biology* **22** (2016) pp. 1608-1627.

MULTIDECADAL HINDCAST OF THE MEDITERRANEAN THERMOHALINE CIRCULATION

G. Sannino^{1*}, A. Carillo¹, M.V. Struglia¹

¹ENEA SSPT-MET-CLIM via Anguillarese 301, 00123 Rome, Italy¹

ABSTRACT. Results from sensitivity studies performed with a stand-alone ocean model of the Mediterranean circulation are presented. Two high resolution climatic simulations of the thermohaline circulation, using different prescription of the fresh water forcing, are compared.

1 Introduction

The Mediterranean area is recognized as one of the region of the planet that can be more sensitive to climate change. The complex topography of the area gives rise to meteorological phenomena characterized by intense air-sea fluxes, triggering localized deep water formation processes which determine the thermohaline circulation (THC) of the whole basin. The need of better understanding the different climate components and their interactions in the Mediterranean region resulted in different international modeling initiatives. The work presented here has been developed as part of the Med-CORDEX initiative [1] in which an ensemble of climate simulations for the Mediterranean basin is produced, using different state of the art regional atmospheric and oceanic models. The models have been run in stand-alone and coupled configurations. ENEA has participated to Med-CORDEX developing a new version of the Mediterranean ocean model. A series of simulations has been performed on CRESCO in order to define the better setup of the model in the perspective of developing the fully coupled regional ocean-atmosphere model.

2 Experiments description

The model used by ENEA is a 3D ocean circulation model (MITgcm) developed by Marshall et al. [2,3] at the Massachusetts Institute of Technology, that represents the state of the art of the ocean numerical models. The model has been used in its hydrostatic, implicit free-surface, partial step topography formulation [4]. MITgcm is designed to run on different platforms, from scalar to vectorial and can be easily compiled on a huge number of different clusters. MITgcm is written in pure Fortran77. MITgcm is parallelized via MPI through a horizontal domain decomposition technique that is the common practice for atmospheric and ocean models.

The MITgcm has been already customized by ENEA for the simulation of the Mediterranean circulation and the validation has been presented in [5].

The model domain covers the entire Mediterranean Sea and has its boundary conditions in the Atlantic Ocean at 11.28 °W. The model has a horizontal resolution of 1/12° corresponding to 570x264 grid points. In the vertical the model is discretized using 75 unevenly spaced Z-levels going from 1 m at the surface to about 300 m in the deepest part of the basin.

¹ Corresponding author. E-mail: gianmaria.sannino@enea.it

The ocean model has been forced by the net heat flux and fresh water flux derived by a downscaled atmospheric simulation of ERA-interim reanalysis [6]. All the simulations have been run on the CRESCO4 cluster and shared the same forcing data, corresponding to the period October 1979 - December 2012.

The choice of a realistic atmospheric forcing allows to check the ability of the models to reproduce the mean observed THC, however some care is necessary in the modalities of assignment of the surface boundary conditions when used in stand-alone ocean simulations, in order to avoid the temporal drift of the model sea temperature and salinity. Usually sea surface temperature (SST) and salinity (SSS) are relaxed toward reference values through a restoring term.

An alternative solution is to add a constant correction with monthly frequency. The correction is computed averaging the SSS relaxation term obtained in a companion simulation, performed using the restoring term. Such a correction has the advantage of not altering either the spatial or the temporal variability of the realistic atmospheric freshwater flux, thus allowing a better investigation of those processes and events strictly linked to interannual variability and local forcings. A series of simulations has been performed to study the effect of different surface forcings, here we present the results of two companion simulations, differing only for the surface salinity flux correction. The first simulation, has been performed restoring SSS to the climatology with a relaxation time length of 1.8 days, and will be referred to in the following as the reference simulation. The second one has the same settings but the constant correction term previously described is adopted.

3 Results

The formation of intermediate and deep waters due to sinking of dense water is one of the fundamental processes taking place in the Mediterranean Sea, in both the Eastern and Western sub-basins. The regions interested by this process are the Gulf of Lion, the South Adriatic, the Cretan Sea and the Rhode Gyre. A diagnostic variable frequently used to identify deep-water formation events is the Mixed Layer Depth (MLD), which is related to thermodynamic properties of the seawater. It is defined as the depth from the surface characterized by a homogeneous density, principally due to the vertical mixing. The highest values reached by the mixed layer depth are both related to strong air sea processes taking place at the surface during winter months, and to the preexisting stratification of the whole water column.

Figure 1 shows the winter (DJFM) climatological mean of MLD for the two simulations considered. Both simulations correctly identify the convective regions, however the flux corrected run shows a more active convective vertical mixing that reaches deeper ocean levels over more extended areas. In Figure 2 the yearly maximum MLD over the Gulf of Lion region and the average over the area of the maximum MLD for the reference simulation and for the flux corrected one are shown. The resulting interannual variability is quite different between the two runs as the flux corrected simulation responds more efficiently to the intensity of the atmospheric forcing. The comparison of maximum and mean values of MLD (solid and dashed lines) gives a hint of the yearly spatial extension of the convective region, that in the flux corrected run is characterized by higher variability. There is observational evidence [7,8] of strong convective events in the Gulf of Lion during years 1987, 2005 and 2012. All of these events are found both in the maximum MLD and in the spatial average series of the flux corrected simulation, while they are less evident in the reference one.

These results are very promising in the light of the fully coupled atmospheric-ocean model. They prove the ability of the model to follow the observed variability of the deep water formation also when the relaxation is not applied, as in coupled runs.

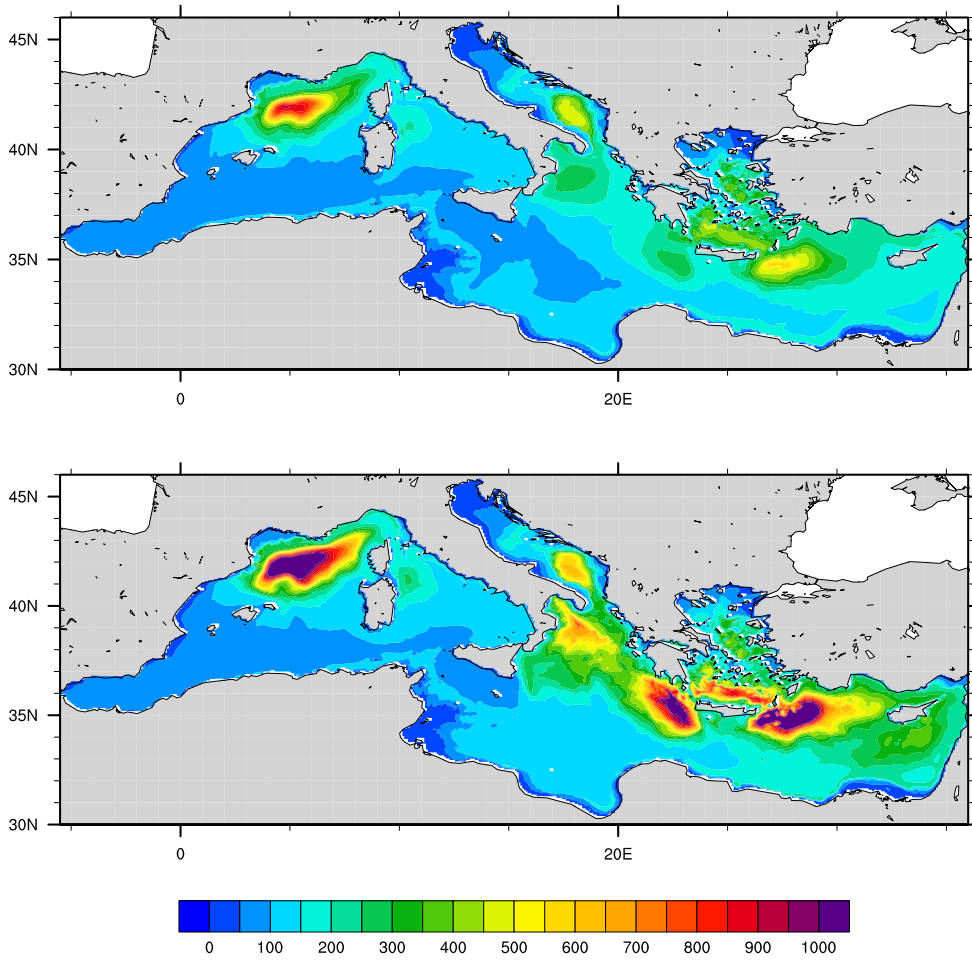


Fig.1: Climatological winter mean of MLD (in meters) for the reference simulation (upper panel) and for the flux corrected simulation (lower panel).

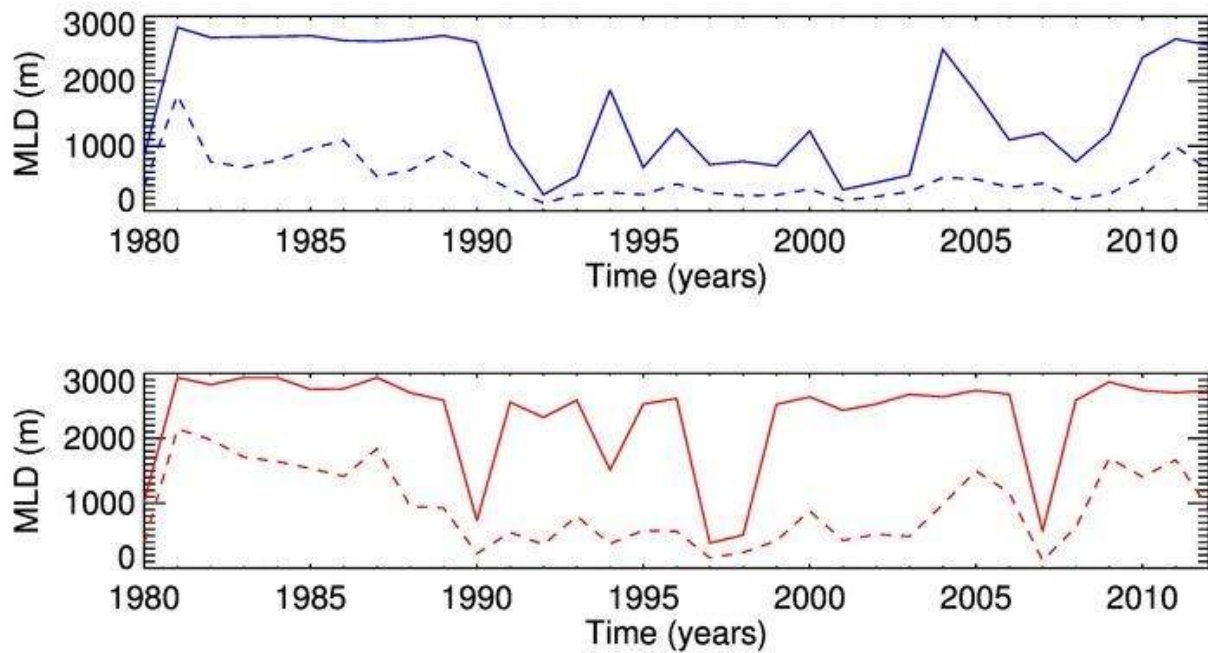


Fig.2: Interannual variability of the MLD (in m) over the Gulf of Lion. Yearly maximum (solid line) and area averaged of yearly maximum (dashed line) for the reference simulation (blue) and for the flux corrected (red).

References

- [1] RUTI P.M. et al. “*Med-CORDEX Initiative for Mediterranean climate studies*”. Bulletin of the American Meteorological Society, American Meteorological Society, **97**-7 (2016), pp.1187-1208. DOI: 10.1175/BAMS-D-14-00176.1
- [2] MARSHALL J., ADCROFT A., HILL C., PERELMAN L., HEISEY C. “*A finite-volume, incompressible Navier Stokes model for studies of the ocean on parallel computers*”. J. Geophys. Res. 102 -C3 (1997) pp. 5753–5766.
- [3] MARSHALL J., HILL C., PERELMAN L., ADCROFT A. “*Hydrostatic, quasi-hydrostatic, and nonhydrostatic ocean modeling*”. J. Geophys. Res. 102 - C3 (1997) pp. 5733–5752.
- [4] ADCROFT A., HILL C., MARSHALL J. “*Representation of topography by shaved cells in a height coordinate ocean model*”. Monthly Weather Review 125 9 (1997), pp. 2293–2315
- [5] SANNINO G. CARILLO A. and PALMA M. “*A high-resolution 46-year hindcast for the Mediterranean Basin*”. In: High Performance computing on CRESCO infrastructure: research activities and results 2012- ISBN 978-88-8286-302-9
- [6] HERRMANN M., SOMOT S., CALMANTI S., DUBOIS C., SEVAULT F. “*Representation of daily wind speed spatial and temporal variability and intense wind events over the Mediterranean Sea using dynamical downscaling : impact of the regional climate model configuration*”, Nat. Hazards Earth Syst. Sci., 11, 1983-2001, (2011) DOI:10.5194/nhess-11-1983-201
- [7] BORGHINI M., BRYDEN H., SCHROEDER K., SPARNOCCHIA S. and VETRANO A: “*The Mediterranean is becoming saltier*”. Ocean Sci. 10, 693-700, 2014. DOI:10.5194/OS-10-693-2014
- [8] MERTENS C. and SCHOTT F. (1998). “*Interannual Variability of Deep-Water Formation in the Northwestern Mediterranean*”, Journal of Physical Oceanography, 28, 1410-1424

The core design of Gen-IV Lead Fast Reactors using the ERANOS code on the CRESCO HPC infrastructure

Massimo Sarotto^{1*}, Giacomo Grasso², Francesco Lodi³

¹ENEA, FSN-SICNUC-PSSN, C.R. Saluggia, Strada per Crescentino 41 – 13040 Saluggia (VC) ¹

²ENEA, FSN-SICNUC-PSSN, C.R. “E. Clementel”, Via Martiri di Monte Sole 4 – 40129 Bologna

³ALMA MATER STUDIORUM UniBo, Faculty of Engineering, Via Zamboni 33, 40126 Bologna

ABSTRACT. Among the six innovative reactor concepts selected by the Generation IV International Forum, the Lead Fast Reactor is gaining consideration as one of the most promising candidates to fulfil the vision for a new generation of nuclear energy systems more safe, clean, economical and proliferation resistant. Inspired by its potentialities, an industrial-scale system was developed by an European consortium along with its demonstration reactor named ALFRED. The preliminary design of ALFRED, put forward within the EURATOM FP7 LEADER project, is now being further developed in the frame of the Programmatic Agreement between ENEA and the Italian Ministry for Economic Development. ENEA, as the responsible for the core design, is presently refining the analyses and the design leveraging on the CRESCO HPC infrastructure, on which state-of-the-art codes - such as the neutronic deterministic code ERANOS - and tools (like the Fortran compiler and the Python interpreter) are available. An overview of the undergoing actions and main achievements, along with some examples of the typical neutronic figures, are here reported.

1 Introduction

In the last years the EURATOM community co-funded different projects for the design of advanced nuclear reactors, by adopting the leading criteria selected by the Generation IV International Forum (GIF), which stand on superior safety, reliability, sustainability, economic competitiveness and proliferation resistance [1]. The Lead Fast Reactor (LFR) is one of the six reactor concepts indicated by the GIF and one of the three chosen by the European Sustainable Nuclear Industrial Initiative (ESNII) [2]. As a fast reactor, the closure of the fuel cycle can be addressed, permitting to reduce by about 2 orders of magnitude: the U consumption, the actinide mass going to geological disposals and the fuel waste long-term radio-toxicity. Furthermore, unparalleled safety features can be targeted leveraging on the inherent properties of the lead coolant, with the possibility of using passive means for the control of the plant even in ultimate conditions.

With this promising perspective, the EURATOM 7th Framework Program (FP7) launched the Lead-cooled European Advanced DEMonstration Reactor (LEADER) project, whose main goal was the preliminary design of the Advanced Lead Fast Reactor European Demonstrator (ALFRED) [3]. In the LEADER project, led by Ansaldo Nucleare (Italy) and gathering 17 partners coming from research institutions, universities and private companies, ENEA had the responsibility to coordinate the core design activities. Afterwards, the ALFRED core design was further refined within the framework of the Programmatic Agreement between ENEA and the Italian MiSE (Ministero dello Sviluppo Economico) in order to correct some revealed criticalities and to establish a new reference design [4-5]. For this purpose, several neutronic calculations were carried out by means of the ERANOS code, running on the CRESCO HPC infrastructure. This report briefly summarises:

- the main characteristics of the ERANOS deterministic code (ported to CRESCO) in §2;
- the main features of the ALFRED core design in §3;
- the typical results of the ERANOS neutronic analyses of the ALFRED core in §4, graphically represented by means of an ad-hoc python script also running on CRESCO.

¹ massimo.sarotto@enea.it

2 Computational tools: ERANOS code and python language

In the European context, ERANOS is the established reference deterministic code for fast reactors analysis. This powerful tool is a complex system that consists of different modules spawning from reactivity analysis to flux assessment, from burn-up evolution to reaction rates evaluation, etc. of a nuclear system in 1, 2 and 3D domains described by cartesian, cylindrical or hexagonal geometries. Despite the fact that ERANOS is a serial code, it is installed on the HPC clusters of the CRESCO infrastructure to take profit of several features, such as:

- each node of CRESCO is equipped with fast processors and a wide amount of RAM, thereby permitting short execution times for each computation;
- the number of available nodes permits launching a number of different instances of the code in parallel (*e.g.*, for parametric investigations), each without impairing the availability of computational resources to the others;
- being CRESCO a shared resource, the installation of a centralized copy of ERANOS permits all authorized users to dispose of an official and (mostly) duly checked, verified and constantly updated version of the code, along with the associated neutron data libraries.

The neutronic analyses for the ALFRED core design (see §3) were performed in ENEA with the ERANOS ver. 2.2 deterministic code [6] coupled with the JEFF3.1 neutron data library [7]. The macroscopic cross-sections of the different core regions were produced by the ECCO cell code in a 1968 energy-group structure and condensed to the standard structure at 33 groups [8]. The macroscopic cross-sections were then used for full core calculations carried out in ERANOS with the TGV module [9], by adopting a 3D hexagonal geometry model of the core (see Fig. 1).

In reactor core studies, the (radial and axial) power distributions are among the main information to be provided as input for the Thermal-Hydraulic (TH) and safety analyses. Then, such data are worth to be illustrated especially for radial distributions in hexagonal geometries: therefore, the python programming language (available on CRESCO) was utilised for their graphical representation (§4).

3 The ALFRED core design

The ALFRED core - 300 MW_{th} power - was designed by taking into account the main technological constraints of LFR systems along with the target performances aimed for this demonstrator, such as [3]: the narrow Temperature (T) range (400/480 °C as core inlet/outlet T), the limiting T for the steel cladding (550 °C), the maximum Pu enrichment (<30%) in the Mixed OXide (MOX) fuel, the achievement of a peak burn-up of 100 GWd/t, the respect of the system integrity even in extreme conditions, etc.. Therefore, the core design was challenging and required many scoping neutronic calculations: for this purpose, the utilisation of a deterministic code resulted to be more suitable for its flexibility and reduced calculation times (especially in comparison with Monte Carlo codes).

The left part of Fig. 1 depicts the plan view of the ALFRED Fuel Assembly (FA): the wrapped hexagonal FA is made of 126 MOX fuel pins arranged in six rows (in a triangular lattice) and of the central structural pin (*i.e.*, an empty clad). The right part of Fig. 1 shows a quarter of the core layout having a 90° symmetry [3]. The core layout, successively refined in [4-5], is essentially made of:

- 57 inner FA and 114 outer FA, having the same architecture but a different Pu enrichment in the fuel in order to flatten the core radial power distribution;
- 12 Control Rods (CR) that enter partially the active region from the bottom during irradiation (to compensate the initial over-criticality) and are progressively withdrawn as far as the refuelling condition is reached (with a fuel cycle made of 5 batches, each 1 year long);
- 4 Safety Rods (SR) located at the core centre, which stay still atop the active zone during normal operation and, in emergency cases, enter the core by gravity to shutdown the reactor;
- the surrounding dummies, having the same structure of the FA but with pins filled by YZrO pellets, acting as reflector for both neutron economy and shielding of the inner vessel.

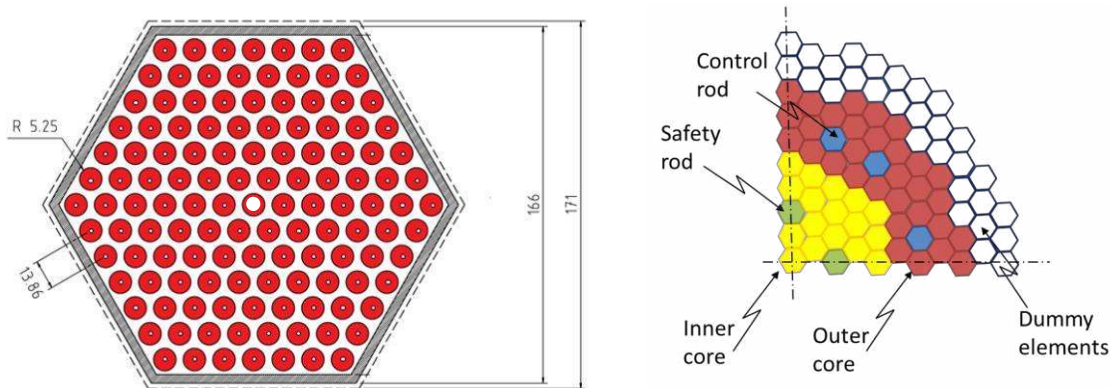


Fig.1: ALFRED FA design (left, [mm]) and core layout (right).

4 The typical neutronic results

The following graphs, created with an in-house post-processing script in python language, give an idea of the level of detail achieved in the ERANOS neutronic analyses of the ALFRED core. Fig. 2 shows the power distributions obtained in nominal conditions: the left part depicts the FA power at the Beginning of Cycle (BoC), while the right part depicts the FA power at the End of Cycle (EoC). By keeping in mind the position of the 12 CR in the outer core zone (see Fig. 1) indicated by white hexagons in Fig. 2, it appears evident that the hot FA belongs to the inner zone at BoC (when the CR are partially inserted) and to the outer zone at EoC (when the CR are completely withdrawn).

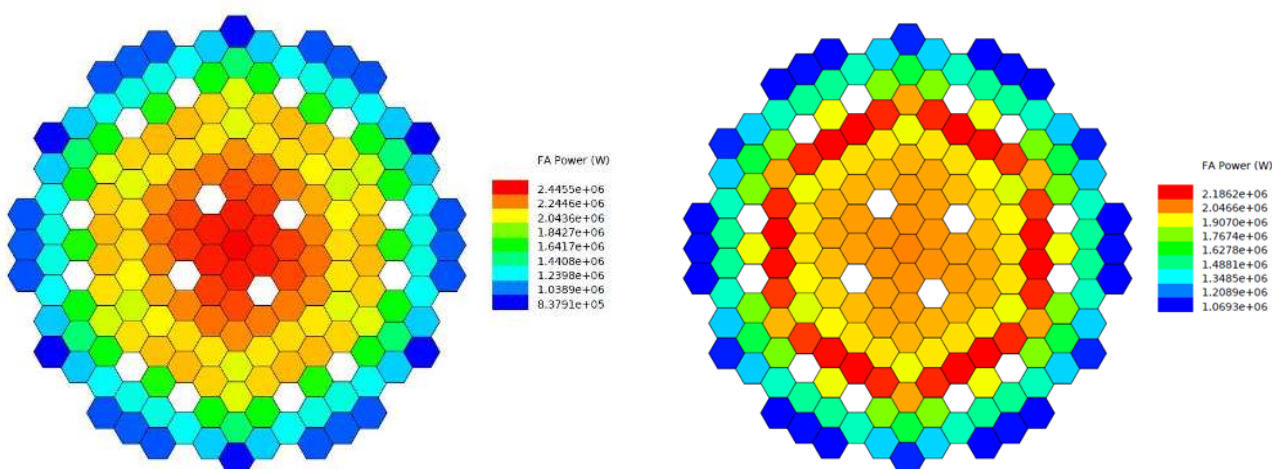


Fig.2: ALFRED core power distributions at BoC (left) and EoC (right).

Fig. 3 shows the power distributions in the hot FA at the level of pin at BoC (left) and EoC (right). The hot pin (in the hot FA) is located toward the centre of the FA at BoC (since, for symmetry reasons, the hot FA is placed in the centre of the inner zone), while it is located at the corner of the FA pointing to the core center at EoC (since the hot FA belongs to the outer zone). To reconstruct the pin power distributions of Fig. 3, an ad-hoc post-processing routine was written in Fortran, to extract the results at the level of single cell as obtained by the ECCO module (in which an accurate 2D hexagonal model of the FA is used, §2) and to super-impose on them data interpolated from the TGV results, which embed information on the shape of the flux in the core.

It can be finally remarked that the neutronic results obtained with ERANOS are being used for detailed TH and transient analyses, with the ultimate goal of quantifying the safety margins of such innovative LFR systems. As an example, Fig. 4 reports the coolant outlet T distributions obtained in

the hot FA at BoC (left) and EoC (right). These results - graphically represented through a python procedure - were obtained by means of the sub-channel code ANTEO+ (ANalisi TERmodraulica Ottimizzata), developed in-house at ENEA specifically for the liquid metal (*e.g.*, Na, Pb and Pb-Bi) cooled systems envisaged in the GIF roadmap [10]. Currently, ANTEO+ is running on a local server, but it will be soon ported to CRESCO in order to make it available to all the ENEA users.

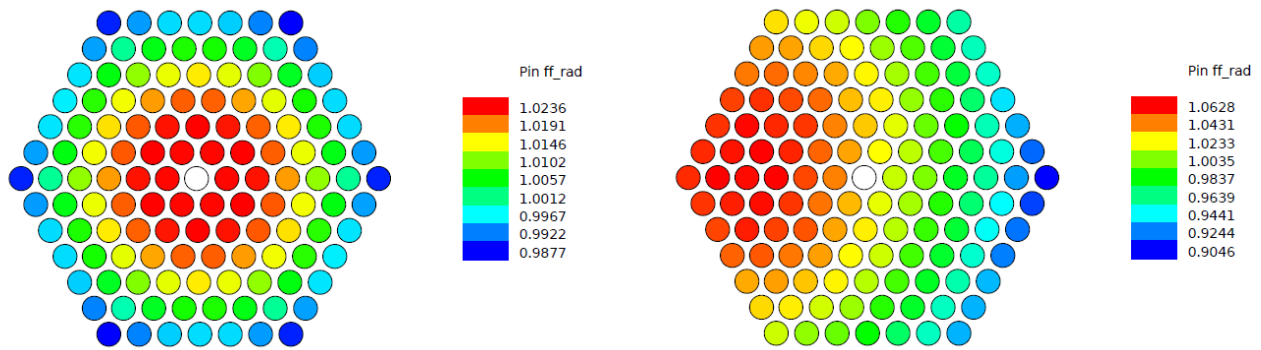


Fig.3: Pin power distributions (in terms of the radial form factor, ff_{rad} , defined as the ratio between the power of each pin and that of the average one) in the hot FA at BoC (left) and EoC (right).

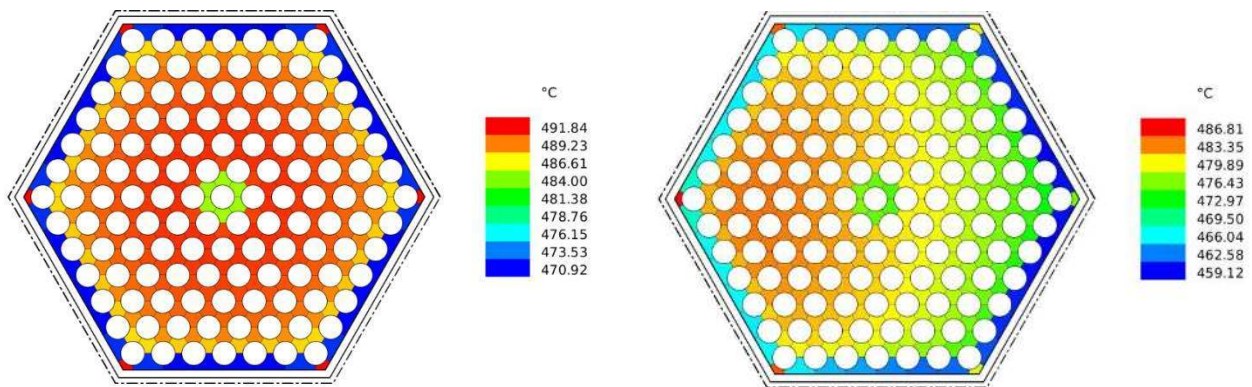


Fig.4: Coolant outlet T in the hot FA at BoC (left) and EoC (right) obtained with the ANTEO+ code.

References

- [1] OECD/NEA, 2014. Technology Roadmap Update for Gen. IV Nuclear Energy Systems, ..
- [2] ESNII, 2013. Strategic Research and Innovation Agenda of the European Sustainable Nuclear Industrial Initiative, <http://www.snetp.eu/>.
- [3] GRASSO, G., *et al.*, 2014. The core design of ALFRED, a demonstrator for the European lead-cooled reactors, Nucl. Eng. and Des., Vol. 278, 287-301.
- [4] GRASSO, G., *et al.*, 2014. Ottimizzazione del progetto di nocciolo di ALFRED. Ricerca di Sistema Elettrico, Technical Report ADPFISS-LP2-050.
- [5] LODI, F., *et al.*, 2015. Characterization of the new ALFRED core configuration. Ricerca di Sistema Elettrico, Technical Report ADPFISS-LP2-085.
- [6] RIMPAULT, G., *et al.*, 2002. The ERANOS code and data system for Fast Reactor neutronic analyses, Proc. Int. Conf. PHYSOR 2002, Seoul, Korea, *October 7-10*.
- [7] KONING, A. *et al.*, 2006. The JEFF-3.1 Nuclear Data Library, OECD/NEA N_6190, JEFF Report 21.
- [8] RIMPAULT, G., 1997. Physics documentation of Eranos: the Ecco cell code, CEA report DERSPRC-LEPh-97-001.
- [9] RUGGERI, J.M., *et al.*, 1993. TGV: a coarse mesh 3 dimensional diffusion-transport module for the CCRR/ERANOS code system, CEA report DRNR-SPCILEPh-93-209.
- [10] LODI, F., *et al.*, 2016. ANTEO+: a sub-channel code for thermal-hydraulic analysis of liquid metal cooled systems, Nucl. Eng. and Des., Vol. 301, 128-152.

Surface functionalization of ZnO for solar energy conversion devices: new insights from a first-principles study

Antonio M. Rodríguez¹, Ana B. Muñoz-García¹, Claudio De Rosa¹ and Michele Pavone^{1*}

¹University of Naples Federico II, Department of Chemical Sciences, Via Cinita 26 80126 Naples, Italy¹

ABSTRACT. ZnO is a wide band gap and transparent semiconductor with good chemical stability and peculiar optoelectronic properties that motivated its wide use in technological devices. In latest generation hybrid solar cells, ZnO has been also exploited as functional constituent in composite materials that are capable of efficient charge generation and transport. In this context, we applied state-of-the-art first-principles methods on the most relevant ZnO NPs surfaces to study how molecular capping agents can affect the electronic properties of the ZnO. In particular, we focused on electronic features that are relevant for solar energy conversion devices (e.g. band gap, work function, band edge absolute positions). We evaluated these properties when the NP surfaces are covered with the molecules that are used in NP synthesis such as aliphatic amines. All the specific molecule-surface interactions are discussed from a quantum-mechanical perspective, thus identifying the key features that modulate the ZnO opto-electronic properties.

1 Introduction

Zinc Oxide (ZnO) based materials present good chemical stability and peculiar optoelectronic properties, which have motivated applications in several technological devices: optical waveguides, chemical and gas sensors, UV emitters and solar cells are few examples. The great interest in these applications inspired several experimental and theoretical studies that addressed the structure-property relationships in zinc oxides nanostructures [1-3]. In the context of solar energy conversion devices, for example, systems made of conjugated polymers and *n*-type ZnO nanoparticles (NPs) have showed promising performances in hybrid bulk-heterojunction cells [4,5]. One strategy to synthesize these ZnO NPs is by using molecular capping agents in the NPs grown environment, which interact with the growing ZnO lower index surfaces, affecting the final NPs morphologies and physico-chemical properties. At the same time, the different surfaces that are exposed and the specific chemical interactions with the capping molecules can affect the optoelectronic properties of the final ZnO NPs. Thus, the capping agents can be exploited for tuning the ZnO NP properties toward specific applications as in solar conversion devices: understanding the main features of these interactions and their effects on the ZnO electronic structure is therefore key for the rational design of new devices. To this end, we present here a first-principle study based on density functional theory (DFT) addressing the structural and electronic modifications of ZnO two apolar surfaces, (10-10) and (11-20), when interacting with an amine-based capping molecule, which is used in the experimental synthesis of the ZnO NPs [6].

2 Methods and computational details

All the calculations were performed with spin-polarized DFT within the generalised-gradient approximation of Perdew-Burke-Ernzerhof (PBE) [7], using the periodic super-cell approach as implemented in the VASP code [8]. Dispersion correction was taken into account with semi-empirical approach of Grimme (D3BJ) [9]. Nuclei and core electrons were modelled using the projector augmented wave (PAW) method, while for valence electrons the plane-wave basis set was expanded up to a kinetic-energy cut-off value of 750 eV. The surface models included a vacuum space larger than 15 Å along the direction perpendicular to the slab surfaces. For asymmetric slabs we used the self-consistent dipole correction. The electronic properties of ZnO surfaces were also refined with hybrid DFT (HSE06) single-point total energy calculations on the PBE-D3BJ minimum-energy surface structures.

* Corresponding author. E-mail: michele.pavone@unina.it

Our DFT calculations were performed on the CRESCO HPC systems with the VASP program as compiled by us with the available openmpi libraries and the intel compiler (including MKL libraries). For all the ZnO systems (surface slabs with adsorbed molecules, ~150 atoms) the equilibrium geometries were optimised on the cresco4open queues with 24h run on 256 processors at the PBE-D3BJ level of theory. These calculations required usually around 20 hours with ~65-70 optimization steps to converge with our selected thresholds, finishing when the convergence criteria were reached. For the HSE06 hybrid density functional calculations, the inclusion of explicit HF exchange increase of one order of magnitude the computational burden, and in these cases we only computed single-point total energies on PBE-D3BJ optimized structures, to achieve these values with a 24h run we exploited the cresco4open queues requiring 512 processors.

3 Results and discussion

The ZnO non-polar surfaces (10-10) and (11-20) were cleaved from the ZnO bulk structure and the corresponding surface energy (γ) values were computed according to:

$$\gamma = \frac{E_{slab} - n \cdot E_{bulk}}{2 \cdot S}$$

where E_{slab} corresponds to the energy of the slab model, E_{bulk} is the bulk energy, n represents the number of unit cells per slab model and S is the surface area. Fig.1 shows the two slab models.

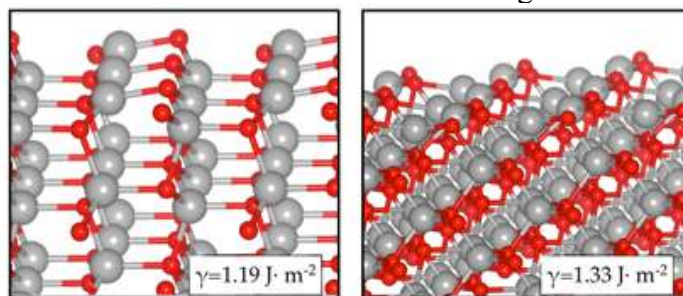


Figure 1 Slab models for ZnO (10-10) (left) and (11-20) (right) surfaces. Surface energy (γ) values are reported in the inset. Grey and red spheres represent the zinc and oxygen atoms.

We studied the structural and electronic modifications of these two ZnO surfaces, when interacting with ethylamine (See Figure 2). The adsorption energies (E_{ads}) are calculated as:

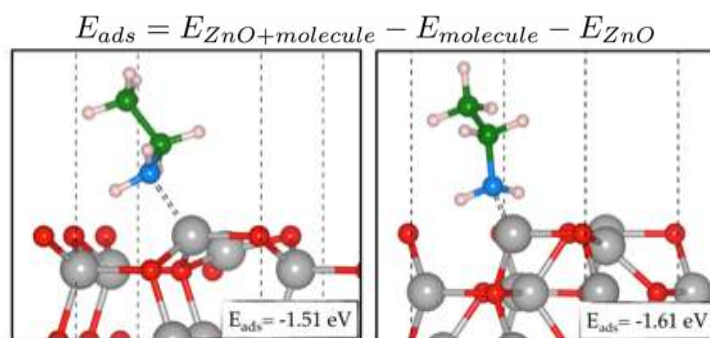


Fig. 2 Minimum-energy structure of amine adsorbed on the ZnO (10-10) (left) and (11-20) (right) surfaces.

This coverage was adopted as full monolayer coverage. To characterize the electronic structure we computed the *density of states* (DOS) with the hybrid density functional HSE06 on of the optimized geometries. The atom- and angular momentum- projected DOS (PDOS) plots are shown in Fig. 3.

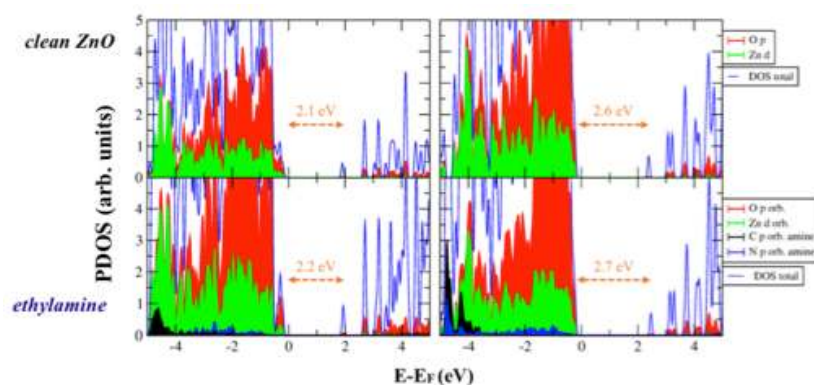


Figure 3 PDOS plots at the HSE06 level of theory for the different slabs: (10-10) (left) and (11-20) (right).

By analysis of the PDOS, we can observe a slight variation of the band gap due to the presence of the molecule. Our results are consistent with those of recent studies on ZnO. Then, we computed the workfunction, *i.e.* the minimum thermodynamic work (*i.e.* energy) needed to remove an electron from a solid (Fermi level) to a point in the vacuum far from the solid surface. The modification of the workfunction contains the complete electronic response of the slab to the absorption of the capping agent. The donor or acceptor character of the molecule can affect differently each surface. The responses to the amine adsorption on each surface are depicted by Figure 4.

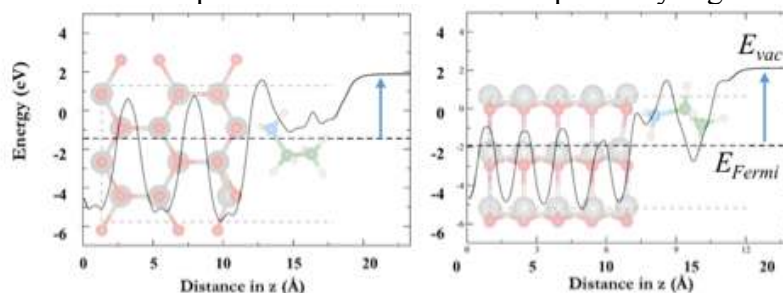


Figure 4. Interactions of ethylamine on ZnO (10-10) (left) and (11-20) (right) surfaces.

Table 1 lists the computed workfunction variations $\Delta\Phi$ at different levels of theory.

Table 1. Workfunction modifications ($\Delta\Phi$) upon amine adsorption.

Method	Surface	$\Delta\Phi$ amine (eV)
PBE(GGA)	10-10	-2.20
	11-20	-1.99
HSE06	10-10	-2.30
	11-20	-1.98

From these results it appears that the workfunction shift is quite insensible to the level of theory. Moreover, we found that this workfunction variation presents a linear behaviour with an incremental coverage of the amine substrate (see Figure 5).

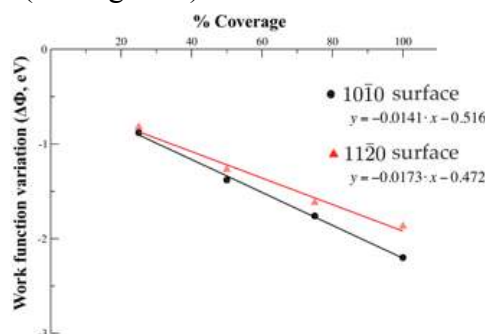


Figure 5. $\Delta\Phi$ values at different coverage of amine on ZnO surfaces.

This result can be useful to finely tune the response of a ZnO NP by controlling the substrate coverage on its surfaces. The results are in good agreement with those obtained experimentally on SAMs. From the workfunction position and the bandgap we can compute the absolute positions of the band edges, the conduction band minimum (CBM) and the valence band maximum (VBM) [10]. For application related to solar energy conversion, these edge states should be positioned particularly in relation to the redox reaction potentials, $E_{\text{CBM}} > E_{\text{red}}$ and $E_{\text{VBM}} < E_{\text{ox}}$ (Figure 6).

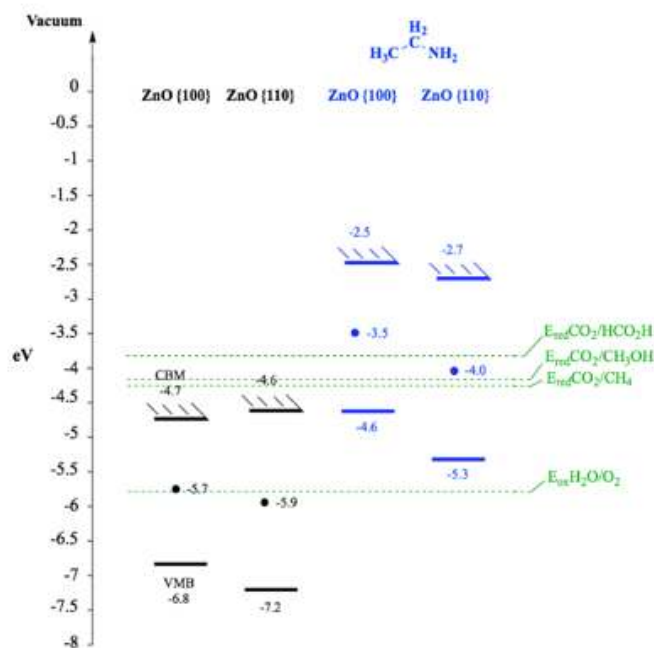


Figure 6. Absolute band edge positions vs the redox reaction potential of some redox potentials.

Conclusions and perspectives

In this study we have exploited the CRESCO HPC facilities to investigate the interaction of ZnO non-polar surfaces with a prototypical capping agent, ethyl amine, used in the synthesis of colloidal ZnO NPs. Our objective has been to set-up and validate a theoretical protocol to study heterogeneous interfaces as the target system. We have tested PBE and HSE06 density functionals. Structural features are well described by PBE, while band gap values are better predicted by the hybrid HSE06 functional. Workfunction variations upon molecular adsorption are much less sensitive to the choice of the density functional. With our validated model, we observed a clear trend for workfunction variation with increasing coverage of the capping agent on the ZnO surfaces. These preliminary results can already help the engineering new hybrid organic-inorganic nanocomposite systems for applications in solar energy conversion devices. The present study paves the route to more advance simulations for considering also the effects of the chemical environment (solvent, polymer matrices) and to address complex charge transfer processes at the interfaces.

References

- [1] MEYER B., MARX D., “Density-functional study of the structure and stability of ZnO surfaces”. Phys. Rev. B **67** (2003), pp 035403.
- [2] IVANOV I., POLLMANN J., “Electronic structure of ideal and relaxed surfaces of ZnO: A prototype ionic wurtzite semiconductor and its surface properties”. Phys. Rev. B **24** (1981), 7275-7296.
- [3] IGLESIAS-JUEZ A., VIÑES F., LAMIEL-GARCIA O., FERNANDEZ-GARCIA M., ILLAS F., “Morphology effects in photoactive ZnO nanostructures: photooxidative activity of polar surfaces”. J. Mater. Chem. A **3** (2015), pp 8782-8792.

- [4] BEEK W. J., WIENK M. M., KEMERINK M., YANG X., JANSSEN R. A., “Hybrid zinc oxide conjugated polymer bulk heterojunction solar cells”. *J. Phys. Chem. B* **109** (2005), 9505-9516.
- [5] LIN Y., DAGA V. K., ANDERSON E. R., GIDO S. P., WATKINS J. J., “Nanoparticle- Driven Assembly of Block Copolymers: A Simple Route to Ordered Hybrid Materials”. *J. Am. Chem. Soc.* **133** (2011), pp 6513-6516.
- [6] COZZOLI P. D., CURRI M. L., AGOSTIANO A., LEO G., LOMASCOLO M., “ZnO Nanocrystals by a Non-Hydrolytic Route: Synthesis and Characterization”. *J. Phys. Chem. B* **107** (2003), pp 4756-4762.
- [7] (a) PERDEW J. P., BURKE K., ERNZERHOF M., “Generalized Gradient Approximation Made Simple”. *Phys. Rev. Lett.*, **77**, (1996), pp 3865-3868; (b) PERDEW J. P., BURKE K., ERNZERHOF M., “Generalized Gradient Approximation Made Simple”. *Phys. Rev. Lett.*, **78**, (1997), pp 1396.
- [8] (a) KRESSE G., HAFNER J., “Ab initio molecular dynamics for liquid metals”. *Phys. Rev. B*, **47** (1993), pp 558-561; (b) KRESSE G., HAFNER J., “Ab initio molecular-dynamics simulation of the liquid-metal–amorphous-semiconductor transition in germanium”. *Phys. Rev. B*, **49** (1994), pp 14251-14269; (c) KRESSE G., FURTHMÜLLER J., “Efficiency of ab-initio total energy calculations for metals and semiconductors using a plane-wave basis set”. *Comput. Mat. Sci.*, **6**, (1996), pp 15-50.
- [9] (a) GRIMME S., ANTONY J., EHRLICH S., KRIEG H., “A consistent and accurate ab initio parametrization of density functional dispersion correction (DFT-D) for the 94 elements H-Pu”. *J. Chem. Phys.*, 2010, **132**, 154104; (b) GRIMME S., EHRLICH S., GOERIGK L., “Effect of the damping function in dispersion corrected density functional theory”. *J. Comput. Chem.*, **32**, (2011), pp 1456-1465.
- [10] TOROKER M. C., KANAN D. K., ALIDOUST N., ISSEROFF L. Y., LIAO P., CARTER E. A., “First principles scheme to evaluate band edge positions in potential transition metal oxide photocatalysts and photoelectrodes”. *Phys. Chem. Chem. Phys.* **13**, (2011) pp 16644-16654.

CAR-PARRINELLO MOLECULAR DYNAMICS OF LIQUID NaNO_3

Roberto Grena¹, Massimo Celino

ENEA, C. R. Casaccia, via Anguillarese 301, 00123 Roma, Italy

ABSTRACT. Liquid nitrates are among the most interesting fluid for heat transfer applications (e.g. in solar plants), yet their characterization is far from complete, and few molecular dynamics studies can be found in literature (none of them using ab-initio method). In this paper the simulation of the most common of these salts (NaNO_3), in liquid phase at 500 °C, is presented, showing its feasibility. The methods can be applied to more complex systems, such as mixtures (e.g. the “solar salt”, a $\text{NaNO}_3/\text{KNO}_3$ mixture, or ternary mixtures containing LiNO_3), and can be used to predict changes in properties in dependence of the relative concentrations or the temperature.

1 Introduction

Molten nitrates are the subject of great interest because candidate to be used as heat storage systems and heat transfer fluids for solar power plants [1]. These fluids enable thermal energy to be stored for extended periods of time, thereby allowing intermittent solar energy to be converted to electricity in a continuous manner. A typical solar salt consists of a mixture of NaNO_3 and KNO_3 . These materials have many favorable properties, including a good thermal stability, low cost, and negligible toxicity. One concern with these mixtures is the melting point: the 60/40 mixture has a solidus temperature of about 220 °C.

In order to use salt mixtures in such processes, several properties must be determined, including heat capacity, thermal conductivity, viscosity, and melting point. It is desirable to have ways of accurately predicting molten salt properties without recourse to extensive experimental studies. One way of doing this is via molecular simulation.

In this work we present a Car-Parrinello simulation of NaNO_3 in liquid state. The aim of the work is mainly to show the feasibility of the full simulation (no constraints are imposed on NO_3^- geometry), well reproducing both the ionic and the covalent interaction (a difficult task for empirical potentials, see [2]), and showing that the technique, initially checked against the NaNO_3 crystal structure, can be applied to the liquid state, without transferability problems.

2 Computational details

All the calculations were performed by using the QuantumEspresso (QE) software [3]. QE is an ab-initio electronic structure and MD program using a plane-wave/pseudopotential implementation of Density Functional Theory (DFT) [4,5]. The software performs Car-Parrinello molecular dynamics too [6]. The GGA functional of Perdew-Burke-Enszerhof (PBE) was used in the computation [7].

The liquid system was simulated in a supercell containing 270 atoms (54 NaNO_3 units). The initial configuration was chosen placing randomly Na atoms and NO_3 units in the cell, with a minimal distance allowed; the configuration obtained was then relaxed in order to reduce the excessive (unphysical) interatomic forces, and then the system was thermalized, increasing the temperature at

¹ Corresponding author. E-mail: roberto.grena@enea.it.

a rate around 100 K/ps, up to 773.15 K (500 °C). In order to estimate the volume, two runs were made with densities of 1.7 g/cm³ (a value close to the experimental one) and 1.9 g/cm³, computing the resulting pressure P and then interpolating to find the volume for $P = 0$. Due to the presence of different interactions (ionic and covalent) and different time scales in the atomic motion, a low fictitious electron mass (100 au) and a short time step (2 au) were required to achieve stability. The simulated time interval for the thermalized system was around 10 ps.

The simulation was run on 256 cores on Cresco4 system. About 50 runs of 24 hours each were required to achieve 10 ps of simulated time.

3 Results

Preliminary computations performed on the crystal phase of NaNO₃ for testing the computational method show a good reproduction of the crystal geometry, obtaining a perfect hexagonal geometry with values of $a = 5.104$ Å, $c/a = 3.2658$ Å, N-O = 1.267 Å; the two parameters a and c have a difference within 1% with respect to the experimental values, and the distance N-O is overestimated by 2%.

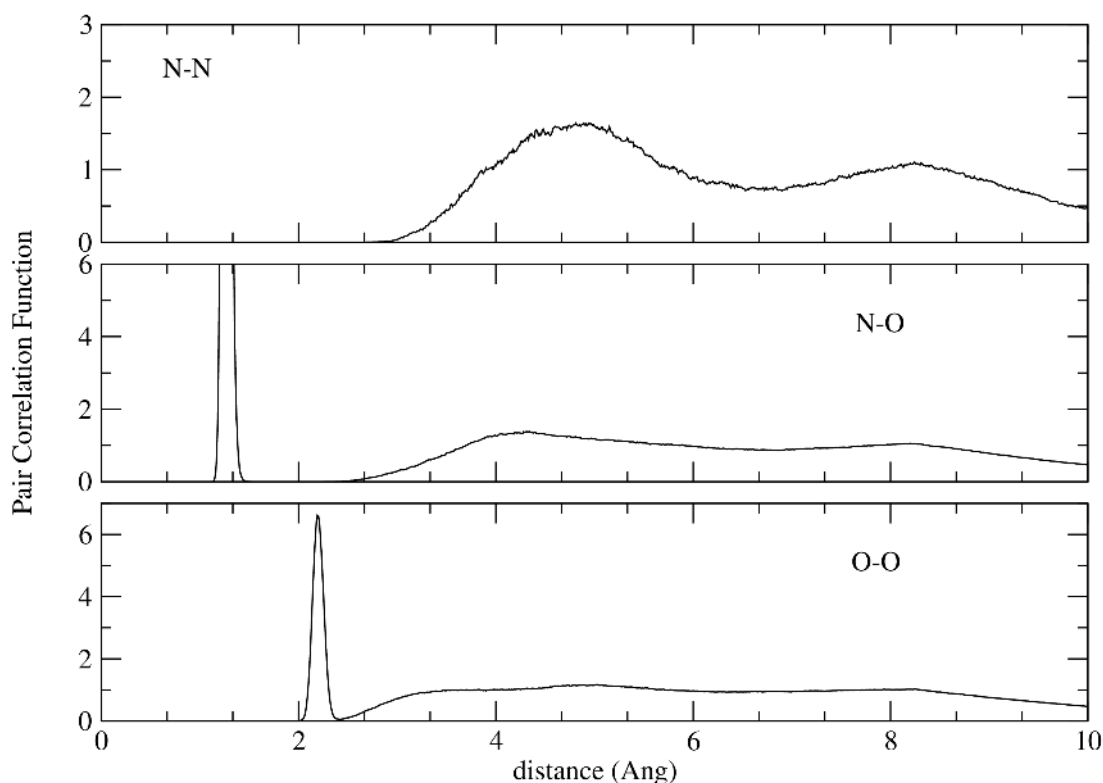


Fig. 1: Pair correlation functions relative to N and O atoms.

The density of the molten NaNO₃ at 500 °C is computed at 1.745 g/cm³, in excellent agreement with experimental data of 1.740 g/cm³ [8]. Figures 1 and 2 shows six pair correlation functions (pcf), for different atomic species. N-O and O-O pcf evidences the nitrate ion stability (the pcfs are characterized by a high peak at the distances N-O and O-O in the anion NO₃⁻); at 500 °C, no evident

perturbations of the NO_3^- systems occur. For larger distances, the two pcfs do not show special features, indicating a high degree of disorder in the system; the same holds for the two pcfs of Na-Na and N-N, showing that, except for the obvious tendency of the same charge ions to avoid each other. More interesting is the pcfs of Na-N (or Na-O), showing a first quite pronounced peak around 2.5 Å (for Na-N) and 2.25 Å (for Na-O). These peaks have no relations with the crystal structure, and in the liquid the relative positions that ions have in the crystal are not privileged.

In summary, distribution functions appear quite typical for a disordered liquid, with the main features given by the presence of NO_3^- units and by the ionic attraction.

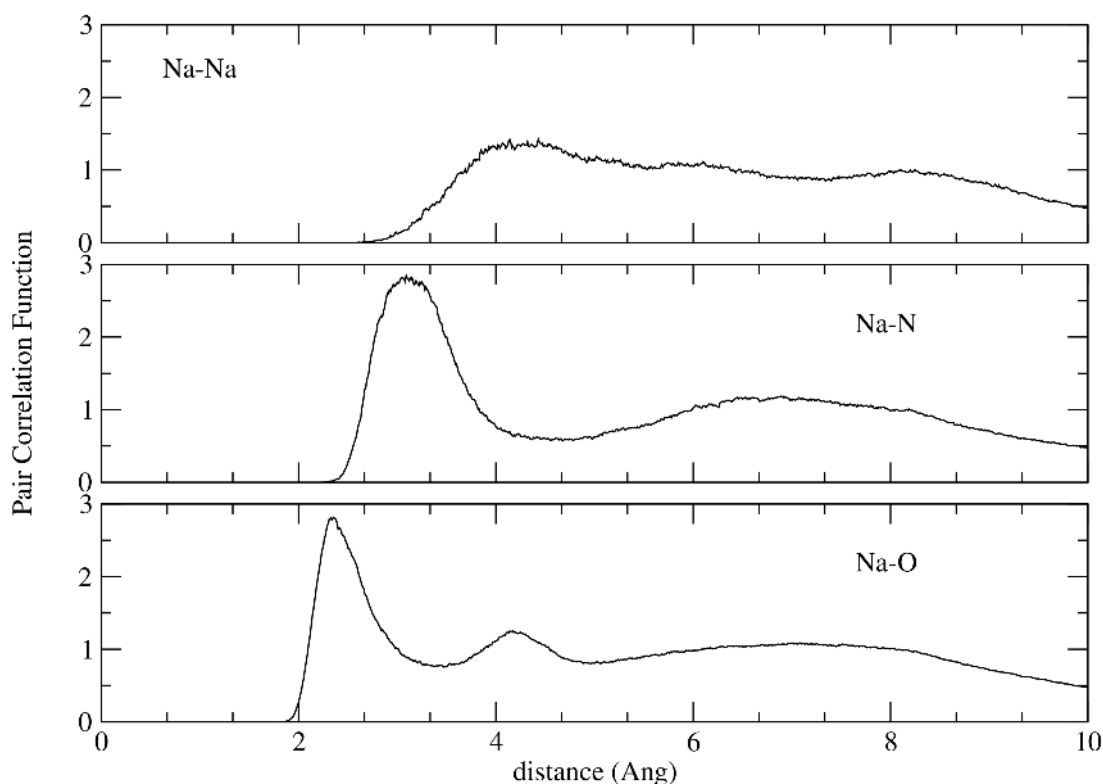


Fig. 2: Pair correlation functions involving Na atoms.

4 Conclusions

An ab-initio simulation of molten NaNO_3 has been performed with Car-Parrinello molecular dynamics, showing its feasibility and discussing the first results. The good agreement with experimental density at 500 °C show that the system is realistic. Pair distribution functions among the various atom speceis has been computed and discussed, evidencing their features: the distributions are typical of disordered liquids, but with some effects due to the ion interaction.

These first results show that the ab-initio simulation of a molten nitrate is feasible, and it can give useful informations on the atomic-scale structure of the liquid. However, macroscopic quantities of technological interest could be computed too, with a longer simulation time and, possibly, a larger system. Heat capacity, viscosity, electrical conductivity and thermal conductivity can be computed from molecular dynamics; the latter is especially interesting due to the difficulties in its measurement. All the computed quantities, microscopic or macroscopic, can be computed in

dependence of the temperature in all the working range of the salts. But the most interesting possibility is probably the simulation of mixtures of different compositions, studying the dependence of various properties from the composition; this could replace a large experimental campaign that would require the study of tens of different samples to obtain the dependence from the relative concentrations of the components.

A final remark should be made on the fact that ab-initio computations can be used to build highly transferable classical potentials, with the force-matching method. This could allow to perform large scale classical MD in order to investigate the melting of mixtures and phase diagrams, an extremely interesting task for technological applications.

Acknowledgements

The computing resources and the related technical support used for this work have been provided by CRESCO/ENEAGRID High Performance Computing infrastructure and its staff [9]. CRESCO/ENEAGRID High Performance Computing infrastructure is funded by ENEA, the Italian National Agency for New Technologies, Energy and Sustainable Economic Development and by Italian and European research programmes, see <http://www.cresco.enea.it/english> for information. This work was supported by the project “Accordo di Programma - Ricerca di Sistema Elettrico” funded by the Italian Ministry of Industrial Development.

References

- [1] PLUKIENER R., RIDIKAS D. “*Modelling of HTRs with Monte Carlo: from a homogeneous to an exact heterogeneous core with micro particles*”. *Annals of Nuclear Energy* **30** (2003) pp. 1573-1585.
- [2] JACKSON R.J., MORT K.A. “*Computer modelling of complex molecular ionic materials*”. *Computational Materials Science* **17** (2000) pp. 230-233.
- [3] GIANNOZZI P. et al. “*QUANTUM ESPRESSO: a modular and open-source software project for quantum simulations of materials*”. *Journal of Physics: Condensed Matter* **21** (2009) 395502.
- [4] HOHENBERG P., KOHN W. “*Inhomogeneous electron gas*”. *Physical Review* **136** (1964) pp. B864-871.
- [5] KOHN W., SHAM L.J. “*Self-consistent equations including exchange and correlation effects*”. *Physical Review* **140** (1965) pp. A1133-1138.
- [6] CAR R., PARRINELLO M. “*Unified Approach for Molecular Dynamics and Density-Functional Theory*”. *Physical Review Letters* **55** (1985) pp. 2471-2474.
- [7] PERDEW J.P., BURKE K., ERNZERHOF M. “*Generalized Gradient Approximation Made Simple*”. *Physical Review Letters* **77** (1995) pp. 3865–3868.
- [8] HONGMIN Z. et al. “*Ultrasonic velocity and absorption-coefficient in molten alkali-metal nitrates and carbonates*”. *Journal of Japanese Institute of Metals* **55** (1991) pp. 937–944.
- [9] PONTI G. et al. “*The role of medium size facilities in the HPC ecosystem: the case of the new CRESCO4 cluster integrated in the ENEAGRID infrastructure*”. *Proceedings of the 2014 International Conference on High Performance Computing and Simulation, HPCS 2014*, art. no. 6903807, pp. 1030-1033.

FIRST-PRINCIPLE DETERMINATION OF EQUILIBRIUM AND OUT OF EQUILIBRIUM EXCITED STATE PROPERTIES OF SURFACES AND 2D MATERIALS

Margherita Marsili^{1*}, Olivia Pulci², Maria Stella Prete², Adriano Mosca Conte² and Paola Gori³

¹ *Dipartimento di Fisica e Astronomia, Università di Padova, via Marzolo 8, I-35131 Padova, Italy*

² *ETSF and Dipartimento di Fisica, Università di Roma Tor Vergata, Via della Ricerca Scientifica 1, I-00133 Rome, Italy*

³ *Roma Tre University, Department of Engineering, Via della Vasca Navale 79, 00146 Rome, Italy*

ABSTRACT. In this report we account for the studies we carried out in the last year using the ENEA-CRESCO facilities. Our studies were mainly devoted on the first-principle determination of ground and excited state properties of 2D systems (surfaces and monolayers). In particular here we report our results concerning the simulation of the transient absorption of monolayer MoS₂, of the low-coverage structure of tartaric acid on Cu(110), and of the electronic and optical properties of 2D nitrides.

1 Transient absorption in monolayer MoS₂

Transition metal dichalcogenides monolayers recently raised great interest for potential optoelectronics and spintronics applications [11] and for the fundamental study of the behaviour of matter at low dimensionalities. Transient absorption (TA) spectroscopy monitors the change over time of the optical properties of a material after it has been driven out of equilibrium by a laser pump. It thus provides a wealth of information on excitation and carrier relaxation processes. The equilibrium absorption spectrum of monolayer MoS₂, one of the best characterized material of this class, is well known [4] and studied. It is characterized by two, strongly bound, spin-orbit-split, excitonic transitions, namely the A and B excitons, at 2.1 eV and 2.2 eV, and a loosely bound exciton, namely the C exciton, at 2.6 eV, see Fig. 1. Interestingly, it was found that, regardless of the excitation energy, i.e. either pumping at the energy of the A, B or C exciton, the same features appear in the MoS₂ experimental TA spectra. In all cases simultaneous bleaching of the three excitonic structures and, correspondingly, the presence of photoinduced absorption at lower energies [6] are found.

1.1 Theoretical approach and codes

To simulate TA spectroscopy we employ a novel first-principle theoretical approach capable to describe both the excitonic character of MoS₂ excited states and the coupling with the laser pump through

*Corresponding author. E-mail: margherita.marsili@nano.cnr.it.

the combination of density-functional and non equilibrium Green’s function theories [13, 5, 3]. The calculation method involves basically two steps: (1) the determination of the non-equilibrium population of the electronic bands due to the laser pump; (2) the calculation of the perturbed response function. In the presence of an external time-dependent potential the evolution of the electronic system can be described by the Kadanoff-Baym equations (KBE) [15]. In particular, in our approach, we follow the evolution of the lesser Green’s function $G^<$ by propagating its equation of motion. From $G^<$ ’s diagonal elements we obtain the non-equilibrium population of the single-particle electronic states [2]. From the knowledge of the non-equilibrium population, in the *adiabatic* approximation and assuming we are in the weak pump field regime [5], we re-compute the optical absorption spectra, either keeping fixed or recomputing the poles of the response functions. For the determination of the ground state properties of our system, i.e its geometry, total energy, single-particle Kohn-Sham orbitals, etc..., we employed density-functional theory (DFT) [10, 12] by using the electronic structure code pw.x of the Quantum Espresso suite [8] which makes use of plane-wave basis set and pseudopotentials [16]. The codes that was used for the determination of equilibrium and non equilibrium excited state properties is the Yambo suite [1]. Both codes are open source, released under the GPL licence, make use of LAPACK and BLAS libraries, and present a hybrid MPI and OpenMP parallelism. The Yambo code makes also use of the NETCDF libraries which were installed locally by one of the users. All run were performed on the CRESCO 4 cluster, using between 64 and 1200 cores (mainly 128 and 256).

1.2 Results

The knowledge of the time-dependent off-diagonal elements of $G^<$ allows to compute the time-dependent polarization function $P(t)$. If the external electric field $E(t)$ is delta-like, then, by Fourier transforming $P(t)$, we obtain the optical susceptibility; this is the so called time-dependent Bethe-Salpeter (TDBSE) approach [2].

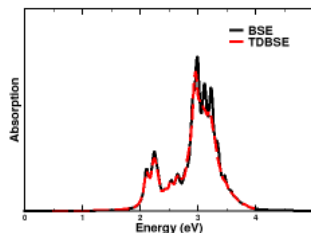


Figure 1: TDBSE absorption spectrum (dashed-red) compared to standard BSE.

In Fig. 1 we see that indeed by using the TDBSE approach the BSE spectrum is recovered. This is an important step in order to check if the scheme is working properly and in order to determine the excitation energies at which the simulated system responds.

We then simulate the ultrafast laser pump by using a sinusoidal time-dependent external potential convoluted with a Gaussian function, centered at the frequency of the excitonic peaks. In the left panel of Fig. 2 we show the generated carrier density upon pumping at the A, B, C exciton energies and off-resonance close (+0.1 eV) to the C peak. As expected, the carrier density is proportional to the intensity of the optical susceptibility at the pumping frequency, and this is clearly shown in the right panel of Fig. 2 where the carrier density is renormalized by the optical susceptibility value.

Once the excited carrier population is known, TA spectrum can be calculated at different levels of sophistication. At low pumping, i.e. low carrier densities regime, the excitation energies of the system (the poles of the response function) could in principle be considered fixed at their equilibrium values.

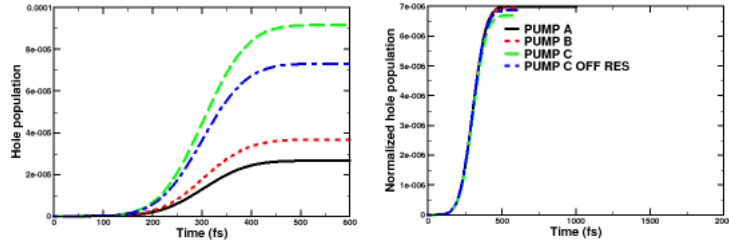


Figure 2: Carrier population

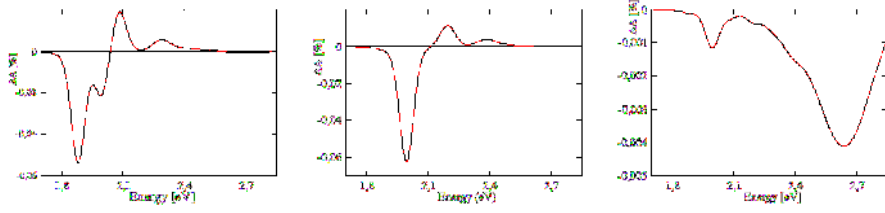


Figure 3: Mo₂ TA spectra including only the effect of Pauli blocking. Left panel: pump A; center panel: pump B; right panel: pump C.

In this way we describe and isolate the, so called, Pauli Blocking effect (PBE). Within the PBE the TA features are ascribed to a different availability of electronic states that quenches possible excitations thus changing the way the systems absorbs light. In the left panel of Fig. 3 we show the TA spectra at the three pumping frequencies including the PBE. We see that there is a bleaching (negative signal) only at the pumping energy, and no photoinduced absorption (positive signal) appears.

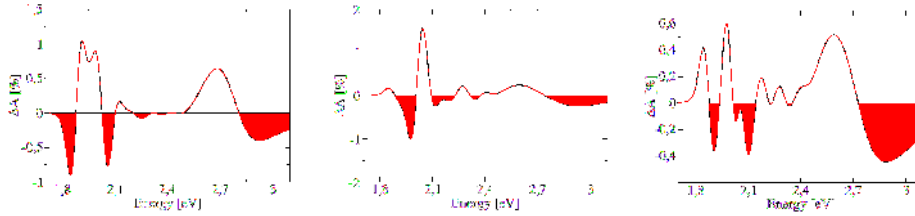


Figure 4: Mo₂ TA spectra including the variation of excitation energies. Left panel: pump A; center panel: pump B; right panel: pump C.

We next take into account the possibility that also the excitation energies are affected by the excited state carrier population. We found that the excitation energies change is mainly affected by the change in the electronic screening. The increased screening capability of the system reduces the binding energy of the excitons and, at the same time, it reduces the quasi-particle gap. These two effects only partially compensate each other and the absorption of the system changes. When we include these effects we obtain the results shown in the right panel of Fig. 4. In this case we recover a stronger agreement with experiments: a bleaching of all the peaks appears, and also photoinduced absorption is present.

2 Low-coverage structure of Tartaric Acid on Cu(110)

Tartaric Acid (TA) presents several different adsorption phases on Cu(110), depending on coverage and temperature [9, 7]. At low coverage ($\theta < 1/6$ monolayer) the doubly deprotonated bicarboxylate form of the molecule interacts with the surface, giving rise to a globally chiral surface with $(90, \pm 12)$ reconstruction for (R,R)- or (S,S)-bitartrate. The adsorption geometry of the (R,R)-bitartrate has been determined by means of DFT calculations using the plane-wave pseudopotential code Quantum Espresso (5.2.0 version) [8]. The number of cores typically used was 256, with parallelization both on k -points and on R and G space. The employed pseudopotentials make use of a semilocal generalized gradient approximation with a Perdew-Burke-Ernzerhof (GGA-PBE) treatment of exchange and correlation energy. A kinetic energy cutoff of 25 Ry was used in the plane-wave expansion. The system was represented in a repeated slab approach, with a $(90, 12)$ surface cell to describe the corresponding adsorption phase. The Cu(110) surface was modeled by a seven-layer slab separated by 25 Å vacuum from its periodic replicas along the direction perpendicular to the surface. The surface Brillouin zone was sampled by a 2×4 Monkhorst-Pack mesh of k -points. The system was relaxed using the Broyden-Fletcher-Goldfarb-Shanno algorithm until the forces on each ion were reduced below 10^{-4} a.u.. Results show that the

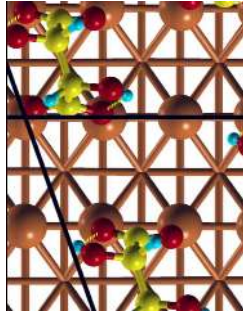


Figure 5: Adsorption geometry of the $(90, 12)$ -phase of (R,R)-TA on Cu(110).

lowest-energy structure (reported in Fig. 5) comprises bitartrate TA molecules stabilized by intramolecular H-bonds (denoted by yellow dashed lines in Fig. 5) and whose adsorption is dictated by a mechanism of stress release of the underlying copper atoms. This makes it more favorable for TA molecules to form, upon adsorption, stripes that are aligned along the $[1-14]$ direction of the substrate, instead than along the $[-110]$ direction of Cu(110) that would allow TA interaction through intermolecular H-bonds.

3 Ab-initio Study of 2D Nitrides

With the aim to develop new light harvesting devices based on 2D Nitrides, we have started a systematic study of the geometric, electronic and optical properties of 2-dimensional group III Nitrides BN, AlN, GaN, InN and TiN. Our results about the geometry and the electronic properties are obtained within Density Functional Theory (DFT-LDA). In all cases we have found that stable unbuckled 2D honeycomb geometries (graphene-like) are stable. Geometric properties and electronic band gap strongly depend on elements nature of compound honeycomb structure. In particular gap opening occurs, due to the different electronegativity of group III elements and Nitrogen, and the electronic gap is often indirect. In Fig 6 we show that with the increasing of the group-III atomic number Z , that is with the increasing of the covalent radii, the 2D lattice constants increase up to 50%, the gaps decrease up to almost 100%, and the 2D dielectric constant increases following the expected chemical trends. As regards the optical properties we have estimated binding energies E_b and the radii r_{exc} of the excitons of this class of materials with a simple analytical model for excitons in two dimensions [14]. We can see in Fig 6 that

going from BN to TiN the excitonic binding energy also decreases, with an increase of the exciton radius, due to the more efficient screening of the electron-hole interaction.

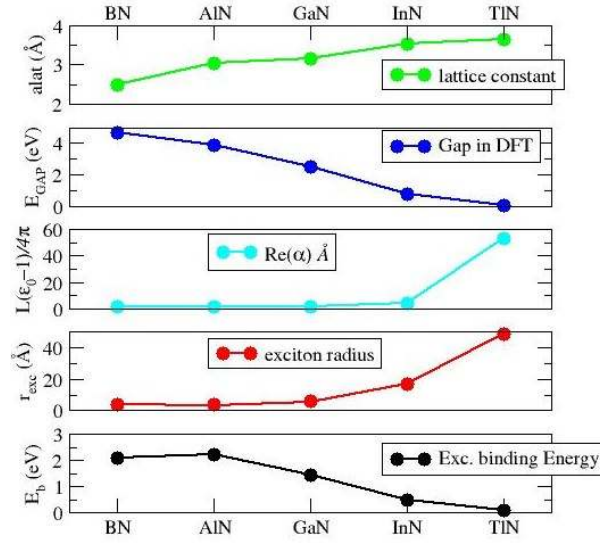


Figure 6: Lattice constant, energy gap (direct), and excitonic results for the III-N sheets compounds studied.

The results demonstrate that 2D sheets possess strongly bond excitons due to the interplay of low dimensionality, depressed screening and the presence of a gap. The only exceptions seems to be TiN that has zero gap. Confinement effect and reduced 2D screening strongly enhance excitonic effects, creating electron-hole pairs with large (\sim eV) binding energy and tunable optical gap, making these materials good candidates for novel optoelectronic devices.

References

- [1] M. Gruning A. Marini, C. Hogan and D. Varsano. *Comput. Phys. Commun.*, 180:1392, 2009.
- [2] M. Gruning C. Attaccalite and A. Marini. *Phys. Rev. B*, 84:245110, 2011.
- [3] C. Manzoni G. Cerullo A. Marini D. Sangalli, S. Dal Conte. *Phys. Rev. B*, 93(19):195205, 2016.
- [4] F.H da Jornada D.Y. Qiu and S.G. Louie. *Phys. Rev. Lett*, 111:216805, 2015.
- [5] A. Marini E. Perfetto, D. Sangalli and G. Stefanucci. *Phys. Rev. B*, 92:205304, 2015.
- [6] D. De Fazio S. Dal Conte C. Manzoni D. Sangalli D. Yoon A. Lombardo A.C. Ferrari A. Marini G. Cerullo E.A.A. Pogna, M. Marsili and D. Prezzi. *ACS Nano*, 10(1):1182–1188, 2016.
- [7] D.A. Duncan et al. *Surface Science*, 606:1435–1442, 2012.
- [8] P. Giannozzi et al. *J. Phys.: Condens. Matter.*, 21:395502, 2009.
- [9] V. Humblot et al. *J. Am. Chem. Soc.*, 126:6460–6469, 2004.
- [10] P. Hohenberg and W. Kohn. *Phys. Rev.*, 136:864, 1964.
- [11] J. Shan K.F Mak, K. He and T.F. Heinz. *Nat. Nanotechnol.*, 7:494–498, 2012.

- [12] W. Kohn and L.J. Sham. *Phys. Rev.*, 140:1133, 1965.
- [13] A. Marini. *J. Phys.: Conf. Ser.*, 427:012003, 2013.
- [14] V. Garbuio P. Gori I. Kupchak F. Bechstedt O. Pulci, M. Marsili. *Phys. Status Solidi b*, 252:72–77, 2012.
- [15] G. Stefanucci and R.. van Leeuwen. *Nonequilibrium Many-Body Theory of Quantum Systems: A Modern Introduction*. Cambridge University Press, 2013.
- [16] N. Troullier and J.L. Martins. *Phys. Rev. B*, 43:1993, 1991.

STUDY OF THE *Zr* DOPING IN THE CERIUM OXIDE THROUGH FIRST-PRINCIPLES CALCULATIONS

F. Rizzo* and G. de Marzi

ENEA, FSN C.R. Frascati, Via Enrico Fermi 45, 00044, Frascati (Rm), Italy

ABSTRACT. The effect of *Zr* doping in CeO_2 is studied using Density Functional Theory (DFT) calculations with the inclusion of the on-site Coulomb correction (DFT+U). A 96-atoms supercell is considered for introducing a doping level x in the system $Ce_{1-x}Zr_xO_2$. The structural and electronic properties of $Ce_{1-x}Zr_xO_2$ are compared to the corresponding properties of the pure cerium oxide CeO_2 compound. Preliminary results show that increasing the doping level x decreases the stability of the compound. The crystal structure is locally distorted. The presence of *Zr* locally decreases the distance with the *O* atoms. Also the Density of States is slightly affected by the introduction of *Zr* atoms in the cerium oxide crystal structure.

1 Introduction

Cerium oxide CeO_2 is a versatile compound studied both as an efficient oxygen storage system in catalysis processes and also as an effective seed layer in thin film deposition processes, able to promote the proper epitaxial growth of superconducting $ReBa_2Cu_3O_{7-x}$ (*YBCO*, $Re = RareEarth$) coated conductor tapes.

This material is peculiarly prone to modify its oxygen content ($CeO_{2-\delta}$), thus leading to a variation of both its structural and electronic properties. In the case of the *YBCO* epitaxial growth, moderate changes of the structural properties could strongly affect the amount of stress due to the lattice mismatch and consequently worsen the quality of the superconducting film.

In particular, in the Metal-Organic Decomposition (MOD) deposition process the high temperatures involved during the growth of the CeO_2 buffer layers in a reducing atmosphere encourage the loss of oxygen from the cerium oxide matrix [1].

A recent experimental study suggested that the introduction of an amount x of *Zr* in the cerium oxide could prevent the oxygen loss [2]. Some theoretical studies of the $Ce_{1-x}Zr_xO_2$ system have been performed [3]-[4], however a clear understanding of the *Zr* doping role in the reducing capabilities of cerium oxide is still lacking.

This work focuses on a preliminary evaluation of the *Zr* doping effect in the variation of structural and electronic properties of $Ce_{1-x}Zr_xO_2$ with respect to the pure CeO_2 system by means of first-principles Density Functional Theory (DFT) calculations. The starting point for correctly taking into account the *Zr* doping is to consider a 96-atoms system ($2 \times 2 \times 2$ supercell). In order to validate the supercell approach, the DOS of the 96-atoms CeO_2 cell is compared with the one resulting from the canonical CeO_2 cell ($1 \times 1 \times 1$). The strongly localized nature of the $4f - Ce$ electronic states is included in the calculations through a Hubbard repulsion term U of 4.5 eV (DFT+U).

*Corresponding author. E-mail: francesco.rizzo@enea.it.

2 Computational methods

DFT+U calculations of structural and electronic properties for pure CeO_2 and $Ce_{1-x}Zr_xO_2$ were performed by using the Quantum ESPRESSO suite [5] available on CRESCO-Frascati. Calculations were done in the framework of the generalized gradient approximation (GGA) for the electron exchange and correlation terms, using the Perdew-Burke-Ernzerhof functionals (PBE) [6]. Electron-ion interactions have been modelled with ultra-soft pseudopotentials (US-PP) in the context of a plane wave expansion basis set. USPPs have allowed the usage of an energy cut-off of 40 Ry for the wave functions and 400 Ry for the electron density. The value of the lattice parameter a for pure CeO_2 supercell was chosen considering the optimized value previously obtained in the single cell description [7]. Also the Hubbard energy term $U = 4.5eV$ was derived from the single cell description [7], [8]. A Monkhorst-Pack \mathbf{k} -point $2 \times 2 \times 2$ mesh was used for the Brillouin-zone integrations.

In the case of $Ce_{1-x}Zr_xO_2$ (Fig. 1), a doping level corresponding to $x \sim 3\%$ (1/32 Zr atoms ratio) was considered. The lattice parameter value was set starting from the pure cerium oxide structure and then relaxing the crystal structure via the Broyden-Fletcher- Goldfarb-Shanno (BFGS) algorithm[9] in connection with the Parrinello-Rhman algorithm[10], to explicitly check the influence of substitutional Zr impurities on the lattice parameters of the non stoichiometric ground state CeO_2 structure. Optimizations have been performed until the convergence threshold of 10^{-3} a.u. for the total force and 10^{-1} kbar for pressure were reached.

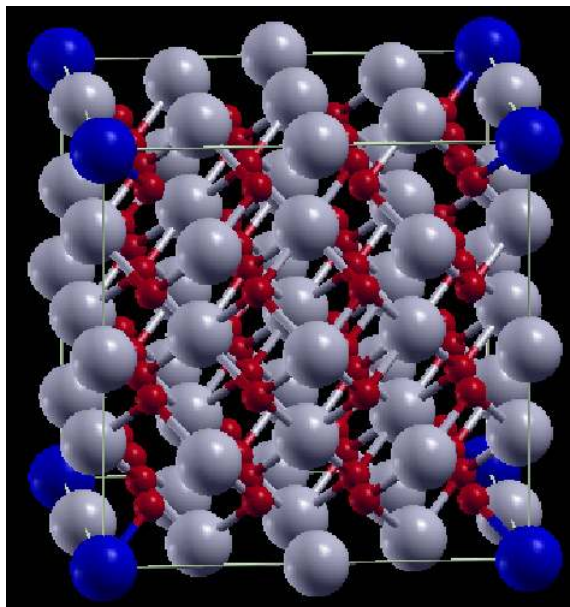


Figure 1: 96 – atoms supercell schematic representation of the Zr-doped structure. Grey atoms are Ce , blue atoms are Zr and red atoms are O .

3 Results

The optimized value for the lattice parameter in the pure cerium oxide supercell is $a_{CeO_2} = 5.52\text{\AA}$, in good agreement with the experimental value 5.41\AA [11]. The corresponding DOS, shown in Fig. 2, is in perfect agreement with the DOS previously evaluated in the single cell representation [7], validating the $2 \times 2 \times 2$ supercell approach. This system is insulating with a band gap between the highest occupied valence state and the lowest unoccupied conduction states of about 1.5 eV. From a structural point of

view, the $Ce - O$ distance is 2.39\AA , while the $O - O$ distance is 2.76\AA and the $Ce - Ce$ distance is 3.9\AA .

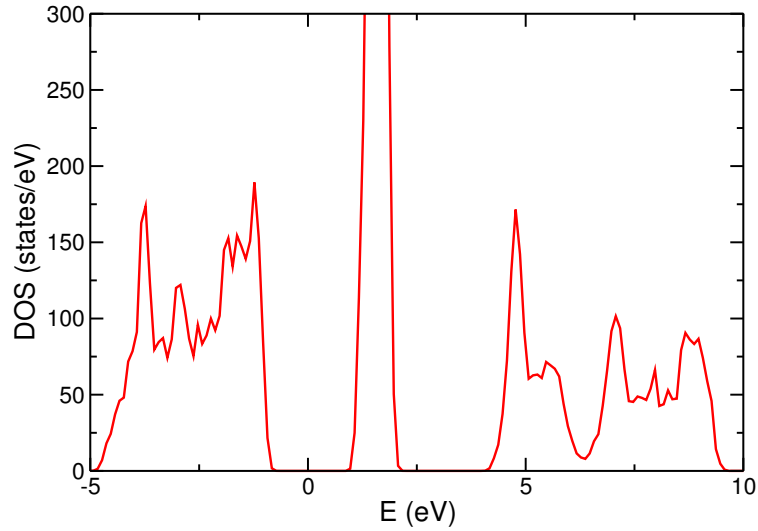


Figure 2: Density of states (DOS) of the pure cerium oxide in the 96 – atoms supercell representation. The Fermi level is set to $E = 0$.

In Fig. 3 the DOS of $Ce_{1-x}Zr_xO_2$ compound with the doping level $x \sim 3\%$ is compared with the DOS of CeO_2 . It is clearly evident that from an electronic point of view the density of states is almost unchanged with respect to the pure cerium oxide case. The most evident difference is the emergence of a small peak around 3.5 eV above the Fermi level. However, the introduction of Zr atoms has a more evident effect in the structural properties of $Ce_{1-x}Zr_xO_2$. The $Zr - O$ distance is 2.28\AA whereas the $Ce - O$ distance is in the range $2.39 - 2.40\text{\AA}$. Therefore, the introduction of Zr atoms causes a local distortion of the crystal lattice. In addition the distance between the Zr atom and the second nearest neighbor Ce atoms is about 3.87\AA . This value is 0.3\AA shorter than the corresponding $Ce - Ce$ distance in pure the CeO_2 compound.

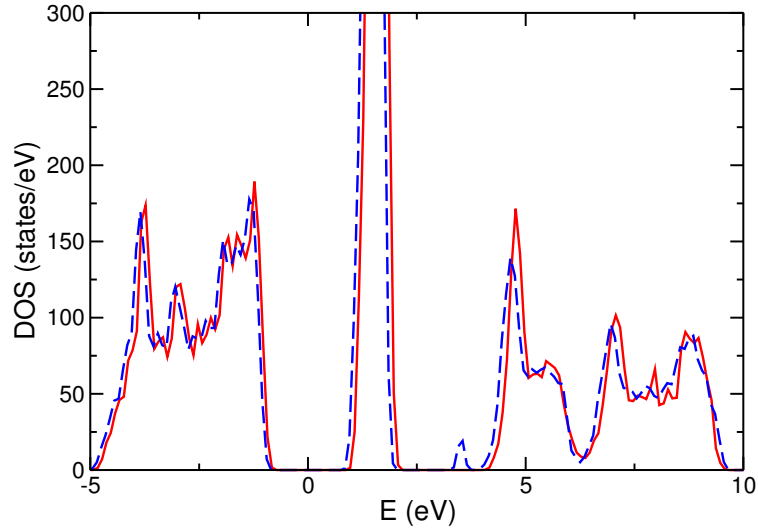


Figure 3: Densities of states (DOS) of CeO_2 (red) and $Ce_{1-x}Zr_xO_2$ with $x \sim 3\%$ (blue dashed). The Fermi level is set to $E = 0$.

4 Conclusions and perspectives

This work focused on the evaluation of the Zr -atoms doping effect in the cerium oxide compound. Starting from a 96 – atoms description of the system with a Zr doping level $x \sim 0.3\%$, both structural and electronic properties of the $Ce_{1-x}Zr_xO_2$ compound were properly evaluated and compared with the corresponding ones of the pure cerium oxide. While the electronic density of states was just slightly modified, the presence of Zr clearly affected the crystal structure. A local distortion affected the O atoms around the Zr atoms and also the Ce second nearest neighbor atoms. In both cases a shrinking of the Zr -to-atom distance was observed.

As following development of the study, several Zr doping concentrations will be considered and the results compared with the current evaluations. In addition, the introduction of one or more oxygen vacancies in the supercell will allow the study of the effect of the Zr (or similar cations) doping in the reducing capabilities of the cerium oxide compound.

References

- [1] M. Coll et al. All chemical YBa 2 Cu 3 O 7-x superconducting multilayers: critical role of CeO 2 cap layer flatness. *J. Mater. Res.*, vol. 24, p. 1446, 2009.
- [2] A. Augieri et al. MOD oxide buffer layers on metallic substrates for YBCO coated conductors. *Mater. Res. Soc. Symp. Proc.*, vol. 1579, 2013.
- [3] Z. Yang et al. Effect of Zr doping on stoichiometric and reduced ceria: A first-principles study. *J. Chem. Phys.*, vol. 124, p. 224704, 2006.
- [4] Hsin-Tsung Chen and Jee-Gong Chang. Oxygen vacancy formation and migration in $Ce_{1-x}Zr_xO_2$ catalyst: A DFT+U calculation. *J. Chem. Phys.*, vol. 132, p. 214702, 2010.
- [5] P. Giannozzi et. al. QUANTUM ESPRESSO: a modular and open-source software project for quantum simulations of materials. *Journal of Physics: Condensed Matter*, 39, 395502, 2009.
- [6] Perdew J. P., Burke K., and Ernzerhof M. *Phys. Rev. Lett.*, vol. 77, p. 3865, 1996.
- [7] F. Rizzo and G. de Marzi. CeO_2 electronic properties from first principles: an introductory study. *High Performance Computing on CRESCO infrastructure: research activities and results 2013*, 2014.
- [8] Fabris S., de Gironcoli S., Baroni S., Vicario G., and Balducci G. *Phys. Rev. B.*, vol. 72, p. 237102, 2005.
- [9] R. Fletcher. *The Computer Journal*, 13(6), 317, 1970.
- [10] M. Parrinello and A. Rhaman. *Phys. Rev. Lett.*, 45, 1980, 1196.
- [11] E. A. Kummerle and G. Heger. *J. Solid State Chem.*, vol. 147, p. 485, 1999.

THE INFLUENCE OF TiO₂ AND Ti DOPANTS ON THE HYDROGEN MOBILITY THROUGH MgH₂-Mg INTERFACE

Radojka Vujasin^{1*}, Jasmina Grbović Novaković¹, Nikola Novaković¹, Simone Giusepponi² and Massimo Celino²

¹*Vinča Institute of Nuclear Sciences, University of Belgrade, P.O. Box 522, 11001 Belgrade, Serbia*

²*ENEA, C.R. Casaccia, via Anguillarese 301, 00123 Rome, Italy*

ABSTRACT. MgH₂-Mg interface doped with TiO₂ and Ti and the effect of dopants on hydrogen mobility in the vicinity of the interface have been studied using density functional theory as implemented in CPMD code. Molecular dynamics simulations confirm that Ti doping is more effective in lowering the desorption temperature than TiO₂.

1 Introduction

Development of appropriate hydrogen storage materials is important for safe and sustainable implementation of hydrogen economy. MgH₂ was proved to be one of the most promising material, due to its high gravimetric storage capacity, reversibility of hydrogenation reaction, availability and low price. Namely, slow kinetics and relatively high dehydrogenation temperature prevents its practical application [1]. Hydrogen sorption properties of MgH₂ can be improved by adding transition metals and their oxides, such as Ti and TiO₂ [2, 3]. Theoretical investigations of MgH₂-Mg interface with TiO₂ and Ti as dopants were performed with the intention to examine its influence on hydrogen mobility through MgH₂-Mg interface and in the near-interface region.

2 Details of calculations and results

MD simulations were performed by CPMD (Car–Parrinello Molecular Dynamics) code [4, 5] which uses a plane wave/pseudopotential implementation of Density Functional Theory (DFT) [6, 7]. We use the CPMD compiled with Intel Fortran Compiler, MKL (Math Kernel Library), ACML (AMD Core Math Library) and MPI (Message Passing Interface) parallelization on the high performance ENEA CRESCO computing facilities [8]. Our system is MgH₂-Mg interface constituted by 132 atoms of Mg, and 120 atoms of H. Interfaces were built using fully relaxed Mg (010) and MgH₂ (110) surfaces (details are reported in CRESCO Annual Report 2014 [9]). Troullier–Martins normconserving pseudopotentials with GGA-PBE exchange–correlation potential were used for all atoms [10, 11]. The electronic wave functions are expanded in plane-wave basis set with a kinetic energy cut-off equal to 80 Ry.

The influence of the dopants on hydrogen mobility of MgH₂-Mg interface was examined by substitution of an atom of Mg with an atom of Ti, or one Mg and two H atoms with one Ti and two O atoms from MgH₂ part at three different distances from the interface. The interfaces are marked with POS1, POS2 and POS3, which means that substituted atoms are in the first, the second and the third Mg layer of MgH₂ side, respectively (see Fig.1).

* Corresponding author. E-mail: radojka.vujasin@gmail.com

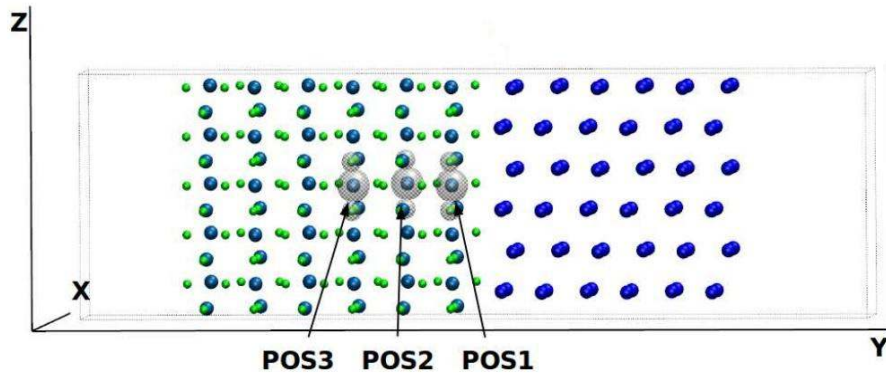


Fig.1: MgH₂-Mg interface in the simulation box. H atoms are in green, Mg atoms are in light blue in the hydride side and dark blue in the magnesium crystalline side. Positions POS_x ($x = 1, 2, 3$) indicate the Mg atoms that are substituted by Ti atoms.

Numerical study of effects of TiO₂ and Ti on the structural destabilisation and improvement of the hydrogen desorption properties of the system was published in CRESCO Annual Report 2014 [9]. MD simulations at constant temperature and constant volume were performed after geometry optimisation of the systems. Temperatures used in simulations were in range 200 -700 K in steps of 100K, but the effects of the interest were in range 400-600 K. MD simulations were performed for about 3 ps with timestep of 4 a.u. at each temperature and hydrogen atoms behaviour were characterized. Two groups of hydrogen atoms (H_a – 5 atoms on the interface, and H_b – 10 atoms just behind the H_a group) are likely to be involved in the H desorption. The average displacements of these two groups of H atoms $\langle d(t) \rangle$ at different temperature show that H atoms in the system doped with Ti start diffusion at 400 K. In the system doped with TiO₂ there are no displacements of H atoms even at higher temperature (Fig.2).

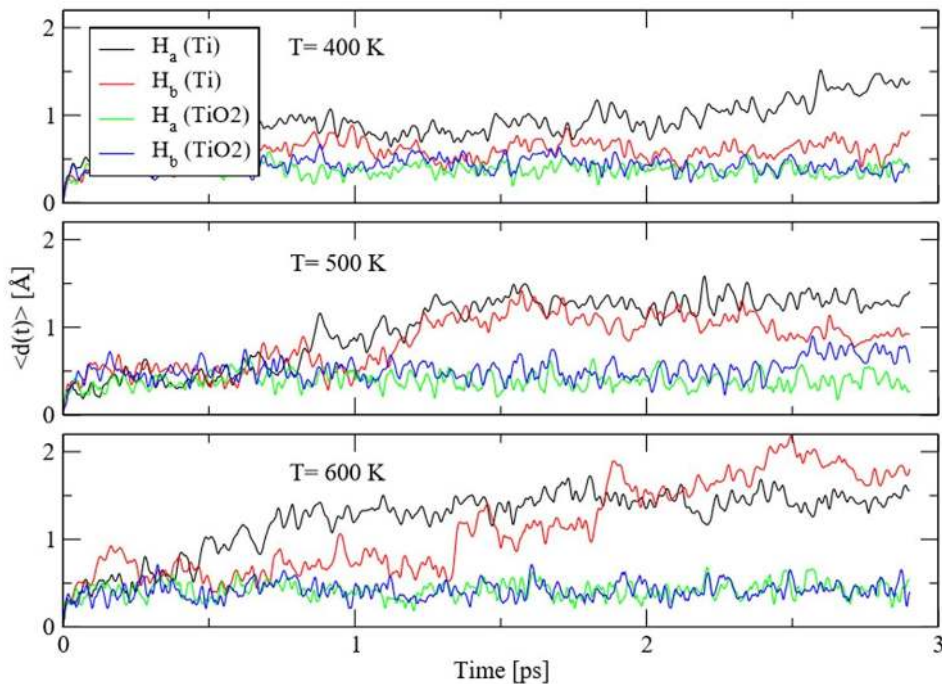


Fig.2: Average displacements of the hydrogen atoms near the interface. The interface is composed by Ti or TiO₂ in POS1.

Influence of the dopants on the H and Mg coordination were examined during the MD simulations at different temperatures and results is diverse behaviour depending on the type of doping, the position POS_x and the temperature. H coordination of MgH₂(Ti)-Mg system with Ti in all three positions have similar trends, lessening of the 3rd and 4th-H shells populations in favour of 1st and 5th-H shells populations after MD simulations relative to the geometry optimisations. As concerning the Mg coordination there is similar behaviour for all POS_x, increment of the atoms in the 1st-Mg shell associated with a decrease of those in the 2nd-Mg shell, and the number of atoms in the 3rd-Mg shell are slightly decrease.

With regard to the H coordination of the MgH₂(TiO₂)-Mg system after MD simulations, for POS1 there is no clear difference between the 1st and the 2nd-H shells, but partial depletion of the 3rd and the 4th-H shells and increase of atoms in the 5th-H shell is observed. This effect is more evident at higher temperature. In the systems with TiO₂ at positions POS2 and POS3, number of H atoms is lesser in the 1st and 4th-H shells but higher in the 2nd and 5th-H shells comparing to the H coordination after GO. Number of H atoms in the 3rd-H shell is not significantly changed. The Mg coordination analysis reveals similar results for POS2 and POS3 interfaces, increment of atoms in the 1st-Mg shell, decrement of atoms in 2nd-Mg shell with no change in the 3rd-Mg shell after MD simulations relative to the GO. In the POS1 interface, there is an oscillating number of atoms in the 1st-Mg shell, increase in the 2nd and decrease of the atoms in the 3rd-Mg shells. During the MD simulations there is no noticeable drift of the oxygen atoms away from the titanium in TiO₂ doped system.

To conclude, we performed MD simulations to investigate influence of the Ti and TiO₂ dopants on hydrogen mobility in the vicinity of MgH₂-Mg interface at different temperature and structural analysis of the system after MD simulations. H and Mg coordination at higher temperature show different results than those obtained for geometry optimisation. Average displacements of H atoms near the interface show that diffusion of H atoms in the system doped with Ti starts at 400 K.

Acknowledgements

We acknowledge ENEA-HPC team for supporting our computational activities on the ENEAGRID infrastructure. This work was supported by the Ministry of Education, Science and Technological Development of the Republic of Serbia under the Grant III 45012, by the project “HYDROSTORE” n. EEO I 00004 funded by the Italian Industria 2015 Program and by COST Action MP1103 “Nanostructured materials for solid state hydrogen storage”.

References

- [1] Schlapbach L., Züttel A. *Nature* **414** (2001) pp. 353-358.
- [2] Liang G., Huot J., Boily S., Van Neste A., Schulz R. *J Alloys Compd* **292** (1999) pp. 247-252.
- [3] Polanski M., Bystrzycki J. *J Alloys Compd* **486** (2009) pp. 697-701.
- [4] Car R., Parrinello M. *Phys. Rev. Lett.* **55** (1985) pp. 2471-2474.
- [5] CPMD V3.15.1 Copyright IBM Corp 1990-2011, Copyright MPI fuer Festkoerperforschung Stuttgart 1997-2001.
- [6] Hohenberg P., Kohn W. *Phys. Rev.* **136** (1964) pp. B864-B871.

[7] Kohn W., Sham L. J. Phys. Rev. **140** (1965) pp. A1133-A1138.

[8] www.cresco.enea.it.

[9] Vujasin R., Giusepponi S., Grbovic Novakovic J., Novakovic N., Celino M. High performance computing on CRESCO infrastructure: research activities and results 2014, pp. 69-72, 2015.

[10] Perdew J. P., Burke K., Erzerhof M. Phys. Rev. Lett. **77** (1996) pp. 3865-3868.

[11] Troullier N., Martins J. L. Phys. Rev. B **43** (1991) pp. 1993-2006.

THE PHASE STRUCTURE OF THE NAMING GAME IN THE STOCHASTIC BLOCK MODEL

Filippo Palombi^{1*} and Simona Toti²

¹*ENEA, Via E. Fermi 45 – 00044, Frascati, Italy*

²*ISTAT, Via C. Balbo 16 – 00184, Rome, Italy*

ABSTRACT. In the Naming Game a population of locally interacting individuals develops a shared vocabulary without the need for external coordination. It is known that on community-based networks the path to consensus passes through metastable multi-language states. These can be used as a mean to detect communities in empirical networks. We show that such states correspond to genuine multi-language phases, arising in the thermodynamic limit when the number of links connecting different communities drops below critical thresholds. We study the phase structure in the stochastic block model.

1 Introduction

The discovery and understanding of complex networks has proven to be one of the major scientific achievements of the last twenty years [1]. Networks are not merely observed in biological, environmental, economic, political and social contexts: in many cases they are found to play an active — and sometimes critical — rôle in modelling the large scale dynamics of systems, whose fundamental degrees of freedom interact only at a microscopic level. The earliest and presumably most famous example of this is represented by the discovery of the absence of an epidemic threshold for the outbreak of viruses on scale-free networks [2].

Among the many complex phenomena which the rise of network science has allowed to investigate on a quantitative basis, one that has attracted the attention of a wide and heterogeneous community of scholars is the emergence of spoken languages in human societies. After some early attempts to ascribe the constitution of language conventions to evolutionary mechanisms [3–8], a simple and successful agent-based model for the self-organization of a globally shared language was proposed in ref. [9]. The model, which is nowadays universally known as the Naming Game (**NG**), was inspired by the seminal work of refs. [10, 11].

The NG is a language-game in the sense of ref. [12], with agents iteratively communicating to each other conventional names for a target object. Each agent is endowed with a notebook, on which he writes names. In the original version of the model all notebooks are initially empty. Elementary interactions involve two agents, playing respectively the rôle of *speaker* and *listener*. In each iteration the speaker is chosen randomly among the agents, while the listener is chosen randomly among the speaker's neighbours. The speaker-listener interaction goes as follows. The speaker proposes a name. If his notebook is empty, he invents the name, otherwise he picks up one randomly from his notebook. The listener checks if the proposed name is already in his notebook. If negative, he adds the name to

*Corresponding author. E-mail: filippo.palombi@enea.it.

his notebook. Otherwise, both speaker and listener erase all names from their notebooks except the proposed one.

2 Mean field equations in the stochastic block model

The stochastic block model (**SBM**) is a generative model for networks with community structure. We consider a graph $\mathcal{G} = (\mathcal{V}, \mathcal{E})$ and a partition $\mathcal{V}_{\mathcal{C}} = \{\mathcal{C}^{(k)}\}_{k=1}^Q$ of \mathcal{V} , *i.e.* we assume $\mathcal{V} = \cup_{k=1}^Q \mathcal{C}^{(k)}$ and $\mathcal{C}^{(i)} \cap \mathcal{C}^{(k)} = \emptyset$ for $i \neq k$. We let $N^{(k)} = |\mathcal{C}^{(k)}| > 0$ and $N = |\mathcal{V}|$, hence we have $N = \sum_{k=1}^Q N^{(k)}$. We observe that $\mathcal{V}_{\mathcal{C}}$ induces a partition $\mathcal{E}_{\mathcal{C}} = \{\mathcal{E}^{(ik)}\}_{i,k=1}^Q$ of \mathcal{E} , *i.e.* $\mathcal{E} = \cup_{i,k=1}^Q \mathcal{E}^{(ik)}$ with

$$\mathcal{E}^{(ik)} = \{ (x, y) \in \mathcal{E} : x \in \mathcal{C}^{(i)} \text{ and } y \in \mathcal{C}^{(k)} \}. \quad (1)$$

We assume $N^{(i)} = N/Q$ for $i = 1, \dots, Q$. Then, we introduce a set of $Q(Q+1)/2$ parameters $\{p^{(ik)}\}_{i \leq k}^{1 \dots Q}$ such that

$$p^{(ik)} = \text{prob} \left\{ (x, y) \in \mathcal{E}^{(ik)} \text{ for all } x \in \mathcal{C}^{(i)} \text{ and } y \in \mathcal{C}^{(k)} \right\}. \quad (2)$$

For $Q = 2$ the SBM yields asymmetric networks whenever $p^{(11)} \neq p^{(22)}$.

We prepare the initial state of the system with agents in a given community being assigned a common name and with different communities being assigned different names. We let A_k represent the name initially assigned to $\mathcal{C}^{(k)}$. Then we introduce a *Rosetta* notebook¹ $\mathcal{D} = \{A_1, \dots, A_Q\}$ and we let $S(\mathcal{D}) = \{D : D \subset \mathcal{D}\}$. At time $t \geq 0$ an agent x has a certain notebook D , hence D represents the state of x at time t .

MFES describe the dynamics of the system in the thermodynamic limit (infinitely extended networks). In the SBM we define this by letting $N \rightarrow \infty$ with $Q = \text{const.}$, $N^{(i)}/N = \text{const.}$ and $p^{(ik)} = \text{const.}$ for all i, k . To derive MFES we take into account and correctly weigh all possible agent-agent interactions yielding an increase/decrease of the fraction of agents in a given state. For each notebook D we introduce local densities

$$n_D^{(i)} = \frac{\text{no. of agents with notebook } D \text{ belonging to } \mathcal{C}^{(i)}}{N^{(i)}}. \quad (3)$$

At each time the vectors $\{n_D^{(i)}\}_{D \in S(\mathcal{D})}$ fulfill simplex conditions separately for each community, that is to say state densities are constrained by equations

$$\sum_{D \in S(\mathcal{D})} n_D^{(i)} = 1, \quad i = 1, \dots, Q. \quad (4)$$

Hence, there is one redundant state per community, whose density we represent in terms of the remaining ones via the corresponding simplex equation. We choose the *Rosetta* notebook \mathcal{D} as redundant state for all communities. If we let $\bar{S}(\mathcal{D}) = S \setminus \mathcal{D}$, then we have

$$n_{\mathcal{D}}^{(i)} = 1 - \sum_{D \in \bar{S}(\mathcal{D})} n_D^{(i)}, \quad i = 1, \dots, Q. \quad (5)$$

Following this choice, we introduce the essential state vector

$$\bar{n} = \{n_D^{(i)} : D \in \bar{S}(\mathcal{D}) \text{ and } i = 1, \dots, Q\}. \quad (6)$$

¹Evidently, this name evokes the famous stone rediscovered near the town of Rashid (Rosetta, Egypt) by Napoleon's army in 1799. The stone contained versions of the same text in Greek, Demotic and Hieroglyphic. As such, it served as a language translation tool.

The domain of \bar{n} is the Cartesian product of Q simplices. Taken as a whole, $\bar{n}(t)$ provides a full kinematic description of the state of the system at time t . Its trajectory in state space is mathematically described by a set of stochastic differential equations, governing the dynamics of the system under the joint action of deterministic drift and random diffusion terms. MFEs follow as the result of switching off all diffusion terms. They read

$$\frac{dn_D^{(i)}}{dt} = f_D^{(i)}(\bar{n}), \quad D \in \bar{S}(\mathcal{D}). \quad (7)$$

The function $f_D^{(i)}$ yields the overall transition rate for the agent state D in the i th community. It includes many contributions $f_D^{(ik)}$, corresponding to interactions involving an agent belonging to $\mathcal{C}^{(i)}$ and a neighbour belonging to $\mathcal{C}^{(k)}$ for all k . Each contribution $f_D^{(ik)}$ is proportional to the probability of picking up an agent x in the i th community and a neighbour x' of x in the k th one. This probability amounts to

$$\pi^{(ik)} = \text{prob} \left\{ x \in \mathcal{C}^{(i)}, x' \in \mathcal{C}^{(k)} \right\} = \frac{1}{Q} \frac{p^{(ik)}}{\sum_{\ell=1}^Q p^{(i\ell)}} = \frac{1}{Q} \frac{\nu^{(ik)}}{1 + \sum_{\ell \neq i}^{1 \dots Q} \nu^{(i\ell)}}, \quad (8)$$

with $\nu^{(ik)} = p^{(ik)}/p^{(ii)}$.

The only case where the phase diagram can be easily studied is for $Q = 2$. For notational simplicity, we introduce symbols $\nu_1 = p^{(12)}/p^{(11)}$ and $\nu_2 = p^{(12)}/p^{(22)}$ in place of $\nu^{(12)}$ and $\nu^{(21)}$ respectively. Notice that ν_1 and ν_2 increase when the inter-community links become denser and also when the intra-community ones rarefy. MFEs can be written down explicitly in this case. They read

$$\begin{aligned} \frac{dn_{A_1}^{(1)}}{dt} &= \pi^{(11)} \left\{ n_{A_1}^{(1)} n_{A_1 A_2}^{(1)} + (n_{A_1 A_2}^{(1)})^2 - n_{A_1}^{(1)} n_{A_2}^{(1)} \right\} \\ &+ \pi^{(12)} \left\{ \frac{3}{2} n_{A_1 A_2}^{(1)} n_{A_1}^{(2)} - \frac{1}{2} n_{A_1}^{(1)} n_{A_1 A_2}^{(2)} + n_{A_1 A_2}^{(1)} n_{A_1 A_2}^{(2)} - n_{A_1}^{(1)} n_{A_2}^{(2)} \right\}, \end{aligned} \quad (9)$$

$$\begin{aligned} \frac{dn_{A_2}^{(1)}}{dt} &= \pi^{(11)} \left\{ n_{A_2}^{(1)} n_{A_1 A_2}^{(1)} + (n_{A_1 A_2}^{(1)})^2 - n_{A_1}^{(1)} n_{A_2}^{(1)} \right\} \\ &+ \pi^{(12)} \left\{ \frac{3}{2} n_{A_1 A_2}^{(1)} n_{A_2}^{(2)} - \frac{1}{2} n_{A_2}^{(1)} n_{A_1 A_2}^{(2)} + n_{A_1 A_2}^{(1)} n_{A_1 A_2}^{(2)} - n_{A_2}^{(1)} n_{A_1}^{(2)} \right\}, \end{aligned} \quad (10)$$

$$\begin{aligned} \frac{dn_{A_1}^{(2)}}{dt} &= \pi^{(22)} \left\{ n_{A_1}^{(2)} n_{A_1 A_2}^{(2)} + (n_{A_1 A_2}^{(2)})^2 - n_{A_1}^{(2)} n_{A_2}^{(2)} \right\} \\ &+ \pi^{(21)} \left\{ \frac{3}{2} n_{A_1 A_2}^{(2)} n_{A_1}^{(1)} - \frac{1}{2} n_{A_1}^{(2)} n_{A_1 A_2}^{(1)} + n_{A_1 A_2}^{(2)} n_{A_1 A_2}^{(1)} - n_{A_1}^{(2)} n_{A_2}^{(1)} \right\}, \end{aligned} \quad (11)$$

$$\begin{aligned} \frac{dn_{A_2}^{(2)}}{dt} &= \pi^{(22)} \left\{ n_{A_2}^{(2)} n_{A_1 A_2}^{(2)} + (n_{A_1 A_2}^{(2)})^2 - n_{A_1}^{(2)} n_{A_2}^{(2)} \right\} \\ &+ \pi^{(21)} \left\{ \frac{3}{2} n_{A_1 A_2}^{(2)} n_{A_2}^{(1)} - \frac{1}{2} n_{A_2}^{(2)} n_{A_1 A_2}^{(1)} + n_{A_1 A_2}^{(2)} n_{A_1 A_2}^{(1)} - n_{A_2}^{(2)} n_{A_1}^{(1)} \right\}. \end{aligned} \quad (12)$$

The phase diagram of the model, obtained by integrating eqs. (9)–(12) numerically, is reported in Fig. 1. We observe three different phases: in region I the system converges to a global consensus state where A_1 colonizes $\mathcal{C}^{(2)}$, in region III it converges to the opposite global consensus state, with A_2 colonizing $\mathcal{C}^{(1)}$, while region II corresponds to a multi-language phase. Here large fractions of both communities keep speaking their original language without ever converging to global consensus. It is interesting to observe that the phase structure of the model is qualitatively similar to that obtained for the binary NG on a fully connected graph when competing committed groups of agents are introduced, see Fig. 1 of ref. [13]. Nevertheless, the phase structure here is fully induced by the network topology. Moreover, the cusp of region II is located at $\nu_1 = \nu_2 = 0.1321\dots$, while in ref. [13] it is located at $p_A = p_B = 0.1623\dots$

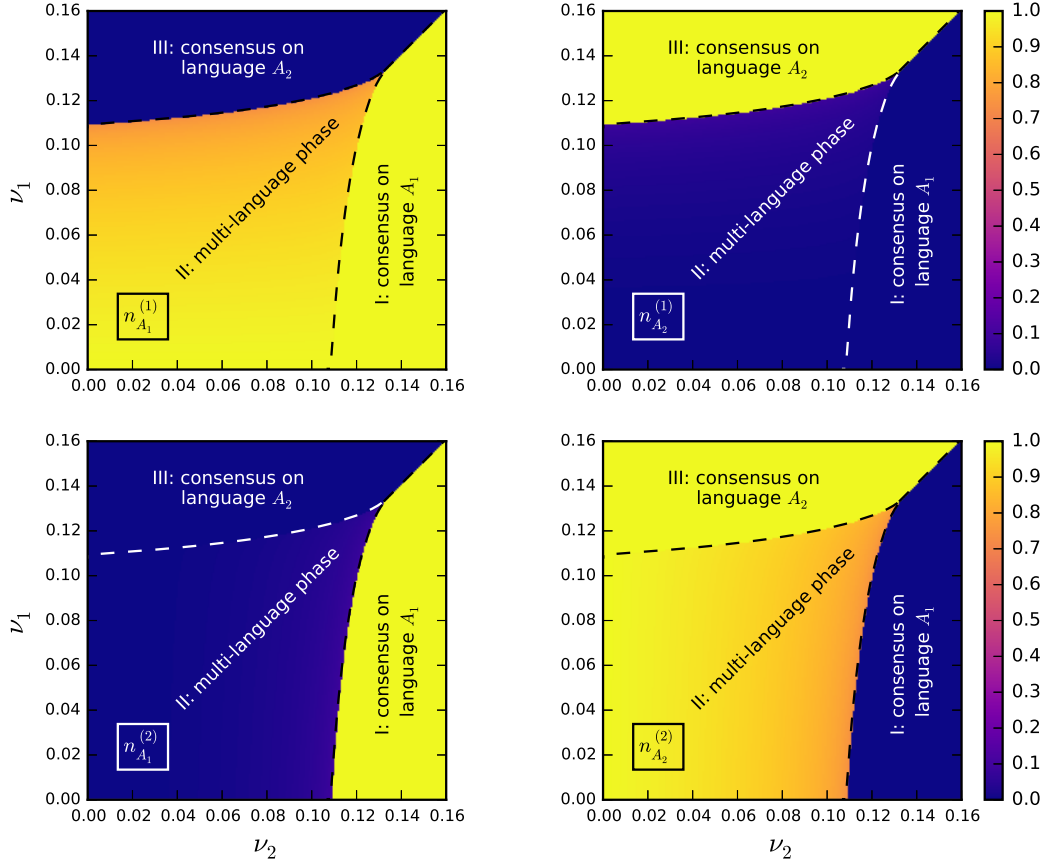


Figure 1: Phase diagram in the SBM with $Q = 2$.

3 Use of CRESCO

Our study made extensive use of CRESCOF, the PC cluster located at the ENEA site of Frascati. Numerical integrations of eqs. (9)–(12) for many choices of ν_1 and ν_2 do not require more CPU time than about one day on a single core. However, the need for computational power becomes massive as Q increases, because the number of MFEs and the number of pairwise interactions contributing to the transition rates increase more than linearly with Q . For instance, integrating MFEs for $Q = 6$ with $\nu_2 = \nu_1$ requires up to one week on a single core, depending on the resolution of ν_1 and t . Apart from this, the largest fraction of CPU time we spent on CRESCOF was devoted to Monte Carlo simulations of the NG on various community-based network, including the SBM, networks with overlapping cliques and complex networks in which communities have internal scale-free degree distributions and are interconnected by links with scale-free topologies. For a full description of these simulations, we refer the reader to ref. [14]. The overall CPU time we spent for this project was about 3 months \times 200 cores of CRESCOF.

4 Conclusions

We studied the phase structure of the NG in the SBM. Prior to our work, it was known in the literature that communities of agents playing the NG tend to develop own long-lasting languages when sufficiently

isolated. We showed that on infinitely extended networks the latter become everlasting. In other words, communities induce genuine multi-language phases in the thermodynamic limit.

References

- [1] A.-L. Barabási. *Linked: How Everything Is Connected to Everything Else and What It Means for Business, Science, and Everyday Life*. Basic Books, 2014.
- [2] R. Pastor-Satorras and A. Vespignani. Epidemic spreading in scale-free networks. *Phys. Rev. Lett.*, 86:3200–3203, 2001.
- [3] P. Niyogi and R. C. Berwick. Evolutionary Consequences of Language Learning. *Linguistics and Philosophy*, 20(6):697–719, 1997.
- [4] M. A. Nowak and D. C. Krakauer. The evolution of language. *Proc. Natl. Acad. Sci. USA*, 96:8028–8033, 1999.
- [5] M. A. Nowak, J. B. Plotkin, and D. C. Krakauer. The Evolutionary Language Game. *J. of Theor. Biol.*, 200(2):147–162, 1999.
- [6] M. A. Nowak, N. L. Komarova, and P. Niyogi. Evolution of Universal Grammar. *Science*, 291(5501):114–118, 2001.
- [7] K. Smith, S. Kirby, and H. Brighton. Iterated Learning: A Framework for the Emergence of Language. *Artif. Life*, 9(4):371–386, 2003.
- [8] N. Komarova and P. Niyogi. Optimizing the mutual intelligibility of linguistic agents in a shared world. *Artif. Intell.*, 154(1):1–42, 2004.
- [9] A. Baronchelli, M. Felici, E. Caglioti, V. Loreto, and L. Steels. Sharp transition towards shared vocabularies in multi-agent systems. *J. Stat. Mech. Theory Exp.*, P06014, 2006.
- [10] L. Steels. A self-organizing spatial vocabulary. *Artif. Life*, 2(3):319–332, 1995.
- [11] L. Steels. Self-organizing vocabularies. In C. G. Langton and K. Shimohara, editors, *Artif. Life V*, pages 179–184. Nara, Japan, 1996.
- [12] L. Wittgenstein. *Philosophical Investigations*. Wiley-Blackwell, 4th edition, 2009 [1953].
- [13] J. Xie, J. Emenheiser, M. Kirby, S. Sreenivasan, B. K. Szymanski, and G. Korniss. Evolution of opinions on social networks in the presence of competing committed groups. *PLoS ONE*, 7(3):e33215, 2012.
- [14] F. Palombi and S. Toti. Topological aspects of the multi-language phases of the Naming Game on community-based networks. 2016, arXiv:1610.08672 [physics.soc-ph].

TRANSCRIPTOME ASSEMBLY OF *C. sativus*

Antonio Conte^{1,1}, Giuseppe Aprea^{1*}, Marco Pietrella^{1,3}

¹*Italian National Agency for New Technologies, Energy and Sustainable Development (ENEA) Casaccia Research Center, Via Anguillarese 301, 00123 Roma, Italy.*

²*Facoltà di Scienze agrarie, alimentari e ambientali U.C.S.C., Piacenza, Italy.*

³*Council for Agricultural Research and Economics, Forlì, Italy.*

ABSTRACT. Saffron is obtained from the stigmas of *Crocus sativus* L. and is one of the most expensive spice in the world. Its unique aroma and taste is due to the accumulation of a large amount of apocarotenoids. To understand the molecular basis of biosynthesis/accumulation of the latter, we performed transcriptome sequencing from five different tissues/organs of *C. sativus* and six stigma developmental stages using Illumina and Roche 454 platforms. After comprehensive optimization of de novo transcriptome assembly, a total of 71,030 unique transcripts (average length of 1137 bp and N50 length of 1573 bp) has been obtained.

Crocus sativus L. belongs to the Iridaceae family; it is a sterile triploid plant and is vegetatively propagated by corms. The characteristic feature of its flower is the presence of three red stigmas, which are dried and used in food industry as a colouring and flavouring agent. Stigmas contain approximately 150 volatile and aromatic compounds belonging to terpenoids and flavonoids. They also contain multiple non-volatile active components, such as zeaxanthin, lycopene, and various α - and β -carotenes derived from anthocyanins and carotenoids. *C. sativus* accumulate in stigmas a large amount (up to 8% of stigma dry weight) of apocarotenoids derived from the oxidative cleavage of zeaxanthin: crocetin and crocetin glycosides (responsible for bright red colouring), picrocrocin (responsible for bitter taste), and safranal (responsible for typical aroma).

RNA sequencing (RNA-seq) is a powerful technique for profiling the complete gene space of any organism due to high-throughput, accuracy and reproducibility. In plants, with large and complex genomes, RNA-seq has accelerated the discovery of novel genes, tissue-specific expression patterns and functional analysis. Recently, two other papers about the transcriptome of *C. sativus* have been published ([3],[9]); however, this work is not only intended to deal with the cultivated plant but is also a preliminary step which will compare transcriptomic data from 13 different *Crocus* species in order to study the biosynthesis of secondary metabolites of interest.

1 Sequencing data

In order to get a better assembly, in this study we used data from both Enea's laboratories and from two other recent work ([3], [9]). There are different tissues: corm, tepal, leaf, stigma, stamen, whole flower and some libraries from six different developmental stages of stigma which are, in chronological order: yellow, orange, red(from tissue changing coloring), two days before anthesis(-2dA), anthesis(0dA)

*Corresponding author. E-mail: giuseppe.aprea@enea.it.

and two days after anthesis(+2dA). Adapters removal and quality trimming with cutadapt ([10]) and trimomatic ([4]) were the first step. Available data, before and after cleaning, is shown in tables 1 and 2.

Table 1: Illumina paired ends data.

Origin	Tissue	Id	Paired ends [Raw]	Bases [Raw]	Paired ends [Cleaned]	%	Bases [Cleaned]	%
ENE A	anther	cc_an_01	15.616.265	7.808.132.500	12.726.713	81,50%	5.084.003.745	65,11%
		cc_an_02	15.325.646	7.662.823.000	12.512.994	81,65%	4.998.711.345	65,23%
	stigma	cc_sg_01	14.557.929	7.278.964.500	12.098.839	83,11%	4.832.022.207	66,38%
		cc_sg_02	14.379.856	7.189.928.000	11.972.828	83,26%	4.785.741.022	66,56%
	tepal	cc_te_01	8.754.069	4.377.034.500	7.874.993	89,96%	3.520.508.744	80,43%
		cc_te_02	8.591.455	4.295.727.500	7.728.062	89,95%	3.460.401.244	80,55%
[3]	flower	cc_fl_01	37.716.452	5.431.169.088	30.055.276	79,69%	4.086.132.233	75,23%
	stigma	cc_sg_03	29.521.835	4.251.144.240	25.057.676	84,88%	3.412.571.578	80,27%
[9]	corm	cc_co_01	17.966.108	3.629.153.816	16.522.635	91,97%	3.141.386.251	86,56%
	leaf	cc_le_01	18.825.172	3.802.684.744	17.368.181	92,26%	3.293.574.555	86,61%
	stamen	cc_sn_01	19.267.794	3.892.094.388	17.734.024	92,04%	3.352.643.053	86,14%
	stigma	cc_sg_04	22.932.750	4.632.415.500	21.073.854	91,89%	4.021.611.569	86,81%
	tepal	cc_te_03	24.156.491	4.879.611.182	22.317.492	92,39%	4.227.370.768	86,63%

Table 2: Single end data.

Origin	Platform	Tissue	Id	Single end [Raw]	Bases [Raw]	Single end [Cleaned]	%	Bases [Cleaned]	%
ENE A	Illumina	stigma(-2d)	cc_sg_05	18.678.838	1.886.562.638	13.043.592	69,83%	1.195.225.543	63,35%
		stigma(orange)	cc_sg_06	13.124.474	1.325.571.874	10.160.697	77,42%	929.896.172	70,15%
	Roche 454	stigma(0dA)	cc_sg_07	121.659	63.445.694	117.861	96,88%	53.242.480	83,92%
		stigma(-2dA)	cc_sg_08	124.239	65.023.674	120.338	96,86%	54.727.869	84,17%
		stigma(orange)	cc_sg_09	107.511	55.135.498	103.867	96,61%	46.307.459	83,99%
		stigma(+2dA)	cc_sg_10	144.278	73.567.303	139.654	96,80%	62.096.794	84,41%
		stigma(red)	cc_sg_11	99.867	50.445.239	96.521	96,65%	42.421.946	84,10%
		stigma(yellow)	cc_sg_12	129.022	65.851.280	124.660	96,62%	55.161.469	83,77%

2 Transcriptome assembly

The assembly was performed adopting a two stages strategy using RunDrup and RunMeta from D-RAP software package ([1]) with some customizations. We divided the libraries into groups depending on their tissue origin as shown in table 3).

During the first stage each group was assembled separately following the RunDrup assembly scheme while at the second stage, a meta-assembly of the previously obtained ones is completed to finally yield the whole plant transcriptome.

2.1 Tissue assembly

For each data group in table 3, we proceeded to a first assembly following these steps:

- multiple reads assembly are done with Trinity [7] using the following kmer values: 21, 23, 25, 27, 29 and 31.
- The contigs obtained in the assemblies were merged.
- The contigs contained in other larger ones were removed.

Table 3: Assembly groups.

Library Id	Assembly group
cc_co.01	corm
cc_le.01	leaf
cc_fl.01	flower
cc_an.01	stamen
cc_an.02	
cc_sn.01	
cc_sg.01	stigma
cc_sg.02	
cc_sg.03	
cc_sg.04	
cc_sg.05	
cc_sg.06	
cc_te.01	tepal
cc_te.02	
cc_te.03	

- CAP3 ([8]) was run for a further contigs assembly according to the OLC paradigm. At this stage that is acceptable as we have relatively much less data compared to the initial Illumina dataset (otherwise the processing is extremely slow and memory demanding) and moreover this algorithm is less sensitive to sequence polymorphism.
- Contigs shorter than 200 bases were removed, and the initial reads were aligned on the remaining ones to correct errors.
- Finally, only contigs with coverage $\geq 1FPKM$ were kept.

2.2 Meta-assembly

The Roche 454 data (libraries cc_sg-[07-12]) had already been assembled ([6]) and, at this stage, is used in the meta-assembly together with the groups assembly just obtained. We followed RunMeta workflow:

- merging of all the contigs obtained in the first step plus the Roche 454 assembly.
- extraction of the longest ORF from each contig.
- ORFs are clustered and for each cluster only the longest ORF is kept. This is a first step of redundancies elimination.
- the original contig is recovered for each ORF and a new clustering step is performed with all the contigs and, again, only the largest sequence for each cluster is retained. This is the second step of redundancies removal and removes those duplicate sequences that had not been previously eliminated due to a frameshift that had compromised the alignment of the amino acid sequence.
- All reads are aligned on the remaining contigs and only those with coverage $\geq 1FPKM$ were selected.
- A chimeras removal step is performed; 253 contigs are removed and 140 are modified.

Assembly metrics are shown in table 4 in comparison to those in the works of [3] and [9].

Table 4: Assembly metrics.

	This study	[3]	[9]
Total contigs	71,030	64,438	105,269
Total assembly length	80,732,761	NA	~ 110,000,000
Mean contig length	1,137	610	1,047
Minimum contig length	122	NA	200
Maximum contig length	14,082	NA	NA
N50	1,573	753	1,404

3 Functional annotation

In order to assign a putative function to each transcript, the latter were aligned against the non-redundant database of protein sequences from NCBI using BLASTX ([2]). The results obtained by BLASTX have been used as input for Blast2Go ([5]), for functional analysis. Finally 49,132 (69%) transcripts could be annotated (58.5% in [3], 54% in [9]).

4 Final remarks

A new comprehensive assembly of *Crocus sativus* L. transcriptome has been done. It yielded ~ 70,000 transcripts with N50 length of 1,573 bp. A functional annotation could be retrieved for 69% of them. This is a fundamental step which will be followed by a differential analysis with other 13 different *Crocus* species in order to study the biosynthesis of apocarotenoids and other secondary metabolites of interest.

References

- [1] De novo RNA-seq Assembly Pipeline.
- [2] Stephen F. Altschul, Thomas L. Madden, Alejandro A. Schäffer, Jinghui Zhang, Zheng Zhang, Webb Miller, and David J. Lipman. Gapped BLAST and PSI-BLAST: A new generation of protein database search programs, sep 1997.
- [3] Shoib Ahmad Baba, Tabasum Mohiuddin, Swaraj Basu, Mohit Kumar Swarnkar, Aubid Hussain Malik, Zahoor Ahmed Wani, Nazia Abbas, Anil Kumar Singh, Nasheeman Ashraf, J Fernandez, N D’Agostino, D Pizzichini, ML Chiusano, G Giuliano, AR Moraga, JL Rambla, O Ahrazem, A Granell, L Gómez-Gómez, F Bouvier, C Suire, J Mutterer, B Camara, SA Baba, AH Malik, ZA Wani, T Mohiuddin, Z Shah, N Abbas, N Ashraf, JL Gainer, FB Brumgard, FI Abdullaev, JJ Espinosa-Aguirre, Z Zhang, CZ Wang, XD Wen, Y Shoyama, CS Yuan, FX Cunningham, E Gantt, S Lu, L Li, R Castillo, L Gomez-Gomez, PF Nohales, JA Pérez, RK Patel, M Jain, MV Bel, S Proost, CV Neste, D Deforce, YV Peer, K Vandepoele, Y Moriya, M Itoh, S Okuda, AC Yoshizawa, M Kanehisa, J Jin, H Zhang, L Kong, G Gao, J Luo, S Tarazona, F García-Alcalde, J Dopazo, A Ferrer, A Conesa, T Yamada, I Letunic, P Bork, RC Edger, N Saitou, M Nei, K Tamura, D Peterson, N Peterson, G Stecher, S Kumar, J Zhang, K Wu, S Zeng, JAT Silva, X Zhao, C Tian, H Xia, J Duan, X Zhang, L Zhao, Z Larson-rabin, D Li, Z Guo, S Liu, H Kuang, Z Lai, GF Tsanakas, AN Polidoros, AS Economou, H Lulin, Y Xiao, S Pei, T Wen, H Shangqin, H Wang, J Jiang, S Chen, X Qi, H Peng, P Li, A Song, Z Guan, W Fang, Y Liao, F Chen, J Bhardwaj, R Chauhan, MK Swarnkar, RK Chahota, AK Singh, R Shankar, SK Yadav,

- S Pradhan, N Bandhiwal, N Shah, C Gaur, S Bhatia, R Tavazza, G Diretto, P Beyer, MA Taylor, N Chaudhary, N Nijhawan, JP Khurana, P Khurana, RK Wang, CE Wang, YY Fei, JY Gai, TJ Zhao, S Frusciante, M Bruno, P Ferrante, M Pietrella, A Prado-Cabrero, L Gomez-Gomez, S Al-Babilic, A Rubio-Moraga, A Fernández-de Carmen, A Trapero-Mozos, D Orzáez, CI Cazonelli, BJ Pogson, PD Matthews, R Luo, ET Wurtzel, F Li, C Murillo, T Isaacson, G Ronen, D Zamir, J Hirschberg, H Park, SS Kreunen, AJ Cuttriss, D DellaPenna, B Pogson, Z Sun, KA McDonald, D Della-Penna, RC Lopez, A Trapero, ML Jimeno, MD Gómez, A Rubio, JL Rambala, M Santaella, DM Gomez, M Verma, R Ghangal, R Sharma, AK Sinha, N Onkokesung, E Gaquerel, H Kotkar, H Kaur, IT Baldwin, I Galis, K Koyama, M Numata, I Nakajima, N Goto Yamamoto, H Matsumura, N Tanaka, Y Yuan, C Wu, Y Liu, J Yang, L Huang, B Pauw, FA Hilliou, VS Martin, G Chatel, CJ Wolf, A Champion, M Pre, B Duijn, JW Kijne, L Fits, J Memelink, K Heijmans, P Morel, M Vandenbussche, S Masiero, L Colombo, PE Grini, A Schnittger, MM Kater, A Tsaftaris, K Pasentsis, A Makris, N Darzentas, A Polidoros, A Kalivas, A Argiriou, D Jain, RA Vishwakarma, S Bartels, MA Gonzalez Besteiro, D Lang, R Ulm, R Priya, and R Siva. Comprehensive transcriptome analysis of *Crocus sativus* for discovery and expression of genes involved in apocarotenoid biosynthesis. *BMC Genomics*, 16(1):698, dec 2015.
- [4] Anthony M. Bolger, Marc Lohse, and Bjoern Usadel. Trimmomatic: A flexible trimmer for Illumina sequence data. *Bioinformatics*, 30(15):2114–2120, aug 2014.
- [5] Ana Conesa, Stefan Götz, Juan Miguel García-Gómez, Javier Terol, Manuel Talón, and Montserrat Robles. Blast2GO: A universal tool for annotation, visualization and analysis in functional genomics research. *Bioinformatics*, 21(18):3674–3676, sep 2005.
- [6] Marco Pietrella Fabrizio Carbone, Giovanni Giuliano, Alberto Pallavicini, Gaetano Perrotta. *Crocus sativus* transcriptome - Unpublished.
- [7] Manfred G Grabherr, Brian J Haas, Moran Yassour, Joshua Z Levin, Dawn A Thompson, Ido Amit, Xian Adiconis, Lin Fan, Raktima Raychowdhury, Qiandong Zeng, Zehua Chen, Evan Mauceli, Nir Hacohen, Andreas Gnirke, Nicholas Rhind, Federica di Palma, Bruce W Birren, Chad Nusbaum, Kerstin Lindblad-Toh, Nir Friedman, and Aviv Regev. Full-length transcriptome assembly from RNA-Seq data without a reference genome. *Nature biotechnology*, 29(7):644–52, 2011.
- [8] Xiaoqi Huang and Anup Madan. CAP3: A DNA sequence assembly program. *Genome Research*, 9(9):868–877, sep 1999.
- [9] Mukesh Jain, Prabhakar Lal Srivastava, Mohit Verma, Rajesh Ghangal, and Rohini Garg. De novo transcriptome assembly and comprehensive expression profiling in *Crocus sativus* to gain insights into apocarotenoid biosynthesis. *Scientific reports*, 6(March):22456, 2016.
- [10] Marcel Martin. Cutadapt removes adapter sequences from high-throughput sequencing reads. *EM-Bnet.journal*, 17(1):pp. 10–12, 2011.

Analysis of current fast neutron-flux monitoring instrumentation targeted for the DEMO LFR ALFRED

Luigi Lepore^{1*}, Romolo Remetti¹, and Mauro Cappelli²

¹*SAPIENZA, University of Rome, SBAI Department, Via Antonio Scarpa, 14 - 00161 Rome – Italy*

²*ENEA FSN-FUSPHY-SCM, Frascati Research Center, via Enrico Fermi, 45 - 00044 Frascati (Rome) - Italy*

ABSTRACT. Among Gen IV projects for future nuclear power plants, Lead cooled Fast Reactors (LFRs) seem to be a very interesting solution due to its benefits in terms of fuel cycle, coolant-safety and waste management. Identification of new models of nuclear instrumentation specialized for LFR neutron flux monitoring asks for an accurate evaluation of the environment the sensor will work in. In this study, thermal-hydraulics and chemical conditions for LFR core environment will be assumed, as the neutron flux will be studied extensively by means of the Monte Carlo transport code MCNPX. The core coolant's high temperature drastically reduces the candidate instrumentation, because only some kind of Fission Chambers and Self Powered Neutron Detectors can be operated in such an environment.

This work aims at evaluating the capabilities of the available instrumentation (usually designed and tailored for Sodium cooled Fast Reactors, SFRs) when exposed to the neutron spectrum derived from ALFRED, a pool-type LFR project to demonstrate the feasibility of this technology into the European framework. This work shows that such class of instrumentation does follow the power evolution, but is not completely suitable to detect the whole range of reactor power, due to excessive burn-up, damages or gamma interferences. Some improvements are possible in order to increase the signal-to-noise ratio, by optimizing each instrument into its appropriate range of reactor power.

The design of some new detectors are here proposed, together with a possible approach for prototyping and testing them by means of a fast reactor.

1 Introduction

Nowadays the Fast Reactor R&D domain has known important improvements, due mainly to the goals proposed by Gen IV International Forum [1] [2].

Among the proposed solution, Lead-cooled Fast Reactors (LFRs) have recently gained a position despite the fact that the main drawback about this coolant, i.e. its chemical compatibility with materials, has not yet been solved. U.S. and Soviet Union acknowledged, in 60's, the corrosion processes and chemical compatibility with materials as the main limitation for this technology [3].

Today R&D in material science made the lead-coolant attractive once again for critical (power reactor) and sub-critical applications (ADS, Accelerator Driven System), due to some advantages on safety, if compared with sodium. As a consequence in the last decade, lead applications for fast reactor experienced a boost.

Inside the European Framework, ongoing LFR projects are MYRRHA (Multi-purpose hYbrid Research Reactor for High-tech Applications) and ALFRED (Advanced Lead Fast Reactor European Demonstrator), the first a sub-critical demonstrator for ADS-type plant (whose operability will confirm the possibility to close the uranium fuel cycle by means of burning all the long-lived actinides), the second being a medium-power demonstrator reactor for electricity production [4] [5]. Currently, MYRRHA is the European pilot plant for the lead technology.

Considering that the SFR technology can count on decades of reactor-years operation, LFR technology appears today not much investigated, as it would deserve.

On the basis of a previous work presented by the authors [6], this paper here focuses on I&C issues about the Demonstrator ALFRED, aiming at showing that the reference neutron instrumentation currently available for SFRs may be not completely suitable when transferred to LFR. Compared with [7], this work benefits from updated calculation on ALFRED simulation model, showing new consideration about the applicability of the analysed instrumentation.

2 Methodology

Neutron-flux monitoring instrumentation performances are usually tested in factory by means of thermal neutron while fast response is never evaluated. This is due to the fact that in Light Water Reactor –the most widespread type of reactor in the world– sensors monitor most of all thermal neutrons in every position they are placed, because the variation of sensor positioning significantly affects the magnitude of the neutron flux, but does not the energy distribution of neutrons.

Fast Reactors behave quite differently. The average energy of neutron spectrum significantly varies when moving from the center to the edge of the core. This means that the detector sensitivity varies substantially with positioning because the spectrum-averaged cross-section of the reaction it uses for counting neutrons is no more constant. In other words, detector performances into a fast reactor environment are practically unknown, because different neutron energy spectra lead to detecting capability strongly related to the positioning.

The selection of the correct LFR instrumentation for neutron-flux monitoring requires: 1) the identification of sensors robust enough to resist the reactor core thermal-hydraulic conditions, 2) the ‘actualization’ of their performances to the particular LFR neutron environment; 3) the evaluation of external constraints that may reduce the counter applicability or lifetime.

The so-called ‘actualization’ has been here realized by means of Monte Carlo calculation by MCNPX (Monte Carlo N-Particles X-version) [8], with the mathematical procedure shown below. A neutron detector response, R (count per second or current), is proportional to the cross-section of the involved reaction ‘i’ weighted by the energy spectrum of neutrons that hit the sensor (1). The more the cross-section varies with the energy, the more the detector sensitivity can change significantly with the spectrum variation. Referring to equation (1), the local value $\bar{\sigma}_i(\vec{r})$ provides information about detector sensitivity in position \vec{r} while its multiplication by local flux $\varphi(E, \vec{r})$ gives the local response $R(\vec{r})$ of the instrument.

$$R(\vec{r}) \propto \int \sigma_i(E) \varphi(E, \vec{r}) dE = \bar{\sigma}_i(\vec{r}) \int \varphi(E, \vec{r}) dE \quad (1)$$

$$R_{fast}(\vec{r}) \propto \bar{\sigma}_i(\vec{r}) \Big|_{fast} \int p(\vec{r}) \psi(E) \Big|_{fast} dE \quad (2)$$

$$R_{thermal}(\vec{r}) \propto \bar{\sigma}_i(\vec{r}) \Big|_{thermal} \int p(\vec{r}) \psi(E) \Big|_{thermal} dE$$

$$ESCF(\vec{r}) = \frac{\bar{\sigma}_i(\vec{r}) \Big|_{fast}}{\bar{\sigma}_i(\vec{r}) \Big|_{thermal}} \equiv \frac{\bar{\sigma}_i(\vec{r}) \Big|_{fast}}{\bar{\sigma}_i \Big|_{thermal}} \quad (3)$$

$$S(\vec{r}) \Big|_{fast} = ESCF(\vec{r}) \cdot S \Big|_{thermal} \quad (4)$$

MCNPX can easily calculate $\bar{\sigma}_i(\vec{r})$ values into (1). Varying the shape factor $\psi(E)$ of the neutron flux $\varphi(E, \vec{r}) = p(\vec{r}) \psi(E)$, e.g. once with fast neutron flux, once with thermal neutron flux, it is possible to calculate the theoretical fast and thermal responses respectively.

Focusing on energy-averaged cross sections $\bar{\sigma}_i(\vec{r}) \Big|_{fast}$ and $\bar{\sigma}_i(\vec{r}) \Big|_{thermal}$ it is possible to calculate the Energy Spectrum Correction Factor $ESCF(\vec{r})$ (3), which is useful for actualizing the performances given by the technical specifications of detector (rated by thermal neutrons) to the current application. Because $\bar{\sigma}_i(\vec{r}) \Big|_{thermal}$ refers to the factory instrument testing with thermal neutron, it does

not depend on reactor position \bar{r} ; therefore, we can indicate it as $\bar{\sigma}_i|_{thermal}$. This value has been calculated with a single MCNPX run with the Maxwell-Boltzmann energy spectrum corresponding to T=293 K.

For the fast neutron spectrum, multiple calculations of $\bar{\sigma}_i(\bar{r})|_{fast}$ have been conducted for each reactor position suitable for installing the detector. So, a set of $ESCF(\bar{r})$ corrections has been evaluated for each studied location (3). Then, the fast sensitivity of the instrument has been updated, retrieving $s(\bar{r})|_{fast}$ values related to reactor position \bar{r} (4).

Section §5 shows the results of the methodology applied to ALFRED.

Once the correct sensitivity has been calculated, the process of instrumentation selection needs to evaluate other parameters, such as the usable lifetime of the detector or the interferences it may experience. In order to make the selection process successful, it is strongly recommended to match the theoretical consideration with experimental tests step by step.

3 Reference LFR reactor and simulation model

The LFR Demonstrator called ALFRED has been proposed in the context of the LEADER Project (Lead-cooled European Advanced DEMonstration Reactor, 2010-2013). Its goal is to demonstrate the feasibility of LFR power reactors, in order to acquire experience for future larger plants like ELFR, European Lead Fast Reactor. ALFRED is a 300 MWth pool-type fast reactor cooled by pure lead: all its constructive details can be found in [9].

In order to reproduce neutron and gamma radiation fields in the position the neutron flux instrumentation is foreseen to be employed, ALFRED has been reproduced into the Monte Carlo code MCNPX in a very detailed way, as to get significant values in terms of spectra and magnitudes of both neutron and gamma fluxes. The simulation model is very complex: currently the MCNPX input deck of the reactor reaches 50,000 lines in length, including all the structure surrounding the core. For easiness of running the code, the reactor pit cover has not been included as the main pumps immersed into the lead coolant, because those elements are quite far from the core itself and their influences on neutron fluxes near the core may be neglected.

High Parallel Computing (HPC) resources have been involved, giving the authors the possibility to improve the previous results. Calculations required running time of a single simulation in the order of 300,000 h*core as to get the accuracies as desired.

The computing resources and related technical support used for this work have been provided by CRESCO/ENEAGRID High Performance Computing infrastructure and its staff [15]. CRESCO/ENEAGRID High Performance Computing infrastructure is funded by ENEA, the Italian National Agency for New Technologies, Energy and Sustainable Economic Development and by Italian and European research programmes, see <http://www.cresco.enea.it/english> for information.

4 Application of the methodology to ALFRED

The methodology described in §2 has been applied to the instrumentation reported in §4.1 when exposed to neutron fluxes and spectra derived from LFR Demonstrator ALFRED.

4.1 Available neutron instrumentation for high temperature environment

This work focuses on some miniaturized sensors designed for being installed into fuel-pin, and normal-sized detectors for dedicated installation all around the core. Only prompt detectors are taken into account.

The main drawback for instrumentation to be put into the LFR reactor environment is the temperature limiting the applicable technologies for measuring the neutron flux to some kinds of

Fission Chambers (FCs) by Photonis and Self Powered Neutron Detectors (SPNDs) by Ari Industries and KWD [16][17][18][19].

4.2 Updating current instrumentation performances to ALFRED fast spectra

The methodology described in §2 has been applied to the ALFRED reactor, evaluating the capability of the selected instrumentation in neutron flux monitoring.

In previous works [7], two reference planes were considered named “core mid-plane” and “nose-plane”, each one provided with six tally-points for energy-averaged cross-section and neutron flux calculation (Figure 1, left). Into this work, new installation points are being considered with a less-invasive approach into the fuel, without failing the neutron core monitoring needs. Two axial segments are being considered (the core central pin –C points– and a reflector pin facing the active zone –R points–), leaving the radial segment only on “nose-plane” –N points– (Figure 1, right). The detectors’ new positioning has been inspired by French experiences on Super-Phénix reactors [10] [11] [12].

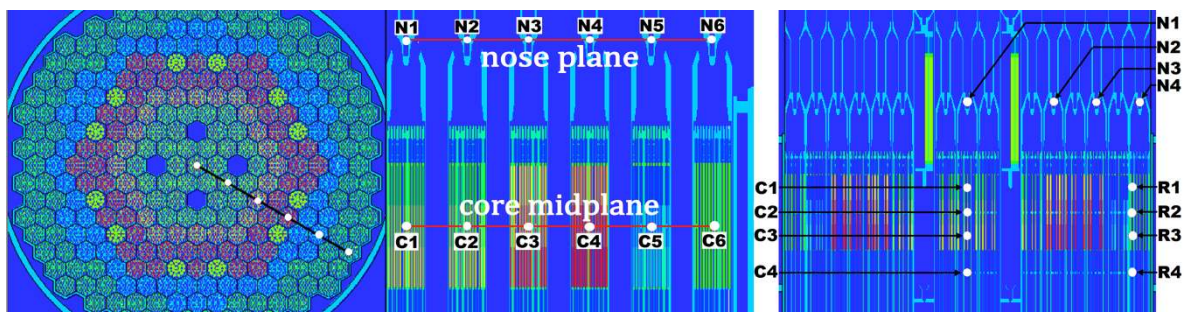


Fig.1: Core plane and points investigated for calculating detectors’ fast sensitivities and responses in previous works (left). New detector’s positioning for calculation in this work (right).

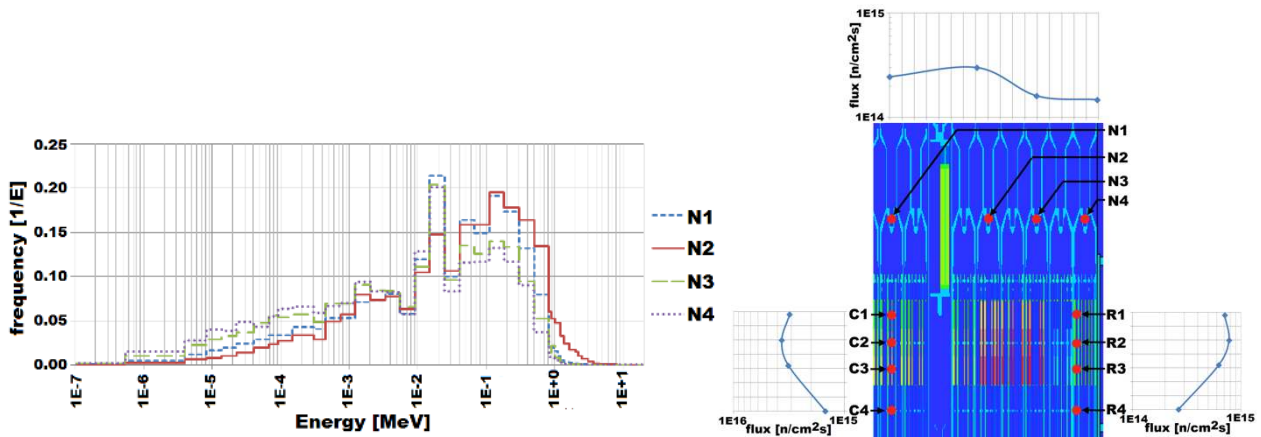


Fig.2: Left: neutron flux spectra comparison in N1 to N4 “nose-plane” points. The averaged energy of the spectrum varies significantly due to scattering and absorber materials. Right: neutron flux magnitude trend in positions suitable for installing neutron detectors.

As can be easily foreseen, the magnitude of the neutron flux reaches the higher values near the fuel active zone, points C1 to C4 and R1 to R4. Installation sites more far, such as points N1 to N4 on “nose-plane”, experience the loss of an order of magnitude in neutron flux if compared with previous points (Figure 2, right). About the neutron energy distribution, for brevity, only some spectra will be presented, e.g. the comparison between the points N1, N2, N3, N4 on “nose-plane” (Figure 2, left), whose variation are easier to understand at a glance. Indeed, spectra vary significantly moving from a position to another, due to the distribution of materials that cause absorption and scattering of neutrons.

As stated in previous works, the sensitivity of the instrumentation may vary significantly (till two orders of magnitude) according to the neutron spectra and the peculiar shape of the reaction cross-section corresponding to the sensitive material of the counter.

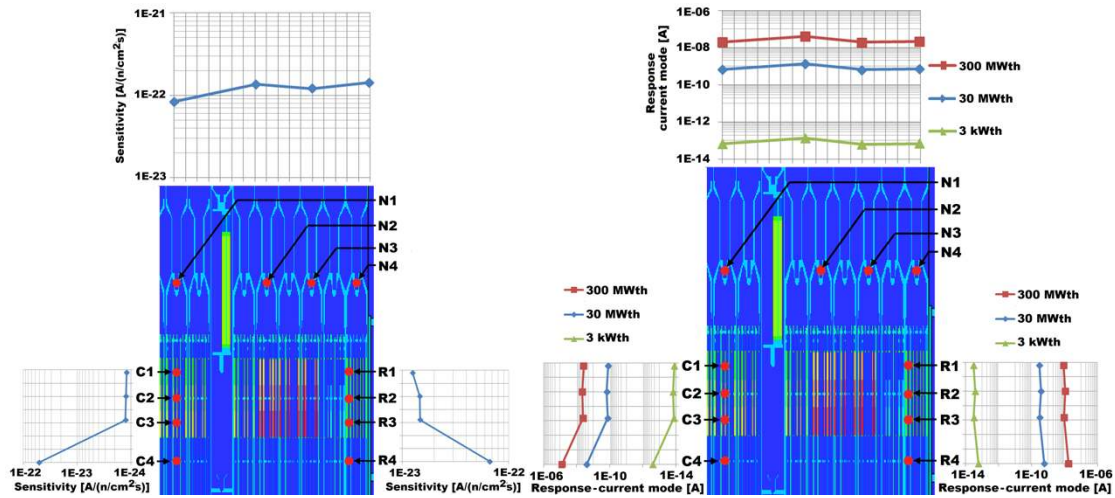


Fig. 3: Left: KWD 5503-Co-210 SPND current-mode sensitivity in the positions studied in Demonstrator ALFRED (uncertainty less than 1%). Right: KWD 5503-Co-210 SPND current-mode response in the positions studied in Demonstrator ALFRED (uncertainty less than 5%).

Among the instrumentation reported in §4.1, only KWD SPND 5503-Co-210 results will be here presented. Figure 3, left, shows significant variations in detector fast sensitivity $s(\vec{r})|_{fast}$ with position \vec{r} : each detector experiences improvements in sensitivity for out-of-core installation due to the reduction of the averaged-energy of neutron spectra and cross-sections' shapes which generally increase when energy reduces.

Unfortunately, moving from the center of the core through the edges, the flux magnitude $\rho(\vec{r})$ decreases stronger than those sensitivity gains; therefore detector responses globally reduce moving away from the core center.

Figure 3, right, shows the detector responses in current-mode, $R(\vec{r})$, vs. different positioning and three different reactor power level, at 0.1%, 10% and 100% of the nominal thermal power.

About KWD SPND 5503-Co-210, in previous works [7] the author showed that the operation of that instrument requires a neutron population of some MW in magnitude, in order to get neutron fluxes sufficient to produce reliable out-coming signals. Its sensitivity ensures the possibility of a fixed installation in the fuel element lattice, enabling the operation of detectors only when a certain minimum power is reached. The durability of this sensor is less critical than in uranium fission chambers, as the burn-up rate is significantly lower, i.e. burn-up at 1 % per year at full-power.

5 Conclusion and future developments

At this stage of the work, prompt-SPNDs seem very promising as in-core instrumentation for neutron flux control purposes in power range. Due to the lack of R&D about prompt-SPND, some significant improvements are envisaged: because of that, those detectors will be the focus of the future steps of this work. In order to optimize the SPND design by means of MCNPX, some experimental tests of commercial SPNDs carried out at ENEA TAPIRO Fast Reactor facility [14] have been reconstructed into the Monte Carlo code. The successful reproduction of the experimental results validates the simulation model for those instruments, elevating MCNPX at a design tool. Future developments will include an extensive study on SPND modifications; new designs of custom-made prompt-SPND could be prototyped and new test scheduled.

References

- [1] Generation IV International Forum, "*A Technology Roadmap for Generation IV Nuclear Energy Systems*", GIF-002-00, 2002.
- [2] M. Salvatores and G. Palmiotti, "*Radioactive waste partitioning and transmutation within advanced fuel cycles: achievements and challenges*," Progress in Particle and Nuclear Physics, 2011.
- [3] L. Lepore, R. Remetti and M. Cappelli, "*Analisi dei sistemi di strumentazione e controllo previsti in alcuni progetti su reattori al piombo attualmente in sviluppo a livello internazionale*", ENEA-MSE Report RdS/2013/030, 2013.
- [4] SCK-CEN, "*Myrrha: an Accelerator Driven System (ADS)*," [Online]. Available: <http://myrrha.sckcen.be/en/MYRRHA/ADS>.
- [5] A. Alemberti, "*ELFR, The European Lead Fast Reactor Design, Safety Approach and Safety Characteristics*," Dresden, 2012.
- [6] L. Lepore, R. Remetti and M. Cappelli, "*Fast Neutron-Flux Monitoring Instrumentation for Lead Fast Reactors: A Preliminary Study on Fission Chamber Performances*," in 22nd International Conference on Nuclear Engineering Proceedings (ICONE22), V006T13A016; 9 pages, Prague, 2014.
- [7] L. Lepore, R. Remetti and M. Cappelli, "*Evaluation of the current fast neutron flux monitoring instrumentation applied to LFR Demonstrator ALFRED: capabilities and limitations*" in 23rd International Conference on Nuclear Engineering Proceedings (ICONE23), Makuhari Messe, Chiba, Japan, 2015.
- [8] J. F. Briesmeister, "*MCNP – A general purpose Monte Carlo code for neutron and photon transport*," Nov 1993.
- [9] A. Alemberti, "*The Lead Fast reactor: Demonstrator ALFRED and ELFR Design*," Paris, 2013.
- [10] J. C. Gauthier, G. Granget e M. Martini, "*Techniques de mesures neutroniques au demarrage de SPX2*," in Proceedings of a Specialists' Meeting on IN CORE INSTRUMENTATION AND REACTOR ASSESSMENT, Cadarache, 1989.
- [11] J. C. Perrigreur, C. Berlin, J. C. Gauthier e J. Gourdon, "*In core neutronic measurements in an industrial environment. Assessment of the performances of the in-vessel neutronic measurements chains of SUPER-PHENIX 1*," in Proceedings of the Specialists' Meeting on IN CORE INSTRUMENTATION AND REACTOR ASSESSMENT, 1989.
- [12] J. C. Nervi, P. Marmonier, A. Eyraud, J. C. Perrigreur, P. Rouches e L. Verset, "*Experimental Devices used for Start-up Operations of the SUPER-PHENIX core*," in International Conference, Richland, USA, 1987.
- [13] J. P. Trapp, S. Haan, L. Martin, J. L. Perrin and M. Tixier, "*High temperature fission chambers: state-of-the-art*," [Online]. Available: <https://www.oecd-nea.org/science/rsd/ic96/4-3.pdf>.
- [14] M. Angelone, A. Klix, M. Pillon, P. Batistoni, U. Fischer e A. Santagata, "*Development of self-powered neutron detectors for neutron flux monitoring in HCLL and HCPB ITER-TBM*," Fusion Engineering and Design, vol. 89, p. 2194–2198, 2014.
- [15] G. Ponti, "*The role of medium size facilities in the HPC ecosystem: the case of the new CRESCO4 cluster integrated in the ENEAGRID infrastructure*," in 2014 International Conference on High Performance Computing and Simulation.
- [16] Photonis, "*Photonis fission chamber for in-core use*," [Online]. Available: <http://www.photonis.com/nuclear/products/fission-chambers-for-in-core-use/>.
- [17] Photonis, "*Photonis fission chamber for out-of-core use*," [Online]. Available: <http://www.photonis.com/nuclear/products/fission-chambers-for-out-of-core-use/>.
- [18] ARi Industries, "*Self Powered Neutron Detectors*," [Online]. Available: http://www.ariindustries.com/catalog/self_powered_neutron_detectors.pdf.
- [19] KWD Nuclear Instruments, "*Self Powered Neutron Detectors*," [Online]. Available: <http://www.kwdnuclearinstruments.se/self-powered-neutron-detectors>.

ANALYSIS OF THE CHAOTIC BEHAVIOR OF THE LOWER HYBRID WAVE PROPAGATION IN MAGNETISED PLASMA BY HAMILTONIAN THEORY

Alessandro Cardinali^{1*}, Andrea Casolari²

¹*Associazione Euratom-ENEA sulla Fusione, C.P. 65 - I-00044 - Frascati, Rome, Italy*

²*Dipartimento di Fisica Enrico Fermi, Università di Pisa, Largo Bruno Pontecorvo 3, I-56127 Pisa, Italy*

ABSTRACT. The Hamiltonian character of the ray tracing equations describing the propagation of the Lower Hybrid Wave (LHW) in a tokamak is investigated in order to study the evolution of the parallel wave number along the propagation path. The chaotic diffusion of the "time averaged" parallel wave number at higher values has been evaluated, in order to find an explanation of the filling of the spectral gap by "Hamiltonian chaos" in the Lower Hybrid Current Drive (LHCD) experiments. The present work shows that the increase of the parallel wave number n_{\parallel} due to toroidal effects, in the case of the typical plasma parameters of FTU, is insufficient to explain the filling of the spectral gap and the consequent Current Drive and another mechanism must come into play to justify the wave absorption by Landau damping.

1 Introduction

Electromagnetic waves in the Lower Hybrid (LH) range of frequencies have long been used as an efficient way of generating a non-inductive current in tokamaks [1]. The problem of describing the propagation of Lower Hybrid Waves (LHW) in such kind of confined plasmas has been studied intensively during the last few decades and simplified models, based on the WKB approximation, have been used because of the easier numerical and analytical implementation respect to the more sophisticated Vlasov-Maxwell full system. In fact the ray tracing technique, based on the WKB expansion of the wave equation [2, 3, 4, 5] allows to study the propagation of the LHW in such plasma, by taking into account the toroidal geometry of the tokamak. The ray tracing equations are formally the Hamilton equations of a mechanical system in which the roles of the momentum and position are assumed by wave vector and position, and the Hamiltonian is the dispersion relation which correlates (ω, \vec{k}) to (t, \vec{r}) , time and space. If the LHW is launched by an antenna, and the condition of Landau absorption is not fulfilled inside the plasma, the wave remains trapped without absorption in the confined plasma. This regime was proposed by P. T. Bonoli [5] in order to explain the filling of the spectral gap in the LHW absorption, by invoking a simple linear mechanism. In this paper we focus on the multi-pass approach and we try to study the dynamical evolution of the rays in the case of long integration time: in this situation the nonlinear effects which stem out from the non-linear ray equations (Hamilton equations) can play a role in the chaotic evolution of the dynamical system. This chaotic evolution of the trajectory can be associated with a chaotic diffusion of the "parallel wave number". In our study we have performed a complete scan in the plasma density to establish the transition to the chaotic behavior of the trajectories.

*Corresponding author. E-mail: alessandro.cardinali@enea.it.

2 The Electromagnetic Dispersion Relation as Hamiltonian function

The starting point is the cold electromagnetic wave equation for the harmonic electric field perturbation ($\vec{E}(\vec{q}, t) = \vec{E}(\vec{q})e^{i\omega t}$) suitable to describe the propagation of Lower Hybrid waves (GHz range of frequencies) in magnetically confined plasmas:

$$\nabla \wedge \nabla \wedge \vec{E}(\vec{q}) + \frac{\omega^2}{c^2} \underline{\underline{\epsilon}}(\vec{p}, \vec{q}) \cdot \vec{E}(\vec{q}) = \gamma(\vec{p}, \vec{q}) \vec{E}(\vec{q}) \quad (1)$$

where \vec{p}, \vec{q} are the wave vector and position respectively, $\underline{\underline{\epsilon}}(\vec{p}, \vec{q})$ is the Hermitian part of the cold plasma dielectric tensor, $\gamma(\vec{p}, \vec{q})$ is the damping factor (Landau damping) related to the anti-Hermitian part of the dielectric tensor, $\vec{E}(\vec{q})$ is the harmonic electric field which depends on position \vec{q} . Eq.1 can be solved by the WKB expansion, assuming the following form for the electric field: $\vec{E}(\vec{q}) = \vec{E}_0(\vec{q})e^{ih^{-1}S(\vec{q})}$, where $\vec{E}_0(\vec{q})$ is the slowly varying amplitude, $S(\vec{q})$ is the phase which varies on a smaller length-scale and $h^{-1} = \omega a/c \ll 1$ is the WKB expansion parameter (a is the plasma minor radius). Applying the form just chosen for the electric field to Eq.1 and using toroidal coordinates $\vec{q} = (r, \theta, \phi)$ and $\vec{p} = (p_r, p_\theta, p_\phi)$, we obtain to the lowest order the following dispersion equation for the conjugated variables \vec{p}, \vec{q} :

$$H(q_i, p_i) = A(r, \theta, p_\theta, p_\phi)p_r^4 + B(r, \theta, p_\theta, p_\phi)p_r^2 + C(r, \theta, p_\theta, p_\phi) = 0 \quad (2)$$

where A, B, C are defined in terms of the elements S, D and P of the cold dielectric tensor in Stix notation [7], $\vec{p} = \nabla S(\vec{q})$, \hat{B}_θ and \hat{B}_ϕ are the poloidal and toroidal magnetic fields (normalized to $|B|$). Eq.2 represents the Hamilton-Jacobi equation for the generating function $S(\vec{q})$, once the substitution $\vec{p} = \nabla S(\vec{q})$ has been made, and $H(\vec{q}, \vec{p})$ is the corresponding Hamiltonian.

3 Numerical results

To check the transition to chaos of the ray dynamics, we performed a series of numerical integrations of the ray trajectories. The position and the wave vector (momentum) evolve according to the Hamilton equations:

$$\dot{r} = \frac{\partial H}{\partial p_r}, \quad \dot{p}_r = -\frac{\partial H}{\partial r}, \quad \dot{\theta} = \frac{\partial H}{\partial p_\theta}, \quad \dot{p}_\theta = -\frac{\partial H}{\partial \theta}, \quad \dot{\phi} = \frac{\partial H}{\partial p_\phi}, \quad \dot{p}_\phi = -\frac{\partial H}{\partial \phi} \quad (3)$$

and the equation for the time variable $t = -\partial H/\partial \omega$. Applying them to the Hamiltonian Eq.2 we obtain the trajectories in the phase-space of the system, in particular those corresponding to the main variables, that is r and p_r , or the corresponding adimensional variables $x = r/a$ and $p_x = c/\omega p_r$. For the simulations we chose the FTU typical plasma and antenna parameters, that is a central density in the range $n_{e0} = 10^{13} \div 10^{14} \text{ cm}^{-3}$, inverse aspect ratio $\epsilon = 0.3$, toroidal magnetic field on axis $B_0 = 4 \div 8 \text{ T}$, plasma current $I_p = 0.3 \div 1 \text{ MA}$, corresponding to $3 < q_a < 10$, LH frequency $f = 8 \text{ GHz}$, launched parallel wave number $n_{\parallel} = 1.32 \div 2.42$. We performed a numerical study on the CRESCO Cluster by using the routine "DIVMRK" of the CRESCO mathematical library IMSL to establish the emergence of the chaos in the ray trajectories integration as function of the central density n_{e0} . This routine is able to integrate simultaneously a system of ordinary differential equations by a Runge-Kutta type algorithm. The routine, incorporated is a code, has been run for a long integration path. Owing to the x86-64 bit architecture of CRESCO, a very high level of accuracy (as required by the physics of the problem) has been maintained for all the integration domain. In our parametric study we varied the central plasma density from $n_{e0} = 5 \cdot 10^{13} \text{ cm}^{-3}$ to $n_{e0} = 1.5 \cdot 10^{14} \text{ cm}^{-3}$ keeping fixed the plasma current $I_p = 0.6 \text{ MA}$ ($q_a \approx 4$). In the set of figures (Figs.1) we present the Poincaré map for 4 different levels of central density corresponding to 4 increasing levels of energy. As it can be seen from the sequence of Figs.1 the

Poincaré section ($P_X - X$) is regular up to a density level $8 \cdot 10^{13} \text{ cm}^{-3}$ (which is the usual range of operating density in LHCD experiments), after this threshold the ray dynamic becomes chaotic. From the numerical solution of Hamiltonian equations it is also possible to study the variation of the parallel wave number. The variation we are looking for is an increase in the average value of $n_{\parallel} = c/\omega k_{\parallel}$, which would be responsible for the wave absorption by Landau damping on the electrons. The increase in the time average $\langle n_{\parallel} \rangle$ is limited enough to be incompatible with an efficient wave absorption by Landau damping, which requires a parallel wave number $n_{\parallel ELD}$ such that [6] $n_{\parallel} > n_{\parallel ELD} = (5 \div 8)/\sqrt{T_e \text{ KeV}}$. In the reported cases of Fig. 2, the time-averaged n_{\parallel} is shown for the case a and b (without chaos), $\langle n_{\parallel} \rangle = 3.2$, $\langle n_{\parallel} \rangle = 2$ respectively, and for the case c and d (in presence of chaos) $\langle n_{\parallel} \rangle = 4.5$ and $\langle n_{\parallel} \rangle = 10.4$ respectively. Only in the case of unrealistic value of central density ($1.5 \cdot 10^{14} \text{ cm}^{-3}$) and strongly chaotic behavior, the average parallel wave number is much higher than $n_{\parallel ELD}$.

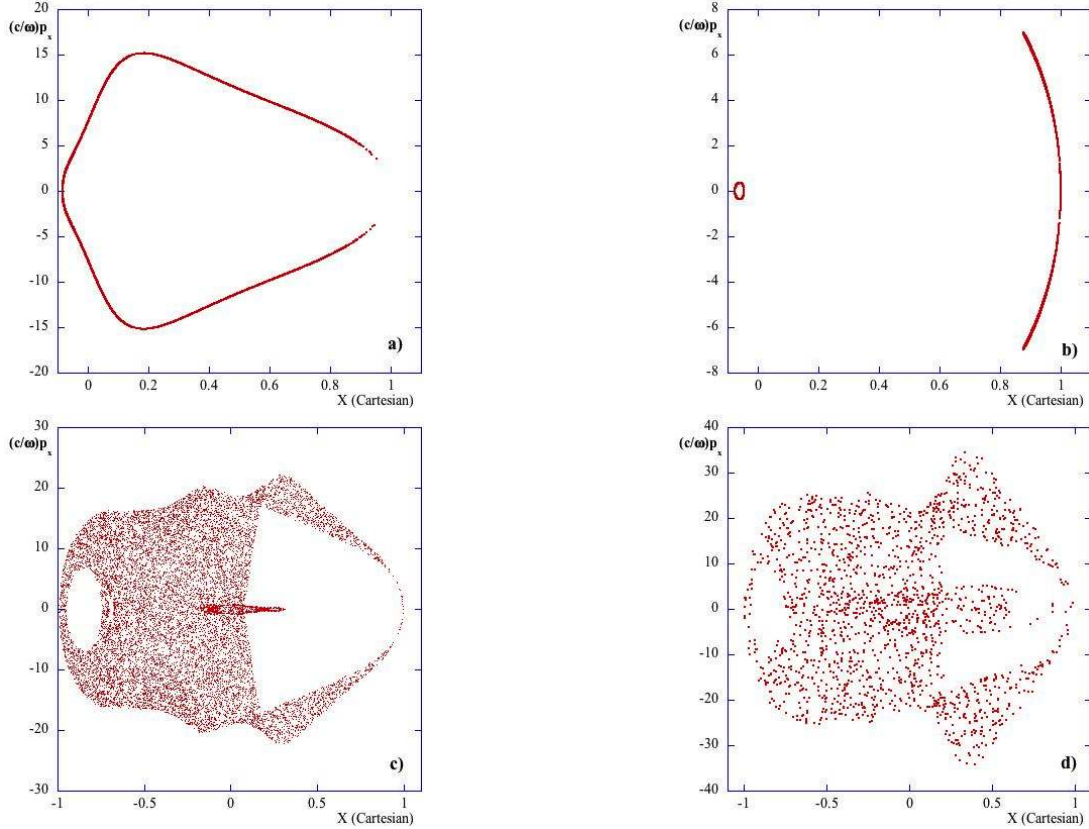


Figure 1: Poincaré section (P_X vs X) for four central densities (a) $n_{e0} = 5 \cdot 10^{13} \text{ cm}^{-3}$ (b) $n_{e0} = 8 \cdot 10^{13} \text{ cm}^{-3}$ (c) $n_{e0} = 9 \cdot 10^{13} \text{ cm}^{-3}$ (d) $n_{e0} = 1.5 \cdot 10^{14} \text{ cm}^{-3}$ and plasma parameters: $\epsilon = 0.3$, $B_0 = 6 \text{ T}$, $I_p = 0.6 \text{ MA}$, $q_a = 4$, $f = 8 \text{ GHz}$, $n_{\parallel 0} = 1.8$.

4 Conclusions

In this paper we studied the LHW propagation in tokamaks by means of the Hamiltonian theory, by identifying the dispersion relation of the LH with an Hamiltonian. The solution of the wave equation by the method of characteristics brings to the Hamilton equations for the position \vec{r} and the wave vector \vec{k} . We performed numerical integrations of the ray equations to study the time evolution of the variables characterizing the system. The results show that the time-averaged parallel wave number, in the range

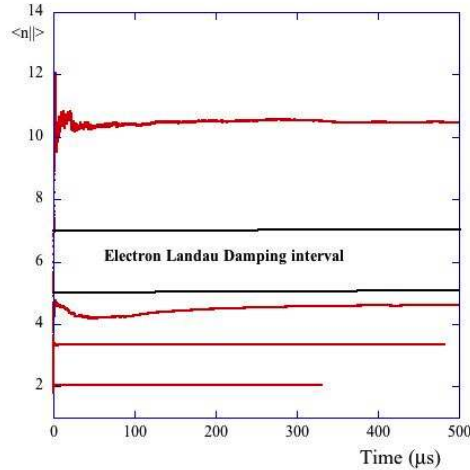


Figure 2: Evolution of the average n_{\parallel} vs time (μs) for the four central plasma densities as in Fig. 1. On the same plot we show the Electron Landau damping interval where absorption is supposed to occur. The plasma parameters are the same of Fig. 1

of parameters typical of the FTU LH current drive experiments, remains limited to low values so that it can't give rise to significant absorption by Landau damping. We observed instead a different behavior in the dynamics of the system depending on the value of the central density n_{e0} . In the lower density case $n_{e0} = 5 \cdot 10^{13} \text{ cm}^{-3}$ we found that the system behaves regularly, with ray trajectories which do not fill completely the "energetically" available phase space portion, a very regular Poincaré section and a small increase in the time averaged n_{\parallel} . In the higher density case $n_{e0} = 10^{14} \text{ cm}^{-3}$ the system shows a chaotic behavior, with ray trajectories which fill almost completely the "energetically" available phase space portion, an irregular Poincaré section and a large increase in the time averaged n_{\parallel} .

References

- [1] Fisch, N. J. Theory of current drive in plasmas. *Reviews of Modern Physics*, **1987**, 59 (1), 175.
- [2] Bernstein, I. B. Geometric optics in space- and time- varying plasmas. *Physics of Fluids*, **1975**, 18 (3), 320-324.
- [3] Baranov, Y. F.; Fedorov, V. I. Lower-hybrid wave propagation in tokamaks. *Nuclear Fusion*, **1980**, 20 (9), 1111.
- [4] Brambilla, M.; Cardinali, A. Eikonal description of hf waves in toroidal plasmas. *Plasma physics*, **1982**, 24 (10), 1187.
- [5] Bonoli, P. T. Linear Theory of Lower Hybrid Heating. *IEEE Transactions on Plasma Science*, **1984** 12 (2), 95-107
- [6] Brambilla, M. Electron Landau damping of lower hybrid waves. *Nuclear Fusion*, **1978**, 18 (4), 493.
- [7] Stix, T. H. *Waves in Plasmas*, AIP, New York, 1992.
- [8] Baranov, Y. F., Piliya, A. D., Esterkin, A. R. Anomalous slowing of lower hybrid waves in toroidal plasma. *Journal of Experimental and Theoretical Physics Letters*, **1990**, 51, 701.

Bi(111) NANOFILMS: QUANTUM CONFINEMENT AND SURFACE STATES

Giovanni Cantele^{1*}; Domenico Ninno^{1,2}

¹*CNR-SPIN, c/o Università degli Studi di Napoli “Federico II”, Compl. Univ. M.S. Angelo, I-80126, Napoli, Italy*

²*Università degli Studi di Napoli “Federico II”, Dipartimento di Fisica, Compl. Univ. M.S. Angelo, I-80126, Napoli, Italy*

ABSTRACT. This report describes ab initio calculations of the structural and electronic properties of bismuth (Bi) nanofilms with thickness ranging from single layer (~ 1.6 Å thickness) to 20 layers (~ 80 Å thickness). Both spin-orbit coupling as well as inter-bilayer van der Waals interaction are taken into account, for an accurate evaluation of the structural properties, with particular reference to the in-plane lattice constant and the inter-bilayer distance. Density of states calculations reveal that surface states around the Fermi energy show up, that survive also in the thickest nanofilms, with negligible dependence on the film thickness. The results might be of interest for the use of such nanofilms in complex interfaces of interest for energy conversion applications (for example thermoelectrics).

1 Introduction

The Bi(111) surface is obtained from the stacking of Bi bilayers oriented according to the rhombohedral (111) direction [4]. Covalent bonds held together each bilayer, whereas much weaker van der Waals forces are responsible for inter-bilayer interactions. This feature makes the Bi(111) surface ideal for epitaxial growth and easily cleavable along the (111) planes. Moreover, the in-plane surface lattice is described by a hexagonal lattice, making this material a potential candidate for conceiving new interfaces with new generation two-dimensional materials [7], to create new functionalities that cannot be implemented in other interfaces. Within each bilayer, each bismuth atom has three nearest neighbours at a distance of ~ 3 Å. A sketch of the 6 bilayer Bi(111) nanofilm is shown in Fig. 1

This material, that in its bulk form is semimetallic [4], has been proposed as a promising candidate for energy applications, due to its good thermoelectric performance at both room and low temperature [3], as well as for low-cost electronics and surface spintronics [1]. In this respect, thin nanofilms and, more generally, nanostructures made of bismuth become very appealing because, for example, it has not yet fully understood how quantum confinement effects, arising when one or more dimensions are reduced down to the nanoscale, show up in Bi nanostructures [4]. More importantly, spin-orbit coupling, that is a relativistic effect important for the electronic structure of heavy atoms and their solids, does play a fundamental role. This is especially true in nanostructures where the breaking of the periodicity causes the lifting of electronic level degeneracies due to the loss of inversion symmetry even in materials that have such a symmetry in the bulk.

*Corresponding author. E-mail: giovanni.cantele@spin.cnr.it.

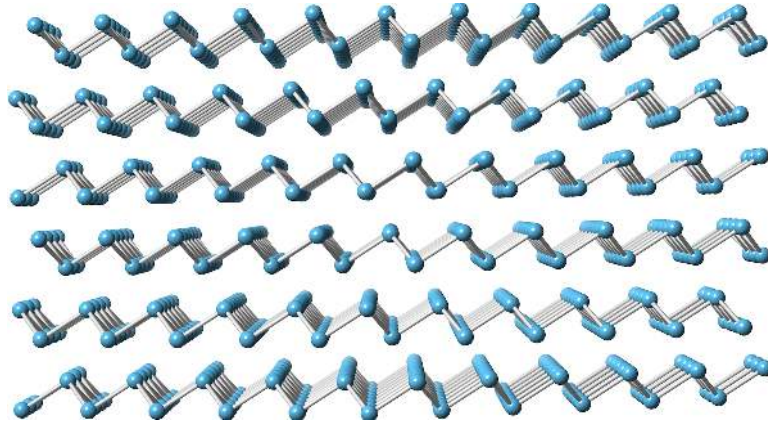


Figure 1: A sketch of the Bi(111) nanofilm composed by 6 bilayers. The stacking of Bi bilayers as well as the covalent bonding within each bilayer can be easily visualized.

2 Software and computational resources

The first principle calculations are based on Density Functional Theory (DFT). Two main computational packages have been used on the CRESCO infrastructure, both based on plane waves to represent the electronic wave functions and charge density and pseudopotential to represent the ion cores: the open source QUANTUM ESPRESSO package [8] and the copyright-protected software VASP (*Vienna ab-initio simulation program*) [5]. Because the adopted frameworks intrinsically deal with periodic systems, low dimensional systems (surfaces and thin films, nanowires, nanocrystals) are studied within the supercell approach, in which periodic replicas along the non periodic direction(s) are separated by vacuum space, large enough to prevent from spurious interactions. The results shown in the present report have been obtained with the use of high performance computing facilities, in particular the CRESCO3 cluster located at the Portici ENEA center. Typical jobs require 64 to 256 computing units and several tens Gb of disk storage (for electronic wave functions and charge density, needed both during the optimization tasks and for post processing purposes). Parallelization is implemented through the MPI environment. For most calculations projector augmented wave (PAW) pseudopotentials [2] are employed.

Fermi surface and thermoelectric properties, that usually require summation over dense grids in the first Brillouin zone, are performed using the Maximally-Localized Wannier Functions (MLWFs) approach, as implemented into the WANNIER90 package [6]. The extended Bloch orbitals, obtained from the DFT calculation(s) are transformed to localized orbitals that allow to describe the material band structure, or part of it (for example, selected energy windows around the Fermi energy), in terms of a tight binding Hamiltonian. This allows also to interpolate the calculation of the band energies over very fine grids in the Brillouin zone, that would very computationally demanding for the ab initio calculation and that are required, for example, for the calculation of the Density of States or of the Fermi surface.

3 Results

The electronic structure of bulk Bi can be described in terms of two filled s bands and three filled p bands, separated by a gap of several eV. This picture is transferred to the nanostructure films, in that only the p orbitals of each Bi atom in the nanofilm contribute to the bands closest to the Fermi level. This is confirmed by the calculation of the MLWFs, that shows that the use of only three orbitals per Bi atom with p character is sufficient to build a tight binding Hamiltonian that exactly describes all the bands around the Fermi level.

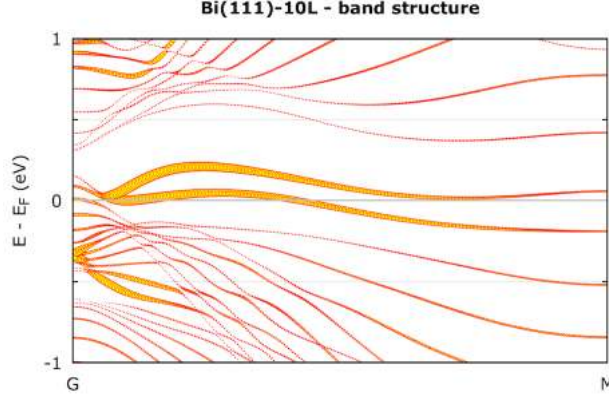


Figure 2: Band structure of the Bi(111) nanofilm composed by 10 bilayers along the Γ - M segment of the Brillouin zone. The size of each point is proportional to the projection of the corresponding Bloch orbital on the atomic orbitals belonging to the outermost bilayers. Zero energy corresponds to the Fermi level E_F . The occurrence of surface states at E_F is clearly evident.

The band structure of the Bi(111) nanofilm composed by 10 bilayers, calculated along the Γ - M segment of the Brillouin zone, is reported in Fig. 2. In this plot, the size of each point is proportional to the projection of the corresponding Bloch orbital on the atomic orbitals belonging to the outermost bilayers. It is evident that surface states show up around the Fermi energy. Calculation on nanofilms with larger thickness also show that the dispersion of such surface states becomes almost thickness independent for sufficiently thick nanofilms.

The electronic structures of the nanofilms progressively approaches that of the bulk crystal, upon increasing the thickness, apart from the presence of the surface states. For example, in Fig. 3 the density of states of the Bi(111) nanofilm composed by 10 bilayers is overlapped with that of the bulk crystal, showing that around the fermi energy the semi-metallic character of the bulk is hidden by a non-zero

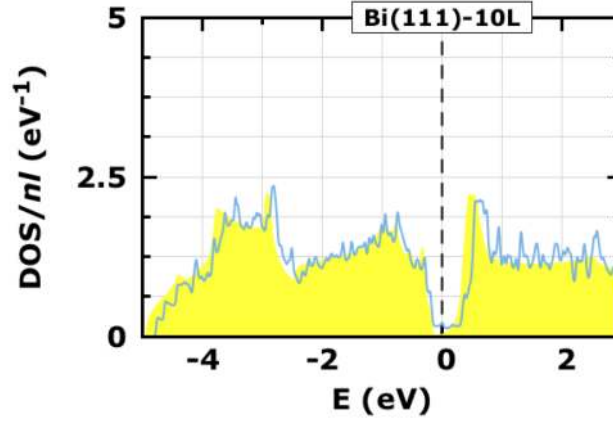


Figure 3: Density of States (DOS) per bilayer calculated for the Bi(111) nanofilm composed by 10 bilayers (solid line). The (yellow) shadowed region is the bulk DOS. The calculations have been performed from the DFT self-consistent calculation by interpolating the computed bands over a fine grid in the Brillouin zone ($128 \times 128 \times 128$ and $128 \times 128 \times 1$ for the bulk and nanofilm, respectively), with the WANNIER90 package.

density of states related to the presence of the surface states.

The use of large computational infrastructures, such as CRESCO, has allowed to span a wide range of film thicknesses, bringing out important properties, also from the structural point of view, such as the shrinking of the lattice parameter upon reducing the nanofilm thickness. Future investigations will concern the interface of such nanofilms with other two-dimensional van der Waals nanofilms and heterostructures.

References

- [1] Guang Bian, Zhengfei Wang, Xiao-Xiong Wang, Caizhi Xu, SuYang Xu, Thomas Miller, M Zahid Hasan, Feng Liu, and Tai-Chang Chiang. Engineering Electronic Structure of a Two-Dimensional Topological Insulator Bi(111) Bilayer on Sb Nanofilms by Quantum Confinement Effect. *Acs Nano*, 10(3):acs.nano.6b00987–3864, March 2016.
- [2] P. E. Blöchl. Projector augmented-wave method. *Phys. Rev. B*, 50:17953, 1994.
- [3] Long Cheng, Huijun Liu, Xiaojian Tan, Jie Zhang, Jie Wei, Hongyan Lv, Jing Shi, and Xinfeng Tang. Thermoelectric Properties of a Monolayer Bismuth. *J Phys Chem C*, 118(2):904–910, January 2014.
- [4] Ph Hofmann. The surfaces of bismuth: Structural and electronic properties. *Prog Surf Sci*, 81(5):191–245, January 2006.
- [5] G. Kresse and D. Joubert. From ultrasoft pseudopotentials to the projector augmented-wave method. *Phys. Rev. B*, 59:1758, 1999.
- [6] A. A. Mostofi, J. R. Yates, Y.-S. Lee, I. Souza, D. Vanderbilt, and N. Marzari. Wannier90: A tool for obtaining maximally-localised wannier functions. *Comput. Phys. Commun.*, 178:685, 2008.
- [7] K S Novoselov, A Mishchenko, A Carvalho, and A H Castro Neto. 2D materials and van der Waals heterostructures. *Science*, 353(6298):aac9439–aac9439, July 2016.
- [8] P. Giannozzi *et al.* Quantum espresso: a modular and open-source software project for quantum simulations of materials. *J. Phys.: Condens. Matter*, 21:395502, 2009.

MULTIPHASE ROTATING TURBULENT FLOWS IN GAS TURBINE INTERNAL COOLING CHANNEL

Domenico Borello^{*}, Franco Rispoli¹, Alessandro Salvagni¹ and Paolo Venturini¹

¹*Sapienza Università di Roma, Dip. Ing. Meccanica e Aerospaziale, Via Eudossiana 18, Rome, Italy*

ABSTRACT. This short report resume the activities on the simulation of the flow in gas turbine internal rotating channel. Such research was carried out using several approaches following two main branches: a) detailed LES study of the multi-phase turbulent flow field in a configuration resembling internal cooling channels in gas turbine blade; b) development of a URANS model for rotating turbulent flows. All the computations were carried out by the authors, by using an in-house Finite Volume code and performed on CRESCO Supercomputing facility [1-5]. For further details on models and results please refer to the cited bibliography.

1 Flow Model

The results here presented refer to three different modelling and simulation approaches: a) dynamic Smagorinsky Large Eddy Simulation; b) rotation-sensitized RANS model; c) multi-phase model.

2.1 Dynamic Smagorinsky Large Eddy Simulation and code setting

In our LES, the subgrid-scale (*sgs*) motion was modelled using the dynamic Smagorinsky approach. Since the turbulence scales are resolved up to and beyond the upper wave-number end of the inertial subrange, no correction was included in the *sgs* model to account for the rotational effects.

The governing equations were solved by means of the well-validated in-house unstructured finite-volume computational code *T-FlowS* from TU Delft, recently advanced at Sapienza Università di Roma [1]. A second-order accurate central-differencing scheme (CDS) was used for the discretization of the convection and diffusion terms. The time integration was carried out using also a second-order scheme. The velocity and pressure were coupled using the SIMPLE algorithm. The linearized algebraic system of the discretized equations was solved using the Preconditioned BiCG solver. The threshold for the global mass balance residual was set to 10^{-6} , while for the momentum and continuity equations it was 10^{-7} .

2.2 Rotation-sensitized URANS model

The basic URANS model is the k - ε - ζ - f elliptic relaxation model of Hanjalic et al. further developed by the authors to include quadratic formulation of the strain-Reynolds Stress link [2-3]. The model is not able to take in account the influence of rotation that generally suppresses turbulence on the stabilizing side (suction surface) and, in a specific range, increases turbulence on the destabilizing side (pressure surface). It must be remarked that when the rotation rate exceeds a threshold, the overall effect is a turbulence suppression.

To model here considered is based on a rotation-sensitized formulation originally developed for the ν - f model. The rotation is considered on the basis of a correction of the coefficient C_μ in the turbulent viscosity model (1) that is made dependent on the rotation angular velocity Ω_k .

$$\nu_t = \frac{C_\mu k^2 \zeta}{\varepsilon} \quad (1)$$

$$C_\mu^* = C_\mu \frac{1 + \alpha_2 |\eta_3| + \alpha_3 \eta_3}{1 + \alpha_4 |\eta_3|} \left(\sqrt{\frac{1 + \alpha_5 \eta_1}{1 + \alpha_5 \eta_2}} + \alpha_1 \sqrt{\eta_2} \sqrt{|\eta_3| - \eta_3} \right)^{-1}, \quad \eta_1 = S_{ij}^* S_{ij}^*, \quad S_{ij}^* = \frac{1}{2} \tau \left(\frac{\partial U_i}{\partial x_j} + \frac{\partial U_j}{\partial x_i} \right) \quad (2)$$

$$\eta_2 = W_{ij}^* W_{ij}^*, \quad W_{ij}^* = \frac{1}{2} \tau \left(\frac{\partial U_i}{\partial x_j} - \frac{\partial U_j}{\partial x_i} \right) + 2 \overline{C_\omega} \varepsilon_{ijk} \Omega_k, \quad \eta_3 = \eta_1 - \eta_2$$

In Fig.1, the results of validation test on a rotating channel and duct flow at $Re_\tau=194$ are reported and compared with DNS results

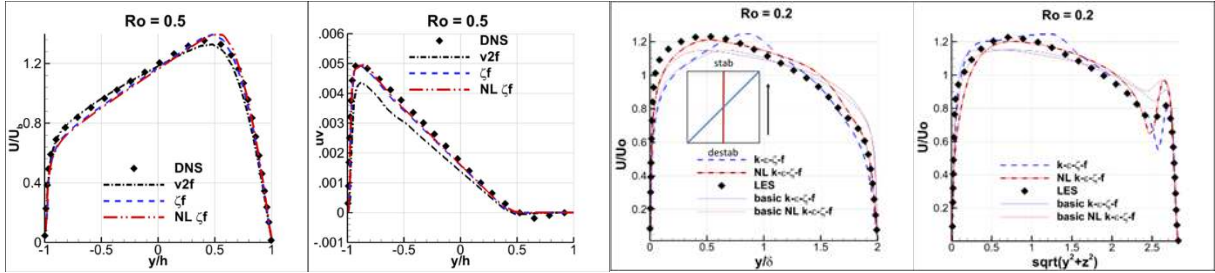


Fig.1: Validation of the rotation sensitized URANS model. From left to right: a) velocity in a fully developed channel flow at $Ro=0.5$; b) uv turbulent stress, same case; c) velocity profile along midplane for a rotating duct $Ro=0.2$; d) velocity profile along the bisector line same case as c)

2.3 Multi-phase model

In the adopted approach, a particle laden model incorporating erosion prediction was used. The solid particles released in the flow are individually tracked by using a Lagrangian framework. In turbomachinery applications the fraction of solid particles entrained by the flow is usually small ($< 10^{-6}$), thus inter-particle collisions are very rare and the effect of particles on the fluid motion is negligible [4-5]. A one-way coupling approach can be used, that is particle motion is affected only by flow motion, but flow is not affected by the presence of particles.

Newton's Second law (in the form of BBO equation) is solved to compute the motion of each particle. Since the average size of particles involved in turbomachinery flows is few μm , the only relevant forces acting on particles are drag as gravity has only a less relevant impact. Therefore, indicating with \vec{v} and \vec{u} respectively particle and gas velocities, the BBO equation writes

$$\rho_p \frac{d\vec{v}}{dt} = -\frac{3}{4d_p} \rho_f C_D (\vec{v} - \vec{u}) |\vec{v} - \vec{u}| \quad (3)$$

In order to account for the relative reference framework, the BBO equation (3) was modified adding the Coriolis and centrifugal forces. Particles are assumed to be spherical, non-rotating and non-reacting.

Erosion is a very complex phenomenon since it involves particle impact velocity and angle, particle shape, and material properties of both particles and target surface. Developing a theoretical model is extremely difficult. According to their experiments, Tabackoff et al. developed an empirical correlation for predicting the erosion per unit mass of impacting particles (ER, in mg/g) of different materials. Their model accounts for the main parameters affecting erosion.

$$ER = K_1 f_\alpha |\vec{v}|^2 \cos^2 \alpha (1 - R_r^2) + f_i \quad (4)$$

where

$$R_r = 1 - 0.0061 |\vec{v}| \sin \alpha, \quad f_\alpha = \left\{ 1 + K_C \left[K_{12} \sin(90\alpha/\alpha_0) \right] \right\}^2, \quad f_i = K_2 (|\vec{v}| \sin \alpha)^4$$

K_1 , K_2 and K_C are empirical constants determined by Tabackoff and coworkers, and are function of material properties of particles and target surface. In the present work it is assumed that the channel walls are made of stainless steel. Notably, Tabakoff's correlation prescribed an angle of maximum erosion α_0 depending on target material; for stainless steel it is set equal to 30 degrees.

2 Some Computational Results

Some results are reported here.

As for LES computations [1], the velocity and turbulent kinetic energy production terms is here reported to demonstrate the effect of rotation (Fig.2 and Fig.3).

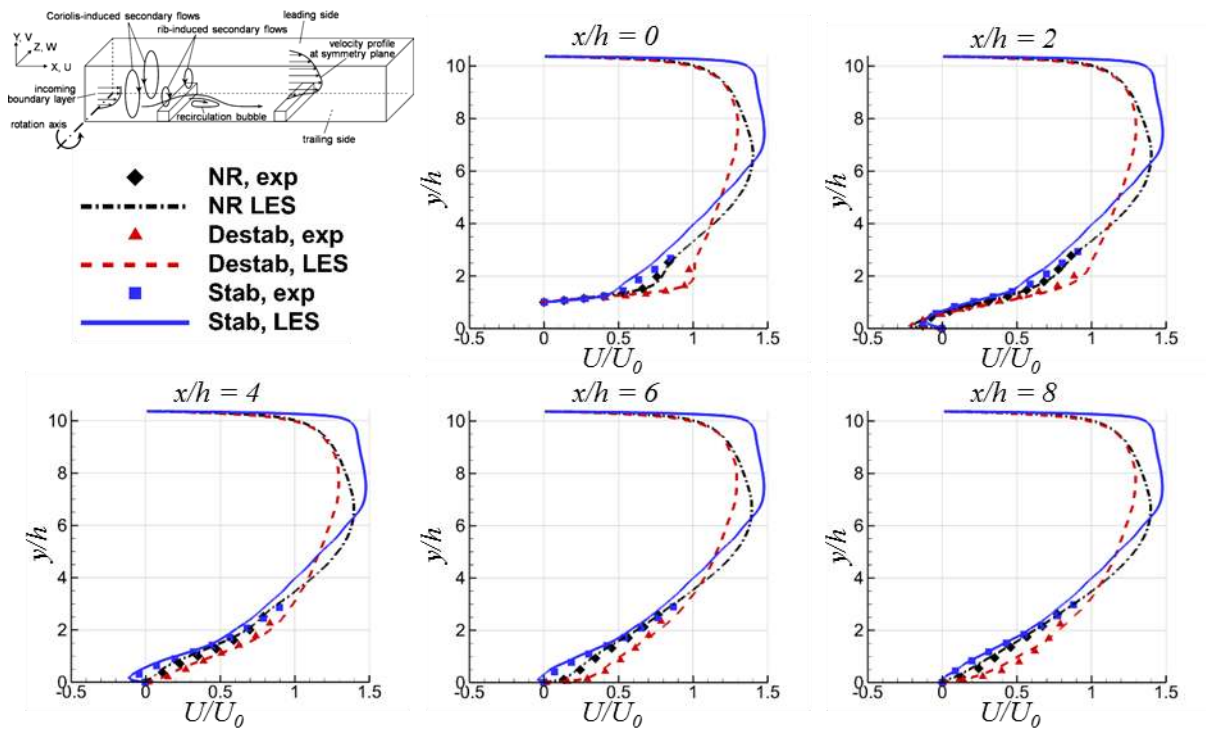


Fig. 2: Top left: sketch of the flow configuration. Mean streamwise velocity profiles at $x/h = 0, 2, 4, 6$ and 8 : Symbols: experiments; lines: LES.

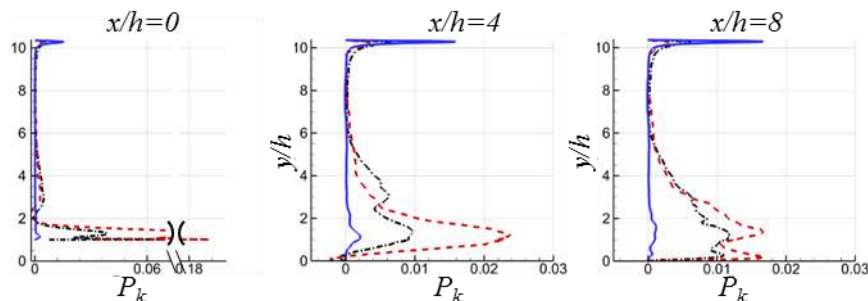


Fig. 3: Production of the turbulent kinetic energy k at selected streamwise locations. Chain-dotted black lines - NR; dashed red lines - destabilizing case; continuous blue lines stabilizing lines

Three configurations are considered: non rotating (NR) case, anti-clockwise rotation, destabilizing boundary layer on the ribbed surface; clockwise rotation, stabilizing boundary layer of the ribbed surface. Velocity profiles show the more turbulent velocity profile in the ribbed surface in several

positions starting from the rib edge (Fig.2). This is confirmed by the distribution of turbulent kinetic energy (k) production (P_k) in Fig.3 that shows in all location that the destabilizing rotation enhances the P_k . The same test case was used to assess the capability of the modified URANS model previously cited [3].

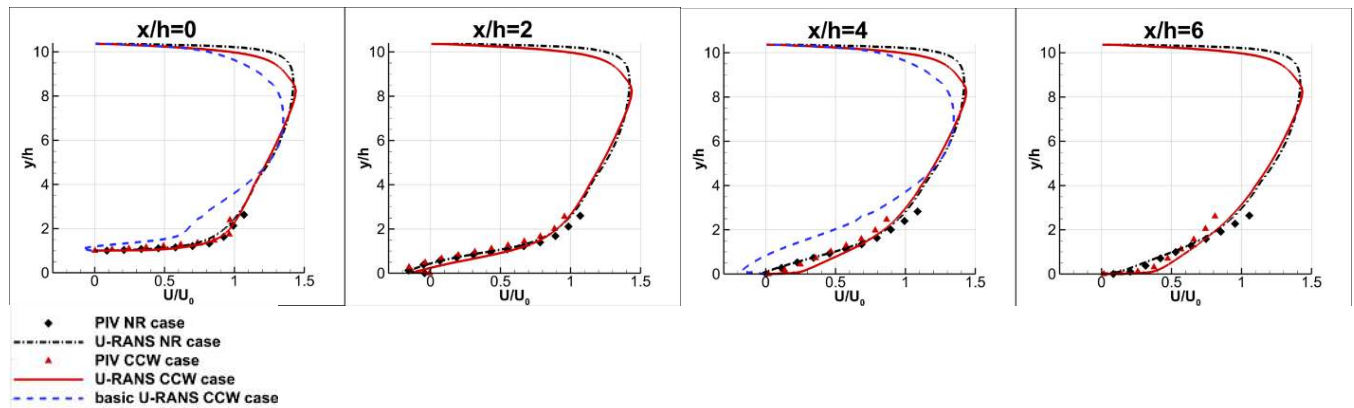


Fig. 4: Mean streamwise velocity profile at different abscissa compared with the experimental data.

Conclusions

A comprehensive computational tool able to account the influence of rotation on turbulent multi-phase flow was presented and accurate description of flow in a rotating configuration resembling internal cooling channels of gas turbine blades. On the ribbed wall the interaction of boundary layer structure and rotation effects showing stabilizing or destabilizing effects depending on rotation direction. A URANS model based on the k - ε - ζ - f was developed, implemented and validated.

References

- [1] BORELLO, D., F., SALVAGNI, A., HANJALIC, K., “*Effects of Rotation on Flow in an Asymmetric Rib-roughened Duct: LES Study*”, International Journal of Heat and Mass Transfer, Elsevier, **36**, (2015), pp. 104-119, DOI: 10.1016/j.ijheatfluidflow.2015.07.012
- [2] SALVAGNI A., BORELLO D., PROPERZI E., RISPOLI F. AND HANJALIĆ K., “*LES scrutiny of non-linear k - ε - ζ - f model sensitized to rotation*”, THMT-15, Sarajevo, September 14-17, (2015)
- [3] SALVAGNI A., BORELLO D., PROPERZI E., RISPOLI F., “*URANS Study of Flow and Heat Transfer in a Rotating Rib-Roughened Internal Cooling Channel*”, ASME ATI UIT, (2015), May 17-20, 2015, Naples, Italy
- [4] BORELLO D., ANIELLI D., RISPOLI F., SALVAGNI A., VENTURINI P., “*Unsteady CFD analysis of erosion mechanism in the coolant channels of a rotating gas turbine blade*”, ASME TurboExpo (2015), 15-19 June 2015, Montreal, Canada
- [5] ANIELLI D., BORELLO D., RISPOLI F., SALVAGNI A., VENTURINI P., “*Prediction of particle erosion in the internal cooling channels of a turbine blade*”, European Turbomachinery Conference (2015), 23-26 March 2015, Madrid, Spain.

CRESCO NUMERICAL COMBUSTION ANALYSIS OF SWIRLING MICRO-MESO COMBUSTION CHAMBERS

Angelo Minotti^{1*}

¹*School of Aerospace Engineering, Sapienza University of Rome, via Salaria 851, 00138, Rome*

ABSTRACT. This report briefly describes the work carried out, by means of the CRESCO infrastructure, during a 3-years European FP-7 project; exactly the “Hybrid Renewable energy converter for continuous and flexible power production” (HRC-Power Project). This project, concluded the 1st of April 2016, aimed at developing a hybrid miniaturized device able to produce energy adopting solar concentration and/or combustion. Combustion is obtained in swirling micro chambers fed by hydrogen/air, with a total inlet thermal power up to 0.5kW. Numerical simulations have been mandatory to investigate configurations that differ for the characteristic dimensions, number of chambers and their relative connections.

1 Introduction

One of the challenges of the last few decades is to develop renewable energy sources able to provide reliable and continuous base-load power, as well as peak-load power when it is needed to match supply demand. For renewable energies, a high level of unused capacity comes from the high variability of the source over time. Their intermittent nature has a large impact: low capacity factors, low flexibility and higher amortization costs.

Among all of the technologies available to produce electrical power, many efforts are investigating thermal to electrical conversion, but the results are currently limited, in conversion efficiencies, by the operation temperature, which is often below 800 K. There is therefore the necessity to reach very high temperature operations, and this is one of the aims of the “HRC-Power” project, which proposes such concepts, adding also the capability to work with both combustion and solar concentration with miniaturized items (converters).

The proposed converter consists of a small parallelepiped brick with inside swirling meso-combustion chambers, which heat up the parallelepiped, emitting material by the combustion of H₂/air (the radiated energy is converted into electrical by a thermo photovoltaic element, TPV), see fig. 1. The parallelepiped converter has fixed Height-Length dimensions (30mm x 30mm) and the chamber has fixed Height (33mm); conversely, the parallelepiped thickness varies accordingly to the chamber diameter (6mm for 3mm of diameter, 9mm for 6mm of diameter and 14mm for 11mm of diameter).

In order to maximize the converter efficiency ($T_{\text{emitting surface}} > 1000[\text{K}]$ and $\Delta T_{\text{emitting surface}} < 100[\text{K}]$) several geometrical configurations have been investigated. They differ for the chamber’s diameter and, in particular, for their mutual interconnection: in fact, separated [1] and connected chambers [2] have been analyzed. In the “connected chambers configuration” the outlet duct of the “n-chamber” coincides with the inlet duct of the “n+1-chamber”, see fig.2 that reports the 5-connected chambers configuration.

The connected configuration has been chosen to increase the overall residence time and to balance the cold and hot points on the emitting surfaces, with the goal of reducing the emitting surfaces delta-temperature (fundamental for efficient TPV energy conversion).

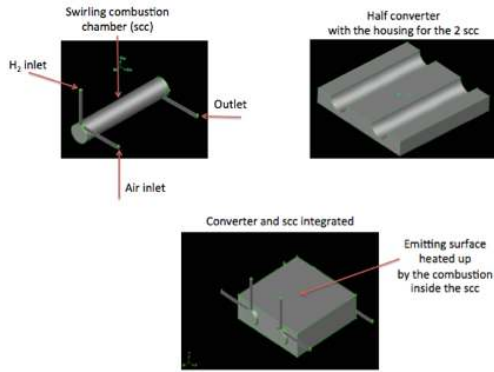


Fig.1: hybrid energy converter concept (combustion configuration).

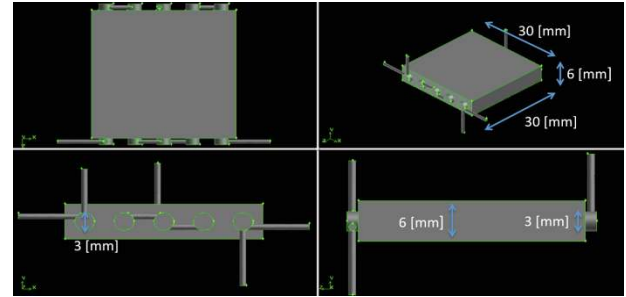


Fig. 2: Swirling combustor converter, length/diameter ratio (Z/D) = 11, 5 connected chambers.

2 Operating conditions and numeric

The separated 2-chambers configuration has been investigated changing the chamber's diameter dimension (D) and the equivalence ratio, according to Table1 below.

Aspect ratio Z/D^1	Total injected chemical power (W)	Φ	Re (Fuel, Air)
11	400	0.4	190, 7500
	400	0.7	190, 4430
	400	1	190, 3100
5	400	0.4	190, 7500
	400	0.7	190, 4430
	400	1	190, 3100
3	400	0.4	190, 7500
	400	0.7	190, 4430
	400	1	190, 3100

Table 1: Operating conditions of 9 “separated-chambers” configurations.

The connected configuration has been investigated changing the number of chambers inside the emitting parallelepiped (up to 5 chambers) and their diameter ($Z/D=3,5$ and 11), according to Table 2 below. The equivalence ratio and the injected thermal power have been fixed to stoichiometric conditions and to 500W.

Aspect Ratio Z/D	Chamber Diameter [mm]	Number of Chambers	Brick dimensions $L \times W \times T$ [mm]	Distance between the chambers [mm]	Chambers' volume [mm ³]
11	3	5	30x30x6	3	1166
5	6	3	30x30x9	4	2798
3	11	2	30x30x14	4	6269

Table 2: Converters, geometrical characteristics.

2.1 Numerics

A grid sensitivity analysis², reported in [1], indicated that a circumferential distance between gridpoints of 0.2[mm], on the chambers, and of 1[mm], on the walls of the brick, is the optimum. The meshes, adopted in the present study, have a total number of cells that varies from 1.4M to 2.2M.

¹ The chamber's height, Z , is fixed to 33 mm for all of the configurations.

² The grid analysis carried out at cold conditions is assumed suitable for the reacting case as well; this is because greater levels of turbulence, and then greater gradients, characterize cold conditions with respect to the same case at reacting

After that, “reordering, smoothing and swapping” techniques were adopted for the three meshes in order to speed up calculations and increase mesh quality. In particular, reordering (the reverse Cuthill-McKee method [3]) was adopted to reduce the bandwidth of the cell neighbor number, in order to speed up the calculations, while “smoothing and swapping” were used, respectively, to reposition nodes (by lowering the maximum skewness of the grid) and to modify the cell connectivity. The latter technique produces a constrained Delaunay mesh [4] in which the minimum angles in the mesh are maximized, tending toward equilateral cells, providing the “most equilateral” grid for the given node distribution. The first point near the wall is at $y^+ < 3$ and $\Delta y^+ < 1$, for all of the configurations (only a few points, in the air inlet ducts where velocities are higher, are close to $y^+ \sim 15$). This means that the first point away from the wall is inside the viscous sublayer.

In micro-meso combustors, laminar zones may locally exist inside turbulent zones and *vice versa*, then the laminar vs. turbulent regime uncertainty poses the problem of the modeling approach. A pure laminar approach would be unable to predict turbulent field zones, of crucial importance when reactions are present, while turbulent models would over-predict transport wherever the actual regime was laminar. Fluid dynamics has been solved adopting the RANS k-eps turbulence approach, with the enhanced wall treatment [5]. This model has been chosen for its ability to reproduce laminar dynamics and for the fact that it solves the eps-unknown, which is

present in the definition of the Kolmogorov scales, $\eta = \left(\frac{\nu^3}{\varepsilon}\right)^{\frac{1}{4}}$. The Kolmogorov scale provides an indication of the actual flow regime and permits to understand the feasibility of a direct numerical simulation (DNS) inside the chamber. The specific heat at constant pressure, C_{pi} , is fitted by polynomials of temperature from the GRIMech Thermo Data file [6], properly introduced in the CFD code, while viscosity and thermal conductivity, μ and k , are predicted by the gas kinetic theory [7]; mixtures are composition-dependent according to Wilke’s formula [8]. The turbulence-combustion coupling is modeled adopting the eddy dissipation concept (EDC) [9, 10], while the hydrogen/air kinetics is modeled with a detailed mechanism of 9 species and 21 reactions [11]. The reactive Navier–Stokes equations were solved adopting a finite-volume solver (Ansys 14 CFD code). The simulations were carried out adopting the pressure-based version of the solver, assuming the PISO scheme [12, 13] to solve the pressure-velocity coupling and the third-order MUSCL scheme [14] for the spatial discretization of all the variables.

Further investigations could consider also higher order discretization algorithms, such as MUSCL fifth order and/or WENO fifth order and/or WENO ninth order [15], in particular with the LES or DNS approach.

3 Conclusion

Simulations demonstrate that both the separated and connected geometrical configurations provide high combustion efficiencies; in fact the H_2 /air combustion efficiency is in the range $91 < \eta < 99.9\%$.

The separated configuration performs worse than the connected configuration in terms of maximum temperature and, in particular, in terms of face temperature distribution (a fundamental variable for an efficient thermal-energy conversion). In conclusion, the best configuration is the $Z/D=11$ (5 connected chambers) that figures out a surface maximum temperature of 1390K and a surface $\Delta T \approx 45K$. Further investigations assuming hydrocarbons and high-pressure conditions have been analyzed and will be reported in the next ENEA-CRESCO report.

conditions and, moreover, combustion is modeled by the EDC confirming the fact that it is the turbulence the focal issue.

References

- [1] Minotti, A. and Teofilatto, P. “Swirling combustors energy converter: H₂/Air simulations of separated chambers”. *Energies* 2015, 8, 9930-9945.
- [2] Minotti, A. “Energy Converter with Inside Two, Three, and Five Connected H₂/Air Swirlin Combustor Chambers: Solar and Combustion Mode Investigations”, *Energies* 2016, 9, 461; doi:10.3390/en9060461.
- [3] Cuthill, E.H.; McKee, J. Reducing Bandwidth of Sparse Symmetric Matrices. In Proceedings of the ACM 24th National Conference, New York, NY, USA, 26-28 August 1969; pp. 157–172.
- [4] Deyer, R.; Zhang, H.; Moller, T. Delaunay Mesh Construction. In *Eurographics Symposium on Geometry Processing*; Alexander, B., Michael, G., Eds.; Simon Fraser University: Burnaby, BC, Canada, 2007.
- [5] Shih, T.H.; Liou, W.W.; Shabbir, A.; Yang, Z.; Zhu, J. A New k-ε Eddy-Viscosity Model for High Reynolds Number Turbulent Flows. *Comput. Fluids* **1995**, 24, 227–238.
- [6] GRIMech 3.0 thermodynamic database. Available online: http://www.me.berkeley.edu/gri_mech/version30/files30/thermo30.dat.
- [7] Anderson, J.D. *Hypersonic and High Temperature Gas Dynamics*; McGraw Hill: New York, 1989; Volume 12, pp. 468–481.
- [8] Mathur, C.; Saxena, S.C. Viscosity of polar gas mixture: Wilke’s method. *Appl. Sci. Res. A* **1966**, 15, 404–410.
- [9] Magnussen, B.F. On the Structure of Turbulence and a Generalized Eddy Dissipation Concept for Chemical Reaction in Turbulent Flow. In Proceedings of the 19th AIAA Aerospace Science Meeting, St. Louis, MO, USA, 12–15 January 1981.
- [10] Gran, I.R.; Magnussen, B.F. A numerical study of a bluff-body stabilized diffusion flame. Part 2. Influence of combustion modeling and finite-rate chemistry. *Comb. Sci. Technol.* **1996**, 119, 191–217.
- [11] Li, J.; Zhao, Z.; Kazakov, A.; Dryer, F.L. An Updated Comprehensive Kinetic Model of Hydrogen Combustion. *Int. J. Chem. Kinet.* **2004**, 36, 566–575.
- [12] Issa, R.I. Solution of Implicitly Discretized Fluid Flow Equations by Operator Splitting. *J. Comput. Phys.* **1986**, 62, 40–65.
- [13] Ferziger, J.H.; Peric, M. *Computational Methods for Fluid Dynamics*; Springer-Verlag: Heidelberg, Germany, 1996.
- [14] Van Leer, B. Toward the ultimate conservative difference scheme V. A second order sequel to godunov’s method. *J. Comput. Phys.* **1979**, 32, 101–136.
- [15] Thornber, B.; Mosedale, A.; Drikakis, D. On the implicit large eddy simulations of homogeneous decaying turbulence. *J. Comput. Phys.* **2007**, 226, 1902–1929.

CFD modeling of a flameless furnace: comparative evaluation of turbulent combustion models with two software on a HPC platforms

Carmine Mongiello^{1*}, Guido Guarnieri¹,
Gaetano Continillo², Daniele Iorio², Giampaolo Maio²
Francesco Saverio Marra³,

¹*ENEA, C.R. Portici, Naples, Italy¹*

²*University of Sannio, Department of Engineering, Benevento, Italy*

³*Institute for Research on Combustion IRC-CNR, Naples, Italy*

ABSTRACT Object of this study is a HEC furnace (High Efficiency Combustion) of a semi-industrial scale, equipped with a pair of NFK burners, of 1 MW_t power fed by natural gas, for which was conducted in campaign of IFRF measures. The experimental data, required for the model validation, and the specifications the application, were provided by the CSM Materials Development Center. The computer code ANSYS Fluent CFD has been made available by the ENEA Centre Research, while the STAR-CCM+ code has been made available in version POD (Power On Demand) from CD-Adapco. The computing resources and its technical support were provided by the computing infrastructure HPC (High Performance Computing) which belong to CRESCO/ENEAGRID and his staff. This computing infrastructure was realized by ENEA using a programs national and European research. The analyzed burners have a strong jet central air, preheated to high temperature, and two side weak jets of fuel at room temperature. For these types of furnaces were already developed some RANS models, based on the approach that has been taken as a reference for the modeling implemented. The scope of this work was to compare different turbulent combustion models based on the approach RANS and compare the results obtained with the two different simulative platforms. For both software, starting from the available technical drawings, furnace and burner geometry of lances were created. In particular, one of the applications involves the use of regenerative burners NFK in the reheating furnaces of the steel industry. The present work is part of a research between the University of Sannio, ENEA Portici Research Center (National Agency for New Technologies, Energy and Sustainable Economic Development), Arcades, the Development Center CSM materials and CD-Adapco Company. The goal is the development of a CFD model finalized to the prediction of operation of the furnaces operating in scheme flameless by the use of two of different simulation platforms. One of the planning techniques most used for the alternative combustion systems development is the CFD simulation applied to the reagents systems; the numerical simulation of turbulent reactive flows has realized meaningful progress due to the improvement in the modeling of physical systems. The development of robust and efficient numerical algorithms, the evolution of the available processing power and the introduction of detailed kinetic schemes able to describe accurately the chemistry of the processes, applied on the real system, allow the CFD simulation to observe phenomena not otherwise easily measured. Therefore, the CFD simulation versatility makes itself an extremely important tool, both in the design of new equipment, both for their subsequent optimal run. A deepen description of a turbulent combustion system represents an extremely complex task and an accurate representation of the chemical phenomena requires the use of kinetic models that include hundreds of thousands of species and reactions. In addition, there is to take into account the difficulty of modeling the interaction between the turbulent flows and chemical reactions in a combustion chamber.

¹ Corresponding author. E-mail: carmine.mongiello@enea.it

1 Introduction

In recent years, the energy consumption in the world has known a continuous and meaningful growth, not only in industrialized countries but also in developing ones, due to the rapid industrialization and the overall improvement of living conditions. The energy requirements increasing, actually satisfied widely by fossil fuels, has caused a relevant growth of carbon dioxide and nitrogen oxides emissions in the atmosphere. On the other hand, also the increasing attention forward to air quality has prompted research towards the development of efficient and sustainable combustion systems, it would be able to optimize the consumption of energy sources both renewable and non-renewable ones which ensure a long-term environmental protection on a global scale. This resulted in a deep change in the technology role that operate on production process with the purification systems in all phases of the same cycle in order to prevent the formation of polluting substances. Another central aspect in this field of combustion research consists in the energy performance improvement; in last times, the research has been focused the attention on the development of combustion systems those allowed to augment the energy efficiency, with no adverse effects related to the formation of NO_x . The decrease of temperature gradients in the system allows to drastically reduce NO_x emissions, even with air preheating temperatures higher than $800\div 900$ °C, in fact this combustion mode is generally referred to combustion without flame (Wünning et Wünning, 1997). The prediction of a combustion chamber behavior in flameless scheme, usually used in industrial field, appears to be a complex operation, in fact, for the HiTAC technology, the study is based on the Excess Enthalpy concept proposed by Weinberg already in 1986. The innovation introduced in HiTAC technology lies in the fact that the air preheating temperatures can be even higher than the ignition temperature of the fuel, allowing, among other things, a stability of the field expansion. HiTAC resides in the fact that the air preheating temperatures can be even superior to the fuel self-ignition temperature enabling, among other things, a stability of the field expansion. Such preheating temperature are naturally only compatible with ceramic matrix regenerative systems. The increase of the air preheating temperature had to be necessarily accompanied by a reduction of the oxygen content in the combustion air through a process of dilution with inert gases for not determining an excessive rise of the emissions of flame temperature and not to consequently increase of NO_x . The reagents dilution has the following effects: limitation of the adiabatic temperature of flame and restriction of the maximum temperature inside the combustion chamber. These preheating temperatures are of course only compatible with ceramic matrix regenerative systems. The increase of the air preheat temperature must be necessarily accompanied by a reduction of the oxygen content of the combustion air through a process of dilution with inert gases for not determining an excessive increase in the flame temperature and not to increase emissions consequently NO_x . The reagents dilution limits the adiabatic flame temperature and the maximum temperature inside the combustion chamber; this technology is known as *flameless* and it has had an extensive application in the industrial field. In particular, one of the applications of this technology involves the use of regenerative burners NFK in reheating furnaces in the steel industry. The flameless technology has an extensive development in industry. In case of mild combustion, realizing a good mixing with the exhaust gas and the oxygen concentration in the reaction zone is much lower than the atmospheric value of 21% and raising the fluid temperatures, the oxidation reactions is limited to a few hundreds of Kelvin degrees, making negligible the effect of air preheating.

2 Methods

The study proceeded by a discretization of the computational domain in such a way that the mesh realized presented a comparable number of cells for the two software. In particular, it is made of a mesh made up of a number of cells such as to obtain a good compromise between the solution quality and the computational cost for the simulation of an industrial reality. Since three different models of combustion at constant turbulence model and many kind of reactive flows adopted (Eddy

Break-Up Hybrid or, equivalently, Eddy-Dissipation/Finite-Rate, PPDF Equilibrium and PPDF *Flamelet*), therefore these models were compared. Subsequently, identified the most suitable combustion simulation model to the application under consideration, it is proposed a comparison between two different turbulence models, the $k-\epsilon$ standard model and the $k-\epsilon$ model in Wilcox formulation in order to evaluate what best suits to predict the thermo-fluid dynamic behavior in furnace. Finally, locate the CFD model most suitable to model the application in question, it proceeded to a comparative evaluation of the results of the simulations in Fluent and STAR-CCM+. Due to highly complexity, we need an accurate representation of chemical phenomena, therefore the analysis requires the use of kinetic models which include many thousands of species and reactions. In addition, there is that we have to take in account the difficulty of modeling the interaction between the turbulent phenomena and reactions chemical those take place in combustion chamber operating in turbulent conditions. The implementation of a predictive model for a *flameless* combustion chamber, used in industrial field, it appears to be an operation complex. The results of research have shown that a significant recirculation of the exhaust gases in the combustion zone, associated with a high preheating of the incoming flows, it allows to modify deeply the typical structure of the flame, resulting in the achievement of a state of widespread reactivity extended to the whole chamber volume. In the FLUENT the computational mesh was made from about 1.3 million cells. In particular, the gas lance, the lance air and the near downstream area of the burner were discretized with polyhedral cells while the remaining part of the domain is realized with hexahedral cells. In the STAR-CCM+ computational mesh it consists of approximately 1.1 million of polyhedral cells. Computing resources that was used to perform the simulations were provided by the computing structure CRESCO HPC/ENEAGRID. In particular, the simulations were performed by discretizing the calculation of 32 cores operating in parallel; with this computational power, the time required for solution convergence was approximately one day for both software type, while lightly higher calculation times were recorded with the STAR-CCM+ software. This is evidently connected to the polyhedral type mesh that has been adopted for the discretization of the computational domain.

3. Results

The achieved objectives of the study subject is a HEC furnace on semi-industrial scale, equipped with a pair of NFK burners of 1 MW_t and feed by natural gas. The simulations performed, with both software, have produced interesting results in similar conditions, for which were applied same considerations. In particular, all the analyzed models are able to predict the overall system behavior. The most significant deviations from the temperature measurements are recorded in the areas immediately near to burner downstream, while, moving further downstream, all the models are able to describe correctly the temperature profiles.

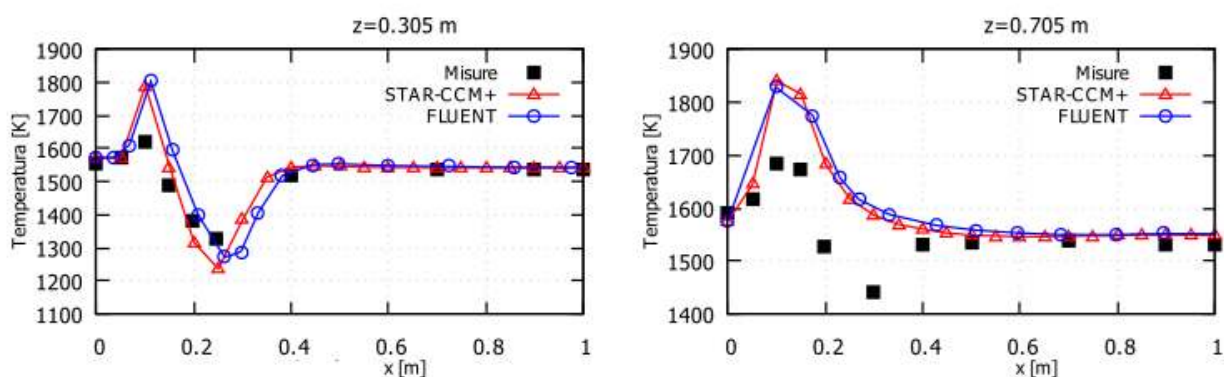


Fig.1-2: Temperature profiles along the spreading in various stations.

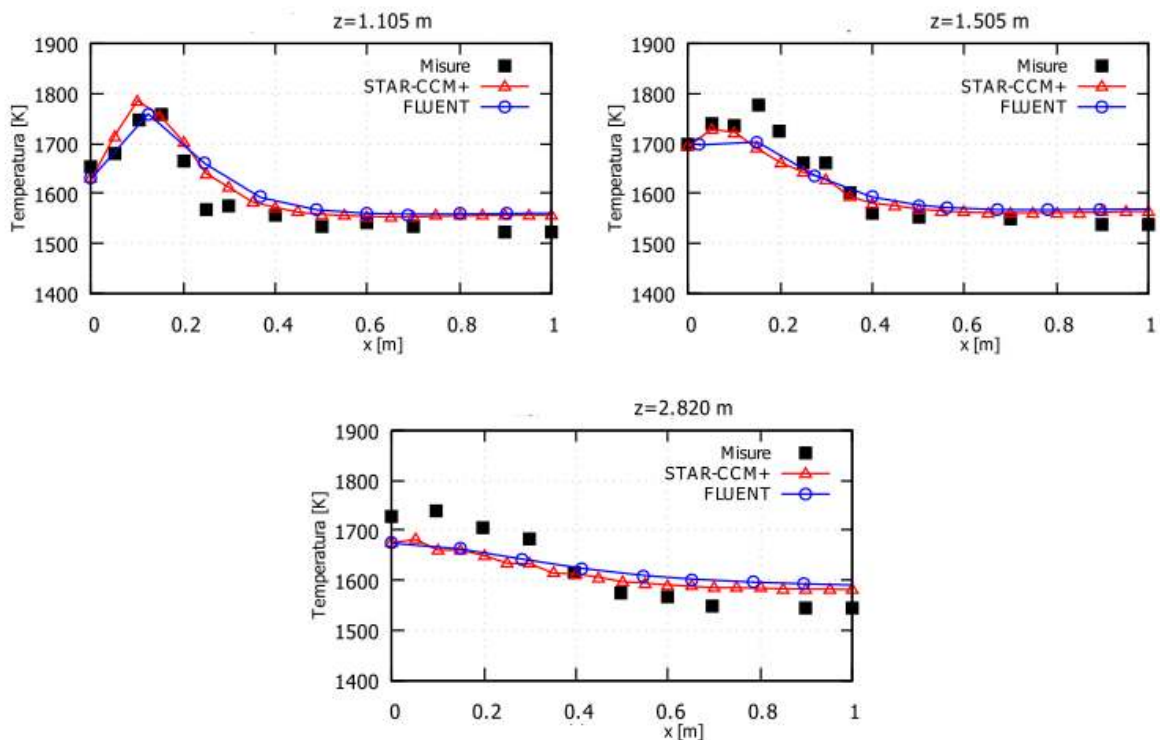


Fig.3-4-5: Temperature profiles along the spreading in various stations.

We have the same behavior for speed.

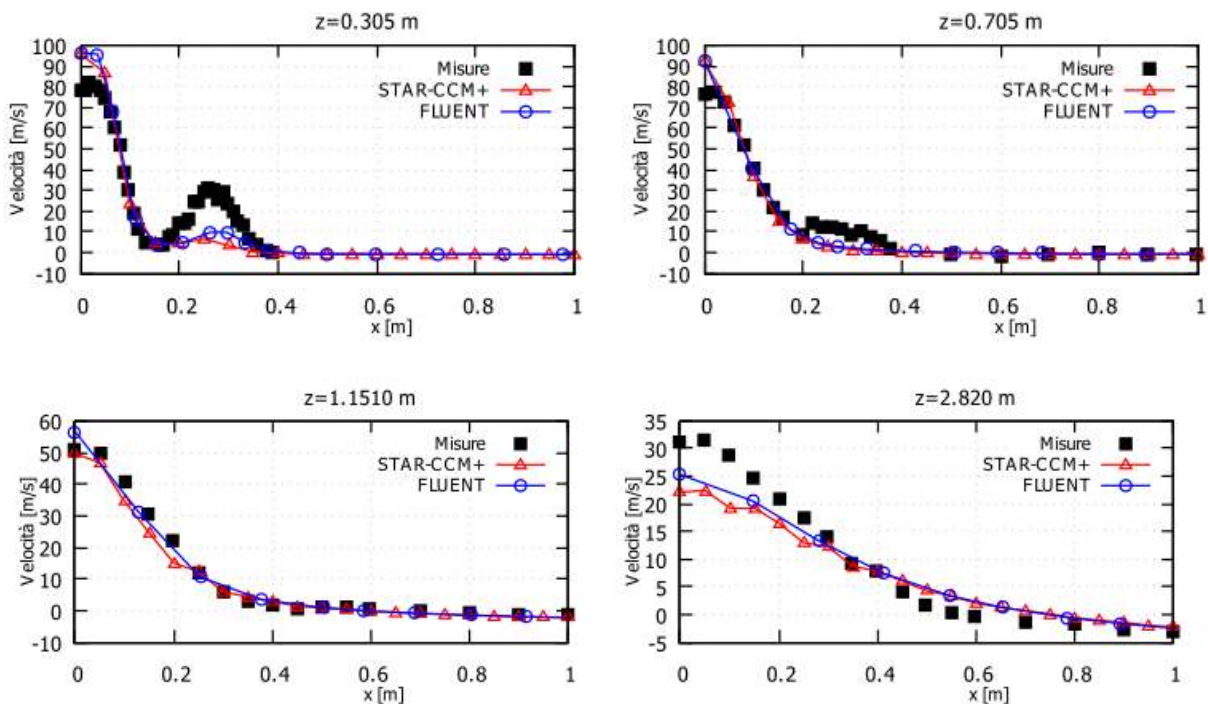


Fig.6-7-8-9: velocity profiles along the spreading in various stations.

The main differences between the simulation results and the available measurements are to be attributed to the limit of turbulence models correctly predict the structure of the jets. Particularly important in order to maintain conditions in the furnace of the flameless analyzed, it is the phenomenon of recirculation and exhaust gas entrainment. This phenomenon is under esteemed, while the turbulence model $k-\epsilon$ while the $k-\epsilon$ model, thanks to the implemented changes, there is a

better estimate of gas recirculation. Inside the flame zone, all the profiles of the measurements of the concentrations of oxygen, carbon dioxide and carbon monoxide show a trend rather flat. In this area, the combustion model Eddy Break-up Hybrid, or equivalently Eddy Dissipation/Finite-Rate, with two reactions is the one that performs better. In particular, with the changes made by IFRF on the constants A and B of the carbon monoxide oxidation reaction, this model is also able to predict the slow chemistry of formation and destruction of CO that is observed in the furnace. The model PPDF Equilibrium and model PPDF *Flamelet*, however, give worse results. In particular, the assumption of chemical equilibrium is not applicable in the first flame zone near the burner. The inadequacy of the PPDF Equilibrium model and PPDF *Flamelet* pattern also emerges in excessive underestimation of the flame temperature and the overestimation of CO formation. Surely, the gas recirculation underestimation exhausted influence this effect. The simulations conducted give rise to a concentration of CO at the exit of furnace nothing. Thus, this is completely destroyed by converting CO₂ in the furnace. From simulations it was carried out that the combustion model Eddy Break-Up Hybrid, or equivalently Eddy-Dissipation/Finite-Rate, with a chemical model in step 2 of Westbrook and Dryer associated with the turbulence model k- ϵ , it is able to provide better results. In particular a combustion model, although it is characterized by a limited number of reactions and species, is able to correctly predict the overall behavior of the system. An improved result may be achieved by the use of computational grids more dense in order to be able to represent a greater level of detail. Furthermore, a correct prediction of the intermediate species of the combustion process may be obtained by implementing more complex models of combustion as the Eddy Dissipation Concept. This model allows the use of a more detailed chemistry of combustion even if the computational burden would be more burdensome. This would make it possible to provide a correct estimate on the NO_x formation. A further development of the application analyzed could relate to the validation of the CFD model developed by the use of alternative fuels such as fossil syngas or renewable nature one. Downstream results of simulations performed with the FLUENT simulation software and STARCCM+ it is possible to conclude that you have comparable results and thus apply for both the same considerations. In particular, all models are able to predict the overall behavior of the jet of air and fuel in the furnace with the corresponding chemical reactions and diffusion processes. The strong jet of combustion air, which converts exhaust gases to the combustion downstream, is well predicted by a CFD models. The spread of temperature and species in this jet, as well as the conditions at the end of this jet, are correctly calculated. The most significant deviations from the temperature measurements are recorded in the zones immediately downstream of the burner while moving downstream, where now the jets are developed, all models are able to properly follow the temperature profiles. This same behavior also records for speed: immediately downstream of the burner is over estimated the speed of the air jet and underestimated the fuel spray velocity; moving on downstream crosspieces models are able to predict correctly the profiles. The exhaust gas injection in small fuel jet is under predicted with the turbulence model k- ϵ ; through this is observable in the underestimation of the temperature and of the concentration of carbon dioxide in jet close to the burner, even before the fuel and oxidizing agent come into contact. The quantity of exhaust gases that penetrate in the fuel jet influences the chemistry of the combustion process. Using the k- ϵ model, the recirculation is more properly predicted, but, in the section immediately downstream, the presence of small jet of fuel is lost almost completely. Inside the flame zone, all the profiles of the measurements of the concentrations of oxygen, carbon dioxide and carbon monoxide are rather flat. In this area, the combustion model Eddy Break-up with two reactions is the one that performs better. In particular, with the changes made by IFRF on the constants A and B of the carbon monoxide oxidation reaction, this model is also able to predict the slow chemistry of formation and destruction of CO that is observed in the furnace. The model PPDF Equilibrium, however, gives the worst results due to non-equilibrium phenomena those occur in the furnace. In particular, the assumption of chemical equilibrium is not applicable in the first flame zone near the burner. The inadequacy of the PPDF Equilibrium model emerges in excessive underestimation; surely the gas recirculation underestimation exhausted influence this effect. Below

they are compared to the contour and the profiles of some variables obtained with the simulation made by two software. These results refer to the k- ϵ turbulence model, which is observed in the best way to predict the recirculation of the exhaust gases, and the combustion model Eddy Dissipation/Finite Rate, or, equivalently, to the model Eddy Break-Up Hybrid.

4. Conclusions

From simulations carried out it can be stated that the combustion model Eddy Break-Up Hybrid, or equivalently Eddy-Dissipation/Finite-Rate, with the chemical model in step 2 of Westbrook and Dryer, associated with the turbulence model k- ω , is able to provide better results. In particular, such a combustion model, although it is characterized by a limited number of reactions and species, is able to quite correctly predict the overall behaviour of the system. An improvement may be achieved through using more fine computational grids those will be able to allocate a greater level of detail. Furthermore, a correct prediction of the intermediate species of the combustion process may be obtained by implementing more complex models of combustion as Eddy Dissipation Concept. This model allows the use of a more detailed chemistry of combustion even if the computational burden would be more burdensome. This would make it possible to provide a correct estimate on the NO_x formation. A further development of the application analysed could relate to the validation of the CFD model developed by the use of alternative fuels, such as syngas of fossil or renewable nature.

References

- [1] FRAU C., PETTINAU A. “*Stato dell’arte sulla simulazione della combustione flameless*” Technical Report RSE/2009/111, ENEA, 2009.
- [2] BILGER R.W. “*Future progress in turbulent combustion research*” Progress in energy and combustion science, 26(4): 367–380, 2000.
- [3] BLAZEK J. “*Computational Fluid Dynamics: Principles and Applications*”. Elsevier, 2005.
- [4] CAVALIERE A. and de JOANNON M. “*Mild combustion*”. Progress in Energy and Combustion science, 30(4): 329–366, 2004.
- [5] Choi G.M. and KATSUKI M. “*Advanced low NO_x combustion using highly preheated air*” Energy conversion and Management, 42(5):639–652, 2001.
- [6] COELHO P.J. and PETERS N. “*Numerical simulation of a mild combustion burner*” Combustion and flame, 124(3): 503–518, 2001.
- [7] COLOMBO E., INZOLI F. and MALFA E. “*Free jet in confined combustion chamber: Numerical model for industrial application in low NO_x burners*” In ASME 2005 Summer Heat Transfer Conference collocated with the ASME 2005 Pacific Rim Technical Conference and Exhibition on Integration and Packaging of MEMS, NEMS, and Electronic Systems, pages 735–740. American Society of Mechanical Engineers, 2005.
- [8] COLORADO A.F., HERRERA B.A. and AMELL A.A. “*Performance of a flameless combustion furnace using biogas and natural gas*”. Bioresource Technology, 101(7):2443–2449, 2010.
- [9] DANON B. “*Furnaces with multiple flameless combustion burners*” TU Delft, Delft University of Technology, 2011.
- [10] de JOANNON M., LANGELLA G., BERETTA F., CAVALIERE A. and Noviello C. “*Mild combustion: Process features and technological constraints*” Combustion science and technology, 153(1): 33–50, 2000.
- [11] FERZIGER J.H. and PERI’ M. “*Computational methods for fluid dynamics*” volume 3. Springer Berlin, 2002.
- [12] ASHWANI K.G. “*Flame characteristics and challenges with high temperature air combustion*” Proceedings of the International Joint Power Generation Conference, pages 23–26, 2000.
- [13] HARDESTY D.R. and WEINBERG F.J. “*Burners producing large excess enthalpies*” Combustion Science and Technology, 8(5-6): 201–214, 1973.
- [14] HEKKENS R.H. “*Non-isothermal CFD model of HEC burner and furnace*” Technical Report IFRF Doc. No. G108/y/3, IFRF, November 2004.
- [15] HOSSEINI S.E., WAHID M.A. and ABUELNUOR A.A.A. “*High temperature air combustion: sustainable technology to low NO_x formation*” International Review of Mechanical Engineering, 6(5): 947–953, 2012.

ROLE OF THE SUB-SURFACE VACANCY IN THE AMINO-ACIDS ADSORPTION ON THE (101) ANATASE TiO₂ SURFACE: A FIRST PRINCIPLES STUDY

Luca Maggi^{1,2}, Fabrizio Gala^{2,3} and Giuseppe Zollo²

¹ *Computational Biomedicine Section (INM-9), Institute for Neuroscience and Medicine (INM), and Institute of Advanced Simulation (IAS), Forschungszentrum Jülich, 52425 Jülich, Germany*

² *Department of Fundamental and Applied Sciences for Engineering, University of Rome "La Sapienza", Via A. Scarpa 14-16, I-00161 Rome, Italy*

³ *Dipartimento di Scienze medico-chirurgiche e di Medicina traslazionale, Università di Roma "La Sapienza", "Ospedale Sant'Andrea", Rome, Italy*

ABSTRACT

The functionalization of metal-oxide surfaces with biological matter is of crucial importance in order to develop new kind of sensor and generally nano-devices in the field of nano-medicine. In this work we give a first interpretation of possible selective interaction, between some amino acids and Anatase (101) induced by the presence of common sub-surface point defects such as the oxygen vacancy. These amino acids can be addressed as the potential responsible of the interaction between physiological peptides which in turn have the particular properties of interact both with biological matter (DNA, cells, proteins etc.) and inorganic material. This work reports the results of first-principles computational studies of two different amino acids on a substrate of titanium oxide surface in presence of an intrinsic defect and water.

1 Introduction

In last years the simultaneous progress in experiments and computational resources to investigate the nano-scale world, allowed the scientists to lead new kind of applications exploiting the atomistic interactions in organic/inorganic systems. In particular there is a new wide area of investigation regarding the functionalization of metal-oxide surfaces with biological matter, aimed to develop new kind of sensors and nano-devices supporting diagnosis and therapy in nano-medicine.

In particular amino-acid interaction with metal oxide surfaces has already been taken into account for the important cases of Rutile and Anatase TiO₂ and ZnO [1].

In the present report we still focus on the TiO₂ case that is known to be bio-compatible and quite common surface in many cases such as, for instance, implants. The studied system is particularly important at the nano-meter scale where it is known that Anatase is the most stable phase [2] and the (101) surface is the most energetically favored surface [3] this representing the most frequent case.

While in the previous cases here referred, ideally built surfaces were considered as the inorganic counterparts of the studied interaction, here we consider the presence of point defects close to the surface that, in the particular case of Anatase (101) TiO₂ surface, is quite a common intrinsic defects in the sub-surface layer that can affect the interaction at a large extent [4].

Moreover, because water could play a crucial role in every physical-chemistry process that occurs in a biological environment, water molecules have been explicitly included in the model both in the surface hydration layer and in the amino-acids hydration shells.

In particular we have focused our attention on two amino-acids, Lysine and Arginine that have been demonstrated to be responsible of peptides adhesion in many cases [1,2].

2 Computational details

Our model is based on a TiO₂ Anatase (101) slab with 108-atoms and normal to the (101) being directed towards the positive z-axis direction. The super-cell has the dimension of 10.42 X 11.23 X 31.00 Å³. The thickness of the slab is about 10 Å. According to previous computational study [4] the oxygen vacancy has been located in a site belonging to a sub-surface layer of this slab (Fig 1a and 1b). All the calculations have been performed in within the Density Functional Theory-Generalized Gradient Approximation (DFT-GGA) scheme using the PBE (Perdew-Burke-Ernzerhof) formula for the exchange-correlation functional as implemented in Quantum Espresso package [5].

Ultra-soft pseudo-potential have been used and the cut-off energy values were set to 60 Ry for the kinetic energy and to 400 Ry for the electronic density. All the calculations have been performed using two low-symmetry k- points in the irreducible Brillouin zone. The ground state configuration has been achieved after a full relaxation using the BFGS quasi-newtonian algorithm until the residual forces were less then 0.003 eV/ Å.

It is known that oxygen vacancies in metal oxides can be quite tricky because of local charges that are typical source of errors for standard GGA functionals as the one here adopted. Therefore our calculations have been also aimed to explore at which extent the popular so called Hubbard U correction to the GGA functional, the GGA+U method, that accounts for the correlation effects related to the presence of the defect contribute to the adsorption physical-chemistry phenomena considered.

Therefore both the standard GGA and the GGA+U functional were employed for this study. The Hubbard U was set to 3.3 eV according to previous computational study on this particular surface [6].

3 Results

3.1 The Oxygen vacancy

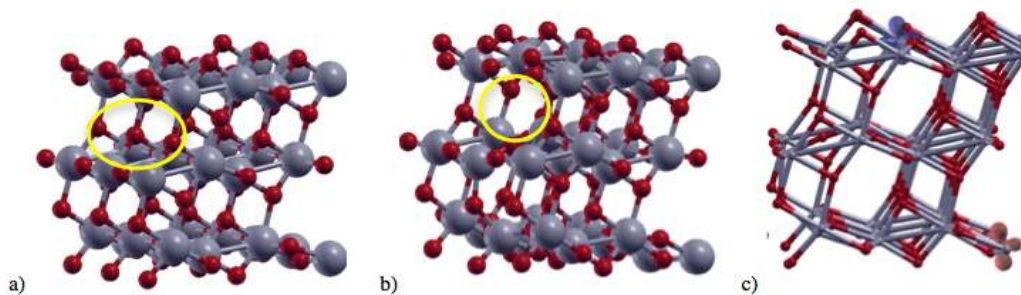


Figure 1: TiO₂ slab without the oxygen vacancy (a); TiO₂ slab without with the oxygen vacancy (b) the green circle shows the exact location of the defect; The localization of the last two electronic states calculated with the GGA+U functional (c). The isovalue used for this spin density plot is ± 0.04

The oxygen vacancy formation energy has been calculated using as:

$$E_{\text{form}} = E_{\text{slab}} - E_{\text{slab+def}} + E_{\text{O}_2}/2$$

where $E_{\text{slab+def}}$ and E_{slab} are the energy of the slab in presence and without the defect respectively and $E_{\text{O}_2}/2$ half the energy of oxygen molecule.

The difference between the GGA and GGA+U functional is not negligible (see Table 1). The spin DOS calculations enlighten why GGA+U must be chosen in order to perform such calculation: indeed the latter predicts the last two occupied electronic states lying below the conduction band, depicting TiO_2 as insulator as it really is, while GGA put these states in the conduction band. According to GGA+U the two states are localized on surface and on a bulk Titanium atoms as shown in the Fig. 1c.

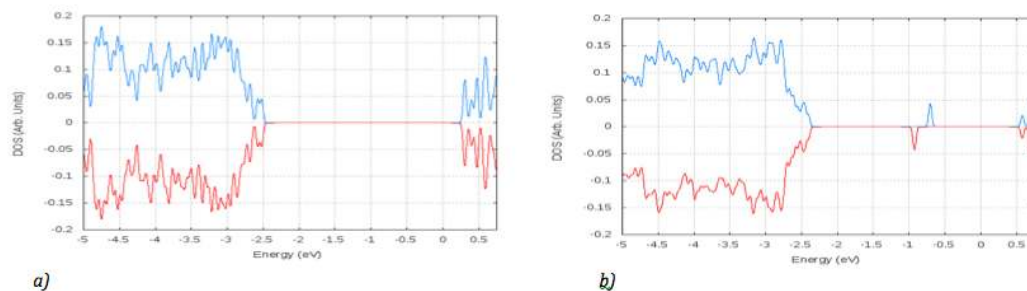


Figure 2: spin DOS plot for the TiO_2 slab with the oxygen vacancy with GGA+U functional (a) and standard GGA (b)

	GGA	GGA+U
E_{form} (eV)	5.07	4.46

Table 1: Formation Energy for the Oxygen vacancy calculated with GGA and the GGA+U functional

3.2 Water adsorption

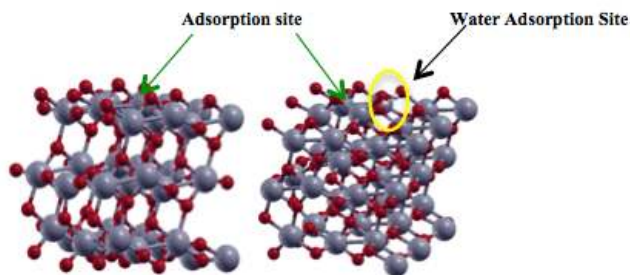


Figure 3: The first water adsorption site

Water adsorption has been studied comparing the results obtained by GGA+U and GGA functional. Moreover a long-range interaction term has been included in the energy functional. The A-(101) TiO_2 surface has six different adsorption sites for water molecules. However according to Ref. 7 in presence of an oxygen vacancy they are not equivalent. The site shown

in Fig. 3, indeed, presents a larger adsorption energy. Using the GGA+U approach, this appears as a consequence of the localization of the vacancy electronic states on the same Titanium atom where the water adsorption occurs [7]. Moreover this is also the reason why the GGA+U method predicts a larger adsorption energy of water then the simple GGA functional at this particular site (see Table 2).

In order to get closer to a biological environment, we have studied the adsorption of two water molecules. Keeping the first water molecule in the most stable site, only two possible configurations exist where two molecules could be arranged: the first one is with two molecules at

adjacent sites of the same row (Fig. 4a and 4b) and the second one where the second water is placed behind the first one, to the right or to the left the vacancy site (see Fig. 4a and 4c). The first configuration shows larger adsorption energy, so this is the configuration used for the further calculation of amino-acids adsorption. We see that, as the number of water molecules increases, the difference between GGA and GGA+U becomes rather small.

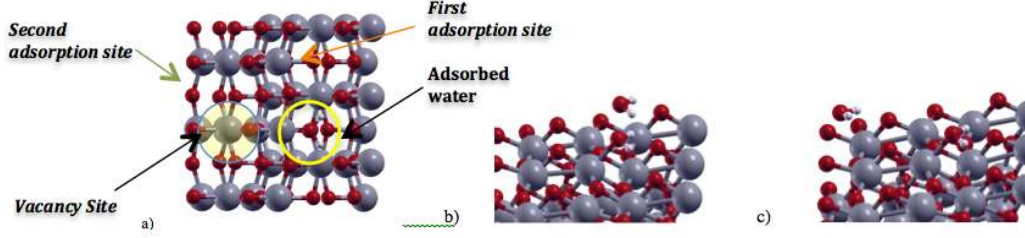


Figure 4: Top view of the slab. The arrows show the possible sites for the second water (a). The first configuration showed by the red arrow is shown in detail in (b) and the second one showed by the orange arrow is shown in detailed in (c).

		GGA+U	GGA
$E_{ads(1H_2O)}$	(eV)	-1.28	-1.11
$E_{ads(2H_2O)(conf\ 1)}$	(eV)	-0.90	-0.85
$E_{ads(2H_2O)(conf\ 2)}$	(eV)	-0.80	-0.78

Table 2: Adsorption Energy per water molecule calculated with GGA and GGA+U for the one-water adsorbed system and the two water-adsorbed systems

We have shown that the GGA+U method is needed to account for the correct correlation energy being mandatory to calculate the correct Oxygen vacancy formation energy and properties; however this method is computationally very expensive and the inclusion of the Hubbard corrections affects just slightly the water adsorption (see Table 2). In order to show this in a more quantitative manner, we have defined and calculated some quantities, for the slab with one or two adsorbed waters, that allowed us to evaluate the error that one commits using a standard GGA functional instead of GGA+U in the adsorption physical-chemistry processes here encountered. The quantities are:

$$\epsilon_n = \frac{\int_{\Gamma} (n_{Hubb} - n_o) d\mathbf{r}}{\int_{\Gamma} n_{Hubb} d\mathbf{r}} \times 100 = \frac{\Delta q_{\Gamma}}{q_{Hubb}^{\Gamma}} \times 100$$

$$\epsilon_V = \frac{\int_{\Gamma} (V_{Hubb} - V_o) d\mathbf{r}}{\int_{\Gamma} V_{Hubb} d\mathbf{r}} \times 100 = \frac{\Delta V}{V_{Hubb}} \times 100$$

Where n_{Hubb} and n_o are the electron density calculated with GGA+U and GGA respectively and V_{Hubb} and V_o are electrostatic potential calculated with GGA+U and GGA respectively. ϵ_V and ϵ_n quantify the difference in the electron density and electrostatic potential and they have been calculated in region Γ above the surface where the adsorption processes take place. Another calculated quantity average difference of the Atomic Displacement (AD):

$$AD = \frac{\sum_i^N |r_i^{Hubb} - r_i^o|}{N}$$

Where r_i^{Hubb} and r_i^o are the position of the i -th atom in the system with GGA+U and GGA respectively and N are the number of atoms. The AD quantifies the geometrical difference between the systems.

The table below shows the values of these three quantities; as these values are very small it is feasible to avoid the calculation of Hubbard correction in the adsorption of amino acids since the enormous increase of the computational costs required is not justified by the small differences found for these quantities and the adsorption energies (Table 2).

	ϵ_n [%]	ϵ_V [%]	AD [\AA]
1H ₂ O-system	5.5	2.4	0.8
2H ₂ O-system	7.5	2.6	1.0

Table 3: ϵ_n , ϵ_V , and AD values calculated for the systems with one and two adsorbed molecules in the surface

3.3 Amino-acids adsorption

The adsorption energies for the Lysine and for the Arginine have been calculated in both “dry” and “hydrated” configuration. Because both the amino-acids are positively charged in environment at pH 7, we simulated them in this protonated state so after a full minimization calculation using a charged cell a counter ion has been introduced achieving a neutral cell. Finally a self-consistent calculation has been performed in order to calculate the energy of the system. This choice has been adopted to avoid the well-known total error due to charged super-cells avoiding the Makov-Payne correction scheme [8] that is not straightforward in such inhomogeneous systems. The adsorption energy is:

$$E_{\text{ads}} = E_t - E_{\text{slab}} - E_{\text{amino}+(\text{H}_2\text{O})+\text{ion}}$$

where E_t is as usual the total energy of the system, E_{slab} is the energy of the slab with the adsorbed waters on it and $E_{\text{amino}+(\text{H}_2\text{O})+\text{ion}}$ is the energy of the amino acids with the water shell (when it is present) and the counter ion.

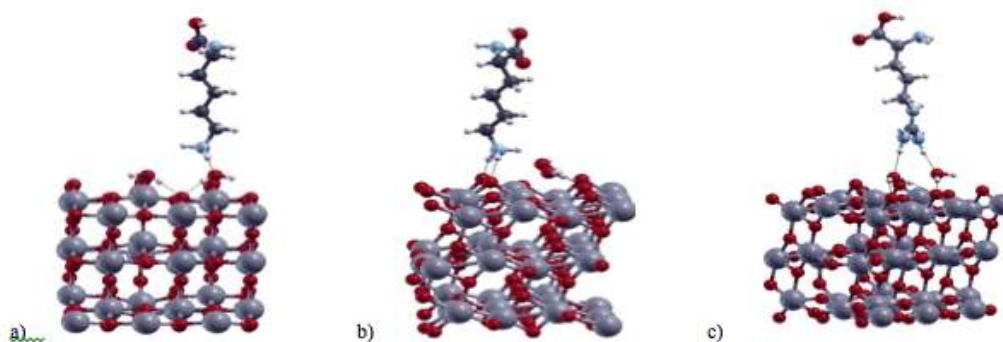


Figure 5: The final configurations of the dry Lysine (a and b) and Arginine (c)

First of all we have examined dry amino-acids, i.e. the adsorption of amino acids without their hydration shells. We choose two different initial configurations for the energy calculation of the Lysine. One of this provides the $-\text{NH}_3$ of the amino-acids side chain between the two adsorbed molecules while the other one, instead, provides this group above one of the molecule. These two initial configurations lead to two different final configurations (Fig. 5a and 5b). In the first final configuration Lysine interacts directly with the surface while in the second one the amino-acid adsorption is fully mediated by waters via hydrogen bonds. The error introduced by neglecting the Hubbard correction is remarkable only for the first configuration (see Table 4). Only one initial configuration has been chosen for the Arginine. The final configuration provides the amino-acids makes two hydrogen bond with the adsorbed water.

Then we have considered the amino-acids with their hydration shells. The water shell surround the two amino-acids is the result of Classical Molecular dynamics simulation runs and the same criteria of previous articles has been followed [1]. Just few water molecules actually mediate the adsorption of the amino-acids with the surface, thus a first minimization run has been performed to identify which of them interacts with the biomolecules; then a second run was performed to calculate the energies.

Two different initial configurations for the Lysine have been chosen that lead to two different final configurations. In the first one the adsorption is mediated only by the waters of the amino-acid hydration shell that form bonds directly with the surface. In the second one the adsorption is mediated by both the amino-acid hydration shell and the TiO₂ surface waters forming H-bonds. The adsorption of the Arginine is mediated by the water molecules belonging to the water shell which makes hydrogen bonds with the adsorbed water molecules on the surface itself. The calculated energies are summarized in the table below.

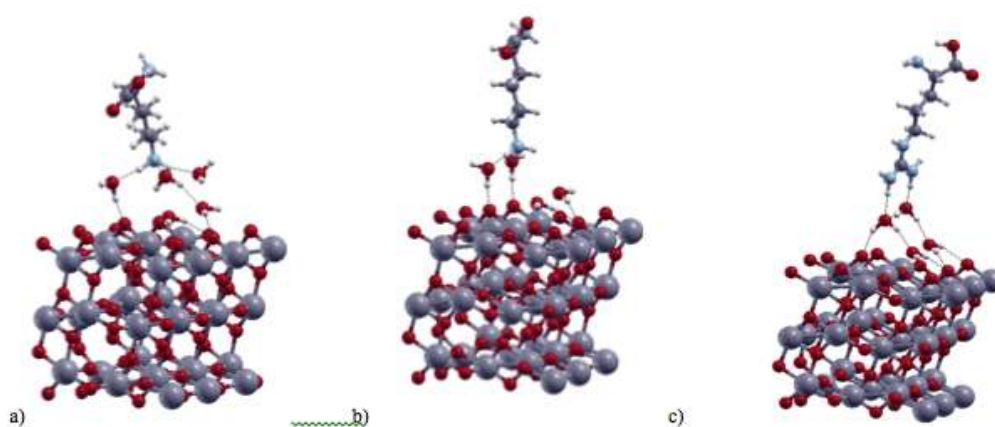


Figure 6: The final configuration of hydrated Lysine (a and b) and Arginine (c)

	<i>Arg.</i>	<i>Lys</i>	
		<i>Conf. 1</i>	<i>Conf. 2</i>
<i>Dry amino (eV)</i>	-2.20	-3.11	-2.52
<i>Hydrated amino (eV)</i>	-2.29	-2.67	-2.56

Table 4: Final Adsorption Energy of dry and hydrated amino-acids

3 Discussion and Conclusions

All the results reported agree in predicting that the presence of a sub-surface oxygen vacancy improve the amino acid adhesion with respect to the slab without defect [1]. This might be due to the localization of an electron in the first layer of the surface which could increase the electrostatic attraction between surface and the amino-acids. The lower adsorption energy (in absolute value) for the Arginine with respect to Lysine is mainly due to its the steric hindrance that keeps its side chain away from the surface; thus it is more efficiently screened by waters and is less affected by the electrostatic and long-range interactions.

This is an important difference between Arginine and Lysine: while Arginine adsorption is mediated by two waters layer, i.e. Arginine is adsorbed above the second water layer, in the Lysine case, for both the final configurations, the amino-acids is adsorbed “within” the second water layer, differently than what occurs on the A-(101) surface without the vacancy. As discussed previously, the lower hindrance of the Lysine amine ending group causes the amino acid to get close to the surface thus increasing the attractive electrostatic and long-range contributes to the total adsorption energy. Finally, it can be noticed from the data reported in Table 4 that the adsorption energies for

the Lysine in the second configuration and for the Arginine are slightly larger in the hydrated case with respect to the dry case. This behavior is unexpected because the second water shell should behave as a screening layer that lowers the electrostatic and the long-range interactions with the surface leading to lower adsorption energies. However, on the other hand, the number of hydrogen bonds in the hydrated configurations increases with respect to the dry configurations for both the amino-acids. The waters belonging to the second shell, indeed, both in the arginine and in the lysine case form extra bonds with the surface. This contribution leads to a larger adsorption energy and thus the competition between the screening due to the second water shell and the formation of the "extra" hydrogen-bonds yields a slightly larger adsorption energy. The competition between these two effects doesn't take place in the first lysine configuration where the second water shell doesn't form new hydrogen bonds with the surface. The adsorption energy for this configuration, indeed, is considerably smaller in the hydrated case. Although it has to be noticed that the first dry lysine configuration is affected by a larger error for neglecting the Hubbard correction.

In conclusion the A-(101) TiO₂ shows a large affinity for both the amino-acids and moreover such a surface seems to be selective between the two examined amino acids with the Lysine showing larger affinity than Arginine. Finally the study of this adsorption phenomenon could be further developed using, for instance, enhanced sampling Molecular Dynamics Techniques, like metadynamics, in order to explore different thermodynamic stable states as the adsorption and the desorption states, including the temperature effect and all the necessary water molecules to reproduce the biological environment.

The computing resources and the related technical support used for this work have been provided by CRESCO/ENEAGRID High Performance Computing infrastructure and its staff [9]. CRESCO/ENEAGRID High Performance Computing infrastructure is funded by ENEA, the Italian National Agency for New Technologies, Energy and Sustainable Economic Development and by Italian and European research programmes, see <http://www.cresco.enea.it/english> for information.

References

- [1] Lorenzo Agosta, Giuseppe Zollo, Caterina Arcangeli, Francesco Buono- core, Fabrizio Gala, and Massimo Celino. Water driven adsorption of amino acids on the (101) Anatase TiO₂ surface: an ab initio study. *Physical Chemistry Chemical Physics*, 17(3):1556–1561, 2015.
- [2] Oskam, Gerko, et al. "The growth kinetics of TiO₂ nanoparticles from titanium (IV) alkoxide at high water/titanium ratio." *The Journal of Physical Chemistry B* 107.8 (2003): 1734-1738.
- [3] Gao, Y., and S. A. Elder. "TEM study of TiO₂ nanocrystals with different particle size and shape." *Materials Letters* 44.3 (2000): 228-232.
- [4] Hongzhi Cheng and Annabella Selloni. Energetics and diffusion of intrinsic surface and subsurface defects on anatase TiO₂ (101). *The Journal of chemical physics*, 131(5):054703, 2009.
- [5] QUANTUM ESPRESSO: a modular and open-source software project for quantum simulations of materials Paolo Giannozzi et al 2009 *J. Phys.: Condens. Matter* 21
- [6] Giuseppe Mattioli, Paola Alippi, Francesco Filippone, Ruggero Caminiti, and Aldo Amore Bonapasta. Deep versus shallow behavior of intrinsic defects in rutile and Anatase TiO₂ polymorphs. *The Journal of Physical Chemistry C*, 114(49):21694–21704, 2010.
- [7] Yunbin He, Antonio Tilocca, Olga Dulub, Annabella Selloni, and Ulrike Diebold. Local ordering and electronic signatures of submonolayer water on Anatase TiO₂ (101). *Nature materials*, 8(7):585–589, 2009.
- [8] G Makov and MC Payne. Periodic boundary conditions in ab initio calculations. *Physical Review B*, 51(7):4014, 1995.
- [9] G. PONTI et al., "The role of medium size facilities in the HPC ecosystem: the case of the new CRESCO4 cluster integrated in the ENEAGRID infrastructure", *Proceedings of the 2014 International Conference on High Performance Computing and Simulation, HPCS 2014*, art. no. 6903807, pp. 1030-1033.

Neutronics calculations for the design of DEMO WCLL reactor

Rosaria Villari^{1*}, Giovanni Mariano², A. Del Nevo¹, Davide Flammini¹ and Fabio Moro¹

¹ENEA, Department of Fusion and Nuclear Safety Technology, I-00044 Frascati (Rome) and Brasimone (Bologna), Italy

² DIAEE, Sapienza University of Rome, Corso Vittorio Emanuele II 244, 00186, Rome, Italy

ABSTRACT. Neutronics calculations with MCNP5 Monte Carlo code have been performed in 2015 to support the design of DEMO reactor and in particular of in-vessel components within EUROfusion Power Plant Physics & Technology program. This paper summarise results of nuclear analyses for the design of a Water Cooled Lithium Lead (WCLL) DEMO blanket concept.

1 Introduction

Neutronics plays an important role for all of design of DEMO activities since it has to provide essential data which are required for the nuclear design of the reactor and its components, its performance assessment and verification. Within EUROfusion Consortium Power Plant Physics & Technology (PPPT) program, ENEA is involved in several sub-projects to assess relevant nuclear response supporting the design of DEMO reactor and its components. In particular in 2015 neutronics analyses were performed for the present design of Water Cooled Lithium Lead (WCLL) DEMO blanket concept.

This blanket concept uses the Pb–15.8Li eutectic for the Tritium breeding and neutron multiplication and the cooling is provided by pressurized water. Neutronics calculations are required to assess the nuclear performances of the present design of WCLL breeder blanket concept, mainly to verify tritium self-sufficiency, shielding capabilities and to assess nuclear loads on the first wall, breeding blanket, supporting structures and manifolds. This paper summarizes the calculations and results of these analyses.

2 Neutronics calculations

Three-dimensional analyses have been performed with MCNP5 [1] Monte Carlo to assess the nuclear performances of the present design of WCLL breeder blanket concept [2]. Coupled neutron and gamma transport simulations were performed by means of parallelized version of MCNP5 Monte Carlo code in MPI on CRESCO4 clusters, to simulate more than 10^9 source particles. Tritium Breeding Ratio (TBR), power distribution, energy multiplication, Neutron Wall Loading (NWL) as well as spatial distribution of the neutron and secondary gamma fluxes, nuclear heating, neutron damage and he-production were assessed. More details can be found in [2,3].

2.1 Water Cooled Lithium Lead Breeding blanket design

Figure 1 shows the WCLL design 2015 of outboard equatorial module with manifold configuration and segmentation. The WCLL Multi Module Segment (MMS) scheme assumes 7 blanket modules both for the inboard and the outboard segment. The design of the blanket module includes a Eurofer steel box with FW, caps, back wall and a back-supporting structure (BSS) with inlet/outline pipes for the water and the LiPb. The box is filled with the LiPb liquid metal and reinforced by horizontal and vertically arranged stiffening plates.

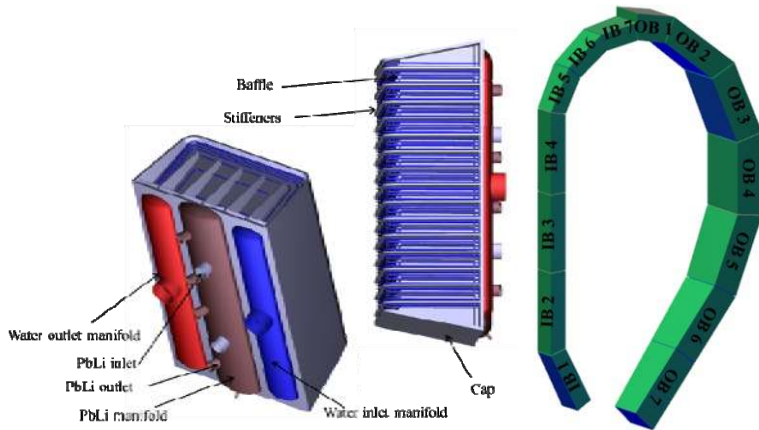


Fig. 1 – Outboard equatorial module of WCLL 2015 design (left) and WCLL segmentation (right)

The DEMO 2015 WCLL MCNP neutronic model developed by ENEA is shown in figure 2. The first wall (FW) and caps are made of Eurofer and water. The breeder zone has homogenised material composition of LiPb, EUROFER and water. Back-supporting structure/manifold configuration is assumed as very compact component with a homogenised material composition of Eurofer, water and LiPb.

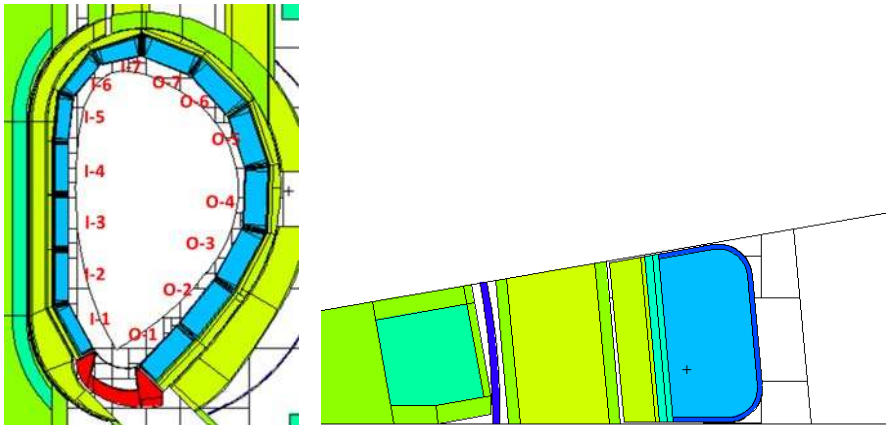


Fig. 2 –2015 DEMO WCLL MCNP model: poloidal-radial section (left) and radial-toroidal sections at z=30 cm in Inboard (right)

2.1 Results of Neutronics Calculations

The poloidal distribution of NWL and TBR for 2037 MW of Fusion power (P_{fus}) are shown in figure 3. Maximum NWL is in the Outboard equatorial modules O3-O4 (1.33 MW/m^2). In the Inboard the maximum is 1.1 MW/m^2 and the poloidal average is 1 MW/m^2 . The calculated global TBR for the analyzed WCLL DEMO configuration is 1.127 that guarantees the self-sufficiency of the reactor. The 99% of the tritium is produced in the breeder zone, and the rest is generated in the back-plate, manifold and in the back-supporting zone.

Neutron flux, nuclear heating, dpa and He-production in steel have been calculated along the inboard mid-plane (see figure 4). The total and fast neutron fluxes at the FW are $5 \times 10^{14} \text{ n/cm}^2/\text{s}$ and $3.4 \times 10^{14} \text{ n/cm}^2/\text{s}$, respectively. The blanket/manifold system provides an attenuation of more than two orders of magnitude to the VV inner shell. The neutron flux further decreases of six orders of magnitude across the VV, being $4.8 \times 10^8 \text{ n/cm}^2/\text{s}$ (total) and $2.9 \times 10^8 \text{ n/cm}^2/\text{s}$ (fast) on the TF, well below the limit ($10^9 \text{ n/cm}^2/\text{s}$).

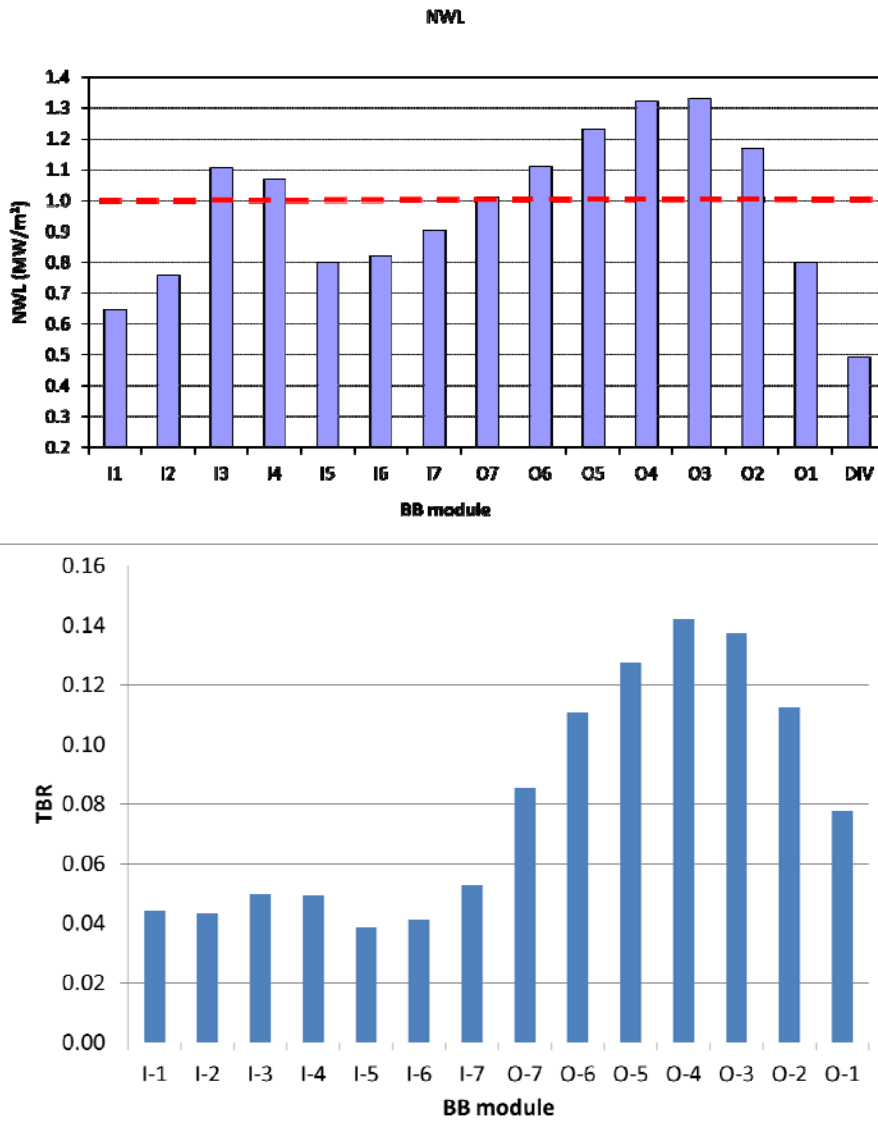


Fig. 3—Neutron Wall Loading (top) and TBR (bottom) poloidal distribution normalized to 2037 MW of fusion power

The dpa/FPY in EUROFER is 9.8 at the FW and it decreases to 0.03 at the VV inner shell steel. Considering the limit on VV of 2.75 dpa, the present configuration is sufficient to protect VV over DEMO lifetime. The maximum values of the nuclear heating on steel components are $\sim 7.5 \text{ W/cm}^3$ on FW Eurofer, 0.1 W/cm^3 on VV inner shell. In the TF coil Inboard leg, first turn the nuclear heating density is $7 \times 10^{-6} \text{ W/cm}^3$, well below the limit of $5 \times 10^{-5} \text{ W/cm}^3$. Concerning He-production in steel, the calculated value at the FW is 130 appm/FPY¹. It drops to about 0.5 appm in the VV and behind the VV it is lower than 10^{-4} appm.

¹ Low boron content is assumed for both SS316 and EUROFER (0.001 wt%)

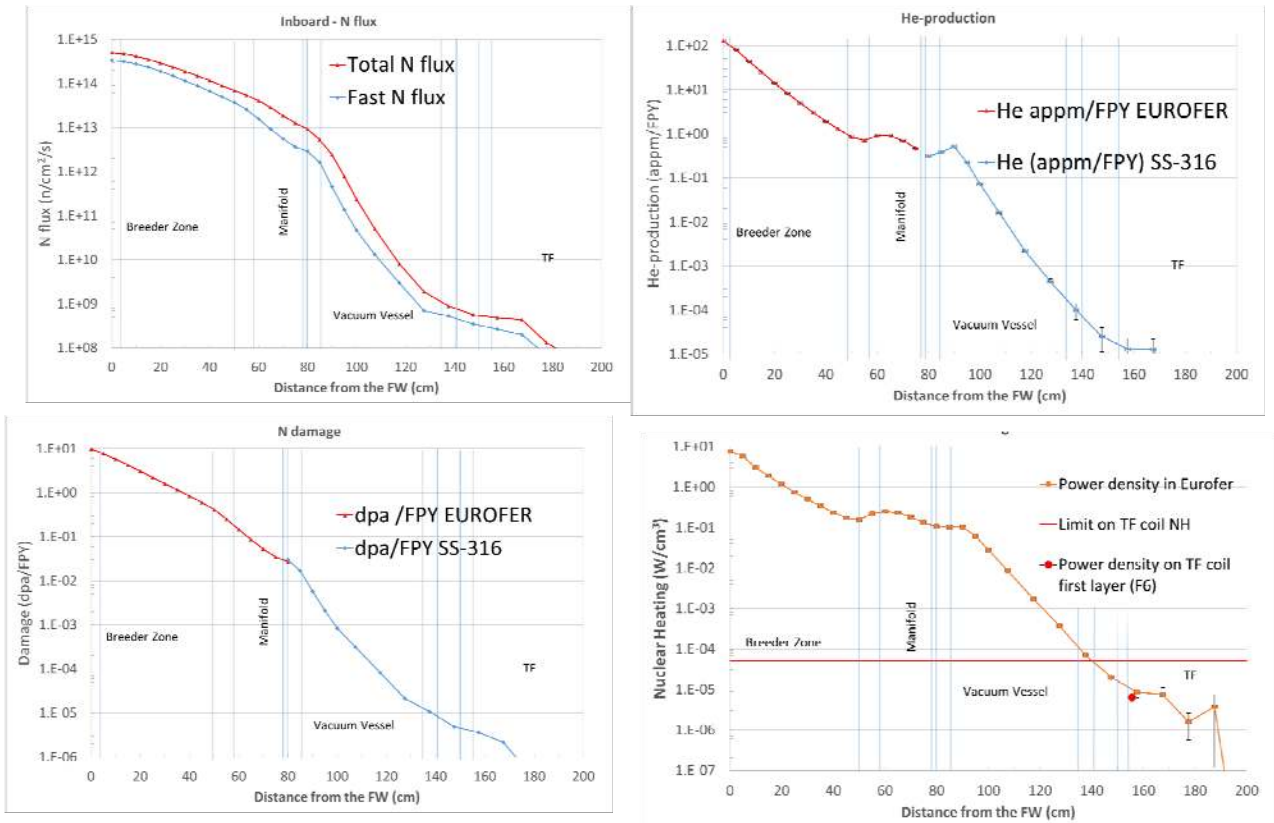


Fig. 4 –Neutron flux, dpa, nuclear heating on steel and He-production radial profile in Inboard (see figure 2 right)

Conclusions

Three-dimensional neutronics calculations were performed with MCNP5 assuming DEMO 2015 configuration and recent WCLL blanket design. Results showed that the tritium self-sufficiency design target and shielding requirements to protect vacuum vessel and toroidal superconductive coils are fulfilled.

References

- [1] X-5 Monte Carlo Team: MCNP - *A General Monte Carlo N-ParticleTransportCode, Version 5*, Los Alamos National Laboratory, Los Alamos, New Mexico, USA, April 2003.
- [2] A. Del Nevo et.al., WCLL Design Report 2015-Internal Deliverable BB-3.2.1-T002-D001, IDM EUROfusion 2N6WLQ
- [3] A. Del Nevo et.al., *WCLL breeding blanket design and integration for DEMO 2015: status and perspectives*, submitted to Fus. Eng. Des.

THE NETWORK ARCHITECTURE UNDERLYING THE CRESCO INFRASTRUCTURE OF ENEA PORTICI

D. Giammattei¹, M. De Rosa¹, A. Colavincenzo², R. Guadagni³

¹ENEA CR Portici, DTE-ICT-RETE, P.le E. Fermi, 1 - 80055 Portici(NA), Italy

²ENEA CR Portici, DTE-ICT-HPC, P.le E. Fermi, 1 - 80055 Portici(NA), Italy

³ENEA CR Casaccia, DTE-ICT-RETE, Via Anguillarese, 301 – 00123 S. Maria di Galeria (Roma)

ABSTRACT. In this paper a short description will be given about the networking infrastructural facilities ensuring the CRESCO (Computational Research Center for Complex Systems) cluster communications through the Ethernet and TCP/IPv4 standard protocols. A short description will be also given about the architectural adjustments to increase the global reliability and reduce the latency values in the TCP/IP communications.

1 Introduction

As you can see in Fig. 1, the CRESCO HPC [2] cluster in Portici, whose last achievements, made up with 304 and 42 nodes, are respectively named CRESCO4 [4] and CRESCO5 (besides the 64 former nodes named CRESCO3), is spread over an eight rack cabinets set. As known, the communications between the CRESCO nodes, with regard to the closely computational aims, currently performed through numerical simulation jobs in a cluster environment, are deployed through the Infiniband protocol.

In all the other situations as, for example, in the ordinary communications with other nodes in the LAN (Local Area Network) or in the WAN (Wide Area Network), standard Ethernet (1GbE or 10GbE or 40GbE) and TCP/IPv4 protocols are used.

The Infiniband communications are managed by a proper Infiniband switching device through a dedicated set of cables connected to each node's Infiniband interface. The data flows other than the Infiniband communications are managed through a set of switching/routing devices, opportunely placed in the inner area of the Portici Campus and based, as said above, on the Ethernet and TCP/IPv4 protocols.

As shown in Fig. 1, seven of the eight CRESCO rack cabinets are provided with a GbE switch stack consisting of two interconnected modules. Into each of them are plugged all the Ethernet cables from the nodes placed in the same cabinet. In detail, all the nodes from five CRESCO4 rack cabinets (just one, which is made up with a few not computational nodes, is connected by a single switching device), together with the nodes from the single CRESCO5 cabinet, are linked with six C5 EN (Extreme Networks) switch stacks. On the other hand, the nodes from the CRESCO3 cabinet, installed formerly than the others, are connected into the two modules of the Cisco 3750 switch stack.

Network scheme

In planning the network architecture two factors are been mainly considered :

- 1) The reduction as much as possible of the value of the latency with regard to the local and geographical communications based over the Ethernet and TCP/IPv4 protocols.
- 2) The improvement of the overall reliability through the redundancy of the physical paths as well as of the switching/routing devices.

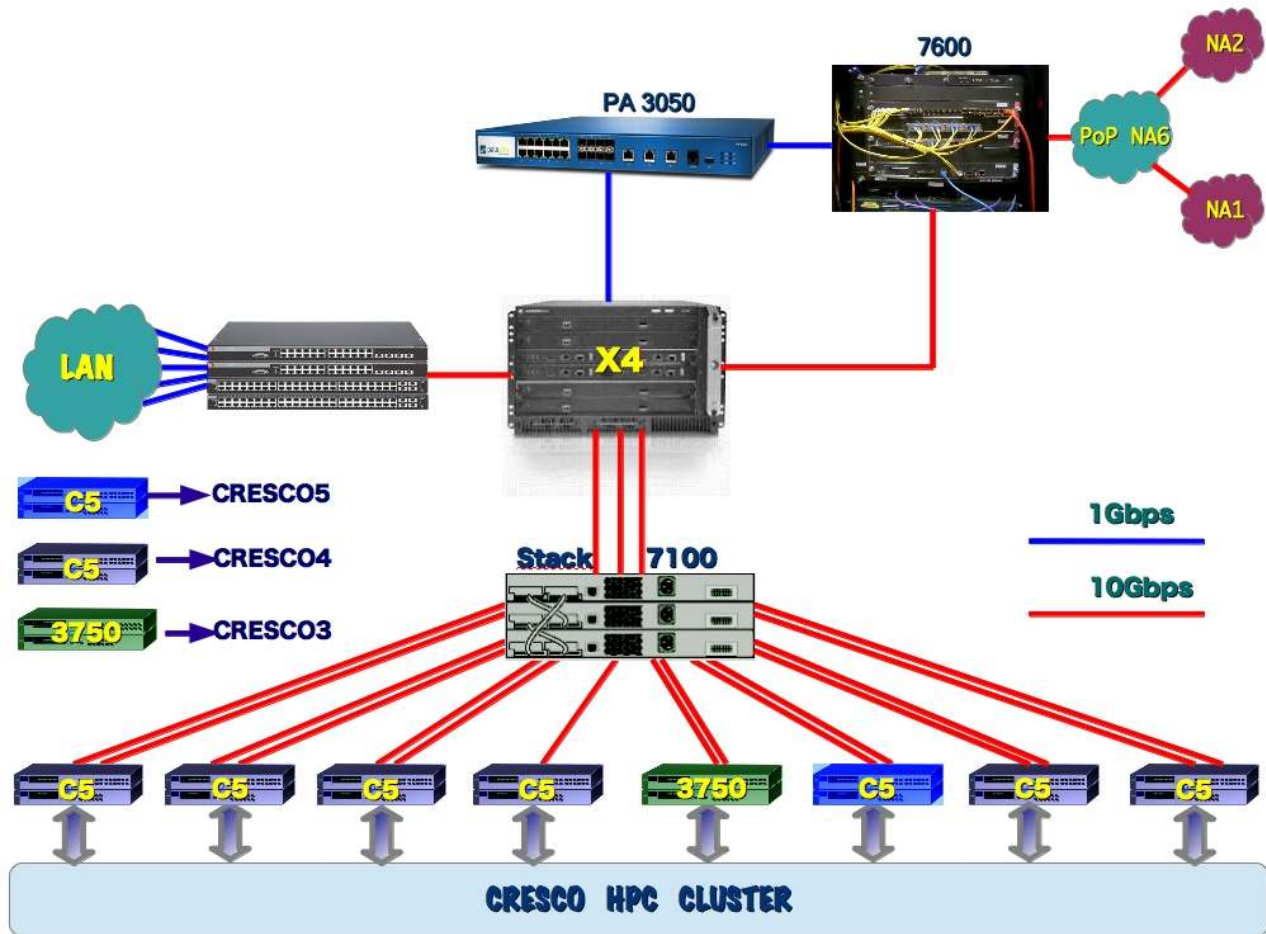


Fig.1 : Network infrastructure of CR Portici

As regards the first point, all the routes between the CRESCO switches and the remote GARR PoPs¹ of the main ENEA HPC clusters (Roma, Bari, Bologna), are been carried out to ensure throughputs with bandwidths of at least 10Gbps all along the entire physical path.

As you can see in Fig. 1 above, indeed, each of modules of the switch stack (one switch stack for CRESCO3, five for CRESCO4 and one for CRESCO5) is connected with a 10Gbps link to the main CRESCO switch EN 7100, made up with three modules connected to each other through 40Gbps network interfaces. So, every switch stack (two modules) will have a double 10Gbps

¹ GARR (Gruppo per l'Armonizzazione delle Reti della Ricerca) is the Italian Academic and Research Network.

PoP (Point of Presence) is a set of network devices owned and managed by the GARR Consortium that allows the whole research community to fully access the Internet network.

connection to the central main switch 7100. This double uplink, realized using LACP protocol (Link Aggregation Control Protocol) is logically equivalent to a single physical uplink.

On the other hand, the EN 7100 switch stack, always using the LACP aggregation method, is connected by three 10Gbps uplinks to the campus switch/router X4 Enterasys, that is the core device managing overall amount of the data flows outgoing and ingoing the Portici Center network. From the X4, at last, a 10Gbps uplink reaches directly the Cisco 7600 outer router. This uplink is an alternate path by which all the HPC data flows may bypass a Palo Alto Networks 3050 firewall, that is the main security managing LAN device inspecting all the TCP/IP data packets outgoing/ingoing the Portici local area network.

This special 10Gbps link has been performed through dedicated “Source Routing” rules opportunely implemented over the X4 core switch and Cisco 7600.

Source Routing, or PBR (Policy Based Routing) is a special way to managing packets data flows widely used among routing devices and also deployed over both our X4 Enterasys switch and 7600 Cisco router. This particular routers programming technique is implemented so that single data flow can be easily splitted into two (or more) physical paths between two networking devices depending on specified and previously fixed policies [1]. As regards our specific needs, each of the two devices involved in PBR technique is programmed to inspect both IP fields named “Source Address” and “Destination Address”, instead of reading the only “Source Address” field as normally occurs in an ordinary managing process of a TCP/IP packets data flow. In this way we are able to address towards a fixed path the only flows that are compliant with fixed policies about “Source Address” and “Source Destination” IP packets. In our case, the aim was to give priority to the ENEAGRID data flows between the HPC nodes, in order to reach the lowest possible latency values. Consequently the PBR rules are been performed, according to the previously mentioned criteria, over the following interfaces:

- 1) The X4 core switch/router interfaces, with regard to the packets data flows originating from the inner LAN (exactly from the CRESCO zone HPC nodes) and outgoing towards the others HPC nodes of the ENEAGRID.
- 2) The WAN interfaces of the 7600 Cisco router, with regard to the packets incoming from the outer ENEA HPC nodes and ingoing towards the CRESCO HPC zone.

So, in this way we have obtained that the “valuable” data exchanges between ENEA nodes, that is those involving the HPC nodes ones, are performed by avoiding the crossing of the data flows through a latency increasing factor, as a Firewall device, and following a congestion-free physical path, that is the 10Gbps bypass line between the X4 and the 7600 devices, without any undesirable bottlenecks. The same techniques are been deployed in the others HPC ENEA data centers.

The 7600 Cisco router is the outermost device in the ENEA Portici LAN and is directly connected, with a 10Gbps link from an interface by its WAN side, to a similar interface of a MX480 Juniper router. Juniper MX480, as subset of the PoP NA6 facilities, is managed directly by the GARR team and is located, with the others PoP networking devices, in a data center room of DTE-ICT-RETE division. The PoP NA6, at last, is connected by means of two 10Gbps uplinks with the main PoPs, named NA1 and NA2, of the neapolitan area and, via these ones, to the geographical GARR grid. Into the wide geographical networking area what mostly affects the effectiveness of the data flows between the ENEAGRID nodes is the throughput involving interconnections between the primary GARR PoPs of Napoli, Roma, Bari, Bologna. At the moment the throughput along the optical physical paths between these primary nodes covers a bandwidth in the range from 20 to 100 Gbps. Obviously along these geographical paths, shared with all the others academic or research entities of the GARR community, the latency values may be randomly affected by undesirable congestion phenomena, mainly in the time slots probabilistically most used, as consequence of the sharing of the same medium between several heterogeneous data flows.

With regard to the second item, concerning the reliability issues, a special care has been focused on reducing the “single points of failure” all along the main CRESCO physical paths by mainly working about redundancy of the uplinks and of the switching/routing devices.

As seen above, each of the C5 switch stacks is connected by a double uplink to the main 7100 switch stack. Each of these uplink is connected to a different module of the 7100 so that, even in case of a failure, the alternate path continues to ensure the connectivity of the C5. A total absence of connectivity occurs only in the eventuality of a simultaneous failure of all three modules of the central switch 7100. On the other hand the 7100 switch is in turn connected through three different physical paths to three different modules of the campus central switch X4. An hypothetic failure of one of these modules would not affect the functionality of the other modules and, therefore, the connectivity of the devices connected to them. If a complete failure of the apparatus would anyway occur, a backup device is arranged able to ensuring the same functionalities and performance of the X4.

Among a short time is also planned the acquisition of a further border device to be connected, by means of the protocol VRRP (Virtual Router Redundancy Protocol), the the existing Cisco 7600 [3]. In this new configuration also a possible failure of 7600 or, alternatively , of the new border router, would not affect at all the continuity of the connectivity also in the WAN perspective.

References

[1] Karl Solie, Leah Lynch: CCIE Practical Studies: “*Configuring Route-Maps and Policy-based Routing*”, Cisco Press, 2003;

[2] G. Bracco etc.: “*CRESCO HPC System integrated into ENEA-GRID environment*” (Proceedings of the Final Workshop of the Grid Projects of the Italian National Operational Programme 2000-2006 Call 1575, 2009;

[3] Teare Diane: “*Implementing Cisco IP Routing (ROUTE)*” Foundation Learning Guide. Cisco Press, 2010;

[4] G. Ponti etc.: “*The role of medium size facilities in the HPC ecosystem: the case of the new CRESCO4 cluster integrated in the ENEAGRID infrastructure*”, Proceedings of the 2014 International Conference on High Performance Computing and Simulation, HPCS 2014, art. no. 6903807, 1030-1033.

ENEA
Promotion and Communication Service

www.enea.it

Printed at the ENEA Technographic Laboratory – Frascati

November 2016

